

**CYCLIC STRESS-STRAIN  
AND  
PLASTIC DEFORMATION ASPECTS  
OF  
FATIGUE CRACK GROWTH**

 **STP 637**

**AMERICAN SOCIETY FOR TESTING AND MATERIALS**

# CYCLIC STRESS-STRAIN AND PLASTIC DEFORMATION ASPECTS OF FATIGUE CRACK GROWTH

A symposium  
sponsored by ASTM  
Committee E-9 on Fatigue  
AMERICAN SOCIETY FOR  
TESTING AND MATERIALS  
St. Louis, Mo., 2-8 May 1976

ASTM SPECIAL TECHNICAL PUBLICATION 637  
L. F. Impellizzeri, symposium chairman

List price \$25.00  
04-637000-30



AMERICAN SOCIETY FOR TESTING AND MATERIALS  
1916 Race Street, Philadelphia, Pa. 19103

©BY AMERICAN SOCIETY FOR TESTING AND MATERIALS 1977  
Library of Congress Catalog Card Number: 77-083428

NOTE

The Society is not responsible, as a body,  
for the statements and opinions  
advanced in this publication.

Printed in Tallahassee, Fla.  
December 1977

## Foreword

The symposium on Cyclic Stress-Strain and Plastic Deformation Aspects of Fatigue Crack Growth was presented at a meeting held in St. Louis, Mo., 2-8 May 1976. The symposium was sponsored by the American Society for Testing and Materials through its Committee E-9 on Fatigue. L. F. Impellizzeri, McDonnell Aircraft Company, presided as symposium chairman.

## Related ASTM Publications

**Manual on Statistical Planning and Analysis for Fatigue Experiments,  
STP 588 (1975), \$15.00 (04-588000-30)**

**The Influence of State of Stress on Low-Cycle Fatigue of Structural Materials:  
A Literature Survey and Interpretive Report, STP 549 (1974), \$5.25  
(04-549000-30)**

**Cyclic Stress-Strain Behavior—Analysis, Experimentation, and Failure  
Prediction, STP 519 (1973), \$28.00 (04-519000-30)**

## A Note of Appreciation to Reviewers

This publication is made possible by the authors and, also, the unheralded efforts of the reviewers. This body of technical experts whose dedication, sacrifice of time and effort, and collective wisdom in reviewing the papers must be acknowledged. The quality level of ASTM publications is a direct function of their respected opinions. On behalf of ASTM we acknowledge with appreciation their contribution.

*ASTM Committee on Publications*

## Editorial Staff

Jane B. Wheeler, *Managing Editor*

Helen M. Hoersch, *Associate Editor*

Ellen J. McGlinchey, *Senior Assistant Editor*

Kathleen P. Zirbser, *Assistant Editor*

Sheila G. Pulver, *Assistant Editor*

# Contents

## Introduction

<b>The General Cyclic Stress-Strain Response of Aluminum Alloys—</b>	
CAMPBELL LAIRD	3
Behavior of Binary Alloys	6
Behavior of Complex Alloys	9
Cyclic Stress-Strain Response Under Variable-Amplitude Loading	23
Conclusions	32
<b>Fatigue Crack Tip Plasticity—J. LANKFORD, D. L. DAVIDSON, AND</b>	
T. S. COOK	36
Plastic Zone Size Calculations	38
Plastic Zone Size	42
Plastic Zone Shape	46
Conclusions	53
<b>Finite-Element Analysis of Crack Growth Under Monotonic and</b>	
<b>Cyclic Loading—J. C. NEWMAN, JR.</b>	56
Methods of Analysis	58
Crack-Growth Criterion	60
Crack Growth Under Monotonic and Cyclic Loading	62
Concluding Remarks	73
Discussion	78
<b>Analysis and Investigation of Small Flaws—A. TALUG AND</b>	
K. REIFSNYDER	81
Analysis	84
Discussion of Results	86
Conclusions	92
<b>Crack Growth During Low-Cycle Fatigue of Smooth Axial Specimens—</b>	
N. E. DOWLING	97
Laboratory Investigation	98
Discussion	105
Conclusions and Recommendations	116
<b>A Fatigue Crack Growth Analysis Method Based on a Simple Repre-</b>	
<b>sentation of Crack-Tip Plasticity—M. F. KANNINEN, C. ATKINSON,</b>	
AND C. E. FEDDERSON	122
Conceptual Basis of the Model	123
Analysis Procedure	126
Computational Results for Constant $\Delta K$ Load Cycles	131
Discussion and Comparison with Alternative Approaches	134
Conclusions	137

<b>Analysis of Crack Growth Following Compressive High Loads Based on Crack Surface Displacements and Contact Analysis—</b>	
H. D. DILL AND C. R. SAFF	141
Crack Surface Displacement Analysis	142
Analysis of COD with Compressive Loads	146
Crack Growth Following Compressive High Loads	147
Effect of Cyclic Strain Hardening/Softening	151
Summary	152
<b>Fatigue Analysis of Cold-Worked and Interference Fit Fastener Holes—</b>	
D. L. RICH AND L. F. IMPELLIZZERI	153
Fatigue Life: Crack Initiation Plus Crack Growth	154
Test Program	156
Analytical Techniques	158
Conclusions	174
<b>Fatigue Crack Growth and Life Predictions in Man-Ten Steel Subjected to Single and Intermittent Tensile Overloads—</b>	
R. I. STEPHENS, E. C. SHEETS, AND G. O. NJUS	176
Material and Test Procedures	178
Test Results	179
Mathematical Model	185
Discussion	187
Summary and Conclusions	188
Discussion	189
<b>Load Interaction Effects on Fatigue Crack Growth in A514F Steel Alloy—</b>	
W. J. MILLS, R. W. HERTZBERG, AND R. ROBERTS	192
Experimental Procedure	194
Presentation and Discussion of Results	195
Conclusions	206
<b>Critical Remarks on the Validity of Fatigue Life Evaluation Methods Based on Local Stress-Strain Behavior—</b>	
D. SCHÜTZ AND J. J. GERHARZ	209
Life Prediction	210
Procedure	213
Results and Discussion	218
Conclusion	221

# Introduction

---

For many years, fatigue analysis simply meant finding the right applied stress-cycles to failure ( $S-N$ ) curve and using Miner's rule. When the importance of plastic deformation at stress concentrations became apparent, analysis procedures and test techniques were developed to include the effects of tensile and compressive residual stresses caused by local yielding and to include strain hardening and softening and cyclic stress-strain hysteresis effects in the fatigue computations. These procedures were used for what could be termed crack initiation analysis. More recently, crack growth analysis using continuum mechanics' principles has emerged as an important tool in designing fatigue- and fracture-resistant structures. The primary objective of this symposium and publication was to focus attention on efforts to combine the disciplines of cyclic stress-strain and plastic deformation analysis and fracture mechanics to further the understanding of fatigue crack growth in structures.

In support of this objective, the following topics were addressed:

1. Cyclic stress-strain and plastic deformation in the region of growing cracks.
2. Significance of material metallurgical characteristics.
3. Significance of variable-amplitude loading as compared to constant amplitude loading.
4. Crack growth analysis methods including the effects of cyclic stress-strain and plastic deformation.
5. Percentage of total fatigue life that can be analyzed using the continuum mechanics approach to crack growth analysis.
6. Combination of residual stress effects and fracture mechanics for cracks originating at points of stress concentration.

This volume includes eleven papers discussing this list of topics from various aspects that should be of use to designers and materials and structural scientists and engineers. It should not be considered a final treatise but rather a contribution to the state of the art to stimulate thinking on this important subject for research and design.

## 2 FATIGUE CRACK GROWTH

Grateful acknowledgment is given to the authors, the reviewers, and Jane B. Wheeler and her staff.

*L. F. Impellizzeri*

Branch Chief, Technology-Strength,  
McDonnell Aircraft Company,  
St. Louis, Mo. 63166; symposium  
chairman.

# The General Cyclic Stress-Strain Response of Aluminum Alloys

---

**REFERENCE:** Laird, Campbell, "The General Cyclic Stress-Strain Response of Aluminum Alloys," *Cyclic Stress-Strain and Plastic Deformation Aspects of Fatigue Crack Growth, ASTM STP 637*. American Society for Testing and Materials, 1977, pp. 3-35.

**ABSTRACT:** The cyclic stress-strain response of a wide range of binary, ternary, and complex commercial and experimental-commercial aluminum alloys has been investigated. In addition to constant-amplitude tests, incremental, block, random loading tests, and other specialized tests have been used in assessing cyclic response. The conditions under which cyclic hardening or softening occur have been elucidated, and general conclusions have been drawn about cyclic response in aluminum alloys.

**KEY WORDS:** stresses, strains, stress cycle, deformation, hardening, softening, aluminum alloys, loading, tests, particles, dispersions, fatigue, damage, fracturing, crack propagation

When a metal or alloy is cycled through a constant- or varying-strain amplitude, large changes normally occur in its flow stress; depending on the metal and its processing history, hardening or softening may occur. Cyclic stress-strain response (CSSR) is the term given to describe the relationships between the flow stress and the cyclic strain, and it recently has been shown to be useful both for understanding the fatigue process and as a phenomenon worth consideration in designing against fatigue. For examples, on the basis of CSSR, Laird has supported the existence of a fatigue limit in most metals and alloys, similar to that well accepted in steels [1],<sup>2</sup> and Wetzel has developed a new method of predicting damage under variable loading [2]. It is reasonable, then, to attempt in this publication to combine cyclic stress-strain response and fracture mechanics with the aim of an improved understanding of crack propagation.

One of the major unsolved problems in crack propagation is the understanding of the role of metallurgical factors in controlling crack propaga-

<sup>1</sup>Chairman, Department of Metallurgy and Materials Science, University of Pennsylvania, Philadelphia, Pa. 19174.

<sup>2</sup>The italic numbers in brackets refer to the list of references appended to this paper.

tion rates. Hahn and Simon [3] and Stoloff and Duquette [4] have reviewed these factors in aluminum alloys recently and conclude:

1. Statically strong alloys, such as 7075-T6, can show higher growth rates than less strong but more ductile alloys, such as 2024-T3.

2. Heat-to-heat variations in composition and processing, small amounts of cold work, and different heat treatments can alter the life of a typical alloy such as 2024-T3 by as much as 100 percent.

3. Brittle fracture modes associated with inclusions or intermetallic particles can double the rate of crack propagation when the advance per cycle is large ( $\sim 1 \mu\text{m}/\text{cycle}$ ).

These variations are not understood in detail, and it is worthwhile to explore whether CSSR, by describing the behavior of the material at a crack tip, may yield their explanation. If in fact the combination of CSSR and fracture mechanics can solve this problem and related problems such as crack propagation rates under variable loading, it is necessary that we have a firm understanding of CSSR in relation to microstructure.<sup>3</sup> One aim of this paper is to explore our present state of knowledge. However, a secondary aim is explained and justified in the following paragraphs.

It often happens that a metal or alloy subject to cyclic strains will harden rapidly in the first few applications of strain, but the hardening rate decreases with accumulating strains and eventually reaches zero, at which point the material is described as being "stable" or in "saturation." A common goal of cyclic hardening studies is to measure the cyclic stress-strain curve associated with this condition, defined as the curve formed by connecting the tips of stable hysteresis loops from constant-amplitude, strain-controlled fatigue tests of several specimens cycled at different strain ranges. Because the cyclic stress-strain curve (CSSC) is useful, engineers have documented it by several methods and for many metals. One special object of study has been developing alternative procedures for determining the CSSC. It was found, for example, that the incremental step test (see Fig. 1 for description) provides a useful method of measuring the CSSR of several metals at room temperature [5]. It is interesting, but perhaps not surprising, that such tests yielded essentially equivalent responses to that of constant-amplitude tests because the metals tested were wavy in slip mode [6], and it is known that metals of this type show history-independent cyclic response in most circumstances [7]. Metals of planar slip behavior can be expected to yield more complex results in incremental step tests, since they show a strong history dependence in their cyclic response [5]. In confirmation of this, Jaske et al, who studied Ni-Fe-Cr Alloy 800 and Type 304 stainless steel [8], found that, even at high temperature, the results of incremental

<sup>3</sup>The "microstructure" treated here is assumed to be uniform through the material and thus does not encompass macrostructural variations caused by processing difficulties such as segregation during solidification, incomplete recrystallization during solid state processing, and so forth. These macrovariations must be important in cyclic response and fatigue fracture, and more work is required for their study.

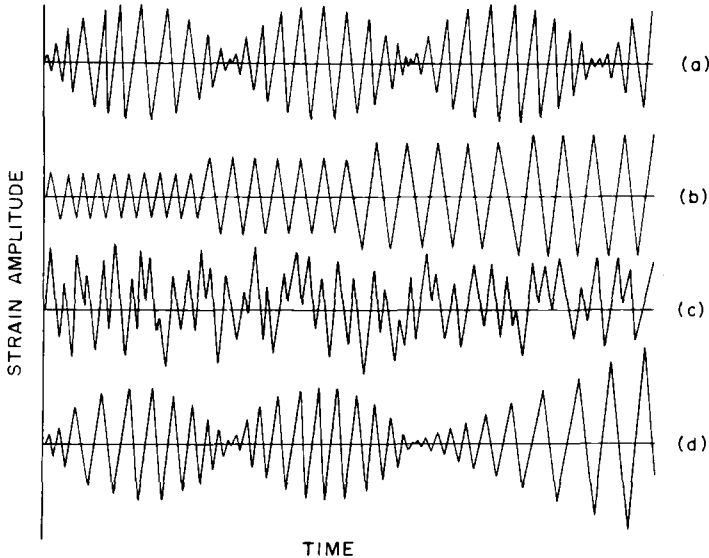


FIG. 1—Methods of testing: (a) incremental test, (b) multiple-step (or block) test, (c) random-loading test, and (d) a test designed to simulate in a regular specimen the strain history experienced by a ligament of material in the path of an advancing crack—namely, an incremental test to simulate the saturation condition followed by a gradually increasing cyclic-strain amplitude to fracture. The block test is controlled by plastic strain, the others by total strain.

step tests were significantly different from those of constant-amplitude tests; the cycles applied at high strains in the incremental steps establish a structure which influences the subsequent cycles at low strain and causes their stress amplitudes to be higher than those observed in constant-amplitude tests.

Because CSSCs now are being applied more widely and successfully in the prediction of cumulative fatigue damage [2,9], it is important to know whether or not the CSSCs obtained under complex strain histories are the same as those under constant-strain amplitudes. In many steels and certain commercial aluminum alloys, it appears that they are the same [2], but Koibuchi and Kotani have obtained a slightly different result [10]. Working with a low-carbon steel, these investigators found that the cyclic stress-strain curve from constant-amplitude tests (or equivalently, from a block test; see Fig. 1b) is somewhat different from that of the incremental step tests; however, that from a random-loading test is essentially identical to that of the incremental step test [10]. It would appear, therefore, that an economical method of studying this question would be to compare results from incremental step tests with those of constant-amplitude tests, provided checks with random tests are also made, and confidence in reproducibility is established.

In spite of the many engineering investigations which have been carried

out on commercial materials and many fundamental studies of materials cycled under constant-strain amplitudes, no fundamental studies, from the viewpoint of a material scientist, have been made to evaluate response under complex varying strains. The present investigation was undertaken with the subsidiary aim of rectifying this matter.

### Behavior of Binary Alloys

In spite of the relatively few investigations of CSSR which have been made of binary aluminum alloys [11-16], the broad outlines of their behavior have been established as follows. When the hardening particles are small and so closely spaced that the dislocations are required by an applied cyclic plastic strain to pass through them because the interparticle bowing stress is too high for the dislocations to do otherwise, then considerable work hardening is caused by the first cycles of strain. Typical precipitates associated with this behavior are Guinier-Preston (GP) zones or, for example, in aluminum-copper alloys,  $\theta''$  plates. As shown in Fig. 2, hardening eventually reaches a peak, and cyclic softening subsequently occurs [12].<sup>4</sup> In a polycrystal, the hardening is associated with the redistribution of strain in the material. In the first few cycles, the grains optimally oriented for slip with respect to the stress axis show the strongest slip markings,

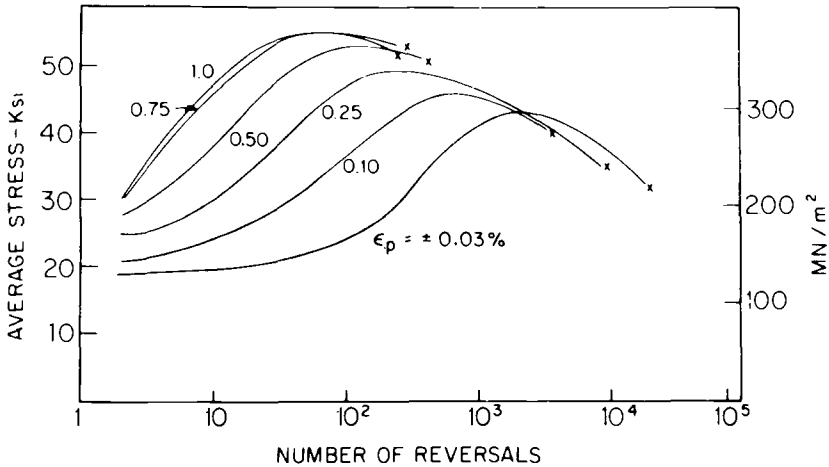


FIG. 2—Cyclic response curves for an Al-4 Cu alloy containing  $\theta''$  particles, showing hardening to a peak stress and then gradual softening until fracture (marked with a cross). The ordinate shows the stress amplitude averaged from succeeding tensile and compressive reversals, and the strains indicated are constant-plastic-strain amplitudes. Courtesy of Calabrese and Laird [12].

<sup>4</sup>In this paper, data points are not shown on cyclic hardening or softening curves because they are so numerous that, on the scale of the plot, the curves consist of a continuous string of points.

and, as they work harden, adjoining grains of "harder" orientation become more marked with slip bands. Dislocations are stored uniformly in tangled masses throughout the grains, but dense dislocation bands, slightly mis-oriented with respect to the grains which contain them, also form and become more numerous until peak hardening is attained. With continued cycling, the dislocation bands become more intense, and it is clear that the bulk of the strain is carried by them. This localization of strain is believed [12] to be associated with the softening which occupies the largest fraction of the life (Fig. 2). Calabrese and Laird investigated this softening in the light of mechanisms previously advanced to explain the poor fatigue properties of strong alloys (the endurance limit being small in relation to ultimate tensile strength [12]), namely: overaging, precipitate reversion, precipitate fracture, and aging inhomogeneities [17-23]. They concluded that none of these was appropriate to aluminum-copper and offered, instead, an explanation of softening based on the following argument, closely akin to one previously discussed by Byrne et al [24] with respect to unidirectional deformation in this type of alloy. Since the dislocations in the active bands are highly jogged and ragged and are continually interacting, their to-and-fro motion generally takes an irreproducible path. Therefore, the to-and-fro motions of dislocations through different paths cause a mechanical scrambling of the atoms in the precipitates, that is, their general structure becomes disordered, and the probability of a cutting dislocation creating different atom pairs is reduced. Softening then results from the loss of the interface steps and ordering contributions to hardening, and it is likely that the elastic properties of the precipitates are affected adversely also.

The CSSR of binary aluminum alloys is completely different from that just mentioned when the hardening particles are large and sufficiently widely spaced for the dislocations to pass between them in Orowan's fashion. As shown in Fig. 3, for such a microstructure, the hardening which occurs at the start of cycling is exhausted quickly, and the material becomes extremely stable. The slip is distributed homogeneously, and all the large plate precipitates are densely packed with dislocations [13]. Calabrese and Laird [13] used Ashby's model of "geometrically necessary" dislocations [25] to interpret such behavior. In this model, the plates are assumed not to deform, and to be strongly bonded to the matrix. If the microstructure is sheared as a whole, the matrix close to the plates cannot shear and must rotate, requiring geometrically necessary dislocations to be stored at the plate-matrix interfaces. The production of such dislocations leads to hardening. As the strain is cycled, the geometrically necessary dislocations are shuttled between plates on the same habit planes, and the hardening is therefore very stable. In addition, the strain distribution in the specimen is highly uniform [13].

Fine and Santner [16] have explored the CSSR of binary aluminum-copper alloy in which the microstructure was manipulated so as to contain the types of precipitates reported previously. In one alloy, Al-3.6Cu, used as a

## 8 FATIGUE CRACK GROWTH

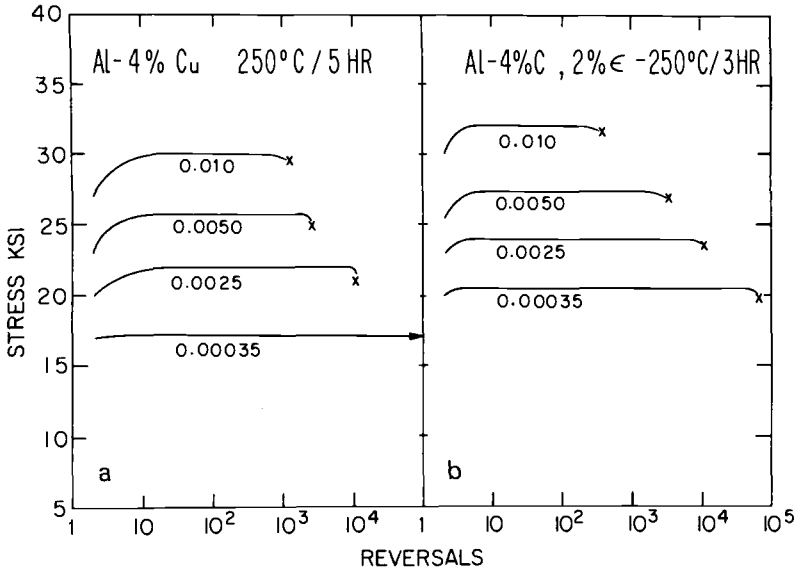


FIG. 3—Cyclic hardening curves for Al-4 Cu alloy aged at 250° C for 5 h so as to produce a uniform dispersion of large  $\theta'$  plates. Cold-working reduces the  $\theta'$  plate spacing and raises the flow stress.

control, the microstructure contained Guinier-Preston I (GPI) zones only. In another, containing 6.3Cu, undissolved, equiaxed  $\theta$  particles 5 to 10  $\mu\text{m}$  in diameter were distributed in a matrix containing GPI zones. As shown in Fig. 4, the aluminum alloy containing GPI zones only first hardened and subsequently softened just like the alloy studied by Calabrese and Laird [12]. The Al-6.3Cu alloy hardened and subsequently softened only at large and intermediate strains. However, at low strains, softening was not observed.<sup>5</sup> The interpretation is that, at high strains, the GPI zones were cut sufficiently to disorder the structure and the alloy softened. At low strains, the large  $\theta$  particles homogenized the strain and thus prevented the localization of the strain required to soften the structure in the active bands. Also shown in Fig. 4 are cyclic hardening curves for 2024-T4. Consistent with the work of Endo and Morrow [26], no softening was observed [16]. Commercial alloys contain more inclusions and dispersed phases than binary Al-6.3Cu alloy and can be expected, therefore, to be more effective in multiplying dislocations and in homogenizing the strain. The role of these particles in cyclic deformation is given extended treatment in the following section.

<sup>5</sup>It is possible that, at really low strains, where lives are greater than  $10^5$  cycles, strain localization may occur on a scale smaller than that of the inter- $\theta$  spacing, in which case, softening might very well occur.

## Behavior of Complex Alloys

### Experimental Details

Since aluminum-zinc-magnesium alloys have not been studied as extensively as commercial alloys more closely related to binary aluminum-copper, aluminum-zinc-magnesium has been chosen for study here. Another reason for the choice relates to the rather poor crack propagation behavior shown by these alloys as compared to that of 2024 and related alloys [3]. The variables selected in this study of CSSR are: (a) types of dispersed phases, (b) initial dislocation content of the material in relation to the hardening particles and (c) the nature of the loading (Fig. 1). A discussion of the nature of the dispersed phases which commonly occur in commercial aluminum alloys is necessary in order to clarify the specific choices of material. The literature

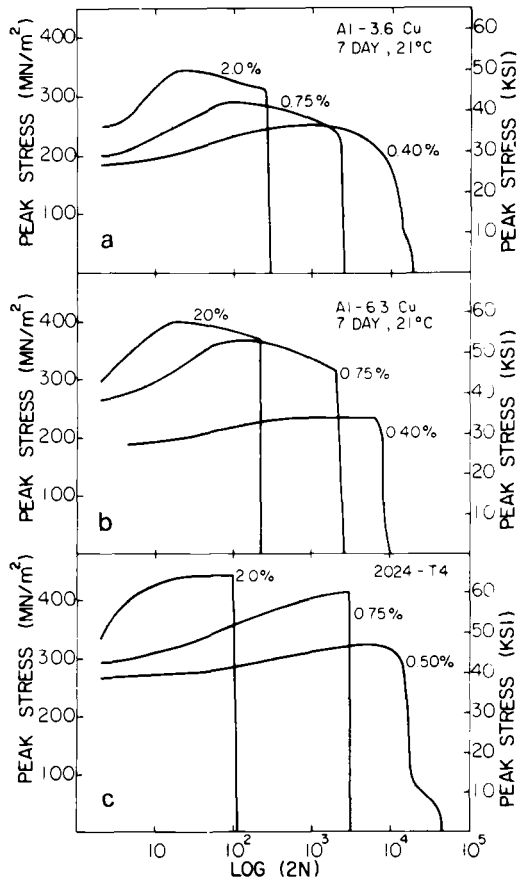


FIG. 4—Cyclic response curves for the aluminum alloys indicated, during plastic-strain-controlled cycling. The peak stress refers to the stress amplitude at the tensile reversal. Courtesy of Fine and Santner [16].

which deals with these phases is extensive, but a good reference which explains the role of the particles in fracture can be found in the review article by Kaufman [27].

The largest particles in aluminum alloys are termed the constituent particles. They are generally greater than  $1\ \mu\text{m}$  in diameter and form by eutectic decomposition during ingot solidification. Since they consist of insoluble particles such as  $\text{Al}_7\text{Cu}_2\text{Fe}$ ,  $\text{Mg}_2\text{Si}$ , or  $(\text{Fe}, \text{Mn})\text{Al}_6$ , they cannot be taken into solid solution during fabrication. Sometimes, the relatively soluble  $\text{CuAl}_2$  or  $\text{CuAl}_2\text{Mg}$  also occur as constituent particles. A second grouping of particles (in the  $0.03$  to  $0.5\ \mu\text{m}$  range), called dispersoids, consist of  $\text{Al}_{12}\text{Mg}_2\text{Cr}$  or  $\text{Al}_{20}\text{Cu}_2\text{Mn}$  formed by solid-state precipitation, and is also difficult to dissolve. During fabrication, these particles suppress recrystallization and limit the growth of grains. The third and finest set of particles consists of the age-hardening precipitates of major alloying elements, GP zones, which impede dislocation motion, and lead to the optimum combinations of strength and toughness.

It is apparent from the chemistry of the particles that the best way of eliminating the constituent particles (which fracture easily in unidirectional deformation and also in fatigue [27]) is to reduce the iron and silicon content of the alloy. The control of the dispersoids is more difficult; one means of reducing their volume fraction is by eliminating chromium, but this makes certain stages of the processing, particularly grain control, difficult. Accordingly, the alloys<sup>6</sup> listed in Table 1 along with their compositions and heat treatments have been selected as a compromise for the following reasons. (a) Conventionally processed 7075-T651 is useful as a basis for comparison with previous investigations; it is supplied in the form of 2-in.-thick plate to permit tests in the short transverse direction. (b) "High-purity" 7075-T651, conventionally processed, is low in iron and silicon, and therefore free of constituent particles; otherwise, it is similar in all respects to conventional 7075 (no differences could be detected between the alloys at the high magnification of the electron microscope). It also was supplied in the form of 2-in.-thick plate. This alloy permits the role of the constituent particles in CSSR to be discriminated from that of the dispersoids. (c) Conventionally processed, high-purity 7075 given a final thermomechanical treatment (FTMT) so as to introduce dislocations into the microstructure, and to modify the hardening precipitates which are known to nucleate heterogeneously on the dislocations was used. This material was supplied as 1-in. plate. (d) A conventional, pure aluminum-zinc-magnesium ternary free of both constituent particles and dispersoids and artificially and naturally aged to develop GP zones containing both solutes. The details of the GP zone structure in this alloy are unknown;

<sup>6</sup>The commercial-type alloys were kindly supplied by J. Waldman and H. Sulinski of Frankford Arsenal, Philadelphia. Full details of their processing, mechanical properties, and microstructures can be found in Refs 28, 29.

TABLE 1—Compositions and treatments of the alloys studied.

Name	Processing	Temper	Composition, weight % (Balance Aluminum)									
			Zn	Mg	Cu	Cr	Si	Fe	Mn	Ni	Ti	
Conventional 7075	conventional	T-651	5.50	2.40	1.72	0.19	0.10	0.27	0.05	...	0.03	
High-purity 7075	conventional	T-651 <sup>a</sup>	5.65	2.23	1.41	0.18	0.02	0.02	0.01	0.01	0.01	
High-purity 7075-FTMT	conventional	FTMT <sup>b</sup>	5.62	2.48	1.48	0.21	0.01	0.01	0.01	...	0.01	
Ternary Al-Zn-Mg	vacuum cast, homogenized, and swaged	T6 <sup>c</sup> T4 <sup>d</sup>	5.70	2.35								

<sup>a</sup>Solution treated 490°C/24 h, cold water quench; 25°C/5 days; aged 121°C/48 h.

<sup>b</sup>Solution treated 482°C/3 h, cold water quench; 25°C/4 days; aged 104°C/6 h; rolled at 190°C, 22 percent reduction in thickness; aged 121°C/8 h.

<sup>c</sup>Solution treated 450°C/24 h, cold water quench; cold worked and recrystallized at 450°C/½ min, quenched, aged 135°C/24 h.

<sup>d</sup>As T6, except aged at 25°C/7 days.

however, since the succeeding metastable phases are known to be ordered, the GP zone structure should be a good candidate to undergo cyclic softening by structural disordering. This material was supplied as 3/4-in. (19.1-mm) rod. In addition, an Al-15Ag alloy was vacuum cast, homogenized, swaged, solution treated at 550°C for 4 h and cold water quenched, swaged again, and solution treated for 2 min in order to recrystallize the structure; it was finally given a 15 percent reduction by swaging to introduce dislocations for heterogeneous precipitation of the hexagonal  $\gamma'$  precipitate [30,31] on subsequent aging, and finally aged at 160°C for 1½ h. The purpose of choosing this alloy and the particular heat treatment adopted was to check whether or not cyclic softening would occur in a material where the dislocations are heavily decorated by precipitation, and it should yield an interesting comparison with respect to the complex 7075 alloy with FTMT.

The monotonic properties of these materials are shown in Table 2. Consistent with the differing compositions, the strengths of the conventional and high-purity 7075 are roughly equal, but the ductility of the latter is improved greatly, especially in the long and short transverse directions. The high-purity 7075-FTMT is the strongest of the alloys listed, but its ductility is still high relative to that of the conventional 7075.

Cyclic deformation tests were carried out by all the loading modes shown in Fig. 1, in addition to tests under constant-plastic-strain amplitude on most of the materials listed. Only selected data required to establish the main points of the CSSR of aluminum alloys are reported here, however. The specimens had threaded ends and usually had a gage section of 0.5 in. (12.7 mm) length and 0.25 in. (6.35 mm) diameter, except for conventional and high-purity 7075 tested in the short transverse direction, in which the specimens had a gage length of 0.2 in. (5.08 mm) and diameter 0.15 in. (3.81 mm). The specimens were electropolished prior to testing, which was carried out by closed-loop, electrohydraulic, computer-controlled equipment, using standard clip-on gages for strain control.

#### *Cyclic Stress-Strain Response—Constant Plastic Strain Amplitude*

Cyclic hardening and softening curves for three of the materials studied are shown in Fig. 5. Both the conventional 7075 (high-purity 7075 was similar) and the aluminum-zinc-magnesium ternary alloys showed regular hardening behavior, the latter consistent with the work of Sanders [32], for the strain amplitudes indicated. The 7075 FTMT showed very high cyclic flow stresses on account of its high strength but was subject to cyclic softening. Presumably, many of the dislocations introduced by the final deformation were pinned inadequately by the final precipitation and thus were capable of rearrangement. The CSSCs of conventional and high-purity 7075 are shown in Fig 6a, which includes measurements for specimens cut from the longitudinal and long and short transverse directions of the material. Two useful conclusions emerge from this figure: (a) the CSSR

TABLE 2—Monotonic properties<sup>a</sup> of the alloys investigated.

Alloy Name	Section	Location in the Plate	0.2% Flow Stress,		UTS		Elongation, %	Reduction in Area, %
			ksi	MPa	ksi	MPa		
Conventional 7075	longitudinal	center	73	503	83	572	11	...
	long transverse	center	73	503	83	572	10	...
	short transverse	center	69	476	78	538	4	...
High purity	longitudinal	quarter thickness	75.2	518	84.7	584	13.3	17.7
	longitudinal	center	82.4	568	92.7	639	11.3	16.9
	long transverse	quarter thickness	72.1	497	82.7	570	9.9	16.0
	long transverse	center	74.9	516	85.0	586	10.3	14.9
High-purity 7075-FTMT	short transverse	center	69.6	480	82.8	571	9.6	18.7
	longitudinal	center	89.2	615	92.9	641	9.1	18.5
Ternary Al-Zn-Mg	longitudinal	center	86.1	594	92.5	638	9.8	21.0
	longitudinal	center	53.8 <sup>b</sup>	371	62.2	429	...	28.6
Binary Al-Ag TMT	longitudinal	center	30.6 <sup>b</sup>	211	40.4	279	...	49.6

<sup>a</sup>Based on specimens 0.505 in. (12.83 mm) in diameter, gage length 2 in. (50.8 mm), except for short transverse specimens and Al-Zn-Mg and Al-Ag specimens which had 0.14 in. (3.56 mm) diameter, 0.5 in. (12.7 mm) gage length.

<sup>b</sup>0.1 percent flow stress.

## 14 FATIGUE CRACK GROWTH

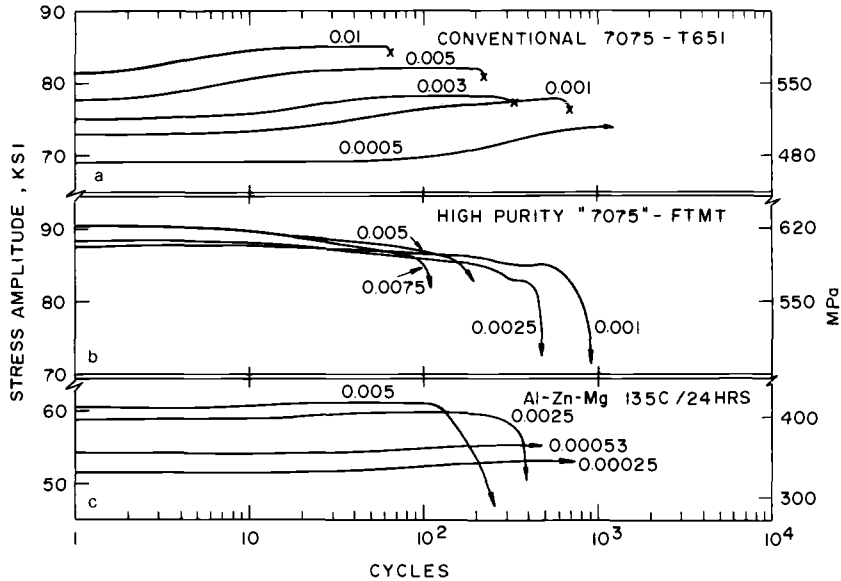


FIG. 5—Cyclic response curves for (a) conventional 7075-T651, (b) high-purity 7075-FTMT, and (c) Al-Zn-Mg, peak strength. The constant-plastic-strain amplitudes for each specimen are indicated, and rapid declines in stress amplitude near the ends of life are all associated with propagation of a large crack.

of conventional and high-purity 7075 are essentially similar, and this shows that the dispersoids, rather than the constituent particles, play the dominant role in improving the CSSR of commercial alloys with respect to the base alloy; (b) there is no significant difference in the CSSCs of the specimens cut from the different directions of the material. However, the fatigue lives of the alloys do vary significantly with direction, specimens cut in the short transverse direction showing lives (in a Coffin-Manson plot) one quarter of those in the longitudinal direction for the conventional 7075 alloy. However, the high-purity 7075 alloy showed no significant effect of processing direction on fatigue life. This means that the CSSR is necessary to describe the fracture rate because it may well control the degree of blunting at the crack tip. However, it will not be sufficient to explain the entire kinetics of crack propagation because static failure mechanisms can be expected to accelerate the rate. Detailed crack propagation studies will have to be carried out to determine the other parameters necessary to describe the kinetics completely.

The CSSC for the aluminum-zinc-magnesium alloy (Fig. 6b) is interesting in that the scatter (maximum ~2 percent) is less than that of the 7075 alloys (~5 percent) and the flow stress much less because of the lower volume fraction of all types of strengthening particles. The difference in scatter can be attributed to the greater difficulty of producing a homogeneous microstructure in a complex alloy. Also shown in Fig. 6b is the cyclic stress-

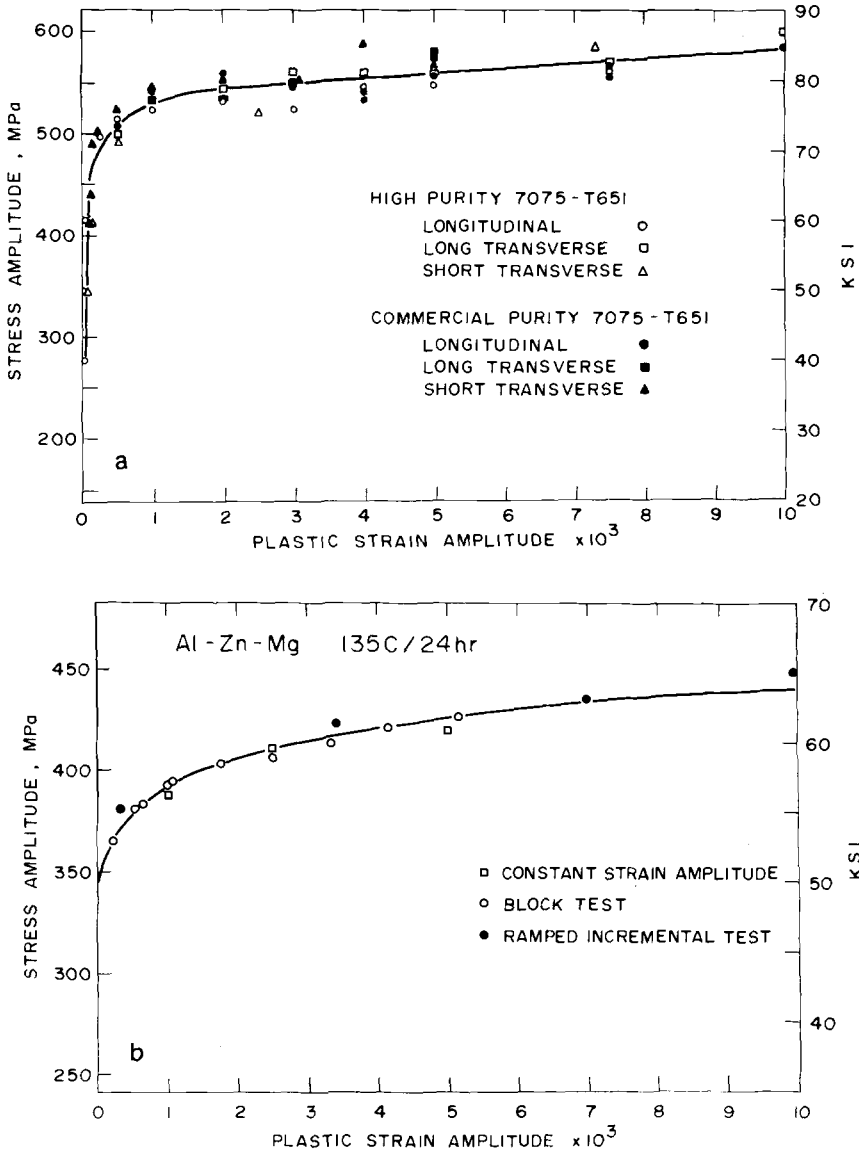


FIG. 6—Cyclic stress-strain curves for: (a) conventional and high-purity 7075-T651, specimens cut parallel and perpendicular to the rolling direction, (b) Al-Zn-Mg ternary alloy.

strain behavior associated with the testing mode shown in Fig. 1d, which might be termed the "ramped-incremental test." This shows that the CSSC is a reasonable approximation for the cyclic deformation behavior of material at a crack tip and can be extrapolated to rather high strains with confidence. In fact, the ramp could not be increased much beyond 5 percent

because the specimens began to buckle; however, the rate of hardening for these materials is becoming quite small at such large strains, and this is the main justification for extrapolation to the still higher strains which would occur at a crack tip.

### *Cyclic Response at Intermediate Strains*

The most unexpected result is that the aluminum-zinc-magnesium ternary does not show cyclic softening down to plastic-strain amplitudes of 0.00025. Transmission electron microscopy of the cycled structures showed that the dislocations were arranged uniformly (Fig. 7a). However, dislocation banding was observed occasionally (Fig. 7b). Since such banding previously has been associated with softening [12], typical bands were explored carefully. Their dark contrast was always associated with slight crystal reorientation, which in Fig. 7b had tilted the crystal locally nearer to the Bragg condition. The dislocation densities in the bands were not significantly different, however, from those of the matrix. It would appear then that the deformation is too widespread to permit structural disordering and softening.

To check this interpretation, attempts were made to strain cycle specimens at still lower strains. However, closed-loop control on the plastic strain, a very small part of the total strain measured by the transducer, was found to be difficult, and it was decided, therefore, to do load-cycling experiments instead. A typical result for a naturally aged specimen is shown in Fig. 8. Consistent with the fairly low yield stress of this material, rather large strains were observed on application of the first few cycles. However, the material work hardened considerably; the plastic strain was reduced considerably by the 50th cycle, and it lay in the microstrain region by the 300th. It subsequently remained there for several thousands of cycles; however, by the 10 000th cycle, the hysteresis loop had widened appreciably, and it continued to widen long before the propagation of a significant crack. Increase of plastic strain under constant-stress cycling is an indicator of cyclic softening; it could also be an indicator that small cracks had nucleated and were showing plastic strain in association with their stress concentrations. To discriminate between these possibilities, two kinds of experiment were carried out: (a) fractography, in order to find out the point in life at which the important cracks had formed, and (b) a cycling experiment where cracks were introduced deliberately by nicking the surface of the gage length with a razor blade. Typical fractographs are shown in Figs. 9 and 10. Since the specimen of which the CSSR is shown in Fig. 8 failed by intergranular fracture, the fracture surface showed very little evidence of striations. However, the fracture surface features shown in Fig. 9 near the two nucleation sites shown (there were seven in all) were rather coarse, which indicate that the cracks started very late in the life. This is supported by fractographic observations (Fig. 10) of a specimen aged at 135°C/24 h. and cycled at the same stress, which lasted for about the same number of

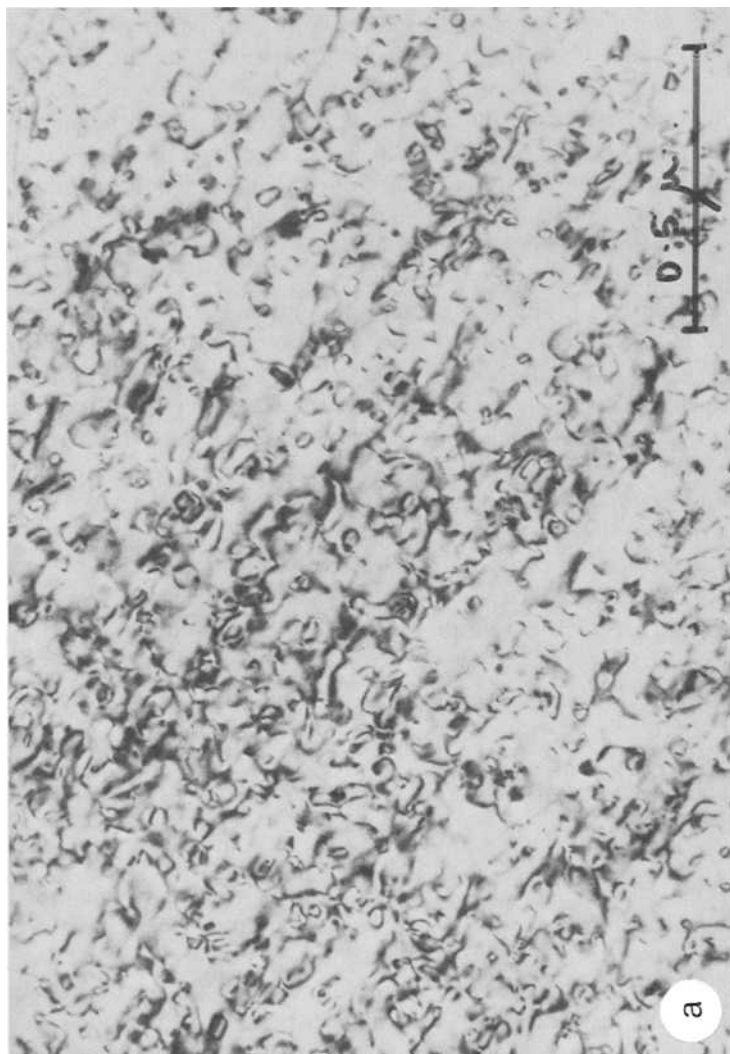
cycles as the specimen shown in Fig. 9 and showed similar softening behavior in its hysteresis loops, but to a lesser degree. In this specimen, fracture occurred with the formation of ductile striations which were quite large close to the nucleation point. Crack nucleation (at least to a depth of  $\sim 5 \mu\text{m}$ ) must therefore have taken place quite late in life. Furthermore, the cracks which nucleated and grew to failure in the specimen shown in Figs. 8 and 9 did so *outside the gage length*, over which the extensometer was measuring strain. In addition, there was no observable effect of surface razor nicks on hysteresis loops until they were of a depth and number greatly larger than the persistent slip bands which were observed on the specimens' surfaces by scanning microscopy. Thus the conclusion that the behavior indicates softening and not cracking is as firm as it is for the higher strain results reported in the previous section on binary alloys.

At first sight, this result would appear to be in conflict with those of Fine and Santner [16] on binary aluminum-copper; namely, that they observed decreased work softening with homogenization of strain at lower strains, Fig. 4b. It is important to note, however, that their lowest strain is 0.004, which is a large plastic strain. With the much lower strains studied here, the strain was highly localized and large enough to cause structure disordering when accumulated over thousands of cycles. This interpretation is consistent with the recent results of Sanders et al [33]. They found that, at low strains, in a great variety of commercial aluminum alloys, the distributions of dislocations became nonuniform, and consequently, the microdeformation was localized. Incidentally, Ref 33 contains excellent transmission electron micrographs of commercial aluminum alloys, and there is no need therefore to show the dislocation structures of the complex alloys reported here.

#### *The Cyclic Stress-Strain Response of Aluminum-Silver Alloy With A Complex Microstructure*

Since high-purity 7075-FTMT showed cyclic softening, it would be interesting to check how general such behavior might be in heavily strengthened alloys. To check this, A1-15Ag alloy was prepared as just described and aged finally after a postsolution-treatment swage. Hren and Thomas [31] found that dislocations in this alloy attracted silver to their stacking faults, separating the partials to large distances and nucleating  $\gamma'$  precipitates between the partials. One should expect, therefore, that a dislocation population introduced before aging should be immobilized effectively by such precipitates. An attempt by electron microscopy to verify that the dislocations are indeed tied up proved difficult, however. As shown in Fig. 11a, the microstructure of the alloy was highly dislocated, and  $\gamma'$  could not be detected against the contrast of the dislocations. However, the elec-

18 FATIGUE CRACK GROWTH



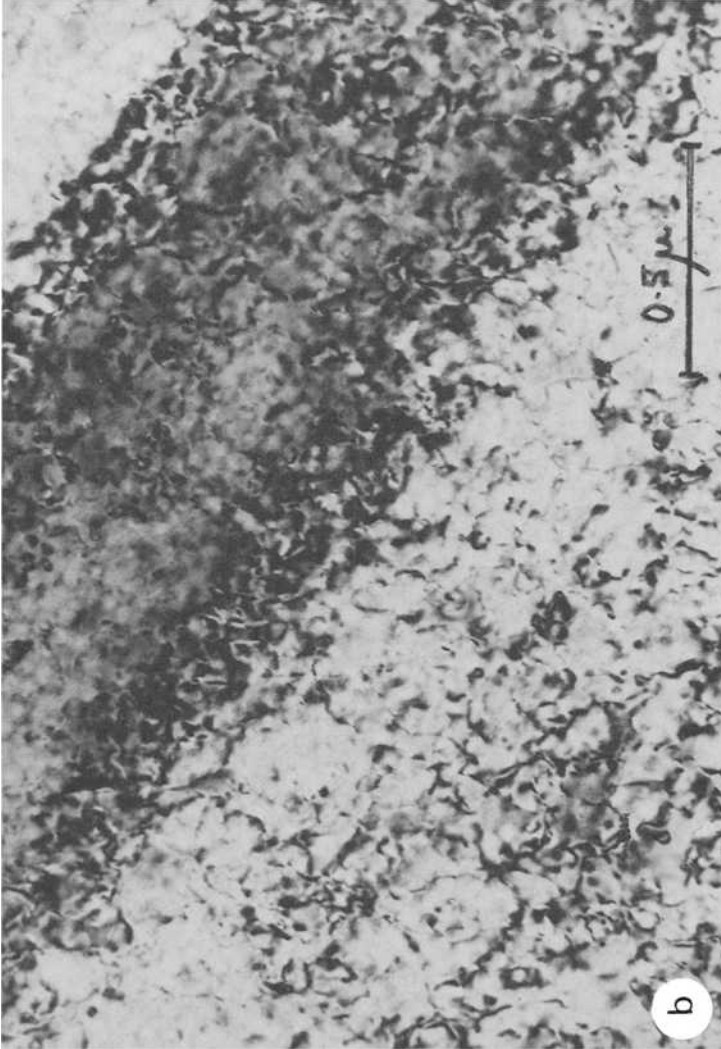


FIG. 7—(a) The uniform dislocation debris in high-strain-cycled Al-Zn-Mg alloy; naturally aged,  $\epsilon_p = \pm 0.005$ ,  $ZA = [110]$ ,  $g = (002)$ . (b) A rare case of dislocation banding in the same specimen as shown in (a), same grain and contrast condition.

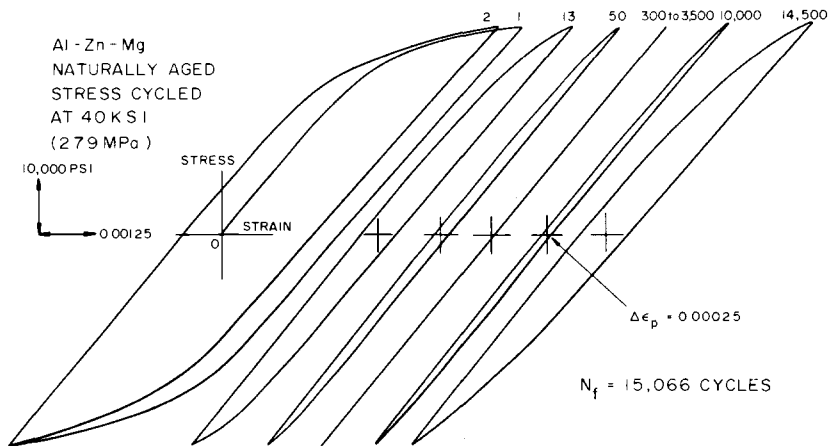


FIG. 8—The hysteresis loops measured in a naturally aged specimen of Al-Zn-Mg at different points in the life, showing initial hardening and subsequent softening. The numbers of the loops refer to cycles and not reversals.

tron diffraction patterns showed streaking of the spots in directions normal to the expected (111) habit plane of  $\gamma'$  particles; it must be concluded then that  $\gamma'$  particles are distributed amongst the dislocations. In addition, rather coarse allotriomorphs (on a scale comparable to that of dispersoids) were observed at dense dislocation walls and other boundaries (Fig. 11b) formed in the preceding steps of processing.

On cycling this material at constant plastic strain, no softening was observed (Fig. 12). Instead, the stress amplitude either remained constant, at the highest strain, or else increased at lower strains. The large stress decreases occurring late in the lives of the specimens shown in Fig. 12 were not "true" deformation phenomena, but were associated with the propagation of large cracks, as clearly shown by asymmetries in the hysteresis loops. Since this binary alloy was quite ductile, the crack propagation mechanism was the plastic blunting process, and neat, ductile fatigue striations were formed (Fig. 13). Counts of striations observed on the fracture surfaces were consistent with the points in the lives of the aluminum-silver specimens at which stress decreases first were noted.

Typical dislocation structures formed in this alloy after cycling are shown in Fig. 14. The structures were rearranged considerably by the cycling, appearing less complex, and there were many more loops than were observed initially. However, the total dislocation density did not appear much affected, remaining reasonably uniform. No evidence of cell formation was observed. It is possible that the loops could be  $\gamma'$  precipitates, but they were too small and the structures too complex to permit positive discrimination by contrast methods. It is apparent, however, that the  $\gamma'$  precipitates initially present in the dislocation structures introduced by

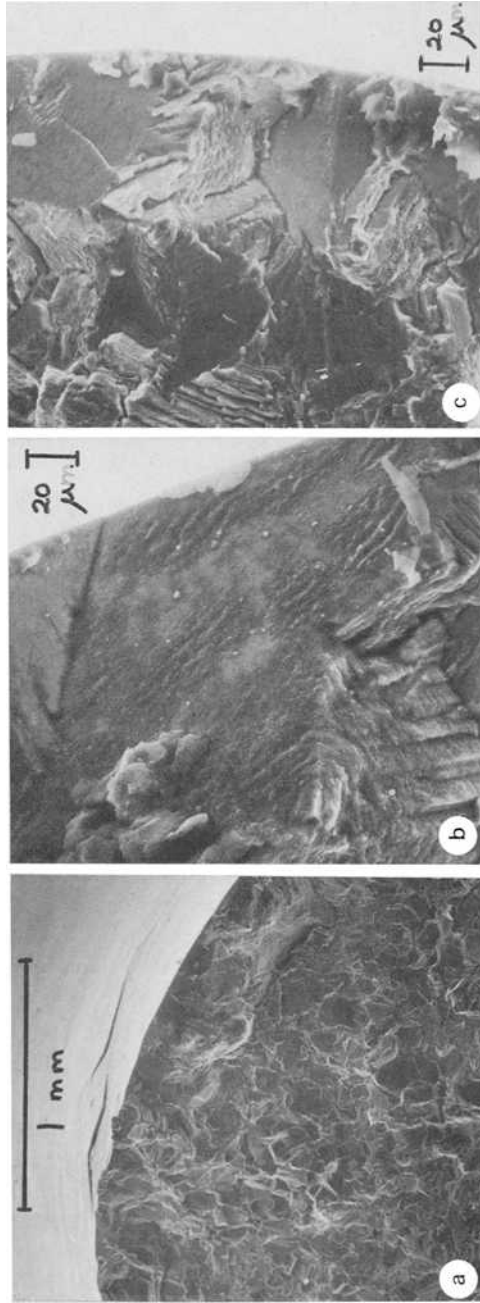


FIG. 9.—Fractographs of the specimen of which CSSR was shown in Fig. 8. (a) general view of fracture, showing intergranular propagation, (b) and (c) typical crack nucleation sites.

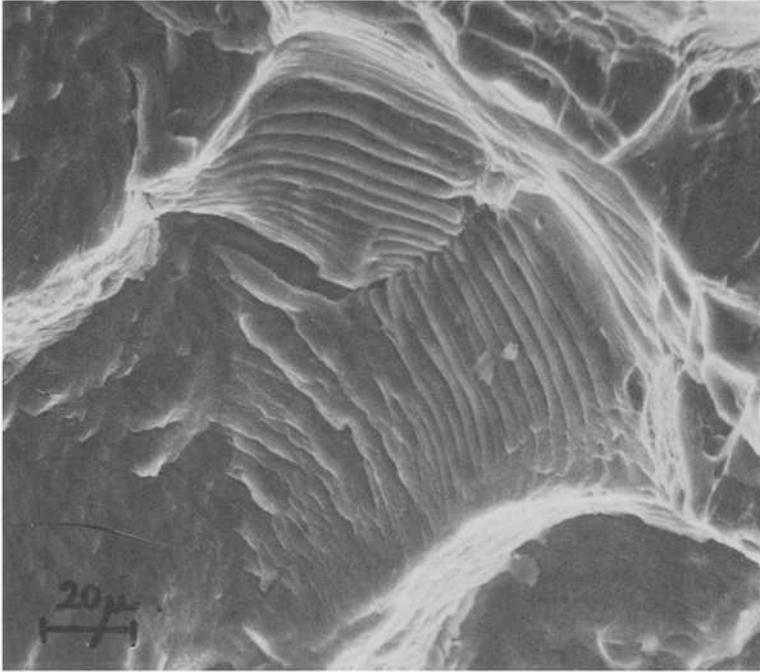


FIG. 10—A region of the fracture surface of an Al-Zn-Mg alloy aged at 135° C/24 h, showing typical striations. This region was less than 0.1 mm from the nucleation site, and the fractograph proves that macrocrack propagation in this sample occupied only a very small fraction of the total life. Stress amplitude  $\pm 40$  ksi (279 MPa), life 15 030 cycles.

the thermomechanical treatment have been effective in preventing work softening. Although the dislocations have been freed from the heterogeneously nucleated  $\gamma'$  precipitates to some extent, as evident from the observed dislocation rearrangements, the precipitates have served to homogenize the deformation and thus to prevent work-softening dislocation interactions. In view of this result, it will be difficult to generalize whether or not thermomechanically treated alloys will undergo cyclic softening because the details of heterogeneous nucleation will vary from one alloy system to another. It is probable, however, that aluminum-silver will be one of the most potent in preventing cyclic softening because the  $\gamma'$  precipitate has a (111) habit plane and will be effective in tying up the initial dislocation structure. Moreover, the most highly strengthened of the thermomechanically treated alloys will have a tendency to soften cyclically because the GP zones or small precipitates associated with the processing dislocations are themselves prone to softening.

## Cyclic Stress-Strain Response Under Variable-Amplitude Loading

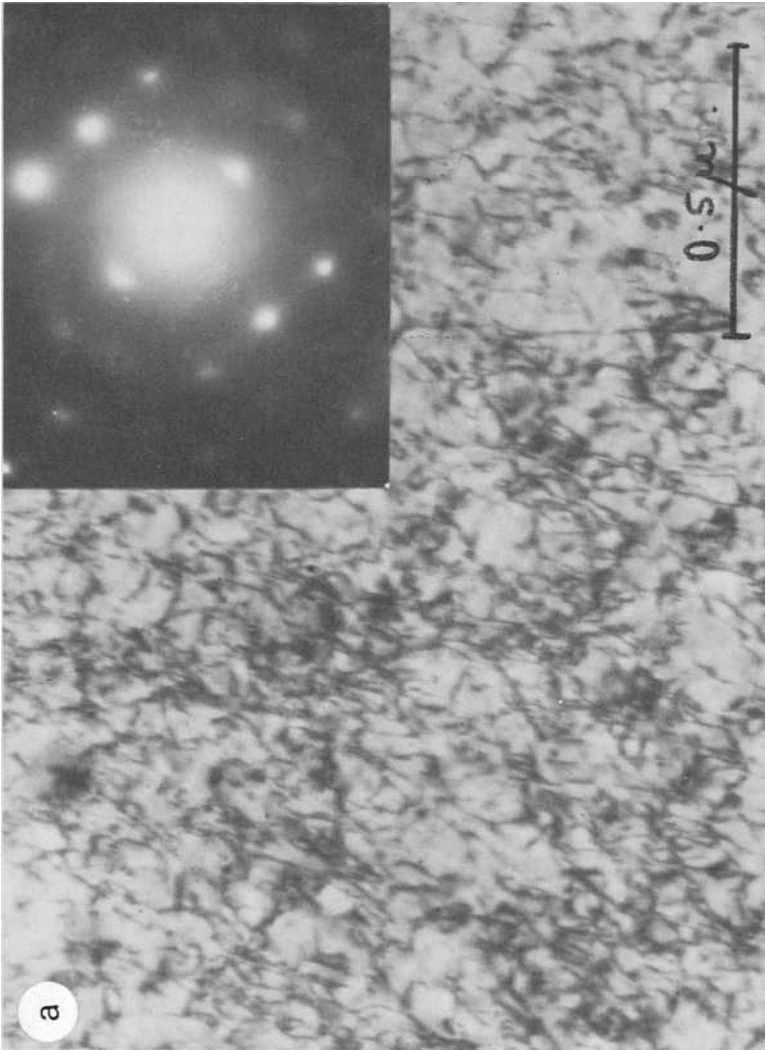
### *Binary Alloys*

In line with the aim of exploring the relationship between cyclic response under constant-amplitude cycling and that under variable-amplitude cycling, incremental tests were made on binary Al-4Cu alloy, heat treated to produce: (a)  $\theta''$  precipitates, given to particle cutting and thus to cyclic softening and (b)  $\theta'$  precipitates, which lead to stable CSSR behavior. A typical result for the microstructure containing  $\theta''$  is shown in Fig. 15, in the form of cyclic stress-strain plots for individual envelopes, including the first. Thus the complete cycling history of the specimen is represented. The first envelope shows asymmetric response because rapid hardening is occurring during the decline of the envelope as well as during the approach to its maximum. Just as in a test run at constant amplitude [12], hardening builds up to a peak (here the 20th envelope) and softening subsequently occurs (see the result for the 40th envelope). It is interesting that softening begins at an accumulated plastic strain roughly equal to that shown in a constant-amplitude test, and the cyclic stress-strain curve obtained in such a test (plotted for the peak stress) is roughly equivalent, within the limits of scatter, to that observed in the incremental tests (Fig. 16).

Again in line with the constant-amplitude behavior, Al-4Cu alloy containing  $\theta'$  hardens very rapidly in an incremental test and reaches a well-maintained saturation (Fig. 17). However, in this case, it will be noted from the arrow on the ordinate of Fig. 17 that the CSSC corresponding to the saturated state lies a little below that of constant-amplitude tests. Presumably, the fluctuations of strain within the envelopes serve to align the geometrically necessary dislocations into neater arrays at the precipitate / matrix interfaces, thus reducing the long-range internal stresses as well as the density of dislocations accumulated between precipitates by trapping processes. To judge by the careful experiments of Koibuchi and Kotani [10], it may be general for alloys or pure metals hardened by dislocations that the CSSC for incremental tests lies slightly below that for constant-amplitude tests. The differences are small, however, and the question of scatter should be explored more carefully.

### *Complex Alloys*

In more complex alloys, the incremental test CSSC also appears to lie at a flow stress a few percent lower than that generated by constant-amplitude tests, for example, ternary aluminum-zinc-magnesium (Fig. 18). Also consistent with the work of Koibuchi and Kotani [10], block test results agree closely with those of constant-amplitude tests. In this alloy, the GP zones



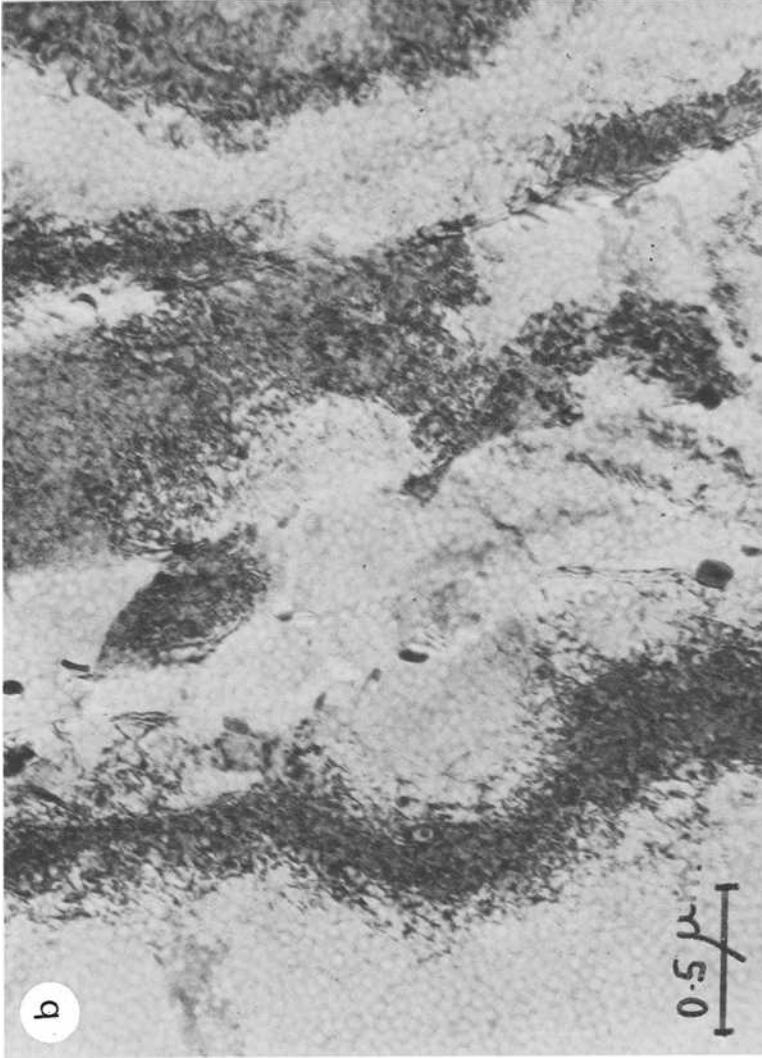


FIG. 11—The microstructure of the Al-Ag alloy prior to cycling, (a) dense tangles of dislocations shown by streaking at matrix spots in selected area diffraction to be decorated with  $\gamma'$  precipitates, (b)  $\gamma$  idiomorphs and allotriomorphs distributed amongst the dense dislocation arrays.

## 26 FATIGUE CRACK GROWTH

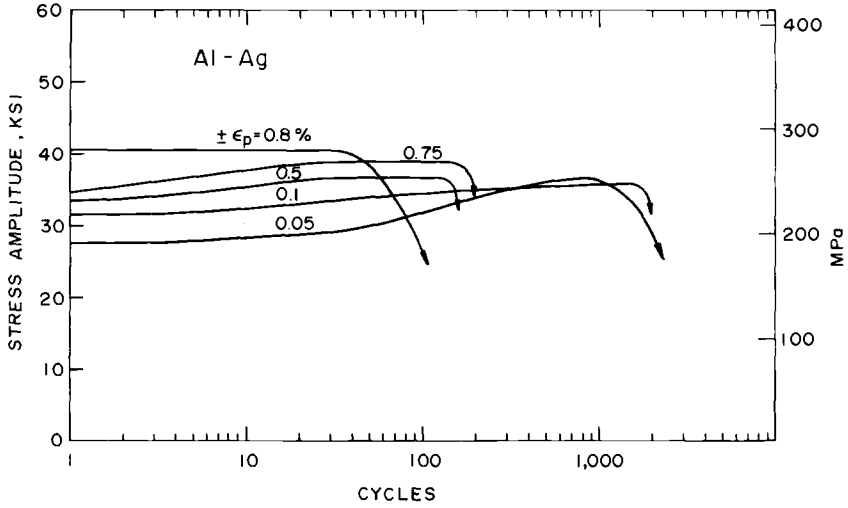


FIG. 12—Cyclic hardening curves for thermomechanically treated Al-Ag alloy.

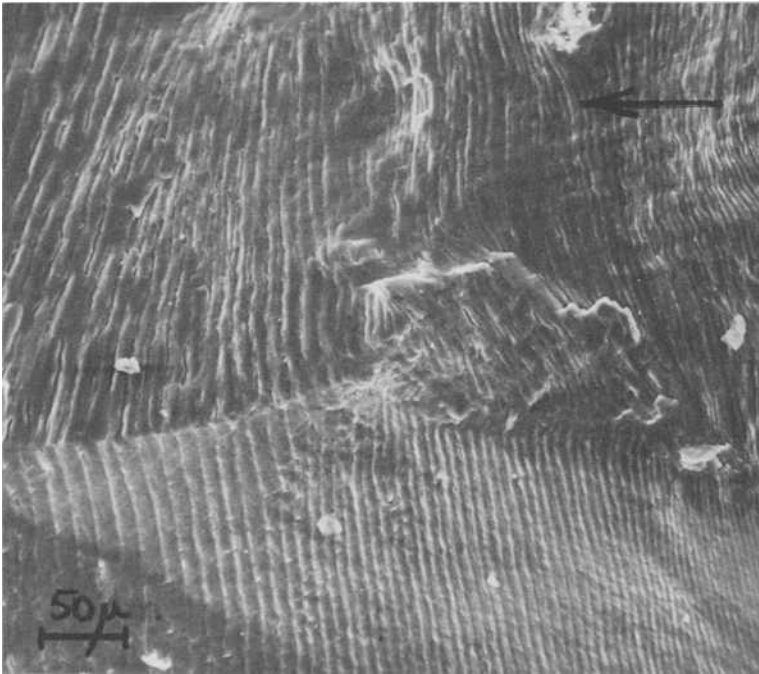


FIG. 13—Ductile fatigue striations in Al-Ag alloy cycled at a plastic-strain amplitude of 0.0025. The arrow marks the direction of crack propagation.

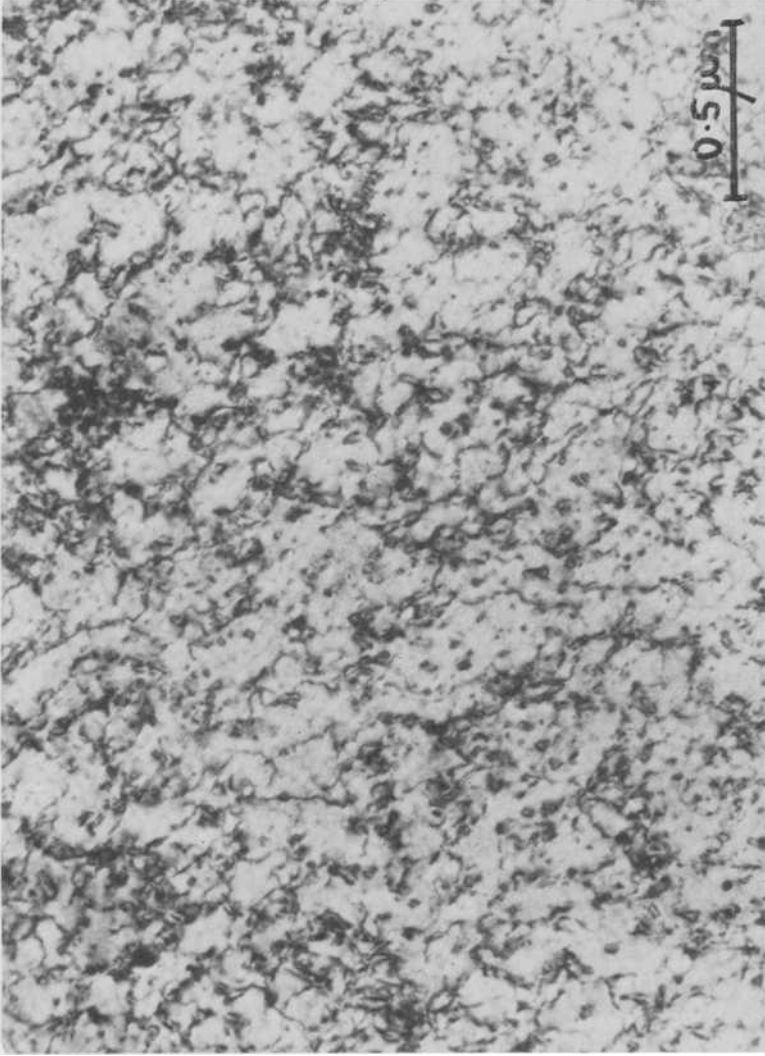


FIG. 14—Dislocation structure in Al-Ag alloy cycled at a plastic-strain amplitude of 0.0025 to failure. The region of observation was well removed from the crack and can be considered representative of the saturated state.  $ZA = [001]$ ,  $g = (200)$ .

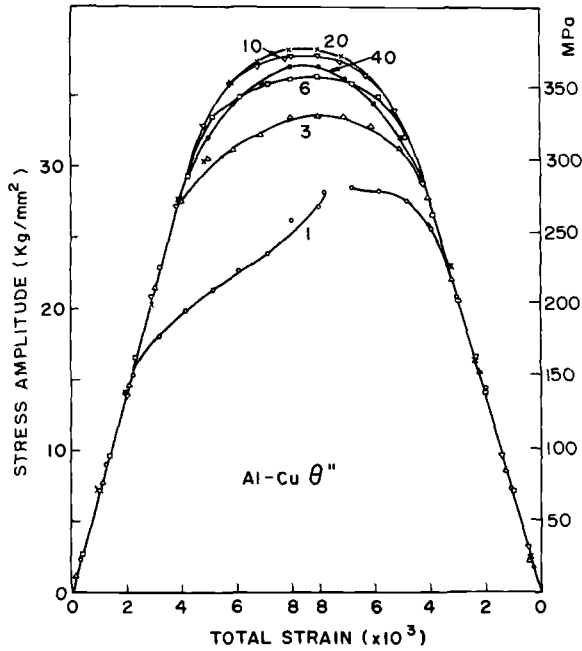


FIG. 15—Cyclic stress-strain response in Al-4Cu containing  $\theta''$  precipitates for selected envelopes recorded during an incremental test, maximum total strain amplitude 0.008. The stresses and strains are associated with the tensile reversals of the envelopes, the numbers of which are indicated. Courtesy of Shinohara and Laird [34].

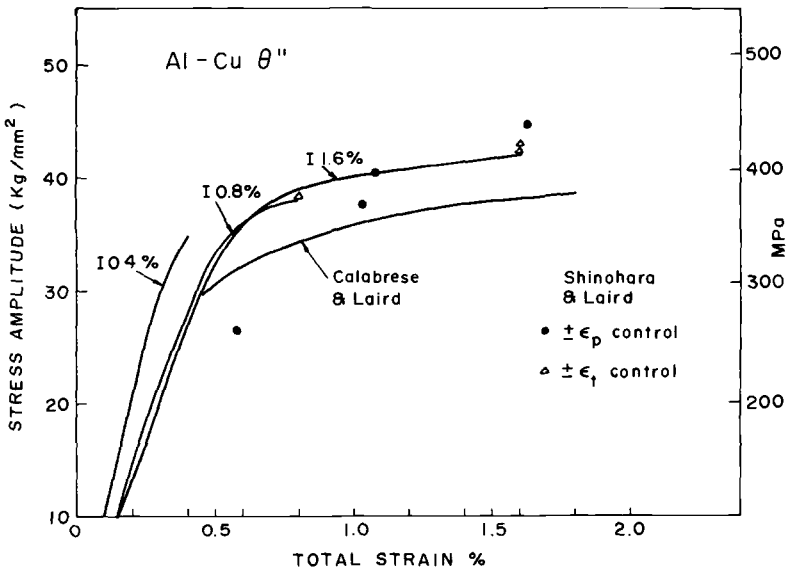


FIG. 16—Comparison of cyclic stress-strain curves obtained from constant-amplitude tests (total strain or plastic strain) and from incremental tests (denoted "I") conducted to various, indicated maxima in total strain. All stresses represent the highest stresses observed prior to softening. The curve indicated "Calabrese and Laird" is taken from Ref 12, and is associated with constant-plastic-strain amplitude cycling. Courtesy of Shinohara and Laird [34].

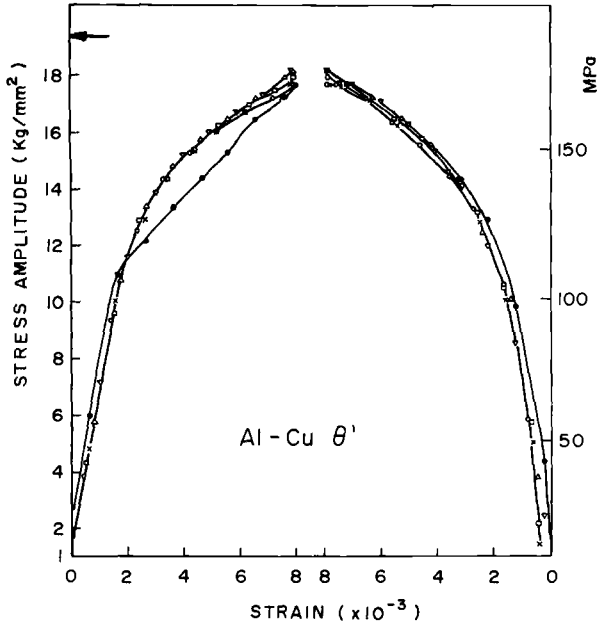


FIG. 17—Cyclic stress-strain response in Al-Cu containing  $\theta'$  precipitates for selected envelopes recorded during an incremental test, maximum total strain amplitude 0.008. The response of the first envelope (filled circles) lies slightly below that of all the others, which are essentially equivalent. The arrow on the ordinate indicates the saturation stress observed for a constant-plastic-strain amplitude test, corresponding to the maximum strain of the envelope.

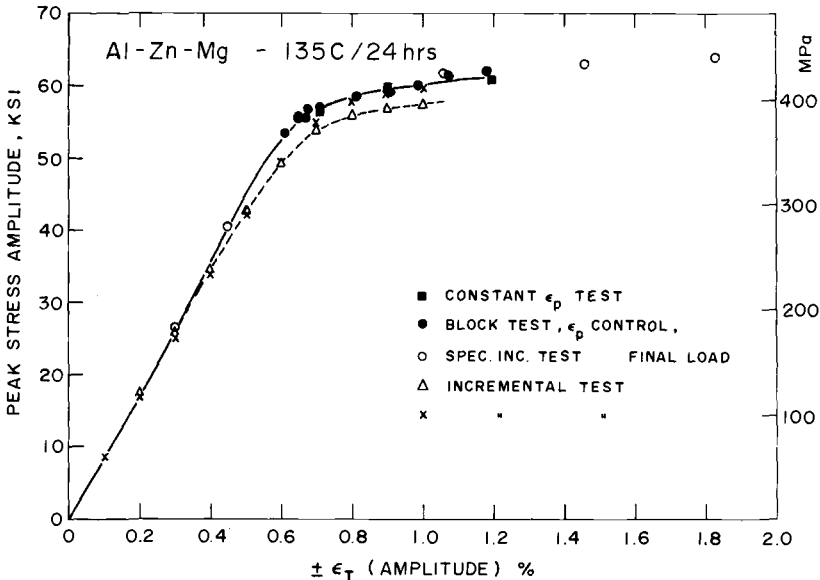


FIG. 18—Comparison of cyclic stress-strain curves obtained from constant-amplitude tests, from block tests and from incremental tests; Al-Zn-Mg. The open circles show the stress-strain curve of the final cyclic ramp in the test illustrated in Fig. 1d.

act to impose a friction stress on the dislocations, but the cyclic hardening associated with dislocation multiplication can show the same kinds of variations between the different tests as in a pure metal. The same result holds for the still more complex alloys which contain dispersoids, because the main difference in CSSR caused by these precipitates is to homogenize the strain, not to produce major variations in dislocation structures.

These small differences in CSSR under different types of loading are interesting when the slip mode of these alloys is considered. Since strong aluminum alloys show localized deformation markings, they can be regarded as planar slip materials. One would expect from the cyclic behavior of monophase planar slip materials that dislocation structures inherited from high-strain cycles would raise the flow stress of low-strain cycles with respect to that observed in constant-amplitude tests. Since opposite behavior is actually observed in the alloys of interest here, it is apparent that the concept of slip mode is not very useful in the context of these alloys.

The thermomechanically treated aluminum-silver alloy showed different behavior, however (Fig. 19). In this alloy, the CSSC of the incremental test lay above that of the constant-amplitude tests; the major cause of this behavior lies in the extraordinary resistance to cyclic softening shown by this microstructure. Thus the dislocation microstructures associated with the highest strains in the envelopes of the incremental test persisted with little change at the lower strains and maintained the flow stress.

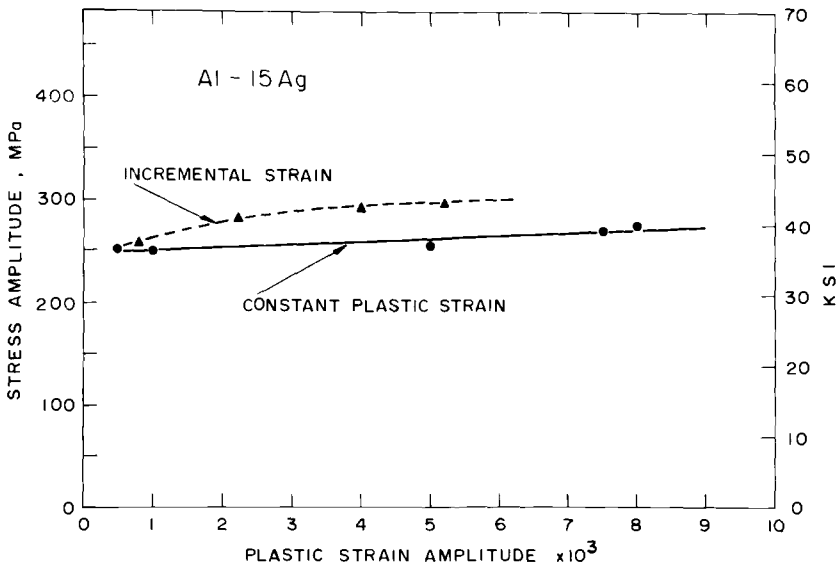


FIG. 19—Comparison of cyclic stress-strain curves obtained from constant-amplitude tests and from an incremental test—Al-15Ag alloy solutionized, swaged, and aged at  $160^{\circ}\text{C}/1\frac{1}{2}\text{h}$ .

Exploration of CSSR under random-load cycling of the type illustrated schematically in Fig. 1c (total strains were selected by a random number generator under a ceiling of 0.5 percent plastic strain) is more difficult. Several approaches for analyzing the measurements were investigated, including those of Wetzel [2] and Koibuchi and Kotani [10]. However, instead of using a computer to follow the cyclic response from the first reversal as Wetzel did [2], analysis was carried out by hand on small groups of hysteresis loops recorded periodically during tests by  $x$ - $y$  plotter. In Wetzel's approach, the method takes into account the stress-strain history, and is especially useful for handling reversals where the load does not change sign. A typical computation of CSSR by this method is shown in Fig. 20, from which it is apparent that scatter is large and the method unsatisfactory, although the results for the random tests do lie in general agreement with those of incremental tests, that is, lower than the constant-amplitude CSSC. From experimentation with the data, the author concludes that following the response from the first reversal would not improve the scatter, which seems more to result from the method of analysis rather than to represent real flow stress variations in the material.

This belief is strengthened when analysis of the results is made by the method of Koibuchi and Kotani [10]. In this method, groups of random-loading, stress-strain plots are broken into well-defined hysteresis loops to which definite stress and strain ranges can be applied, after the manner shown in Fig. 21. These ranges are then normalized against the maxima

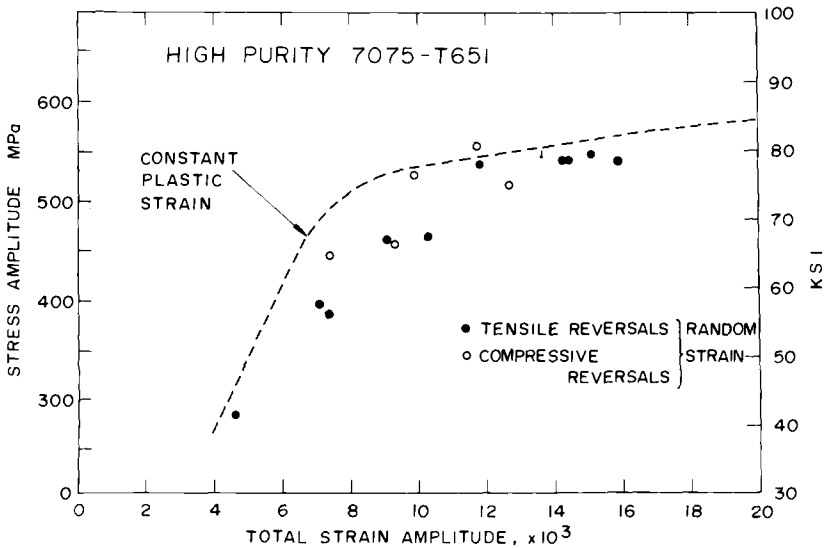


FIG. 20—Comparison of cyclic stress-strain curves obtained from constant-amplitude tests and from a random test which was analyzed by the method of Wetzel [2]. The material was high-purity 7075-T651.

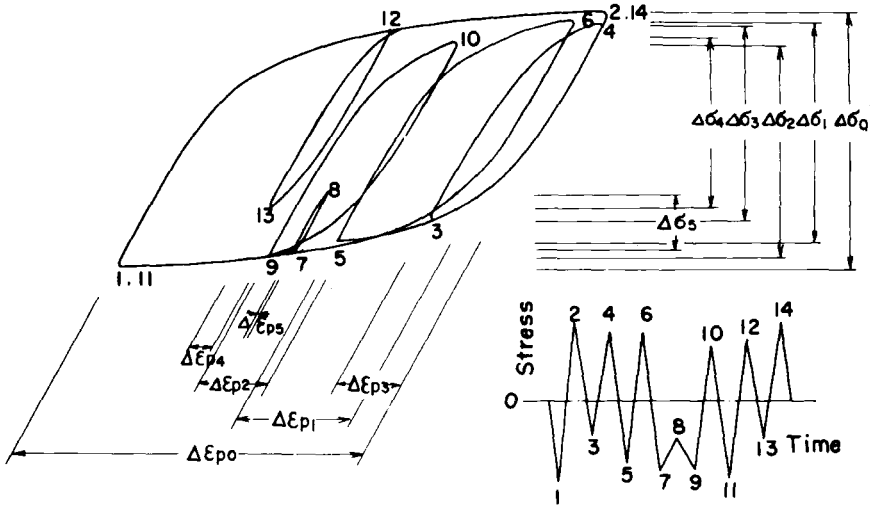


FIG. 21—Stress-strain response recorded from complex loading analyzed into hysteresis loops, showing their specific stress and strain ranges. Courtesy of Koibuchi and Kotani [10].

stress and strain ranges encountered in the loading history (arbitrarily fixed, as mentioned previously at 0.5 percent plastic strain here), and the CSSC is plotted in the form

$$\Delta\epsilon_{pi} / \Delta\epsilon_{p0} = (\Delta\sigma_i / \Delta\sigma_0)^n$$

where

$n$  = stress-strain exponent,

$\Delta\epsilon_{pi}$ ,  $\Delta\epsilon_{p0}$  = loop plastic strain and maximum plastic strain ranges, respectively, and

$\Delta\sigma_i$  and  $\Delta\sigma_0$  = loop stress and maximum stress ranges, respectively.

Typical results treated in such a manner are shown in Fig. 22, which illustrates the following: (a) consistent with the results of Koibuchi and Kotani [10], the CSSR for incremental and random tests are essentially equivalent, (b) the CSSR for complex loading differs from that measured by constant-amplitude tests, and (c) the cyclic compressive stresses in incremental loading are higher than those of the tensile reversals, just as they are known to be in constant-amplitude tests. No satisfactory explanation has been offered yet for this effect.

**Conclusions**

On the basis of the previous studies reviewed and the results reported here, the following general conclusions are drawn about the CSSR of aluminum alloys:

1. Cyclic hardening always occurs in strain-controlled tests of aluminum

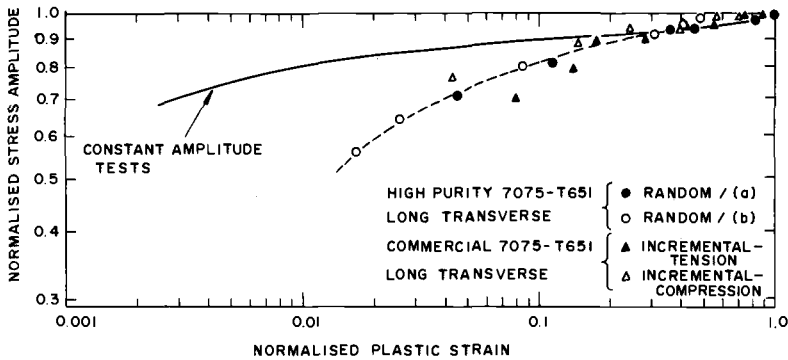


FIG. 22—Cyclic normalized stress-strain plots for high-purity 7075-T651 and conventional 7075-T651 subject to the complex loading indicated, compared to the CSSC obtained from constant-amplitude tests. Only the random loading tests are strictly treated in the manner described in the text. The incremental test is treated on the basis of amplitudes.

alloys by dislocation multiplication and interaction, but this hardening can be reduced by softening associated with dislocation/precipitate interactions.

2. Cyclic softening is observed most frequently in binary alloys and is enhanced by strain localization. Complex alloys are less prone to softening by dislocation/precipitate interactions, partly because the processed structure, including the GP zones, is more disordered than that of binary alloys and therefore is less capable of cyclic disordering and softening, and partly because complex alloys contain constituent particles and dispersoids which homogenize the strain. Softening nevertheless can occur in complex alloys by dislocation/dislocation interactions, for example in thermomechanically treated alloys.

3. The CSSR of complex alloys is dominated by the GP zones and dispersoids in combination. The constituent particles do not play an important role, unless dispersoids are absent, in which case they would homogenize the strain to a limited degree.

4. The CSSR of complex alloys is not influenced by the orientation of the specimen with respect to processing direction, in marked contrast to fracture behavior.

5. The concept of slip mode is difficult to apply to the CSSR of complex alloys, and has not been found useful in interpreting such behavior.

6. By suitable combinations of alloying and processing (for example, thermomechanical treatment of Al-15Ag alloy), cyclic softening by dislocation/dislocation interactions can be inhibited, but it is unlikely that this result can be applied effectively to the strongest commercial aluminum alloys.

7. CSSCs measured from block tests are coincident with those obtained from constant-amplitude tests, and CSSCs from incremental tests agree with those from random tests.

8. CSSCs of complex aluminum alloys obtained from complex loading histories generally lie below the CSSC obtained from constant-amplitude tests. The differences, however, are minor at high strains, and the CSSC obtained from constant-amplitude tests is a good first approximation to that from any loading history.

9. The cyclic stress-strain behavior at a crack tip can be obtained to a good approximation from the CSSC of bulk material, by extrapolation to the high strains expected in the neighborhood of crack tips.

10. The conclusions drawn here can be expected to apply to a wide range of alloys based on other metals, such as copper, nickel, iron, and titanium. In applying these conclusions, careful consideration must be given to the details of the microstructures of interest, because, even in aluminum alloys, wide variations in behavior are observed. Support for this conclusion, in application to steels, can be found in the studies of Fine and his coworkers [35, 36].

#### *Acknowledgments*

The results which are reported briefly here could not have been obtained without the help of R. de la Veaux and V. J. Langelo. The contributions of Mr. de la Veaux in mechanical testing have been especially helpful. J. Waldman of the Frankford Arsenal, Philadelphia, supplied much of the material for which we are extremely grateful, as we are to the Army Research Office, under Grant No. DAAG28-75-G-129 for support of the investigation.

#### **References**

- [1] Laird, C., *Materials Science and Engineering*, Vol. 22, 1976, pp. 231-236.
- [2] Wetzel, R. M., "A Method of Fatigue Damage Analysis," report, Ford Motor Co., Dearborn, Mich., 1971.
- [3] Hahn, G. T. and Simon, R., *Engineering Fracture Mechanics*, Vol. 5, 1973, pp. 523-540.
- [4] Stoloff, N. S. and Duquette, D. J., *Critical Reviews*, CRC Press, Cleveland, Ohio, Vol. 4, 1974, pp. 615-687.
- [5] Landgraf, R. W., Morrow, J., and Endo, T., *Journal of Materials*, Vol. 4, 1969, pp. 176-188.
- [6] Feltner, C. E. and Laird, C., *Acta Metallurgica*, Vol. 15, 1967, pp. 1621-1632.
- [7] Laird, C., de la Veaux, R., Schwartzman, A., and Finney, J., *Journal of Testing and Evaluation*, American Society for Testing and Materials, Vol. 3, 1975, pp. 435-441.
- [8] Jaske, C. E., Mindlin, H., and Perrin, J. S. in *Cyclic Stress-Strain Behavior—Analysis, Experimentation, and Failure Prediction*, ASTM STP 519, 1973, pp. 13-27.
- [9] Landgraf, R. W. in *Cyclic Stress-Strain Behavior—Analysis, Experimentation, and Failure Prediction*, ASTM STP 519, 1973, pp. 213-228.
- [10] Koibuchi, K. and Kotani, S. in *Cyclic Stress-Strain Behavior—Analysis, Experimentation, and Failure Prediction*, ASTM STP 519, 1973, pp. 229-245.
- [11] Abel, A. and Ham, R. K., *Acta Metallurgica*, Vol. 14, 1966, pp. 1495-1503.
- [12] Calabrese, C. and Laird, C., *Materials Science and Engineering*, Vol. 13, 1974, pp. 141-157.
- [13] Calabrese, C. and Laird, C., *Materials Science and Engineering*, Vol. 13, 1974, pp. 159-174.
- [14] Kralik, G. and Schneiderhan, H., *Scripta Metallurgica*, Vol. 6, 1972, pp. 843-849.
- [15] Park, B. K., Greenhut, V., Luetjering, G., and Weissman, S., Technical Report, AFML-TR-70-195, Air Force Materials Laboratory, Aug. 1970.

- [16] Fine, M. E. and Santner, J. S., *Scripta Metallurgica*, Vol. 9, 1975, pp. 1239-1241.
- [17] McEvily, A. J., Clark, J. B., Utley, E. C., and Hernstein, W. H., *Transactions*, Associate of the Institute of Metallurgical Engineers, Vol. 221, 1963, pp. 1093-1097.
- [18] Clark, J. B. and McEvily, A. J., *Acta Metallurgica*, Vol. 12, 1964, pp. 1359-1372.
- [19] Gatto, F., *Revue de Metallurgie*, Vol. 55, 1958, pp. 1085-1089.
- [20] Laird, C. and Thomas, G., *International Journal of Fracture Mechanics*, Vol. 3, 1967, pp. 81-97.
- [21] Krause, A. R. and Laird, C., *Materials Science and Engineering*, Vol. 2, 1967, pp. 331-347.
- [22] Stubbington, C. A. and Forsyth, P. J. E., *Acta Metallurgica*, Vol. 14, 1966, pp. 5-12.
- [23] Wells, C. H. and Sullivan, C. P., *Transactions*, American Society for Metals, Vol. 57, 1964, pp. 841-855.
- [24] Byrne, J. G., Fine, M. E., and Kelly, A., *Philosophical Magazine*, Vol. 6, 1961, pp. 1119-1145.
- [25] Ashby, M. F., *Philosophical Magazine*, Vol. 21, 1970, pp. 399-424.
- [26] Endo, T. and Morrow, J., *Journal of Materials*, Vol. 4, 1969, pp. 159-175.
- [27] Kaufman, J. G., "Design of Aluminum Alloys for High Toughness and High Fatigue Strength," *AGARD Conference Proceedings No. 185*, Advisory Group for Aerospace Research and Development, 1975.
- [28] Waldman, J., Sulinski, H., and Markus, H., "New Processing Techniques for Aluminum Alloys," Pitman-Dunn Laboratory, Frankford Arsenal, Philadelphia, May 1973.
- [29] Sulinski, H. and Waldman, J., "Thermal Mechanical Processing of High Strength Aluminum Alloy Ingots," FY 75 RDT & E Annual Summary, AM CMS Cole 62105.11.H8400, Airborne Mine Countermeasure System, July 1975.
- [30] Laird, C. and Aaronson, H. I., *Acta Metallurgica*, Vol. 15, 1967, pp. 73-103.
- [31] Hren, J. and Thomas, G., *Transactions*, Associate of the Institute of Metallurgical Engineers, Vol. 227, 1963, pp. 308-318.
- [32] Sanders, T. H., Jr., "The Relationship of Microstructure to Monotonic and Cyclic Straining in Two Al-Zn-Mg Precipitation Hardening Alloys," Ph.D. Thesis, Georgia Technical University, Atlanta, 1974.
- [33] Sanders, T. H., Jr., Staley, J. T., and Mauney, D. A., "Strain Control Fatigue as a Tool to Interpret Fatigue Initiation of Aluminum Alloys," Alcoa Laboratories, Alcoa Center, Pa., Sept. 1975.
- [34] Shinohara, K. and Laird, C., unpublished research, University of Pennsylvania, Philadelphia, Pa.
- [35] Thielen, P. N., Fine, M. E., and Fournelle, R. A., *Acta Metallurgica*, Vol. 24, 1976, pp. 1-10.
- [36] Fournelle, R. A., Grey, E. A., and Fine, M. E., *Metallurgical Transactions*, Vol. 7A, 1976, pp. 669-682.

*J. Lankford,<sup>1</sup> D.L. Davidson,<sup>1</sup> and T.S. Cook<sup>1</sup>*

## Fatigue Crack Tip Plasticity

---

**REFERENCE:** Lankford, J., Davidson, D. L., and Cook, T. S., "Fatigue Crack Tip Plasticity," *Cyclic Stress-Strain and Plastic Deformation Aspects of Fatigue Crack Growth, ASTM STP 637*, American Society for Testing and Materials, 1977, pp. 36-55.

**ABSTRACT:** Theoretical calculation and experimental measurement of fatigue crack tip plastic zone size are reviewed, and recent plastic zone measurements using selected area electron channeling are presented. The relationships between state of stress, measurement technique, and plastic zone shape and size are discussed. It is shown that there exists only limited agreement between theory and experimental measurements, but that general conclusions concerning the appropriate plastic zone dimensions for various conditions can be drawn. The importance of plastic zone shape is demonstrated for the case of overload-induced crack growth retardation.

**KEY WORDS:** stresses, strains, fatigue, alloys, cracking, plastic limit, stress cycle

### Nomenclature

- a* Crack length
- b* Shear gage length
- d* Shear displacement
- K* Stress intensity factor
- $\Delta K$  Cyclic stress intensity factor range
- N* Number of cycles
- r* Distance ahead of crack
- r*<sub>1</sub> Distance from crack tip to yield boundary, based on asymptotic elastic solution
- r*<sub>2</sub>, *r*<sub>3</sub>, *r*<sub>4</sub>, *r*<sub>5</sub> Various approximations to true plastic zone size
- r*<sub>p</sub> Maximum plastic zone dimension measured from crack tip
- r*<sub>θ</sub> Plastic zone dimension in the  $\theta$  direction
- $\alpha$  Coefficient relating monotonic plastic zone size and  $(K/\sigma_y)^2$
- $\alpha'$  Coefficient relating cyclic plastic zone size and  $(K/\sigma_y)^2$
- $\bar{\alpha}_{P\sigma}$  Average  $\alpha$  for monotonic plane stress plastic zones
- $\bar{\alpha}_{P\epsilon}$  Average  $\alpha$  for monotonic plane strain plastic zones

<sup>1</sup>Senior metallurgists and senior engineer, respectively, Department of Materials Sciences, Southwest Research Institute, San Antonio, Tex. 78284.

- $\bar{\alpha}'$  Average  $\alpha'$  for all materials
- $\gamma$  Shear strain
- $\nu$  Poisson's ratio
- $\sigma_y$  Yield stress
- $\sigma_{yy}$  Normal stress ahead of crack
- $\sigma_{zz}$  Normal stress perpendicular to plane of plate
- $\Delta\sigma$  Cyclic stress range
- $\theta$  Angular direction of plastic zone radius relative to plane of crack
- $\epsilon_{zz}$  Normal strain perpendicular to plane of plate

The tips of propagating fatigue cracks are attended by plastic zones. The size and shape of these zones are important because many aspects of cyclic crack growth are directly related to the extent of plastic yielding. For example, changes in mode of crack growth (striation to dimple, superposition of static fracture onto cyclic extension) can be explained in terms of plastic zone size versus the size or spacing of metallurgical parameters (inclusion spacing, grain size). Crack tip opening displacement seems to be a function of plastic zone size, and fatigue crack propagation following overloads or during spectrum loadings is known to be controlled, to a large extent, by overload plastic zone characteristics.

A variety of theories have been developed to predict the sizes of plastic zones. These theories were first employed as correction factors for fracture mechanics calculations. Although certain simplifying physical assumptions are required in order to permit solution of the difficult equations which describe crack tip yielding, the recent calculations of both size and shape of plastic zones have been particularly useful in understanding trends in fatigue crack growth behavior.

In addition, some headway has been made in recent years in the direct characterization of fatigue crack tip yield zones. Numerous techniques have been used, including etching, X-ray microbeam, microhardness testing, transmission electron microscopy, and image distortion/optical interferometry. Recently, the authors have applied two new techniques to this problem, and the results, in conjunction with those of earlier experimenters, show promise of increasing our understanding of the manner in which complex phenomena such as spectrum loadings, environmental effects, and thickness effects can affect fatigue crack growth through modification of plastic zone parameters. Moreover, the results are useful in evaluating the relative success of the various applicable plastic zone theories.

In the following, the range of theories relating to crack tip yielding is summarized. The authors' techniques for plastic zone characterization are discussed briefly; plastic zone measurements for a variety of metals and alloys under cyclic loading are then presented and compared with theoretical predictions. Effects due to overloads are discussed, and certain general conclusions pertaining to fatigue crack tip plasticity are drawn.

### Plastic Zone Size Calculations

The early treatment of the effects of plasticity on fracture was by Orowan [1]<sup>2</sup>, when he interpreted the surface energy term in the Griffith energy criterion as the total work of fracture. This meant that not only the work to create new surface, but also the work done during plastic deformation at the crack tip, must be included in the global energy balance. Since this argument was made in general terms through the energy balance relation, it did not entail specific crack tip details. The plastic zone size estimates for fatigue cracks all have their origins in calculations made for monotonic loading, usually as correction factors for tough materials not conforming to the assumptions of linear fracture mechanics. This section analyzes some plastic zone size estimates used frequently and assesses the range of values of plastic zone size predicted by them.

Rice [2] has thoroughly reviewed the continuum mechanics approach to the calculation of plastic zone size. The simplest estimate of the plastic zone size is based on the elastic solution for the stresses at the tip of a sharp crack. If we consider a crack in an infinite plate as in Fig. 1, the normal stress ahead of the crack is given by

$$\sigma_{yy} = K/\sqrt{2\pi r} \quad (1)$$

The material ahead of the crack will yield, and  $\sigma_{yy}$  will equal the yield stress,  $\sigma_y$ , at  $r_1$ , the maximum extent of the plastic zone in the crack plane. Solving Eq 1 for  $r$  estimates the zone size as

$$r_1 = [1/(2\pi)] (K/\sigma_y)^2 \quad (2)$$

Since the material at the crack tip can support only two to three times  $\sigma_y$  a region of plastic flow will form having stresses of this magnitude, causing the volume of stressed material to be increased to plastic zone size  $r_2$  in Fig. 1. Rice suggested that  $r_2 \cong 2 r_1$ ; in a later analysis, Broek [3] showed that this approximation is reasonable, that is

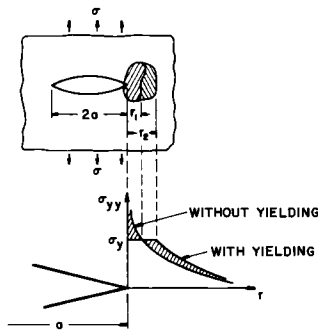


FIG. 1—Schematic illustration of plastic relaxation at loaded crack tip.

<sup>2</sup>The italic numbers in brackets refer to the list of references appended to this paper.

$$r_2 = 2r_1 = 1/\pi (K/\sigma_y)^2 \tag{3}$$

Irwin [4] argued that, while the plastic zone is larger than  $r_1$ , in many problems, it is not necessary to know the exact size and shape of the plastic zone. What is needed is an estimate of the additional crack length so that the elastic stress field for the lengthened crack would approximate the real stress field beyond the plastic zone. He termed this value the plastic zone correction factor,  $r_p$ , and found it to be in the range  $0.3 r_1 < r_p < 0.5 r_1$  for plane strain. For computational purposes, he chose the value

$$r_p = r_1 / (2\sqrt{2}) = [1 / (4\pi\sqrt{2})] (K / \sigma_y)^2 \approx [1 / (6\pi)] (K / \sigma_y)^2 \tag{4}$$

It is important to note that this is not an estimate of the plastic zone size, but rather is only a fraction of the zone; however, it is used frequently as the former.

In these estimates of zone size, the shape of the plastic zone is not a consideration. This is not true with the Dugdale model [5] which assumes that yielding takes place in a narrow strip ahead of the crack, as depicted in Fig. 2. This situation may be modeled by an infinite plate loaded at infinity, containing a crack of length  $2(a + r_3)$  where  $r_3$  is an extension of the actual crack, but is prevented from opening by restraining stresses equal to the yield stress,  $\sigma_y$ . To obtain the solution for this totally elastic problem, we make use of the fact that the stress is finite at  $a + r_3$ , that is, the stress intensity factor vanishes. Superimposing the two configurations in Fig. 2 and assuming  $r_3 \ll a$  in the stress intensity factors from Ref 6, it can be shown that

$$r_3 \approx \pi/8 (K^2 / \sigma_y^2) \tag{6}$$

This is approximately equal to  $r_2$ .

It should be noted that this model is often referred to as the Dugdale-Barenblatt or BCS model. Blarenblatt [7] independently developed a similar model with the restraining yield stresses replaced by molecular cohesive forces in an effort to overcome the physical objections to the crack tip stress singularity. Bilby, Cottrell, and Swinden [8] also used this type of model, but utilized continuously distributed dislocations to develop the governing equations. The results of the three methods are very similar.

The three dimensionality of the plastic zone size is also an important factor. To compute the elastic-plastic boundary accurately, and therefore the plastic

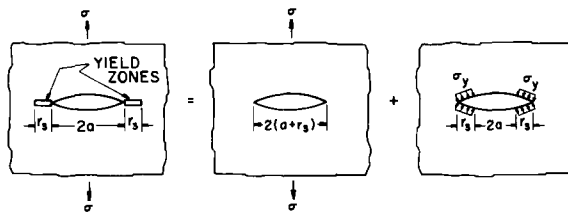


FIG. 2—Superposition involved in Dugdale Model.

zone size, a yield condition must be specified. The two most commonly used conditions are the Tresca, or maximum shear stress, and the Mises, or maximum strain energy. When applying these conditions to a two-dimensional problem, either plane strain or plane stress must be specified; a comparison of the two predicted shapes for a Mises yield criterion is given as shown in Fig. 3a [3]. (The surface produced by a Tresca condition is similar.) The plane strain zone is much smaller than the plane stress zone; at  $\theta = 0$  and  $\pi/2$ , zone dimensions are

<p>Plane Stress</p> $r_p(\theta = 0) = \frac{K^2}{2\pi\sigma_y^2}$ $r_p(\theta = \pi/2) = \frac{5K^2}{8\pi\sigma_y^2}$	<p>Plane Strain</p> $r_p(\theta = 0) = \frac{(1 - 2\nu)^2 K^2}{2\pi\sigma_y^2}$ $r_p(\theta = \pi/2) = \frac{[(1 - 2\nu)^2 + (3/2)]K^2}{4\pi\sigma_y^2}$
--	--

(7)

From these results, it is clear that the plastic zone size estimates given in Eqs. 2, 3, and 6 provide reasonable estimates for plane stress sizes, but overestimate the plane strain zone size.

Figure 3b shows the three-dimensional plastic zone through the thickness of a plate [3]; it is assumed that the plate is sufficiently thick to develop plane strain conditions in the center of the plate. At the outer surface of the plate,  $\sigma_{zz} = 0$ , and plane stress exists; as the depth of penetration increases, the stress state changes over to plane strain. Although  $\epsilon_{zz} = 0$ , the material does develop large stresses in the  $z$  direction due to the constraint. Thus, a large hydrostatic stress is created directly ahead of the crack tip. For a non-hardening Mises material, this results in stresses of three times the uniaxial yield stress; a strain hardening material has even higher stresses. The stress

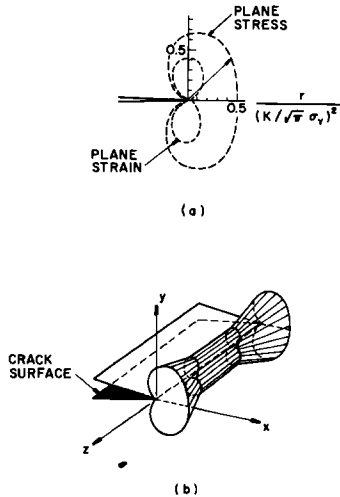


FIG. 3—Relationship between plane-strain and plane-stress plastic zones, and the effect of specimen thickness.

elevation ahead of the crack tip is not due to strain hardening in the sense of cyclic deformation, but rather is due to the constraint and the resulting high hydrostatic stress, which increases the effective yield stress. (For a full discussion of this point, including the effects of large geometry change at the crack tip, see Rice and Johnson [9].) This latter point has given rise to a large number of plastic zone estimates through the substitution of an appropriate effective yield stress reflecting the amount of constraint present in the specimen. McClintock and Irwin [10] noted that, while the plane stress plastic zone is nine times the plane strain zone (for  $\nu = 0.33$  at  $\theta = 0$ , this is obtained from Eq 9), this full degree of constraint is not likely. Based on this estimate and the fact that Eqs 2 and 3 represent plane stress zones, two additional estimates may be made

$$r_4 = \frac{r_1}{3} = \frac{1}{6\pi} \left( \frac{K}{\sigma_y} \right)^2 \quad (8)$$

and

$$r_5 = \frac{r_2}{3} = \frac{1}{3\pi} \left( \frac{K}{\sigma_y} \right)^2 \quad (9)$$

Given the extremely difficult nature of the elastic-plastic solutions, the bulk of the elastic-plastic analysis has been performed numerically. Finite-element methods allow the inclusion of almost any flow rule and degree of material hardening and, through incremental analysis, can fully account for stress redistribution and unloading that take place during plastic deformation. Much of this work has been performed by Rice and his coworkers [11,12], and, with the special crack tip elements developed by Tracey [13,14], great insight into the development of plastic zones has been attained. For small-scale yielding, plane strain conditions, the plastic zone constants are as shown in Table 1, where  $r = \alpha (\Delta K / \sigma_y)^2$ . The first two computations are made for perfectly plastic materials, while in Ref 14, Tracey dealt with an isotropic hardening material; hence, the specific zone size will depend on the hardening exponent. These computations show that, when stress redistribution is taken into account, the plane strain zone is not symmetric about the  $y$  axis, but is rotated toward the positive  $x$  axis so that the maximum zone extent occurs about  $\theta = 70$  deg. This led Rice [2] to suggest that a simple model of plane strain plastic behavior could be represented by a discrete slip line and Dugdale yield zone acting at an angle to the plane of crack advance. For  $\theta = 70$  deg, this estimates the zone size as

$$r_p = 0.175 \left( \frac{K}{\sigma_y} \right)^2 \quad (10)$$

The plastic zone size calculations just discussed are only a few of the many estimates made, but they do represent the full range of numerical values determined. They are summarized in Table 2.

Thus far, only the plastic zone size due to monotonic loading has been considered; however, since fatigue loading is cyclic, a plastic zone associated with this type of loading has been postulated [2] and apparently observed

TABLE 1—Numerical plastic zone calculations.

$\alpha =$	Levy et al [11]	Rice and Tracey [12]	Tracey [14]
$\frac{r(\theta = 0)}{(K/\sigma_y)^2}$	0.036	0.041	0.03 to 0.04
$\frac{r(\max)}{(K/\sigma_y)^2}$	0.157 ( $\theta \approx 70$ deg)	0.152 ( $\theta = 71$ deg)	0.13 to 0.15 ( $\theta = 70$ deg)
$\frac{r(\theta = \pi/2)}{(K/\sigma_y)^2}$	0.138		

experimentally [15]. Computational estimates of this zone of reverse loading assume that an effective yield stress, usually the cyclic yield stress, can be put into Eq 1. A second approach, used by Rice [2], employs a superposition argument to demonstrate that, under reversed loading, the yield stress should be replaced by two times its value. Thus, from Eq 1, the cyclic yield zone will be one fourth the monotonic plastic zone (Fig. 4).

### Plastic Zone Size

#### Measurement Techniques

For some time, the authors have been using the relatively new technique of selected area electron channeling to map out crack tip plastic zone boundaries and to quantify the strain distribution within plastic zones. The method of measuring plastic zone parameters has been described completely elsewhere [15–17]. Briefly, the procedure involves rocking the collimated electron beam in the scanning electron microscope (SEM) about a point ( $\sim 10 \mu\text{m}$  diameter) on the specimen surface. Deformation causes systematic degradation in the resulting electron channeling patterns (ECP). The crack tip plastic zone is determined by interrogating numerous small volumes of material with the electron beam, as is illustrated schematically in Fig. 5. Strains within the plastic zone are obtained by comparing the electron channeling patterns with those from a calibration specimen. Strains up to 5 to 10 percent (depending on material) may be determined to an accuracy of about  $\pm 0.5$  percent using this technique.

Large amplitude strains near the crack tip are measured by a very simple technique. Reference scratch offsets caused by crack tip shearing are obtained by replicating specimens in the loaded condition and then examining the metallized [18] replicas at high magnification in the SEM. The measured offsets can be interpreted in terms of shear strains. Previous work by the authors has indicated that shear strains as small as 5 percent can be detected in this way, so that electron channeling and reference mark displacement can be employed to define the monotonic and cyclic crack tip plastic zones, respectively [15].

Other techniques also have been found to yield information regarding plastic zones. In particular, microhardness testing apparently shows evidence of both cyclic and monotonic zones [19–22] for materials in which the plastic zones are large relative to the size of the indenter. With considerably

TABLE 2—Theoretical plastic zone size predictions.

$$r_{\theta} = \alpha \left( \frac{K}{\sigma_y} \right)^2$$

$\alpha$ , Plane Stress		Reference	$\alpha$ , Plane Strain		Reference
$\alpha_{90}^a$	$\alpha_0^b$		$\alpha_{90}^a$	$\alpha_0^b$	
0.392	0.318	[2]	...	0.053	[4]
0.199	0.159	[3]	...	0.106	[3,10]
...	0.382	[5]	0.138	...	[11]
0.199 to 0.392	0.159 to 0.382	range	~0.150	0.041	[12]
			~0.140	0.035	[14]
			0.138 to 0.150	0.035 to 0.106	range

<sup>a</sup>  $\alpha_{90}$  determined by calculating  $r_p$  normal (90 deg) to the plane of the crack.

<sup>b</sup>  $\alpha_0$  determined by calculating  $r_p$  parallel (0 deg) to the plane of the crack.

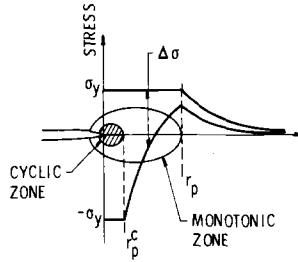


FIG. 4—Schematic illustration of the monotonic and cyclic plastic zones [2].

more difficulty, transmission electron microscopy (TEM) has shown [23] the presence of two distinct fatigue crack tip dislocation subcell structures, presumably characteristic of cyclic and monotonic zones. The monotonic zone boundary has been detected by X-ray microbeam (XMB) [24], by image distortion /interferometry [25,26], and by etching [27,28]; under certain conditions [27], the latter may also reveal the inner cyclic zone. In each of the methods cited, the cyclic zone boundary is delineated from the monotonic zone as a discontinuity in the radially varying, measured values of strain or strain-induced damage.

#### *Plastic Zone Size Measurements*

In the following section, the results of measurements carried out by the authors are presented, along with the results of tests performed under similar, but not identical, conditions by other experimenters. Specimen preparation and the configuration used in our tests, as well as the mechanical properties of our alloys (6061-T6 aluminum, 304 stainless steel, low-carbon steel, and Fe-3Si), are described elsewhere [15,17]. All tests were carried out under ambient laboratory conditions (laboratory air, ~50 percent relative humidity), with the cyclic load ratio  $R$  approximately zero. Readers are directed to the references for the details of tests performed by other cited researchers. It should be noted that Wilkins and Smith [23] cycled their specimens in push-pull, that is,  $R = -1$ ; in this case,  $\Delta K$  was calculated on the basis of the nominally tensile portion of the load cycle. All of the measurements to be discussed were obtained from fatigue-loaded specimens, with the exception of the data from the statically loaded, fatigue-precracked

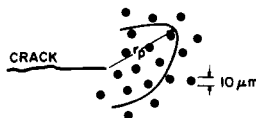


FIG. 5—Schematic illustration of ECP sampling during determination of monotonic plastic zone boundary.

7075-T6 specimens of Pettit and Hoepfner [25], which are included for purposes of comparison with other aluminum alloys.

As shown in Fig. 6, the maximum monotonic plastic zone size  $r_p$  for all materials correlates in a linear fashion with  $(K/\sigma_y)^2$ . For most materials, the correlating coefficient  $\alpha$  lies between 0.05 and 0.14. Notable exceptions are the values for 2024-T3 [26] and 7075-T6 [25], for which the  $\alpha$ s are 0.3 and 0.4, respectively. There does exist evidence [29,30] for  $\alpha \cong 0.15$  for 2024-T3 cycled in the range  $7 \text{ MN m}^{-3/2} \leq K \leq 20 \text{ MN m}^{-3/2}$ . Recent work by the authors on 2024-T4, using the electron channeling technique, indicates that, for this material,  $\alpha$  may be closer to 0.25.

Data for the 7075-T6 work are confusing. Pettit and Hoepfner [25] list two different  $\alpha$ s ( $\sim 0.15$  and 0.65). However, the data plotted in their figures yield  $\alpha = 0.4$ , which is the value used in Fig. 6. This value probably should be used with caution.

Except for these two alloys, the maximum monotonic plastic zone sizes are correlated by a fairly narrow range in  $\alpha$  for materials whose yield strengths range from 38 to 1790  $\text{MN/m}^2$  (Table 3). Stacking fault energy (SFE) does not seem to be a major influence in controlling plastic zone size.

The spread in  $\alpha$  can be rationalized somewhat on the basis of plane stress-plane strain considerations. Measurements taken on specimen surfaces

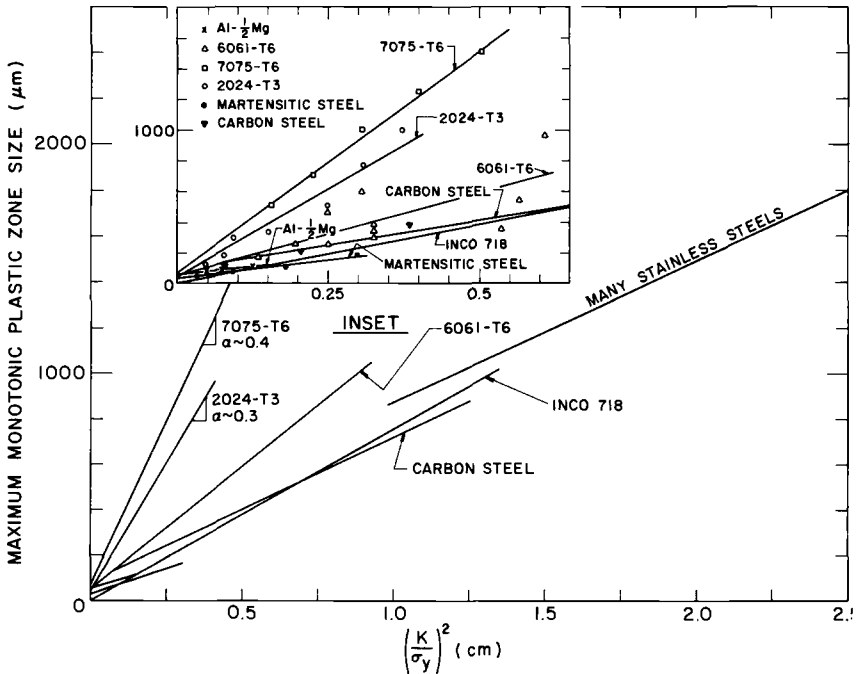


FIG. 6—Maximum plastic zone size versus  $(K/\sigma_y)^2$  for various alloys. Inset shows details near the origin.

tend to reflect a predominantly plane stress ( $P\sigma$ ) situation, while midplane or interior measurements are more nearly plane strain ( $Pe$ ). Averaging all of the  $\alpha$ s in Table 3 generated from surface measurement yields  $\bar{\alpha}_{P\sigma} \approx 0.1$ ; similarly, from midplane (interior) measurements,  $\bar{\alpha}_{Pe} \approx 0.06$ , so that one finds  $\bar{\alpha}_{P\sigma}/\bar{\alpha}_{Pe} \cong 1.67$ . This result is in good agreement with the theoretical determination by Rice [2] that  $\bar{\alpha}_{P\sigma}/\bar{\alpha}_{Pe} = 2$ .

A remarkable consistency is evidenced in nearly all determinations of  $\alpha'$ , the correlating coefficient for the maximum cyclic plastic zone radius. The range in this parameter is 0.007 to 0.028, but  $\bar{\alpha}' = 0.014$  lies within 10 percent of most of the individual values of  $\alpha'$ . The magnitude of  $\alpha'$  seems to be independent of the state of stress, the alloy system, and the method of measurement. Earlier, Hahn et al [27], in their elegant etching studies of Fe-3Si, had observed that the cyclic zone size seemed to be unaltered by changes in the state of stress which nevertheless affected  $r_p$  to a marked extent. The present work extends the generality of that observation to a wide range of alloys.

### Plastic Zone Shape

The preceding results have been generalities to the extent that only maximum plastic zone sizes have been discussed. Inclusion of plastic zone shape brings to light important discrepancies between various experimental methods and between theory and experiment.

#### *Cyclic Plastic Zone Shape*

The state of knowledge regarding fatigue crack tip plastic zone configurations, based on experimental measurement, is summarized in Fig. 7 (recall Fig. 3, which showed the theoretically predicted plane stress and plane strain plastic zone shapes). The monotonic zone (solid line) is sketched to scale relative to the cyclic zone (dashed line). When these shapes are taken into account, it is possible to tabulate (Table 4) monotonic plastic zone sizes in the plane of the crack ( $\alpha_0$ ) and normal to it ( $\alpha_{90}$ ). Reasonable agreement between theory and experiment is indicated, where appropriate, by the underlining of such entries in the table.

Generally, the measured plastic zone size lies below or within the lower range of predicted values. The best theoretical to experimental agreement, that is, in terms of both  $\alpha_{90}$  and  $\sigma_0$  appears to exist for the present 304 stainless steel measurements, and for the Fe-3Si etching measurements of Hahn et al [27]. On the other hand, there remains the question of how to explain the poor theoretical to experimental agreement shown by microhardness for other stainless steels, including 16-13 and 24-20 [20], and 301 and Fe-34Ni [21]. Similarly, there is an apparent discrepancy between the Fe-3Si surface etching results of Hahn et al [27] and the electron channeling plastic zone determinations. Possible reasons for each of these two cases follow.

TABLE 3—Maximum plastic zone size measurements.

Material	Yield Strength, MN/m <sup>2</sup>	SFE, erg/cm <sup>2</sup>	$\alpha^d$	$\alpha^{d,b}$	Measurement Location	Nominal State of Stress		Reference
						Measurement Technique	Measurement Location	
Al-1/2Mg	117	<200	0.08	0.015	interior	$P\epsilon$	TEM	Wilkens and Smith [23]
6061-T6	296	<200	0.14	0.016	surface	$P\sigma$	ECP, replication	Davidson and Lankford [15]
2024-T3	393	<200	0.30	...	surface	$P\sigma$	grid displacement	Liu and Ino [26]
7075-T6	517	<200	0.40	...	surface	$P\sigma$	image distortion	Pettit and Hoepfner [25]
Low-carbon steel	220	...	...	0.007	surface	$P\sigma$	channeling contrast	Davidson et al [17]
Low-carbon steel	220	...	0.07	0.009	surface	$P\sigma$	XMB, slip lines	Yokobori et al [24]
Fe-3Si	420	...	0.10	0.009	surface	$P\sigma$	ECP	Davidson and Lankford [15]
Fe-3Si	460	...	0.17	0.028	surface	$P\sigma$	etching	Hahn et al [27]
Fe-3Si	460	...	0.08	0.028	midplane	$P\epsilon$	etching	Hahn et al [27]
16-13 stainless steel	193	~25	0.05	0.012	midplane	$P\epsilon$	microhardness	Bathias and Pelloux [20]
24-20 stainless steel	276	...	0.05	0.012	midplane	$P\epsilon$	microhardness	Bathias and Pelloux [20]
304 stainless steel	224	~20	0.144	0.006	surface	$P\sigma$	ECP, replication	Davidson and Lankford [15]
Fe-34Ni	262	50	0.053	0.01	midplane	$P\epsilon$	microhardness	Pineau and Pelloux [21]
301 stainless steel	360	25	0.053	0.01	midplane	$P\epsilon$	microhardness	Pineau and Pelloux [21]
Annealed maraging steel	960	...	0.06	...	midplane	$P\epsilon$	microhardness	Bathias and Pelloux [20]
Maraging steel	1790	...	0.10	...	midplane	$P\epsilon$	microhardness	Bathias and Pelloux [20]
Copper	53	55	0.056	0.014	midplane	$P\epsilon$	microhardness	Saxena and Antolovich [19]
Cu-2.2Al	83	31.5	...	0.011	midplane	$P\epsilon$	microhardness	Saxena and Antolovich [19]
Cu-4.2Al	127	13	...	0.013	midplane	$P\epsilon$	microhardness	Saxena and Antolovich [19]
Cu-6.3Al	138	5.5	...	0.0135	midplane	$P\epsilon$	microhardness	Saxena and Antolovich [19]
Single-crystal copper	38	55	0.08	0.025	interior	$P\epsilon$	microhardness	Purcell and Weertman [22]
INCO 718	1070	...	~0.12	...	surface	$P\sigma$	etching	Clavel et al [28]
INCO 718	1070	...	~0.075	...	interior	$P\epsilon$	etching	Clavel et al [28]

$$r_p^a = \alpha \left( \frac{K}{\sigma_y} \right)^2$$

$$b r_p^c = \alpha' \left( \frac{\Delta K}{\sigma_v} \right)^2$$

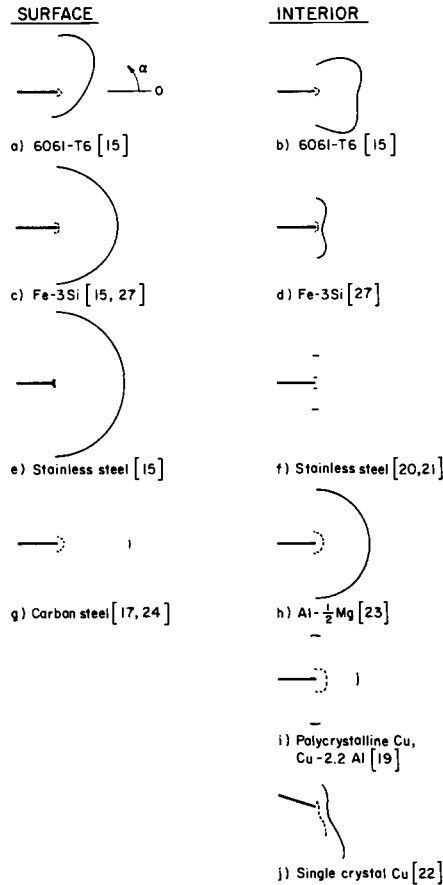


FIG. 7—Monotonic and cyclic plastic zone relative size and shape for several materials.

Pelloux et al [20,21] used the microhardness approach to measure plastic zones in maraging steels, as well as for the stainless steels just mentioned. Saxena and Antolovich [19] used the same technique for copper alloys. For the maraging steels,  $\alpha_{90}$  ranged from 0.06 to 0.10. For all of the other materials, microhardness experiments produced an  $\alpha_{90}$  of about 0.05, well below the minimum theoretical plane strain value of 0.138, and below the writers' finding of  $\alpha_{90} = 0.144$  at the surface.

The generally low values of  $\alpha_{90}$  determined by means of microhardness testing bring into question the relative sensitivity of the technique. Accordingly, an experiment was carried out to determine this point. Microhardness tests performed on a calibrated tapered tensile specimen showed that a discernible increase in hardness did not occur until a strain of ~6 percent was attained. Earlier electron channeling data [31] obtained from the same tapered tensile specimen showed the least detectable plastic strain to

TABLE 4—Measured versus predicted plastic zone sizes.

Material	$\alpha_{90}$	$\alpha_0$	$\alpha_{90}^{theory}$	$\alpha_0^{theory}$	Nominal State of Stress
Stainless steels [20,21]	0.05	...	0.138 to 0.150	...	$P\epsilon$
304 stainless steel [this work]	0.144	0.144	0.199 to 0.392	0.159 to 0.382	$P\sigma$
Carbon steel [24]	...	0.07	...	0.159 to 0.382	$P\sigma$
Maraging steel [20]	0.06 to 0.1	...	0.199 to 0.392	...	$P\epsilon$
Polycrystalline copper [19]	0.056	0.056	0.138 to 0.15	0.035 to 0.106	$P\epsilon$
Single-crystal copper [22]	...	0.08	...	0.035 to 0.106	$P\epsilon$
6061-T6 [this work]	0.14	0.09	0.199 to 0.392	0.159 to 0.382	$P\sigma$
Al-1/2Mg [23]	0.08	0.08	0.138 to 0.15	0.035 to 0.106	$P\epsilon$
2024-T3 [26]	...	0.3	...	0.159 to 0.382	$P\sigma$
7075-T6 [25]	...	0.4	...	0.159 to 0.382	$P\sigma$
Fe-3Si [27]	0.17	~0.17	0.199 to 0.392	0.159 to 0.382	$P\sigma$
Fe-3Si [27]	0.08	~0.03	0.138 to 0.15	0.035 to 0.106	$P\epsilon$
Fe-3Si [this work]	0.10	0.10	0.199 to 0.392	0.159 to 0.382	$P\sigma$
INCO 718 [28]	0.07 to 0.09	...	0.199 to 0.392	...	$P\sigma$
INCO 718 [28]	0.03 to 0.05	...	0.138 to 0.392	...	$P\epsilon$

be about 0.4 percent. Other electron channeling work [15] has shown that, for 304 stainless steel, the plastic zone radius corresponding to 6 percent tensile strain occurs at approximately one quarter of the largest monotonic zone dimension established on the basis of 0.4 percent strain sensitivity. This factor of one quarter is in reasonable agreement with the observed difference between plastic zone radii in stainless steels determined by channeling and microhardness tests. Consequently, it appears that the difference can be resolved simply on the basis of greater sensitivity on the part of electron channeling to small plastic strain amplitudes.

In the case of the Fe-3Si experiments, the difference probably lies in the fact that the tests performed by Hahn et al [27] were carried out at 100°C, rather than at room temperature [15]. The purpose of the higher temperature was to promote plasticity and avoid the cleavage mode of fatigue crack growth characteristic of Fe-3Si at 23°C; the success of this maneuver is indicated by the excellent correlation which was obtained between the experimental etching results and the fully plastic solution [3].

Hahn, Sarrate, and Rosenfield [32] earlier had shown that, at room temperature,  $\alpha_{90}$  for Fe-3Si was about 0.13, in good agreement with the present value of  $\alpha_{90} = 0.10$ . Further evidence of the good correlation between channeling and etching, when plastic zone measurements are carried out under similar conditions, is shown in Fig. 8. Here the 1 percent strain monotonic boundary determined from electron channeling (before etching) is shown to match the boundary of the dark etching monotonic plastic zone about a fatigue crack in Fe-3Si reasonably well.

It is apparent that there now exists considerable evidence, as shown in Table 3, that the relative monotonic and cyclic plastic zone sizes for a number of alloys (6061-T6 aluminum [15], low-carbon steel [24], 304 stainless steel [15], Fe-3Si [15,17]) are not accurately predicted by simple theory [2]. In particular, the ratio of the maximum monotonic to cyclic plastic zone size seems to be of the order of 10:1, rather than 4:1. Considering that the 4:1 ratio found for stainless steels [20,21] and copper-aluminum alloys [19] using microhardness probably is too low, as just discussed, further strengthens this view. However, it should be borne in mind that Rice [2] had realized and pointed out the idealizations inherent in the model on which the 4:1 ratio rests, particularly that the material was assumed to be elastic-perfectly plastic in its flow behavior. It is likely that, by taking into account this factor, as well as by using cyclic rather than monotonic plasticity, the theoretical plastic zone size ratio would be increased.

### *Overload Plastic Zone Morphology*

The importance of plastic zone shape, as contrasted with mere average or maximum zone size, can be demonstrated through consideration of the effect of an overload cycle upon subsequent fatigue crack propagation in 6061-T6 aluminum. This problem has been investigated recently in con-



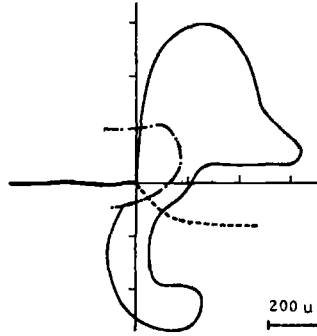


FIG. 9—Cyclic and overload plastic zone boundaries and their relation to postoverload crack growth, 6061-T6 alloy, 100 percent overload,  $\Delta K = 10.5 \text{ MN/m}^{3/2}$ .

in Fig. 11a. Since the zone does not extend directly ahead of the crack, no retardation is observed (Fig. 11b). Following a 100 percent overload, a larger overload zone appears, which extends a finite distance ahead of the crack (Configuration 2) and causes retarded crack growth (Fig. 11b), while the crack traverses the distance to the nearest boundary. A still higher overload closes the "arms" of the overload zone, leaving a relatively undisturbed "hole" (Configuration 3), which allows the crack a momentary acceleration (Fig. 11b) during the retardation period. Finally, still higher overloads produce a solid zone (Configuration 4), whose maximum dimension must be

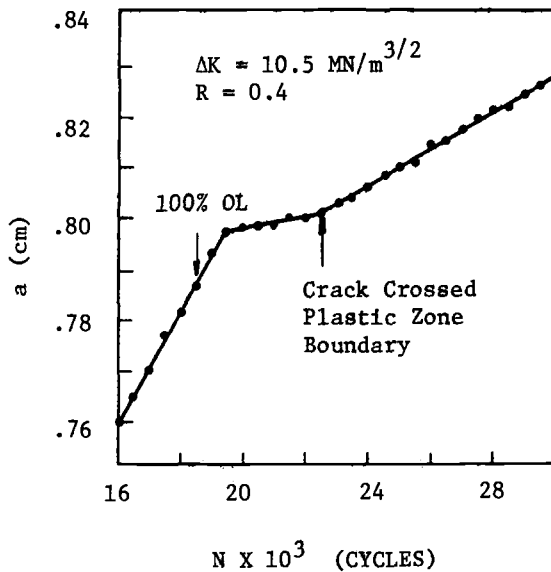


FIG. 10—Crack growth versus cycles for overload test shown in Fig. 9.

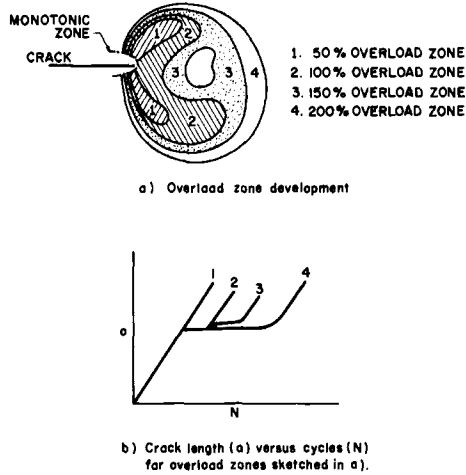


FIG. 11—Schematic illustration of overload zone shape upon postoverload fatigue crack growth.

traversed by the crack. Such large overloads also are known to arrest cracks completely [33], or to cause them to renucleate at the monotonic zone boundary [16] and later rejoin the main crack front. It should be noted, however, that, prior to application of the largest overload, retardation is controlled (in 6061-T6) to a major extent by plastic zone morphology, and the overload-affected crack length could not be predicted based on a simple notion of plastic zone change.

### Conclusions

Based on the preceding findings, certain conclusions regarding fatigue crack tip plastic zones may be drawn.

1. For most materials, a good estimate of the maximum monotonic plastic zone size can be obtained using  $\alpha \approx 0.06$  to 0.10.

2. For most of the materials studied, the maximum cyclic plastic zone size corresponds to  $\alpha' \approx 0.014$ , independent of the state of stress.

3. Monotonic plastic zone sizes frequently vary with direction relative to the plane of the crack.

4. Measured values of  $\alpha$  are often smaller than theoretical values.

5. Plastic zone measurements by microhardness may not reflect the maximum extent of the monotonic zone.

6. Cleavage modes of fatigue crack growth correspond to smaller plastic zones than in similar, fully plastic situations.

7. For most materials, measurements indicate that

(a)  $\alpha_{90, P_e} \approx 0.05$  to 0.1

(b)  $\alpha_{0, P_e} \approx 0.03$  to 0.08

(c)  $\alpha_{90, P_\sigma} \approx 0.1$  to 0.17

(d)  $\alpha_{0, P_\sigma}$  is unclear

8. Plastic zone shape can affect crack growth subsequent to an overload.

### Acknowledgments

The authors are grateful for the financial support of the Air Force Office of Scientific Research, Contract F44620-75-C-0050, during the course of this work.

### References

- [1] Orowan, E., "Energy Criteria of Fracture," *The Welding Journal Research Supplement*, March 1955.
- [2] Rice, J. R., *Fatigue Crack Propagation, ASTM STP 415*, American Society for Testing and Materials, 1967, pp. 247-311.
- [3] Broek, D., *Elementary Engineering Fracture Mechanics*, Noordhoff International Publishing, The Netherlands, 1974.
- [4] Irwin, G. R., "Plastic Zone Near a Crack and Fracture Toughness," *Proceedings, Seventh Sagamore Conference*, 1960, p. IV-63.
- [5] Dugdale, D. S., *Journal of Mechanics and Physics of Solids*, Vol. 8, 1960, p. 100.
- [6] Sih, G. C., *Handbook of Stress Intensity Factors*, Institute of Fracture and Solid Mechanics, Lehigh University, 1973.
- [7] Barenblatt, G. I., *Advances in Applied Mechanics*, Vol. 7, 1962, pp. 55-129.
- [8] Bilby, B.A., Cottrell, A. H., and Swinden, K. H., *Proceedings of the Royal Society*, Vol. A272, 1963, pp. 304-310.
- [9] Rice, J. R. and Johnson, M. A., *Inelastic Behavior of Solids*, M. F. Kanninen et al, Eds., McGraw-Hill, New York, 1970, pp. 641-672.
- [10] McClintock, F. A. and Irwin, G. R., *Fracture Toughness Testing and Its Applications, ASTM STP 381*, American Society for Testing and Materials, 1965, pp. 84-113.
- [11] Levy, N., Marcal, P. V., Ostergren, W. J., and Rice, J. R., *International Journal of Fracture Mechanics*, Vol. 7, 1971, pp. 143-156.
- [12] Rice, J. R. and Tracey, D. M., *Numerical and Computer Methods in Structural Mechanics*, S. J. Fenves et al, Eds., Academic Press, New York, 1973, pp. 585-623.
- [13] Tracey, D. M., *Engineering Fracture Mechanics*, Vol. 3, 1971, pp. 255-265.
- [14] Tracey, D. M., *Journal of Materials Technology*, Vol. 98, April 1976, pp. 146-151.
- [15] Davidson, D. L. and Lankford, J., *Journal of Engineering Materials and Technology*, Vol. 98, Jan. 1976, pp. 24-29.
- [16] Lankford, J. and Davidson, D. L., *Journal of Engineering Materials and Technology*, Vol. 98, Jan. 1976, pp. 17-23.
- [17] Davidson, D. L., Lankford, J., Yokobori, T., and Sato, K., *Engineering Fracture Mechanics*, Vol. 12, Aug. 1976, pp. 579-585.
- [18] Lankford, J. and Barbee, J. G., *Journal of Materials Science*, Vol. 9, Sept. 1974, pp. 1906-1908.
- [19] Saxena, A. and Antolovich, S. D., *Metallurgical Transactions A*, Vol. 6A, Sept. 1975, pp. 1809-1828.
- [20] Bathias, C. and Pelloux, R. M., *Metallurgical Transactions*, Vol. 4, May 1973, pp. 1265-1273.
- [21] Pineau, A.G. and Pelloux, R. M., *Metallurgical Transactions*, Vol. 5, May 1974, pp. 1103-1112.
- [22] Purcell, A. H. and Weertman, J., *Metallurgical Transactions*, Vol. 5, Aug. 1974, pp. 1805-1809.
- [23] Wilkins, M. A. and Smith, G. C., *Acta Metallurgica*, Vol. 18, Sept. 1970, pp. 1035-1043.
- [24] Yokobori, T., Sato, K., and Yaguchi, H., *Reports of the Research Institute for Strength and Fracture of Materials*, Tohoku University, Sendai, Japan, Vol. 9, No. 1, Nov. 1973, pp. 1-10.
- [25] Pettit, D. E. and Hoepfner, D. W., *Engineering Fracture Mechanics*, Vol. 5, Dec. 1973, pp. 923-934.
- [26] Liu, H. W. and Ino, N., *Fracture 1969*, Chapman and Hall, London, 1969, pp. 812-823.

- [27] Hahn, G. T., Hoagland, R. G., and Rosenfield, A. R., *Metallurgical Transactions*, Vol. 3, May 1972, pp. 1189-1202.
- [28] Clavel, M., Fournier, D., and Pineau, A., *Metallurgical Transactions A*, Vol. 6A, Dec. 1975, pp. 2305-2307.
- [29] Von Euw, E. F. J., Hertzberg, R. W., and Roberts, R., *Stress Analysis and Growth of Cracks*, ASTM STP 513, American Society for Testing and Materials, 1972, pp. 230-259.
- [30] Trebules, V. W., Roberts, R., and Hertzberg, R. W., *Progress in Flaw Growth and Fracture Toughness Testing*, ASTM STP 536, American Society for Testing and Materials, 1973, pp. 115-146.
- [31] Davidson, D. L., *Scanning Electron Microscopy* 1974, 1974, pp. 927-934.
- [32] Hahn, G. T., Sarrate, M., and Rosenfield, A. R., *Proceedings of the Air Force Conference on Fatigue and Fracture of Aircraft Structures and Materials*, AFFDLTR-70-144, Sept. 1970, p. 425.
- [33] Himmelein, M. K. and Hillberry, B. M., *Mechanics of Crack Growth*, ASTM STP 590, American Society for Testing and Materials. 1976, pp. 321-330.

J. C. Newman, Jr.<sup>1</sup>

# Finite-Element Analysis of Crack Growth Under Monotonic and Cyclic Loading

---

**REFERENCE:** Newman, J. C., Jr., "Finite-Element Analysis of Crack Growth Under Monotonic and Cyclic Loading," *Cyclic Stress-Strain and Plastic Deformation Aspects of Fatigue Crack Growth*, ASTM STP 637, American Society for Testing and Materials, 1977, pp. 56-80.

**ABSTRACT:** An elastic-plastic (incremental) finite-element analysis, in conjunction with a crack-growth criterion, was used to study crack-growth behavior under monotonic and cyclic loading. The crack-growth criterion was based on crack-tip strain. Whenever the crack-tip strain equals or exceeds a critical strain value, the crack grows. The effects of element-mesh size, critical strain, strain hardening, and specimen type (tension or bending) on crack growth under monotonic loading were investigated. Crack growth under cyclic loading (constant amplitude and simple variable amplitude) were also studied. A combined hardening theory, which incorporates features of both isotropic and kinematic hardening under cyclic loading, was also developed for smooth yield surfaces and was used in the analysis.

**KEY WORDS:** stresses, strains, fatigue (materials), crack propagation, fractures, elastic analysis, strain hardening

## Nomenclature

- a* Crack length defined in Fig. 1, m
- a*<sub>0</sub> Initial crack length, m
- C* Crack-growth constant in Eq 5
- E* Young's modulus, N/m<sup>2</sup>
- K<sub>I</sub>* Elastic (Mode I) stress-intensity factor, N/m<sup>3/2</sup>
- K<sub>T</sub>* Elastic stress concentration
- M* Applied moment, N·m
- n* Crack-growth constant in Eq 5
- m* Linear strain-hardening coefficient
- R* Stress ratio (ratio of minimum to maximum applied stress)
- S* Applied stress, N/m<sup>2</sup>
- W* Specimen width, m

<sup>1</sup>Research engineer, NASA-Langley Research Center, Hampton, Va. 23665.

$x, y$	Cartesian coordinates
$\alpha_x, \alpha_y, \alpha_{xy}$	Coordinates of origin of yield surface, $N/m^2$
$\beta$	Kinematic-hardening coefficient
$\epsilon$	Strain
$\epsilon_{cr}$	Critical strain
$\bar{\epsilon}_{yy}$	Nodal average strain in $y$ -direction
$\Delta\alpha$	Increment crack growth, $m$
$\Delta K_{eff}$	Effective stress-intensity factor range, $N/m^{3/2}$
$\Delta S_{eff}$	Effective stress range, $N/m^2$
$\Delta N$	Incremental number of cycles
$\sigma$	Stress, $N/m^2$
$\sigma_x$	Normal stress in $x$ -direction, $N/m^2$
$\sigma_y$	Normal stress in $y$ -direction, $N/m^2$
$\tau_{xy}$	Shear stress, $N/m^2$
$\sigma_{ys}$	Uniaxial yield stress, $N/m^2$
$\bar{\sigma}$	Current yield stress, $N/m^2$
$\{d\sigma\}$	Incremental stress, $N/m^2$
$\{d\alpha\}$	Incremental shift in origin of yield surface, $N/m^2$

Experiments [1]<sup>2</sup> on metals have shown that, under monotonic loading to failure, a crack goes through three stages of behavior: (a) a period of no crack growth, (b) a period of stable crack growth, and (c) crack-growth instability. Under monotonic and cyclic loading, the separation between the periods of no crack growth and stable crack growth has been shown to be influenced by the crack-closure effect [2] or, more precisely, the crack-opening stress.

Finite-element analyses have been used to model crack-growth behavior under either monotonic [3,4] or cyclic loading [5-8]. But these analyses simulated crack growth somewhat artificially by only allowing the crack to extend at prescribed loads.

In the present paper, a more realistic crack-growth criterion was incorporated into an existing nonlinear finite-element analysis program [5]. The crack-growth criterion was based on crack-tip strain. Whenever the crack-tip strain (nodal average) equals or exceeds a critical value, the crack grows. Crack growth under both monotonic and cyclic loading was studied using this criterion. The effects of element-mesh size, critical strain, strain hardening, and specimen type (tension or bending) on crack growth under monotonic loading were investigated. Crack growth under cyclic loading (constant amplitude and simple variable amplitude) was also studied. The crack-closure effect was accounted for in the analysis. Strain hardening under cyclic loading was assumed to be either isotropic, kinematic, or a combination of the two. A combined hardening theory, which incorporates features of both isotropic and kinematic hardening, was also developed for use with any smooth yield surface and was used in the analysis.

<sup>2</sup>The italic numbers in brackets refer to the list of references appended to this paper.

### Methods of Analysis

The elastic-plastic analysis of center-crack tension and edge-crack bend specimens (Fig. 1) employed the finite-element method and the initial-stress concept [9]. The finite-element model for these specimens, Fig. 2, was composed of two-dimensional, constant strain, triangular elements (unit thickness). Four different mesh sizes were used to model the crack-tip region, Fig. 3. Table 1 shows the elastic-stress concentration, the smallest element size, and the total number of elements and nodes used for the four different meshes. Fictitious springs were used to change the boundary conditions associated with crack growth, crack closure, or crack opening. The use of the springs was found to be computationally efficient. For free nodes along the crack surfaces, the spring stiffnesses were set equal to zero, and, for fixed nodes, the stiffnesses were assigned extremely large values. (See Ref 8 for details.)

For simplicity, the material stress-strain behavior was assumed to be bilinear, as illustrated in Fig. 4. In the analysis, the modulus of elasticity was selected as  $70\,000\text{ MN/m}^2$ , the yield stress,  $\sigma_{ys}$ , was  $350\text{ MN/m}^2$ , and  $m$  was either zero or 0.1. These properties are representative of aluminum alloy materials. The cyclic stress-strain behavior was also taken to be the stabilized behavior, that is, the stress-strain relation was assumed to be

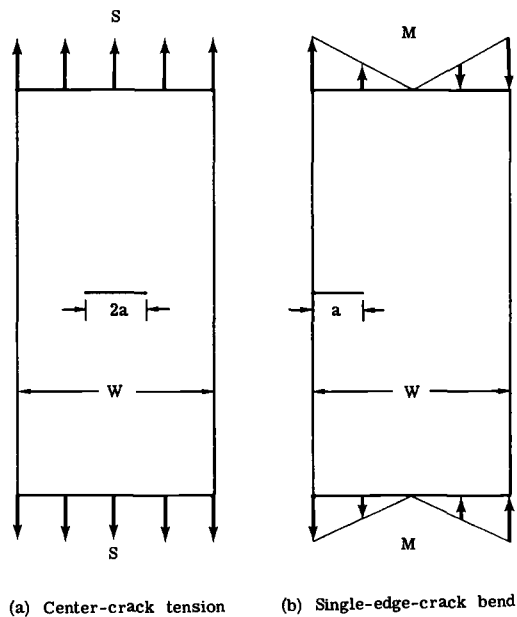


FIG. 1—Specimen configurations analyzed.

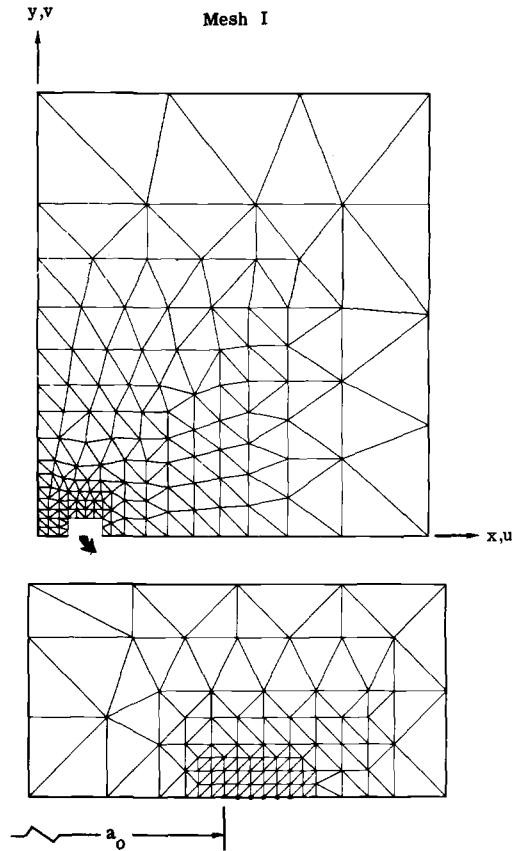


FIG. 2—Finite-element idealization of the specimens analyzed.

unaffected by further cycling. The solid lines show the behavior under cyclic loading for kinematic hardening [10]. Kinematic hardening accounts, to some extent, for the Bauschinger effect exhibited by most materials. The dashed lines show the behavior for isotropic hardening [11]. The dotted lines show the behavior for a combined hardening theory. The combined hardening theory, developed in the Appendix, is similar to that proposed by Hodge [12,13], but applies here for any smooth yield surface. The combined theory allows for an expansion and translation of the yield surface and provides a more accurate description of the hardening behavior. Reference 14 has shown that strain-hardening behavior under cyclic loading generally falls between that predicted by isotropic and kinematic hardening. The yield surface was assumed to have a form similar to the von Mises yield criterion (see the Appendix). For isotropic hardening, the yield surface used herein reduces to that proposed by von Mises.

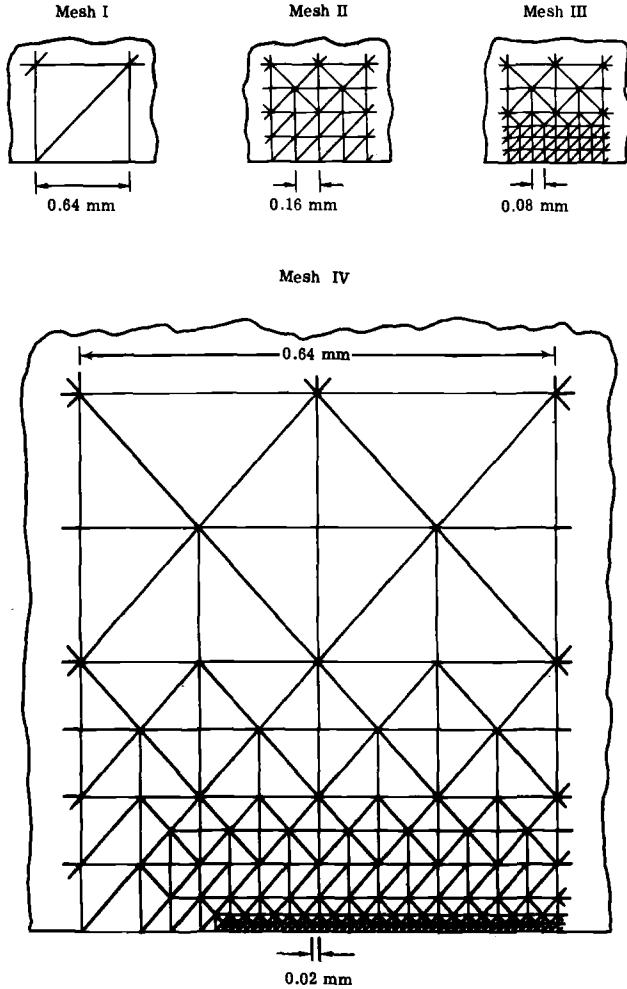


FIG. 3—Typical crack-tip region element sizes for Meshes I, II, III and IV.

### Crack-Growth Criterion

The present study incorporates a realistic crack-growth criterion into the analysis. Previous studies [3-8] used an artificial growth criterion where the crack was allowed to grow only at prescribed loads. The crack-growth criterion used herein was based on the crack-tip strain. The crack-tip strain was the nodal average strain,  $\bar{\epsilon}_{yy}$ , computed from the normal strains on all of the elements connected to the crack-tip node. During incremental loading (monotonic or cyclic), whenever the nodal average strain,  $\bar{\epsilon}_{yy}$ , equalled or exceeded a preset critical strain,  $\epsilon_{cr}$ , the crack-tip node broke (spring stiffness set equal to zero), and the crack advanced to the next node

TABLE 1—Comparison of stress concentration, smallest element size, and the number of elements and nodes for Meshes I, II, III, and IV.

Mesh	$K_T$	$\Delta a,^a$ mm	Elements	Nodes
I	7.2	0.64	398	226
II	14.4	0.16	533	300
III	20.9	0.08	639	358
IV	41.7	0.02	865	494

<sup>a</sup> $a_0 = 28$  mm;  $W = 450$  mm for the center-crack specimen, and  $W = 225$  mm for the single-edge-crack specimen.

(one element size). The restraining force at the crack-tip node was then released and redistributed. The nodal average strain on the new crack-tip node was monitored to see if it was greater or less than the critical strain. If the new crack-tip strain was greater than  $\epsilon_{cr}$ , the crack continued to grow. If the strain was less than  $\epsilon_{cr}$ , the applied load was increased until the new crack-tip strain reached the critical value, and the crack again moved forward. This process was repeated until the desired load was

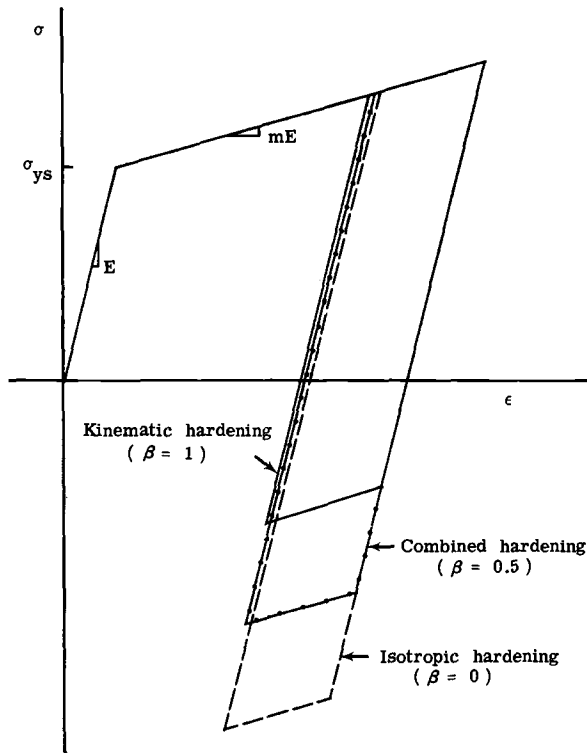


FIG. 4—Assumed stress-strain properties under cyclic loading.

reached or until the crack growth became unstable (the crack continued to grow without any further increase in load).

### Crack Growth Under Monotonic and Cyclic Loading

The finite-element analysis with the crack-tip strain growth criterion was used to study crack-growth behavior under either monotonic or cyclic loading. Under monotonic loading, the effects of mesh size, critical strain, strain hardening, and specimen type (tension or bending) on crack growth were investigated. Crack growth under either constant-amplitude or simple variable-amplitude loading was also studied. The effects of assuming either isotropic hardening (uniform expansion of the yield surface) or combined hardening (expansion and translation of the yield surface) on crack growth were also investigated.

#### *Monotonic Loading*

Figure 5 shows the typical crack-growth behavior that was obtained from the finite-element analysis using the critical strain criterion. The figure shows applied load plotted against crack length. During initial loading, a plastic zone developed at and to the right of the crack tip as illustrated in Insert (a). At a certain load, the crack-tip strain became critical and the crack moved forward one element size while the applied load was held

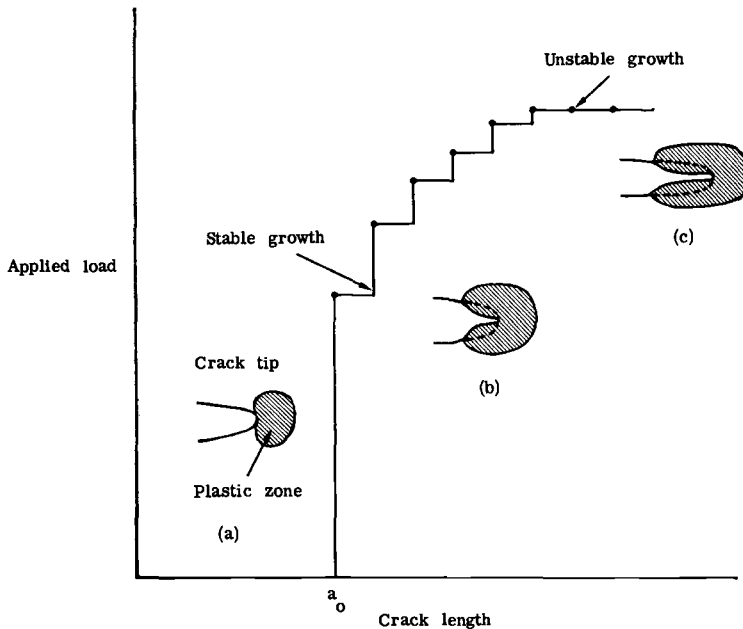


FIG. 5—Typical crack-growth behavior under monotonic loading.

constant. The nodal average strain on the new crack tip node was found to be less than the critical strain. The dashed curve in Insert (b) shows what the crack-surface displacements would have been if plastic deformations occurred only at and to the right of the crack tip. The plastic deformations remaining in the wake of the advancing crack (shaded region to the left of the crack tip) shield the new crack tip and cause the elements in the crack-tip region to undergo less strain to meet compatibility with adjacent elements. Thus, an increase in applied load was required to advance the crack further. This process was repeated until the desired load was reached, or until the crack growth became unstable. Crack-growth instability (inferred from the finite-element analysis) was believed to be caused by a stabilizing effect from the plastic deformations on the crack-tip strain, that is, the crack-tip elements received no additional strain reduction from leaving more plastic deformations in the wake of the advancing crack. At the instability load, the strain on the new crack tip was always equal to or greater than the critical strain, and the crack continued to grow from node to node.

*Mesh Size*—Figure 6 shows the effects on crack growth of using a coarse, medium, and fine mesh (Meshes II, III, and IV, respectively) in the crack-tip region. The typical mesh patterns in the crack-tip region for these meshes are shown in Fig. 3. The material was assumed to be elastic-perfect plastic

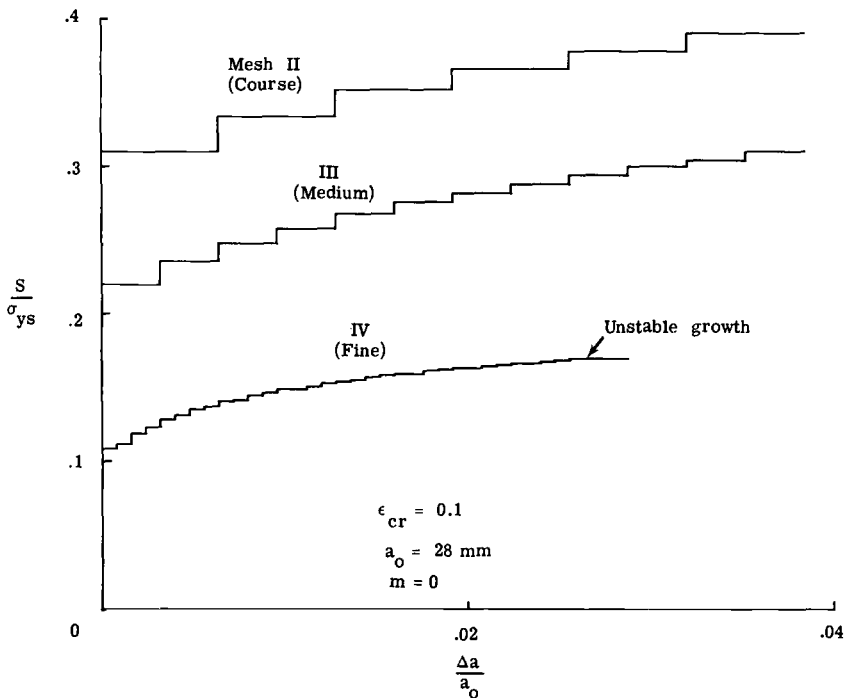


FIG. 6—Effect of mesh size on crack growth.

( $m = 0$ ). The initial crack length ( $a_0$ ) in the center-crack specimen was 28 mm, and the critical strain was selected as 0.1. The figure shows the applied stress (normalized by the yield stress) plotted against the ratio of crack growth ( $\Delta a$ ) to the initial crack length. These results show that crack growth in a finer mesh initiates at a lower stress level than in a courser mesh. In an effort to predict the stress level at the onset of crack growth as a function of mesh size, Neuber's equation [15] was compared to the results from all meshes and was found to be fairly accurate. Neuber's equation, reformulated in terms of remote stress and local stress-strain behavior, was given by

$$S_i = \sqrt{\frac{\sigma_{ys} \epsilon_{cr} E}{K_T}} \quad (1)$$

where

$K_T$  = elastic stress concentration (ratio of highest normal stress  $\sigma_{yy}$  to applied stress) for a particular mesh and

$S_i$  = stress level at the onset of crack growth.

Table 1 gives the  $K_T$  values for all meshes considered. Thus, Eq 1 can be used to predict the stress level at the onset of crack growth as a function of mesh size for an elastic-perfect plastic material. Figure 7 shows the crack

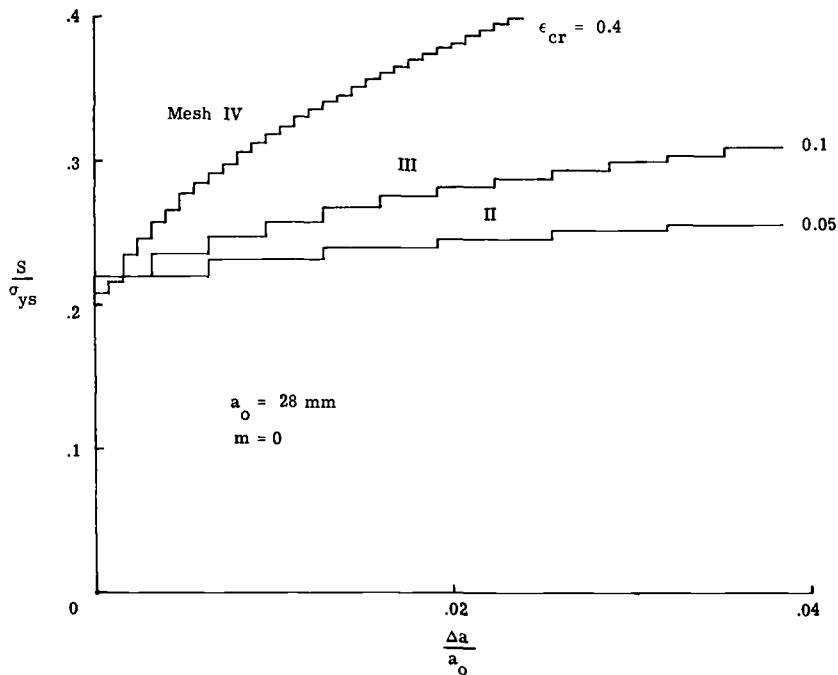


FIG. 7—Effect of mesh size and critical strain on crack growth.

growth results from Meshes II, III, and IV with critical strains of 0.05, 0.1, and 0.4, respectively. These critical strains were calculated from Eq 1 to give the same stress level at the onset of crack growth. Although the stress levels at the onset of crack growth were almost the same for all meshes, the subsequent crack growth behavior was considerably different. These results show that a finer mesh gives a steeper slope on the stress-crack growth curve than a courser mesh.

*Critical Strain*—Figure 8 shows the results of varying critical strain using the finest mesh (Mesh IV) for an elastic-perfect plastic material. For larger critical strain values, the stress level at the onset of crack growth and the slope of the stress-crack growth curve were larger.

The results shown in Figs. 6—8 indicate that the stress-crack growth curve using the critical strain criterion was a function of mesh size. In order to fit the finite-element results to experimental crack-growth data, both the mesh size and critical strain must be varied.

*Strain Hardening*—The effects of varying the linear strain-hardening coefficient ( $m$ ) on crack growth is shown in Fig. 9 using Mesh IV. The strain-hardening coefficient was either zero or 0.1. The insert shown in the figure shows the stress-strain curves for the elastic-perfect plastic material ( $m = 0$ ) and for the linear strain-hardening material ( $m = 0.1$ ). The initial crack length

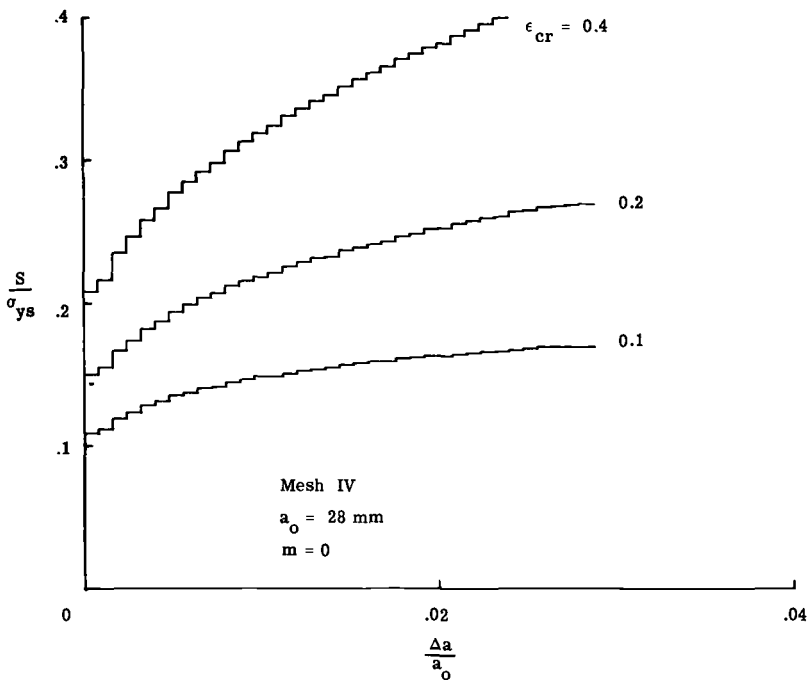


FIG. 8—Effect of critical strain on crack growth.

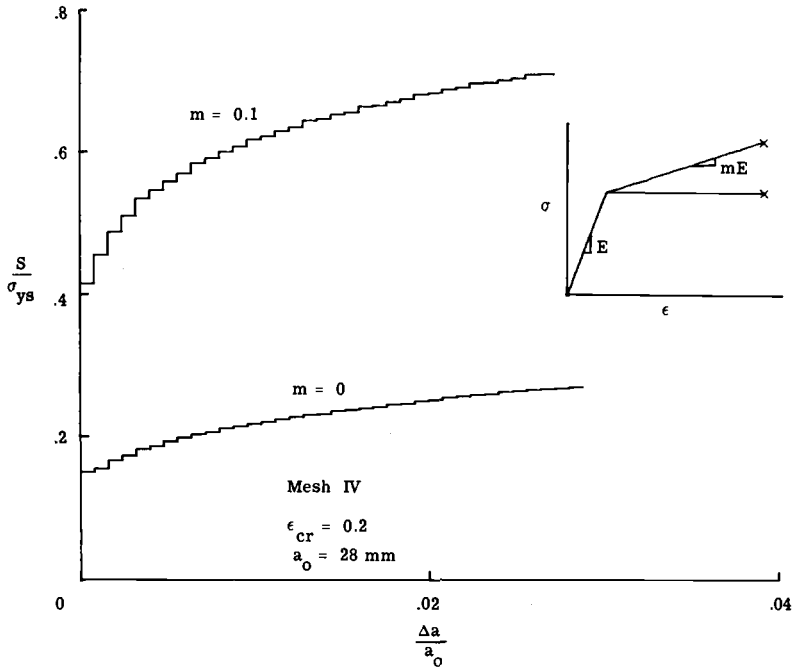


FIG. 9—Effect of strain hardening on crack growth.

in the center-crack specimen was 28 mm, and the critical strain was selected at 0.2. For the material with the larger strain-hardening coefficient, the stress level at the onset of crack growth and the average slope of the stress-crack growth curve were larger. Also, the stress-crack growth curve for the higher strain-hardening material had more curvature than the lower strain-hardening material. These results indicate that the shape of the stress-strain curve has a significant influence on the stress-crack growth curves.

*Specimen Type*—Figures 10 and 11 show the effects of monotonically loading a center-crack tension and a single-edge-crack bend specimen for linear strain-hardening materials with  $m = 0$  or 0.1, respectively. The same element mesh (Mesh IV) was used to model both specimens. The mesh modeled one quarter of the center-crack tension specimen and one half of the single-edge-crack bend specimens. The initial crack length,  $a_0$ , was 28 mm, and the critical strain was selected as 0.4 for both specimens.

In order to compare the results from the two specimen types, the stress-intensity factor concept was used. The stress-intensity factor for the center-crack tension specimen was obtained from [16] as

$$K_I = S \sqrt{\pi a \sec \frac{\pi a}{W}} \quad (2)$$

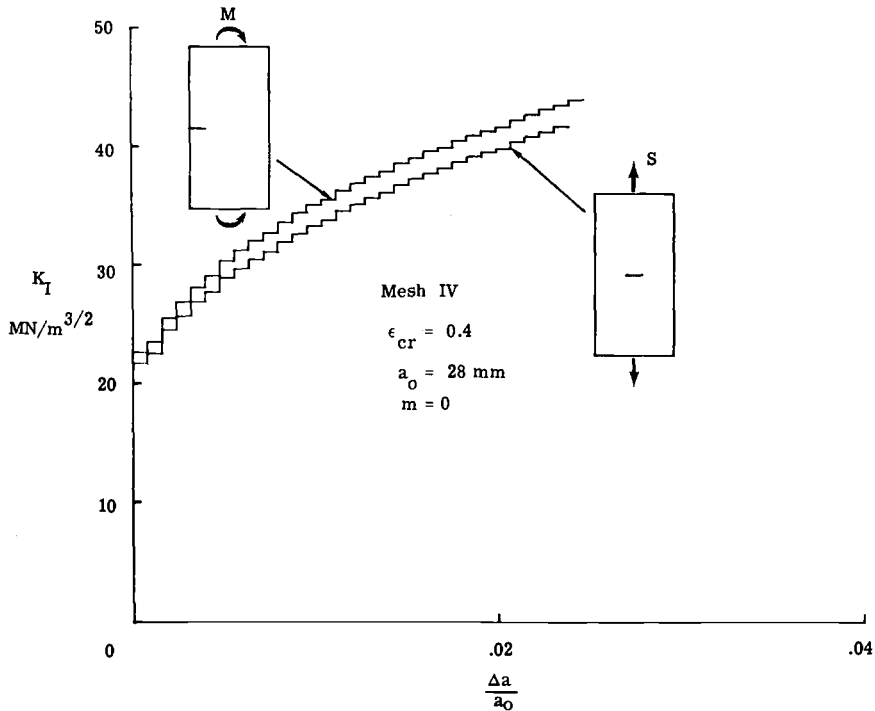


FIG. 10—Effect of specimen type on crack growth for an elastic-perfect plastic material.

and the stress-intensity factor for the bend specimen was also obtained from Ref 16 as

$$K_I = \frac{6M}{tW^2} \sqrt{a} F \tag{3}$$

where  $t$  is specimen thickness

$$F = 1.99 - 2.47 \lambda + 12.97 \lambda^2 - 23.17 \lambda^3 + 24.8 \lambda^4 \tag{4}$$

and  $\lambda = a/W$ .

Figure 10 shows the results for the elastic-perfect plastic material ( $m = 0$ ). The stress-intensity factor,  $K_I$ , was plotted against the ratio of crack growth ( $\Delta a$ ) to the initial crack length. The results for the bend specimen were about 5 percent higher than those for the tension specimen.

Figure 11 shows the results for the linear strain-hardening material with  $m = 0.1$ . For the linear strain-hardening material, the stress levels at the onset of crack growth were considerably higher (by a factor of 3) than those for the elastic-perfect plastic material (Fig. 10). The stress-intensity against crack growth curve for the bend specimen was 10 to 30 percent higher than that for the tension specimen.

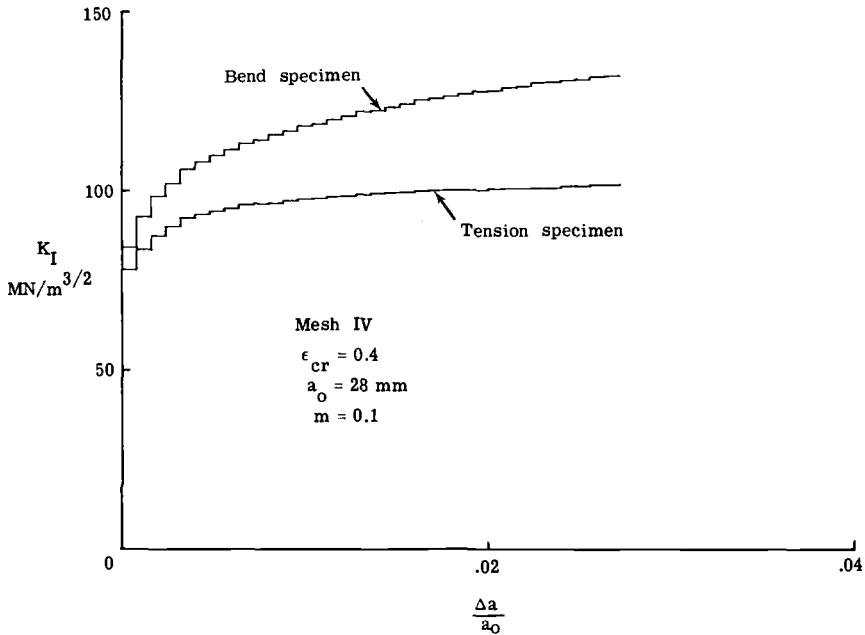


FIG. 11—Effect of specimen type on crack growth for a linear strain hardening material.

The results from Figs. 10 and 11 demonstrate that, for low stress levels, the crack-growth behavior for the two types of specimens can be correlated using the stress-intensity factor concept. However, for high stress levels, the crack-growth behavior for the two specimen types cannot be correlated by the stress-intensity factor concept.

### Cyclic Loading

The analysis of crack growth under cyclic loading is similar to that presented for monotonic loading except that, during unloading, the crack-closure effect was accounted for in the analysis. When the crack surfaces close, stiff springs along the crack surfaces in contact allow the surfaces to transmit compression. During cyclic loading, the finite-element analysis with the growth criterion predicts a crack-growth increment per cycle (or a crack-growth rate). These calculated crack-growth rates will be compared with experimental observations.

*Constant-Amplitude Loading*—Figure 12 shows the results of applying three cycles of  $R = 0$  loading to the finite-element model (Mesh IV) of the center-crack tension specimen. The material was assumed to be elastic-perfect plastic with a critical strain of 0.2. The maximum applied stress was 0.2 of the yield stress of the material. The figure shows the applied stress normalized by the yield stress plotted against crack growth ( $\Delta a$ ) from the

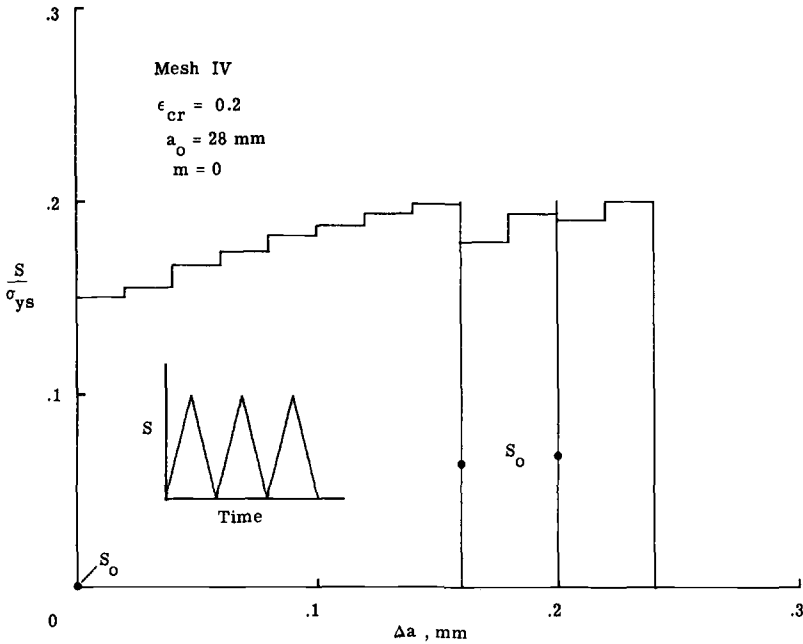


FIG. 12—Cyclic crack growth under constant-amplitude loading ( $R = 0$ ).

initial crack length ( $a_0 = 28$  mm). During initial loading, the crack opens at an infinitesimal stress. The crack-opening stresses,  $S_0$ , are indicated by the solid symbols. The first tensile loading caused the crack to grow eight element sizes (0.16 mm). During unloading, all of the nodes along the new crack surface associated with the previous crack growth closed. Upon reloading, the crack opened at about one third of the maximum applied stress, and the crack grew only two element sizes (0.04 mm). The crack-opening stress is defined as the stress level required to open the crack surfaces completely. In the third cycle, the crack-opening stress was slightly higher and the crack-growth increment was identical to that which occurred in the second cycle. Elber [2] has proposed that the “effective” stress range,  $\Delta S_{eff}$  (maximum applied stress minus the crack-opening stress), was the parameter controlling the amount of crack growth per cycle. To investigate his hypothesis, Fig. 13 shows the applied stress (normalized by the yield stress) plotted against the crack-tip strain,  $\bar{\epsilon}_{t,y}$ , normalized by the critical strain,  $\epsilon_{cr}$ , during unloading and reloading after the first tensile peak (see the solid lines in the insert on the figure). At the maximum applied stress ( $0.2 \sigma_{ys}$ ), the crack-tip strain was less than critical. The solid curve indicates the crack-tip strain during unloading and reloading. The arrows indicate the direction of loading. During unloading, the crack surfaces were closing, and the material in the crack-tip region was undergoing compressive yielding. Upon reloading, the crack-tip strain does not increase rapidly until after the

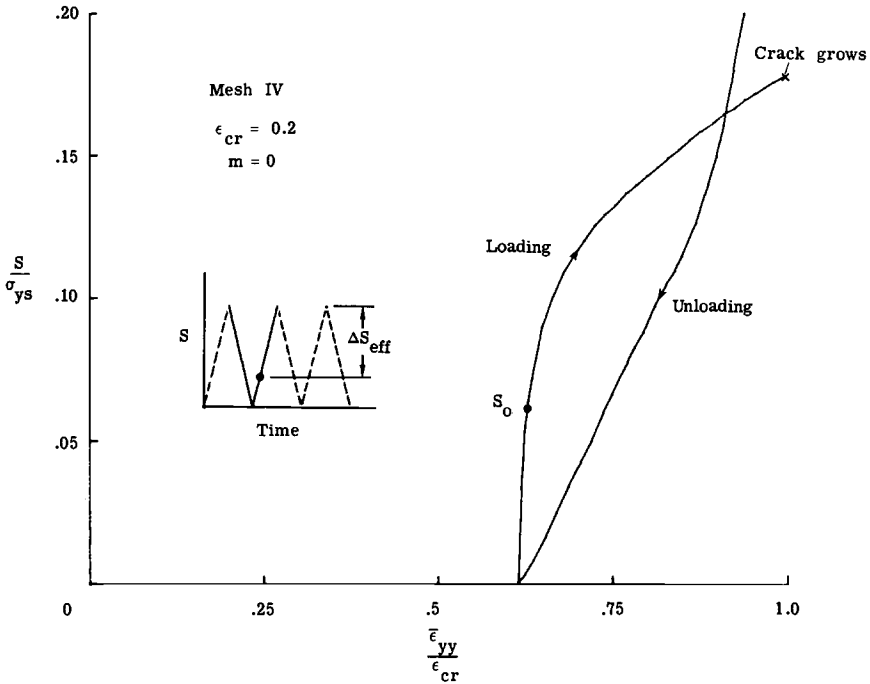


FIG. 13—Crack-tip strain as a function of applied stress.

crack surfaces have opened completely. The solid symbol indicates the crack-opening stress,  $S_0$ . The x symbol indicates the stress at which the crack-tip strain was critical and the crack grew. These results indicate that Elber's hypothesis was reasonably correct in that the crack tip does not experience a buildup in strain until after the crack is fully open.

Figure 14 shows the results of applying two cycles of  $R = -1$  loading to the center-crack specimen. The material properties and critical strain value were identical to those used for the previous loading ( $R = 0$ ). The results for the first tensile loading were identical to those for the  $R = 0$  case (Fig. 13). However, during unloading, the applied stress was  $-0.2\sigma_{ys}$ , and the crack surfaces in contact yielded more in compression than in the  $R = 0$  case. Consequently, upon reloading the specimen, the crack-opening stress was significantly lower than that obtained from the  $R = 0$  case. During the second cycle, the crack grew five element sizes (0.1 mm), in contrast to two element sizes in the  $R = 0$  case. Thus, lowering the crack-opening stress caused a larger crack-growth rate.

Elber [2], on the basis of fatigue crack-closure experiments under constant-amplitude loading, proposed the following equation for fatigue-crack-propagation rates

$$\frac{\Delta a}{\Delta N} = C (\Delta K_{eff})^n \tag{5}$$

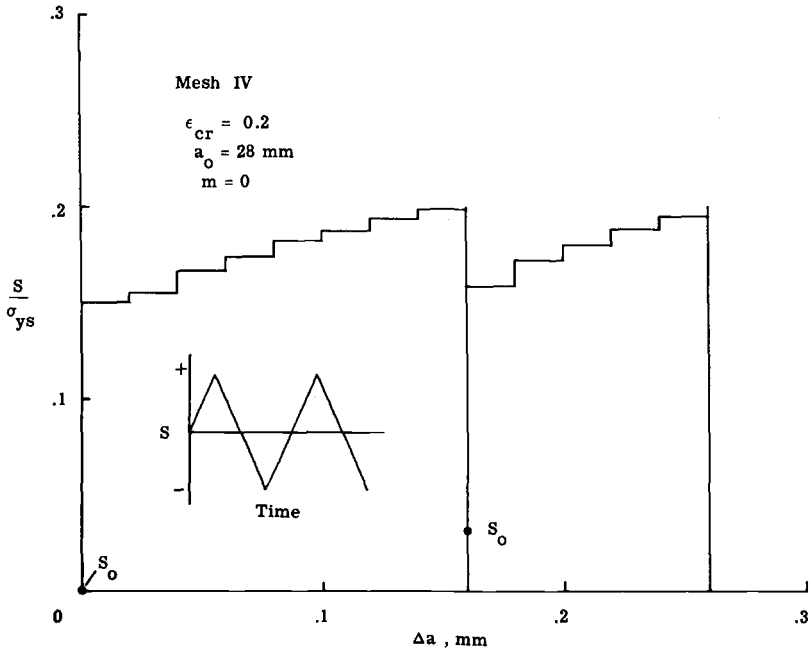


FIG. 14—Cyclic crack growth under constant-amplitude loading ( $R = I$ ).

where

$C, n$  = material constants and  
 $\Delta K_{eff}$  = effective stress-intensity factor range.

He proposed that the effective stress-intensity factor range be calculated by

$$\Delta K_{eff} = \Delta S_{eff} \sqrt{\pi a} F \tag{6}$$

where

$a$  = half length of the crack,  
 $F$  = boundary-correction factor, and  
 $\Delta S_{eff}$  = effective stress range,

given by

$$\Delta S_{eff} = S_{max} - S_0 \text{ for } S_0 \geq S_{min} \tag{7}$$

where

$S_{max}$  = maximum stress,  
 $S_{min}$  = minimum stress, and  
 $S_0$  = crack-opening stress.

Thus, the crack is assumed to propagate only during that portion of the

load cycle in which the crack tip is open. Equations 5 to 7 suggest, then, that the crack-opening stress can influence crack growth significantly under both constant- and variable-amplitude loading.

To compare the finite-element results with crack-growth increments computed from Eq 5, the first cycle in the  $R = 0$  case (Fig. 13) was used to evaluate the crack-growth coefficient,  $C$ . The coefficient  $n$  was assumed to be 3.6 and was obtained from Ref 2 for a 2024-T3 aluminum alloy material. For a variety of materials, the coefficient  $n$  ranges from 3 to 4. From the results of the first cycle,  $\Delta K_{\text{eff}} = 20.43 \text{ MN/m}^{3/2}$  ( $S_0 = 0$ ) and  $\Delta a = 0.16 \text{ mm}$ , the coefficient  $C$  was calculated from Eq 5 and was  $3.1 \times 10^{-9}$ . (Incidentally, the coefficient  $C$  for the 2024-T3 material in Ref 2 was  $1.2 \times 10^{-9}$ .) Table 2 shows a comparison between the crack-growth increments calculated from Eq 5 ( $C = 3.1 \times 10^{-9}$  and  $n = 3.6$ ) and the finite-element results for the second cycle in Figs. 13 and 14. In Eq 5, the crack-opening stresses were obtained from the finite-element results and are given in Table 2. The agreement between the crack-growth increments calculated from Eq 5 and those from the finite-element analysis was considered good.

*Simple Variable-Amplitude Loading*—Figure 15 shows the results of applying a simple variable-amplitude loading (see the insert) to the center-crack specimen (Mesh IV). Again, the material properties and critical strain were assumed to be identical to that used in the constant-amplitude loading. The results for the first two cycles are identical to that shown in Fig. 13 ( $R = 0$ ). The spike loading caused the crack to grow 14 element sizes (0.28 mm). The next two cycles of  $R = 0$  loading caused the crack to grow only one element size each. The compressive loading caused the subsequent crack-opening stress to be lower than that obtained from the previous cycle and, consequently, caused the crack to grow more (two element sizes). All of the crack-growth increments from the finite-element analysis were consistent with the calculations from Eq 5 (using the values of  $C$  and  $n$  obtained from the constant-amplitude loading) except for the spike loading. Equation 5 had predicted a crack-growth increment equivalent to about six element sizes for the spike loading. The finite-element analysis had predicted a crack-growth increment of 14 element sizes. The reason for this discrepancy is not known.

*Isotropic and Kinematic Hardening*—Figure 16 shows the results of applying three cycles of  $R = 0$  loading to the finite-element model (Mesh IV) of the center-crack tension specimen, assuming either isotropic hardening ( $\beta = 0$ ) or combined hardening ( $\beta = 0.5$ ). The kinematic-hardening co-

TABLE 2.—Comparison of calculated crack-growth increments from Eq 5 and the results from the finite-element analysis under constant-amplitude loading.

$R$	$\frac{\Delta S_{\text{eff}}}{\sigma_{\text{ys}}}$	$\Delta a_{\text{eq}}$ , mm	$\Delta a_{\text{FE}}$ , mm
0	0.134	0.0375	0.04
-1	0.170	0.089	0.10

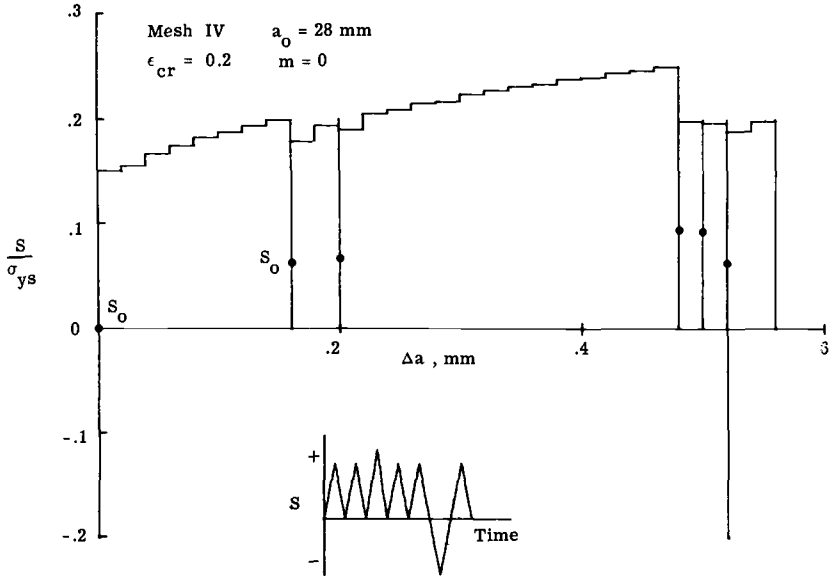


FIG. 15—Cyclic crack growth under simple variable-amplitude loading.

efficient,  $\beta$ , was selected as 0.5 because Ref 14 has shown experimentally that hardening under cyclic loading falls about halfway between that predicted by isotropic- and kinematic-hardening theories. (The Appendix gives the details on the combined-hardening theory.) The material was assumed to be linear-strain hardening with  $m = 0.1$ , and the critical strain was selected as 0.2. The figure shows the applied stress normalized by the yield stress plotted against crack growth ( $\Delta a$ ) from the initial crack length ( $a_0 = 28$  mm). The solid and dashed lines show the results from the finite-element analysis for isotropic- and combined-hardening, respectively (the dashed lines have been offset slightly so that the lines would not overlap). In the isotropic-hardening material, the crack grew more than in the combined-hardening material. Also, the crack-opening stresses in the combined-hardening material were lower than those for isotropic hardening because the former yields more in compression than the latter. These results indicate that cyclic hardening behavior has a significant influence on crack-growth rates and on crack-opening stresses.

**Concluding Remarks**

An elastic-plastic (incremental) finite-element analysis, in conjunction with a crack-growth criterion based on crack-tip strain, was used to study crack-growth behavior under monotonic and cyclic loading. Whenever the crack-tip strain was equal to or greater than the critical strain, the crack would grow.

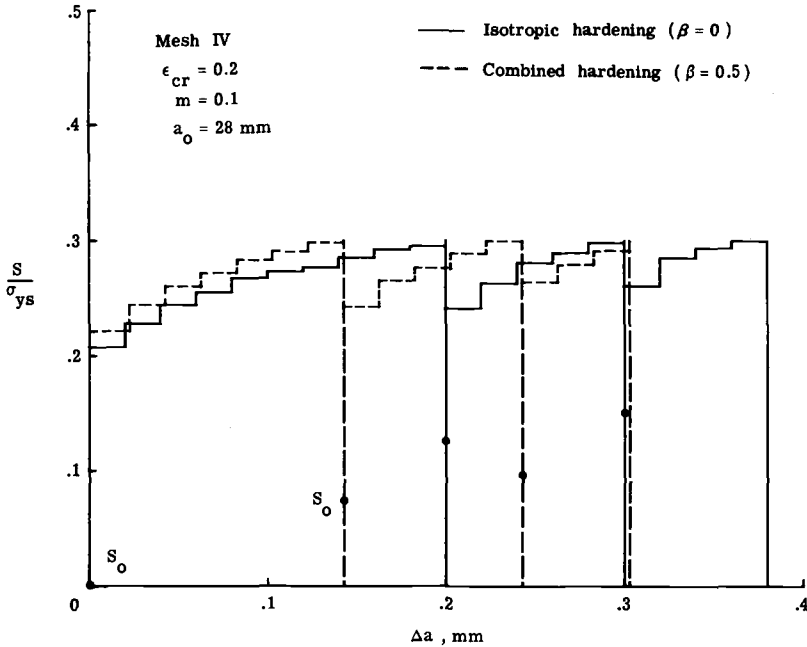


FIG. 16—Effect of assuming isotropic or combined hardening on crack growth under cyclic loading.

The finite-element analysis predicted three stages of crack-growth behavior under monotonic loading: (a) a period of no crack growth, (b) a period of stable crack growth, and (c) crack-growth instability. Such stages of crack-growth behavior have been observed experimentally in metallic materials. Under monotonic loading, the effects of element-mesh size, critical strain, strain hardening, and specimen type (tension or bending) on crack growth were investigated. Crack growth was found to be dependent upon the mesh size. As the mesh size was reduced, the stress level at the onset of crack growth was also reduced for a given value of critical strain. Thus, to fit the results from the finite-element analysis to experimental data, both the mesh size and the critical strain must be varied. For larger values of critical strain, the stress level at the onset of crack growth was found to be higher, and the amount of stable crack growth was larger. The material strain hardening had a significant influence on crack-growth behavior. For materials with larger strain-hardening coefficients, the stress level at the onset of crack growth and the slope of the applied stress against crack growth curve were larger. Also, the shape of the stress-crack growth curve was found to be influenced by strain hardening. At low applied stress levels, the stress-intensity factor against crack-growth curves for the center-crack tension and the single-edge-crack bend specimens were within 5 percent of

each other. However, at high applied stress levels (large amounts of plasticity), the stress-intensity factor against crack-growth curve for the single-edge-crack bend specimen was 10 to 30 percent higher than the crack-growth curve for the center-crack tension specimen.

Crack growth under cyclic loading was also studied. The center-crack tension specimen was subjected to either constant-amplitude or simple variable-amplitude loading. The crack-closure effect was accounted for in the analysis. A combined hardening theory, which incorporates features of both isotropic and kinematic hardening under cyclic loading, was also developed for smooth yield surfaces and was used in the analysis. Under constant-amplitude loading (zero-to-tension or tension-to-compression), the crack-growth rates computed from the analysis were consistent with growth rates computed from an equation proposed by Elber. Under a simple variable-amplitude load spectrum, the crack-growth rates from the analysis were qualitatively consistent with experimental observations and were fairly consistent with calculations from Elber's crack-growth rate equation. For strain-hardening materials, the assumption of either isotropic or kinematic hardening under cyclic loading had a significant effect on crack-growth rates and on crack-opening stresses.

The elastic-plastic, finite-element analysis with the crack-tip strain growth criterion predicted crack-growth behavior under monotonic and cyclic loading that was consistent with experimental observations. The analysis performed here gives further insight into the mechanism of crack growth and how various parameters influence the crack-growth behavior.

## APPENDIX

### Strain-Hardening Theory

Previous theories of strain-hardening plasticity have been based upon the assumption that strain hardening was either isotropic, kinematic, or a combination of the two. Isotropic hardening [11] assumes that, during plastic flow, the yield surface expands uniformly about the origin in stress space, maintaining the same shape, center, and orientation. Figure 17a shows, on the basis of a two-dimensional stress state, the initial yield surface and the subsequent yield surface during isotropic hardening when the stress state shifts from Points 1 to 2. Unloading in the reverse direction results in yielding at a stress state represented by Point 3. The isotropic-hardening behavior does not account for the Bauschinger effect exhibited by most materials. Kinematic hardening or Prager hardening [10] assumes that, during plastic flow, the yield surface translates as a rigid body in a direction normal to the yield surface, maintaining the size, shape, and orientation of the initial yield surface. Kinematic hardening does account, to some extent, for the Bauschinger effect during cyclic loading. Figure 17b shows the initial yield surface and the subsequent yield surface during kinematic hardening when the stress state shifts from Points 1 to 2. Unloading in the reverse direction results in yielding at a stress state represented by Point 3. Hodge [12,13] developed a general hardening theory which was a combination

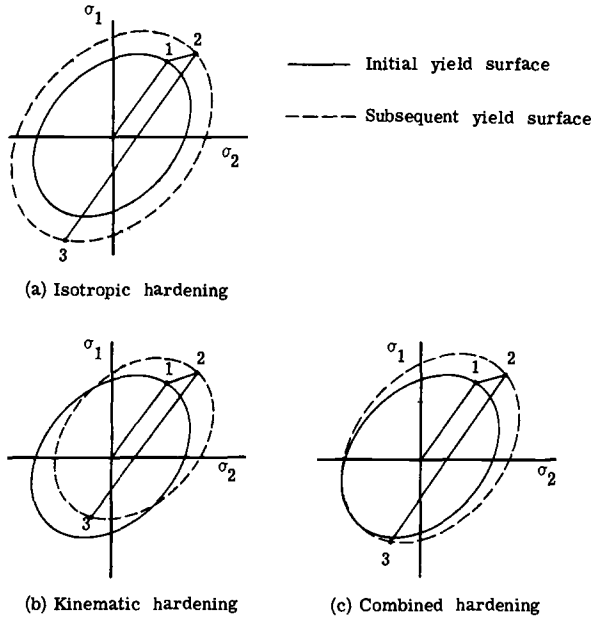


FIG. 17—Strain-hardening theories under cyclic loading.

of both isotropic and kinematic hardening. His combined hardening theory allowed for both an expansion and translation of the yield surface. However, Hodge developed the combined theory in conjunction with the Tresca yield condition.

In the present paper, a combined theory, similar to that proposed by Hodge, was developed for use with any smooth yield surface. The combined theory, shown in Fig. 17c, shows how the initial yield surface expands and translates when the stress state shifts from Points 1 to 2. Unloading in the reverse direction results in yielding at Point 3. Reference 14 has shown that strain-hardening behavior under cyclic loading generally falls between that predicted by isotropic and kinematic hardening. Thus, the combined theory will allow for more accurate description of the elastic-plastic, stress-strain behavior under cyclic loading.

In the present analysis, the yield surface selected takes a form similar to the Mises yield surface (plane-stress conditions) and is

$$\Phi = [(\sigma_x - \alpha_x)^2 + (\sigma_y - \alpha_y)^2 + (\sigma_x - \alpha_x)(\sigma_y - \alpha_y) + 3(\tau_{xy} - \alpha_{xy})^2]^{1/2} - \bar{\sigma} \quad (6)$$

where

- $\sigma_x, \sigma_y, \tau_{xy}$  = current stress state,
- $\alpha_x, \alpha_y, \alpha_{xy}$  = the translation of the center of the yield surface, and
- $\bar{\sigma}$  = current yield stress.

If the state of stress is such that  $\Phi < 0$ , the material is in an elastic state. When  $\Phi = 0$ , a plastic state is obtained, and a flow theory of plasticity [17] is used to determine subsequent plastic behavior under increasing stress or strain. When yielding is occurring, the stress state must remain on the translated yield surface. This condition is stated by the total differential of Eq 6 as

$$d\Phi = \left\{ \frac{\partial \Phi}{\partial \sigma} \right\}^T \{d\sigma\} + \left\{ \frac{\partial \Phi}{\partial \alpha} \right\}^T \{d\alpha\} - d\bar{\sigma} = 0 \quad (7)$$

$$\left\{ \frac{\partial \Phi}{\partial \sigma} \right\} = - \left\{ \frac{\partial \Phi}{\partial \alpha} \right\} \quad (8)$$

Eq 7 becomes

$$\left\{ \frac{\partial \Phi}{\partial \sigma} \right\}^T \left\{ d\sigma - d\alpha \right\} - d\bar{\sigma} = 0 \quad (9)$$

For simplicity,  $\{\alpha\}$  was assumed to be constant ( $d\alpha = 0$ ) in determining the change in the stress state  $\{d\sigma\}$ . Thus, Eq 9 becomes

$$\left\{ \frac{\partial \Phi}{\partial \sigma} \right\}^T \left\{ d\sigma \right\} - d\bar{\sigma} = 0 \quad (10)$$

where

$$\left. \begin{aligned} \frac{\partial \Phi}{\partial \sigma_x} &= \frac{(\sigma_x - \alpha_x)^{-1/2} (\sigma_y - \alpha_y)}{\bar{\sigma}} \\ \frac{\partial \Phi}{\partial \sigma_y} &= \frac{(\sigma_y - \alpha_y)^{-1/2} (\sigma_x - \alpha_x)}{\bar{\sigma}} \\ \frac{\partial \Phi}{\partial \tau_{xy}} &= \frac{3(\tau_{xy} - \alpha_{xy})}{\bar{\sigma}} \end{aligned} \right\} \quad (11)$$

The "initial" stress method as outlined in Ref 9 was used to determine  $\{d\sigma\}$  where  $\{\partial \Phi / \partial \sigma\}$  was given by Eq 11.

For purely isotropic hardening ( $d\alpha = 0$ ), the shift in the yield surface [9] was given by

$$d\bar{\sigma} = \left\{ \frac{\partial \Phi}{\partial \sigma} \right\}^T \left\{ d\sigma \right\} \quad (12)$$

and for purely kinematic hardening ( $d\bar{\sigma} = 0$ ), the shift in the yield surface [18] was given by

$$\left\{ d\alpha \right\} = \left\{ \frac{\partial \Phi}{\partial \sigma} \right\} \frac{\left\{ \frac{\partial \Phi}{\partial \sigma} \right\}^T \left\{ d\sigma \right\}}{\left\{ \frac{\partial \Phi}{\partial \sigma} \right\}^T \left\{ \frac{\partial \Phi}{\partial \sigma} \right\}} \quad (13)$$

Equation 12 or 13 shifts the yield surface in a direction normal to the yield surface.

In the present analysis, the shift in the yield surface was given by a linear combination of Eqs 12 and 13 as

$$d\bar{\sigma} = (1 - \beta) \left\{ \frac{\partial \Phi}{\partial \sigma} \right\}^T \left\{ d\sigma \right\} \quad (14)$$

$$\left\{ d\alpha \right\} = \beta \left\{ \frac{\partial \Phi}{\partial \sigma} \right\} \frac{\left\{ \frac{\partial \Phi}{\partial \sigma} \right\}^T \left\{ d\sigma \right\}}{\left\{ \frac{\partial \Phi}{\partial \sigma} \right\}^T \left\{ \frac{\partial \Phi}{\partial \sigma} \right\}} \quad (15)$$

where  $\beta$  is defined herein as the kinematic-hardening coefficient. When  $\beta = 0$ , the hardening behavior is purely isotropic, and the shift in the yield surface is entirely in  $\bar{\sigma}$  with  $\{d\alpha\} = 0$ . When  $\beta = 1$ , the hardening behavior is purely kinematic, and the shift in the yield surface is entirely in  $\{\alpha\}$  with  $d\bar{\sigma} = 0$ . If  $\beta$  is between zero and unity, the yield surface both expands and translates normal to the yield surface. Of course, Eqs 14 and 15 apply only for small incremental changes in the stress state.

## References

- [1] Strawley, J. E. and Brown, W. F., Jr., *Fracture Toughness Testing and its Applications*, ASTM STP 381, American Society for Testing and Materials, 1965, pp. 133-198.
- [2] Elber, W. in *Damage Tolerance in Aircraft Structures*, ASTM STP 486, American Society for Testing and Materials, 1970, pp. 230-242.
- [3] Kobayashi, A. S., Chiu, S. T., and Beeuwkes, R., *Engineering Fracture Mechanics*, Vol. 5, No. 2, 1973, pp. 293-305.
- [4] Anderson, Hans, *International Journal of Fracture*, Vol. 9, 1973, pp. 231-233.
- [5] Newman, J. C., Jr., "Finite-Element Analysis of Fatigue Crack Propagation—Including the Effects of Crack Closure," Ph.D. Thesis, Virginia Polytechnic Institute and State University, May 1974.
- [6] Newman, J. C., Jr., and Armen, Harry, Jr., *AIAA Journal*, American Institute of Aeronautics and Astronautics, Vol. 14, No. 8, Aug. 1975, pp. 1017-1023.
- [7] Ohji, K., Ogura, K., and Ohkubo, Y., *Engineering Fracture Mechanics*, Vol. 7, 1975, pp. 457-464.
- [8] Newman, J. C., Jr., in *Mechanics of Crack Growth*, ASTM STP 590, American Society for Testing and Materials, 1976, pp. 281-301.
- [9] Zienkiewicz, O. C., Valliappan, S., and King, I. P., *International Journal for Numerical Methods in Engineering*, Vol. 1, 1969, pp. 75-100.
- [10] Prager, W., *Journal of Applied Mechanics*, Dec. 1956, pp. 493-496.
- [11] Hill, R., *The Mathematical Theory of Plasticity*, Oxford, 1950.
- [12] Hodge, P. G., Jr., "Piecewise Linear Plasticity," Ninth International Congress of Applied Mechanics, Brussels, Sept. 1956.
- [13] Hodge, P. G., Jr., *Journal of Applied Mechanics*, Sept. 1957, pp. 481-484.
- [14] Hunsaker, B., Jr., Vaughan, D. K., and Stricklin, J. A., "A Comparison of the Capability of Four Hardening Rules to Predict a Material's Plastic Behavior," Transaction of the ASME, *Journal of Pressure Vessel Technology*, Feb. 1976.
- [15] Neuber, H., *Transactions*, American Society of Mechanical Engineers, Series E., *Journal of Applied Mechanics*, Vol. 28, 1961, pp. 544-550.
- [16] Brown, W. F., Jr., and Strawley, J. E., *Plane Strain Crack Toughness Testing of High Strength Metallic Materials*, ASTM STP 410, American Society for Testing and Materials, 1966.
- [17] Drucker, D. C., *Proceedings of the 1st U.S. National Congress on Applied Mechanics*, 1951, pp. 487-491.
- [18] Isakson, G., Armen, H., Jr., and Pifko, A., "Discrete-Element Methods for the Plastic Analysis of Structures," NASA CR-803, Oct. 1967.

## DISCUSSION

---

*H. Fuhring*<sup>1</sup> (*written closure*)—I was astonished to read that the criterion for onset of crack growth under monotonic loading—that is, exceeding a critical strain level  $\epsilon_{cr}$ —is applicable to constant-amplitude crack-growth

<sup>1</sup>Research assistant, Institut für Statik und Stahlbau, Technical University of Darmstadt, F. R. Germany.

calculation, as well. It seems to me that the second part of Newman's paper dealing with cyclic loading by using the  $\epsilon_{cr}$  criterion is in error.

Considering stable material response (with or without hardening), the stress/strain/displacement state of the  $(i + 1)$  reversal point equals the one of the  $(i - 1)$  reversal point in the case of constant-amplitude loading and unchanged physical crack length between  $(i - 1)$  and  $(i + 1)$ . Consequently, all loops should close when the load reaches the upper reversal point, irrespective of the kind of diagram. Newman's results contradict the described behavior to be seen in Fig. 13.

His load-strain curve is shown in Fig. 18a where I extrapolated the loading branch up to maximum load level, assuming  $\epsilon_{cr}$  to be greater than originally taken. Here, the subsequent load cycle starts, and the curve is supposed to resemble the first one—just as unclosed and showing an increased maximum strain, etc. Though, for ideal-plastic response, the loop seems to be closed, the local stress-strain curve, too, is unclosed at maximum load indicated by loop drifting, Fig. 18b. The behavior which should be expected by using stable conditions is shown in Fig. 18c,d. For the sake of simplicity, Newman's unloading branch and the loading portion associated with full contact removal are taken to be valid. However, the prolongation of the loading curve above the  $S_{op}$  level must look somewhat like the solid line in order to reach the initial maximum loading state.

The conclusion is that a prescribed strain level is exceeded either during monotonic loading to maximum load or never. Hence, Newman's numerical results and his failure criterion must be questioned.

It must be emphasized that local failure under cyclic loading is usually seen in connection with the strain range. From smooth specimen tests, we know that the number of cycles to failure is a function of plastic strain range applied. Under certain simplifications, this leads to the crack growth law

$$\frac{da}{dn} = C \cdot \Delta\epsilon_{pl}^m$$

where  $\Delta\epsilon_{pl}$  is the plastic strain range of the crack tip element. As long as we don't know the direct relationship between the constants and the pure material behavior, there is no way to calculate crack growth other than to (a) extend the crack by fictitious cutting, (b) redistribute the released stresses, (c) calculate the strain range of the new state, and (d) make a single fit of associated experimental data in order to obtain the constants.

*J. C. Newman, Jr. (author's closure)*—In reply to Dr. Fuhring on the use of the critical strain criterion for crack growth under cyclic loading, I would like to comment on why the remote applied stress against local crack-tip strain (nodal average) curve (Fig. 13) does not close. The difference in opinion hinges on the stage at which applied stress against local strain curve is monitored. The crack-tip strain is a function of the residual plastic deformation remaining in the wake of the advancing crack and is directly related to the crack-opening displacement at the crack tip. For the same applied stress level and crack length, larger amounts of residual plastic deformation cause

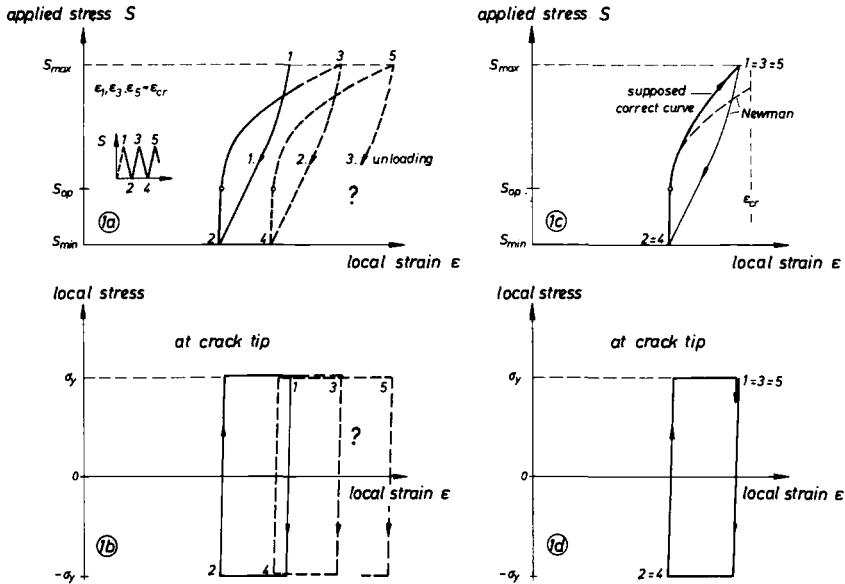


FIG. 18—Comparison of remote and local stress against local strain histories in the crack-tip region.

lower crack-opening displacements and, consequently, lower crack-tip strains. This feature is what causes the crack to grow in a stable manner. The residual plastic deformation during the unloading branch is larger than that during the reloading branch because the crack surfaces in contact yield in compression. These differences in residual plastic deformation cause the crack-closure load (Ref 8 of the paper) to be much higher than the opening load. Also, the differences in residual plastic deformation cause the applied stress against crack-opening displacement curve to be open after one reversal. Hence, the applied stress against local crack-tip strain curve is also open after one reversal. However, during further cycling (without any further crack growth), the loop will close because the materials in contact will not yield further in compression.

In regard to relating the crack-growth rates to the total plastic strain range of the crack-tip element, the results from my paper are not completely inconsistent with that approach. The total strain range from Fig. 13 is approximately the same during the next cycle. But, as would be expected, the strains are calculated on a new crack-tip element at a slightly larger crack length. Because the plastic strain ranges are approximately equal, the crack-growth rates also would be approximately the same.

A. Talug<sup>1</sup> and K. Reifsnider<sup>1</sup>

## Analysis and Investigation of Small Flaws

---

**REFERENCE:** Talug, A. and Reifsnider, K., "Analysis and Investigation of Small Flaws," *Cyclic Stress-Strain and Plastic Deformation Aspects of Fatigue Crack Growth*, ASTM STP 637, American Society for Testing and Materials, 1977, pp. 81-96.

**ABSTRACT:** Stress analysis of a single-edge-cracked specimen under uniaxial tension is performed by employing a Williams stress function and the boundary point collocation method. Full-field and singular stress fields are analyzed for small and large cracks, and it is shown that the inclusion of the nonsingular stresses in the description of the state of stress in the vicinity of the crack tip becomes significantly more important as the crack length decreases.

**KEY WORDS:** stresses, strains, fatigue, defects

The phenomenon of fatigue can be said to have attracted three major groups of investigators. There is a group which attempts to characterize and describe fatigue on the basis of engineering observables such as the fatigue life, stress or strain amplitude, endurance limit, and stress ratio. With the help of notch concentration factors, rainflow stress (strain) history procedures, and various other representations of physical behavior, they are responsible for most of the design of practical components in the presence of fatigue loading.

A second group, also of early origin, consists of investigators bent on explaining the fatigue phenomenon rather than just describing it. This group has a high density of metallurgists and has made large contributions to our understanding of how and why fatigue occurs. Their philosophy is based principally on dislocation theory, for the most part (although there are notable exceptions), and their achievements do not include the ability to predict a fatigue life or other practical observables.

A third group has grown out of the discovery that certain singular stress problems can be solved in two dimensions using established elasticity

<sup>1</sup>Instructor, Engineering Science and Mechanics Department, and chairman, Materials Engineering Group, respectively, Virginia Polytechnic Institute and State University, Blacksburg, Va. 24061.

formulations. This group, using the now-famous linear elastic fracture mechanics (LEFM) approach, has shown that crack growth can be described in terms of the local field stress intensity,  $K$ , for many important situations. This rather sophisticated collective effort has had considerable impact on design in situations where economy or weight restrictions or both have required that design must be based on the possibility of inspectable flaw growth.

Small flaws (in the engineering sense) have received relatively little attention from any of these groups. The fracture mechanics group is concerned primarily with the growth of flaws of inspectable size, that is greater than 2.5 mm order of magnitude in length. The fatigue mechanisms group usually concerns themselves with submicroscopic flaws such as dislocations, and the group involved in characterization does not deal specifically with cracks at all.

The motivation for examining small cracks or flaws, however, is becoming more obvious as our understanding of fatigue develops. The most important engineering fatigue property of a material is its endurance limit, which can be thought of as the stress (strain) amplitude for which the initiation of cracks of detectable size constitutes 100 percent of the fatigue life or the amplitude at which preexisting small flaws do not grow at all. In either case, design frequently is based on this quantity which is controlled by small flaw behavior. In fact, while crack propagation rates are relatively insensitive to alloying and conventional mechanical and metallurgical factors, high-cyclic fatigue crack initiation properties are related to conventional strength parameters [1].<sup>2</sup> Hence, while crack growth of large flaws is not a material selection criterion, the behavior of small flaws, especially as they are involved in initiation, is critical to the selection of fatigue-resistant materials.

A second general type of motivation is provided by the fact that, in many fatigue life evaluation and design situations, it is convenient to define fatigue life as the number of cycles (reversals, random blocks, etc.) required to initiate a crack for all ranges of stress, including notch effects, environmental effects, and other influences. This is especially true, for example, when the popular Neuber-based notch analysis is used to handle the effects of stress concentrators [2,3].

There are several basic questions that come to mind when the concept of a small crack or flaw is specifically considered. We will address three questions that have, in the spirit of this publication, some direct or indirect relationship to fracture mechanics. First, if one describes the rate of crack growth in terms of the amplitude of stress intensity,  $\Delta K$ , it is known that there exists a  $\Delta K_{\min}$  below which crack growth vanishes. Is  $\Delta K_{\min}$  related to the endurance limit for short crack situations? A second question arises from another physical observation, which we illustrate with some of

<sup>2</sup>The italic numbers in brackets refer to the list of references appended to this paper.

the following data. Figure 1 shows a typical data set for crack growth rate under constant  $\Delta K$  conditions as calculated by the corrected relationship of Brown and Srawley [4] for a series of tests on single-edge-notched aluminum specimens performed in our laboratory. We found that short cracks grow faster in terms of  $\Delta K$  than long ones. That observation has been made by other investigators. Most notably, Pearson specifically examined the growth of very short cracks as well as their initiation in aluminum alloys [5]. He observed that the rate of crack growth for very short cracks (of the order of 0.005 in. (0.127 mm) for his case) was much greater than would be predicted by rate versus  $\Delta K$  data for long cracks. Why is this so?

A final question embraces the other two questions to some extent. We simply ask, what is a short crack? Is there anything distinctive about a crack of decreasing or vanishing length? Is there anything distinctive about the stress field or the nature of the boundary value problem, or the function of fracture mechanics for a short crack?

To gain at least a preliminary insight into these and other matters, an analytical stress analysis was performed as described next. Our approach was analytical, rather than numerical, because information is needed both in

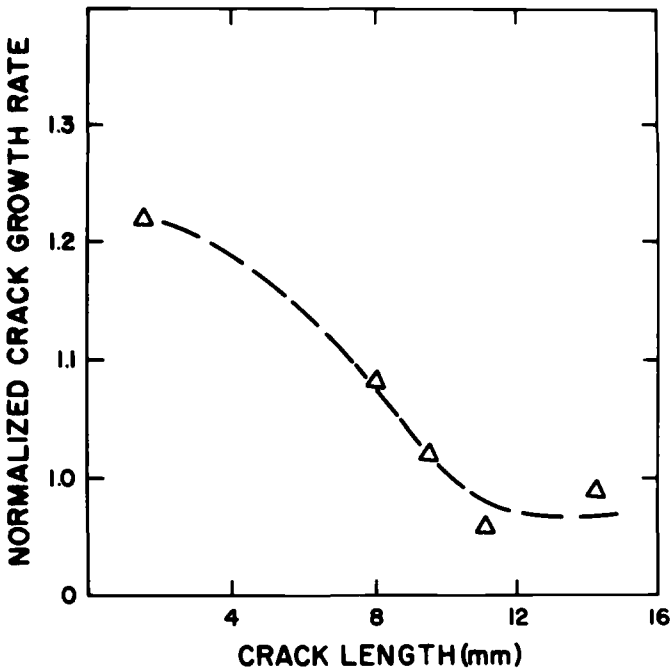


FIG. 1—Small crack growth rates as a function of crack length.

the neighborhood of a singularity and a boundary for short cracks. The approach is unique in that it concentrates on the full-field solution for a short crack. Although the determination of the field stress intensity is much simpler, we believe that the answers to the questions just posed require a precise determination of the region of influence of the singular stress field (which can only be determined if the full-field solution is available) and a clear understanding of the stress distribution around a short flaw, especially when the flaw size approaches some characteristic material dimension such as the grain size. Finally, the approach utilizes an established stress function, not only for convenience and validation, but also to facilitate interpretation of the new results in terms of more familiar ones.

### Analysis

A stress analysis of a single-edge-cracked specimen of rectangular shape is carried out with the remote stress,  $\sigma^0$ , applied in the normal direction to the crack axis,  $x$ , as shown in Fig. 2.

The problem is to find a stress function  $\Phi$  that satisfies the biharmonic equation and the boundary conditions implied by the chosen geometry and

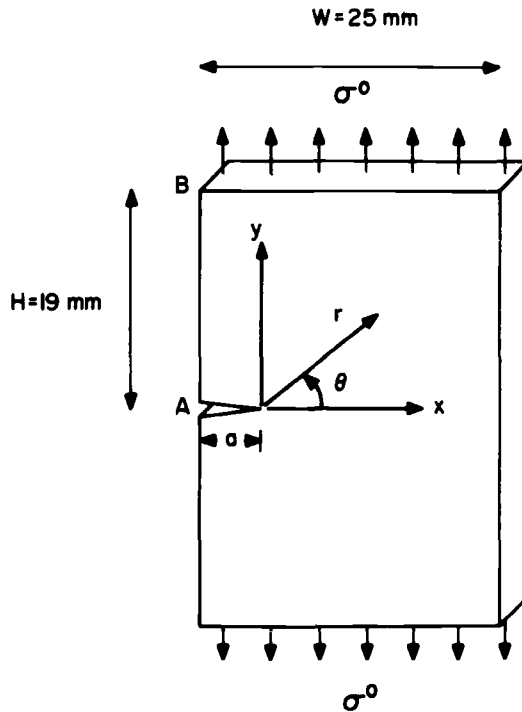


FIG. 2—Specimen geometry.

mode of loading. Considering the symmetrical character of the problem, analysis need be carried out only over the domain defined by the half of the specimen lying above (or below) the crack axis. Hence  $\nabla^4 \Phi = 0$ , subject to

$$\sigma_x = \tau_{xy} = 0, \quad x = -a, \quad 0 \leq y \leq H \tag{1}$$

$$\sigma_y = \sigma^0, \quad \tau_{xy} = 0, \quad -a \leq x \leq W - a, \quad y = H \tag{2}$$

$$\sigma_x = \tau_{xy} = 0, \quad x = W - a, \quad 0 \leq y \leq H \tag{3}$$

$$\sigma_y = \tau_{xy} = 0, \quad -a \leq x \leq 0, \quad y = 0 \tag{4}$$

Choosing  $\Phi$  to be the Williams stress function [6] one has

$$\begin{aligned} \Phi(r, \theta) = \sum_{n=1}^{\infty} \left\{ (-1)^{n-1} C_{2n-1} r^{n+\frac{1}{2}} \left[ -\cos\left(n - \frac{3}{2}\right)\theta + \frac{2n-3}{2n+1} \cos\left(n + \frac{1}{2}\right)\theta \right] \right. \\ \left. + (-1)^n C_{2n} r^{n+1} \left[ -\cos(n-1)\theta + \cos(n+1)\theta \right] \right\} \end{aligned} \tag{5}$$

where

- $\tau$  = shear stress,
- $x, y$  = Cartesian coordinates,
- $2H$  = specimen height,
- $W$  = specimen width,
- $r, \theta$  = polar coordinates,
- $n$  = summation index in Eq 5, and
- $C_i$  = coefficients of the Williams stress function.

The stresses in terms of  $\Phi(r, \theta)$  are calculated from

$$\sigma_{rr} = \frac{1}{r} \frac{\partial \Phi}{\partial r} + \frac{1}{r^2} \frac{\partial^2 \Phi}{\partial \theta^2} \tag{6}$$

$$\sigma_{\theta\theta} = \frac{\partial^2 \Phi}{\partial r^2} \tag{7}$$

$$\sigma_{r\theta} = -\frac{1}{r} \frac{\partial^2 \Phi}{\partial \theta \partial r} + \frac{1}{r^2} \frac{\partial \Phi}{\partial \theta} \tag{8}$$

The coefficients  $C_i$  in the series for  $\Phi$  are obtained by the boundary point collocation method where the prescribed Boundary Conditions 1, 2, 3 only are satisfied at selected points with approximately equal spacing on the

appropriate segment of the boundary. No collocation is needed for the crack surfaces since conditions (4) are automatically satisfied by the Williams stress function (5).

At every point along the boundary, there are two boundary conditions required; hence for  $n$  collocation points,  $2n$  linear equations result in the unknowns  $C_1$  through  $C_{2n}$  which are sufficient to determine the first  $2n$  terms in the infinite series for  $\Phi$ . A double precision Gaussian elimination procedure with full pivoting is employed for the solution of this system of linear equations. Once the coefficients are determined, the components of the stress tensor are first determined through a term-by-term analytical differentiation of the potential function by making use of Eqs 6–8, and the determined coefficients are substituted in the resulting series for stresses.

### Discussion of Results

The collocation procedure was applied to two specimens with different size cracks: one with a 0.254-mm crack and another with a 6.350-mm crack. These will be referred to as a “short crack” and “long crack,” respectively, in the following discussion. The first coefficients  $C_1$  for various crack lengths and applied stresses obtained from the numerical solution procedure were checked against those published by Gross et al [7] and were found to be in agreement.

The solution procedure was applied in both the long and short crack cases with a successively increasing number of collocation points. It was found that a practical limit ( $N_{cr}$ ) to the number of collocation points ( $N$ ) that can be taken exists. When  $N = N_{cr}$ , the matrix of coefficients for the linear system of equations on the  $2N$  unknowns,  $C_i$ , becomes ill conditioned in such a way that a possible rank  $R$  less than  $2N$  is encountered. This was judged to be due to a too-close spacing of collocation points in regions where the potential function has relatively small gradients, resulting in equations obtained from adjacent points conveying essentially the same information. These limiting values were found to be  $N_{cr} = 35$  for the long crack and  $N_{cr} = 27$  for the short one. It must be emphasized that solutions are possible for  $N > N_{cr}$ , but a loss of significance in the elimination process occurs for these cases, rendering the accuracy of the solution for  $C_i$  questionable. This problem could possibly be eliminated by employing an iterative solution scheme rather than the direct elimination type used in this investigation. However, further details of numerical procedures lie beyond the intent of this present paper. Therefore, the analysis is carried out with  $N = N_{cr}$  in each case. The value of the first coefficient  $C_1$  was checked to make certain that it converged with less than  $N_{cr}$  boundary points.

The series obtained from the term-by-term differentiation of  $\Phi(r, \theta)$  for the stresses were found to be of divergent character outside the region defined by  $r/a < 1$ . This behavior is demonstrated in Fig. 3. The conver-

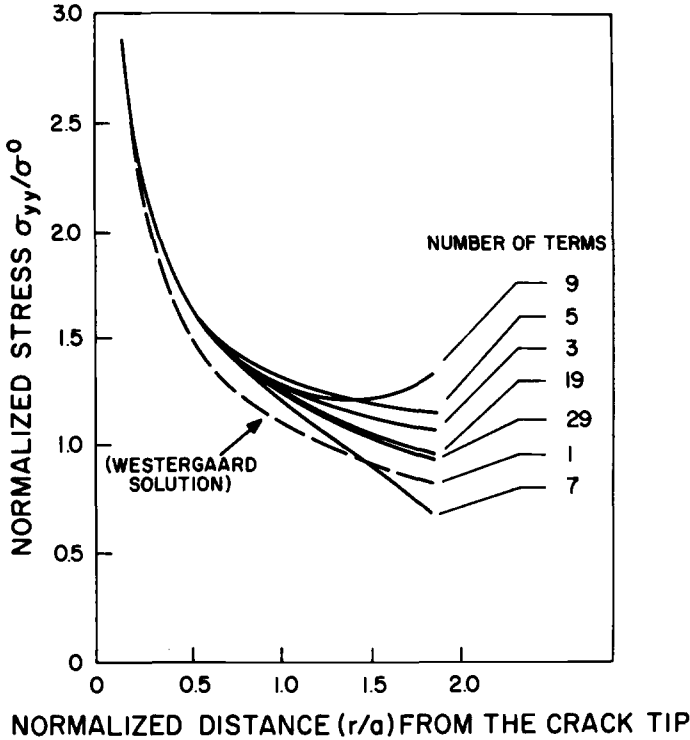


FIG. 3—Normalized stress distributions on the crack axis for  $a/w = 0.25$  obtained by collocation.

gence of  $\sigma_{yy}$  at discrete points selected on the axis ahead of the crack tip as a function of terms retained in the series is shown in Fig. 4. It is seen that, within  $r/a \leq 1$ , convergence requires only a few terms.

A more detailed observation of the convergence of the series for stresses can be made by means of Fig. 5 where the variation of  $\sigma_{yy}$  on the crack axis at a distance  $r/a = 3/4$  as a function of the number of terms is shown for the long and short crack cases. It was observed that the longer crack requires more terms for convergence than the short crack, although the magnitude of the remote stress was arranged so as to render approximately the same  $K_I$  value. This was accomplished by increasing the applied nominal stress for the short crack over that for the long one until the first coefficients ( $C_1$ ) in both cases were the same.

By comparing the Westergaard solution

$$\sigma_{yy} = \frac{K_I}{\sqrt{2\pi r}} \left[ 1 + \sin \frac{\theta}{2} \sin \frac{3\theta}{2} \right] \cos \frac{\theta}{2} \tag{9}$$

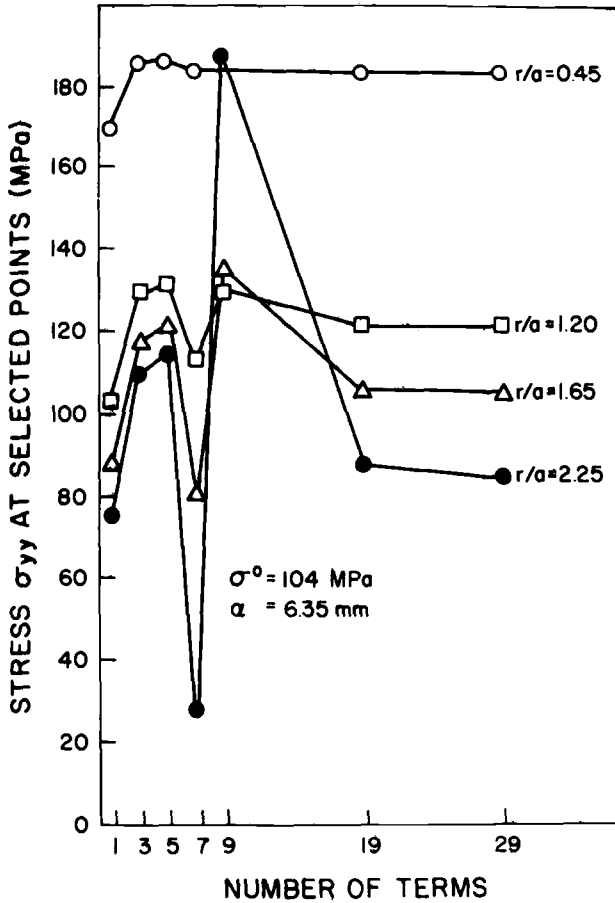


FIG. 4—Convergence characteristics for  $\sigma_{yy}$  on the crack axis at various distances from the crack tip.

with that obtained from the Williams stress function by retaining only the first term

$$\sigma_{yy} = \frac{-C_1}{\sqrt{r}} \left[ 1 + \sin \frac{\theta}{2} \sin \frac{3\theta}{2} \right] \cos \frac{\theta}{2} \quad (10)$$

it can be concluded that

$$K_I = -\sqrt{2\pi} C_1$$

Hence this procedure ensures that the amplitude of the singular part of the solution is the same in both cases.

It can be observed from Fig. 5 that, at the same relative distance ( $r/a$ ) from the crack tip, the discrepancy between the one-term singular solution

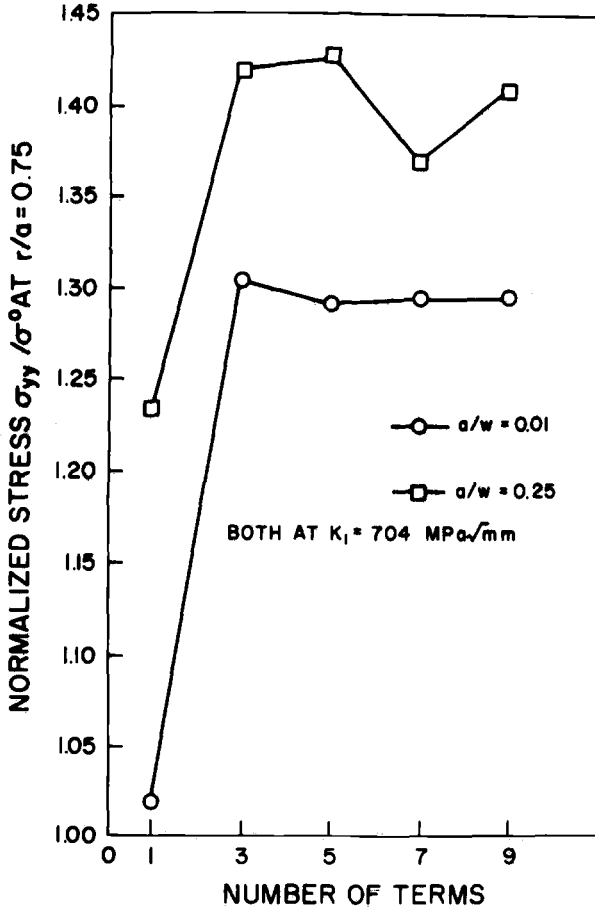


FIG. 5—Comparison of convergence of  $\sigma_{yy}$  at a given point on the crack axis for a long and a short crack.

and the converged full-field solution is less for the long crack at constant  $K_I$ . Figures 6 and 7 show the contours of constant  $\sigma_{yy}/\sigma^0$  for short and long crack cases, respectively. The area covered by each graph is defined by  $-a \leq x \leq a$ ,  $0 \leq y \leq a$ .

The effect of the traction-free specimen edge  $AB$  on the stress distribution is observed to increase with decreasing crack size. The high stress region which could be considered to lie to the right of the  $\sigma_{yy}/\sigma^0 = 1$  contour is bent toward the crack axis for the short crack, indicating a tendency of the region subjected to higher stresses to concentrate more along the crack axis. This can be regarded as a deviation of the full-field solution from the  $\theta$  dependence of the single parameter solution given by Eq 9. Furthermore, a change in the distribution of the stresses,  $\sigma_{yy}$ , on the axis ahead of the crack tip is seen as the crack length decreases. This can be demonstrated

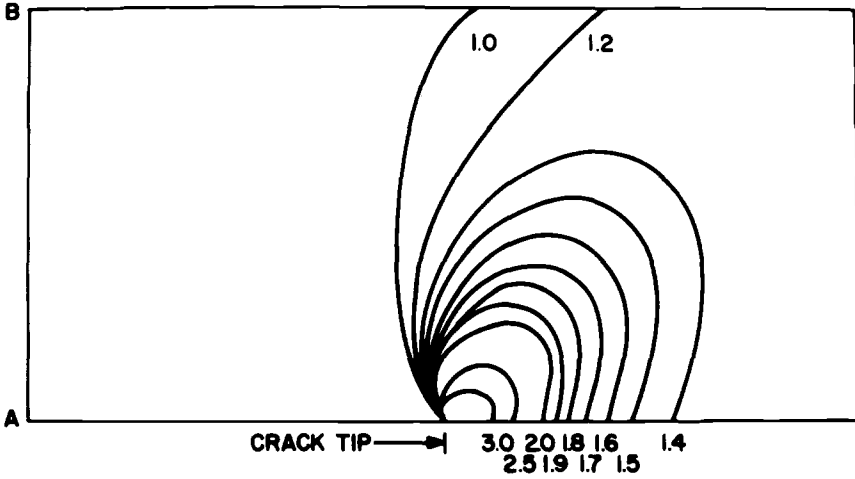


FIG. 6—Contours of  $(\sigma_{yy}/\sigma^0) = \text{constant}$  for  $a/w = 0.01$ .  $K = 704 \text{ MPa}\sqrt{\text{mm}}$ .

best by means of Figs. 8 and 9 where  $\sigma_{yy}/\sigma^0$  versus  $r/a$  is plotted for both the single parameter solution and the full-field solution under constant  $K_I$  for long and short cracks, respectively. A comparison of these two figures suggests that the full-field solution follows the singular solution more closely for the longer crack as  $r$  increases. The effect of the free edge  $AB$  as it approaches the crack tip (as  $a$  decreases) is to cause the higher stresses to redistribute themselves along the crack axis, resulting in higher stresses than those predicted by the singular solution. The same phenomenon is also shown in Fig. 10 where  $\sigma_{yy}$  at points along the crack axis is plotted against

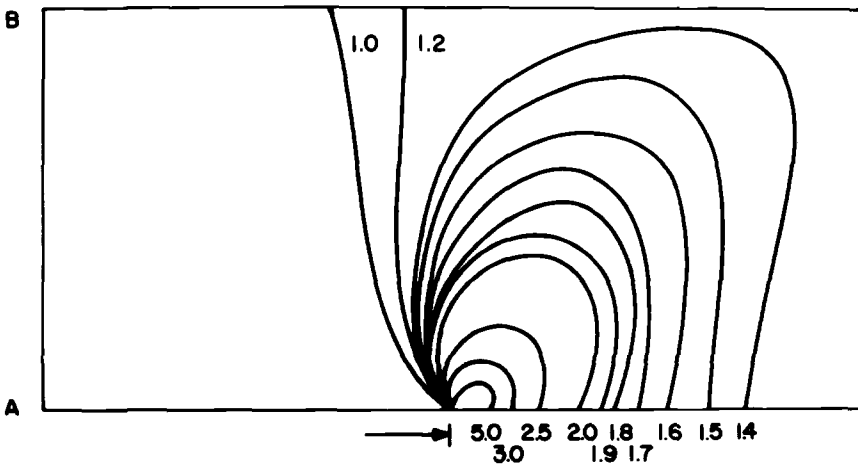


FIG. 7—Contours of  $(\sigma_{yy}/\sigma^0) = \text{constant}$  for  $a/w = 0.25$ .  $K = 704 \text{ MPa}\sqrt{\text{mm}}$ .

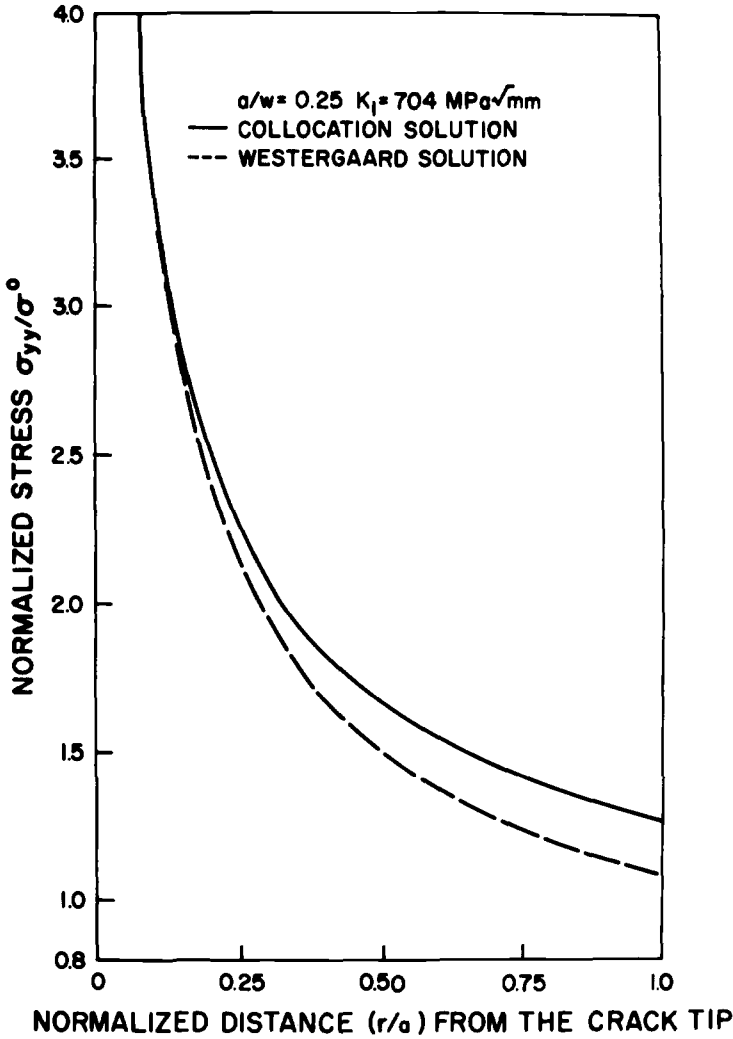


FIG. 8—Comparison between the Westergaard and full-field collocation solutions for a long crack.

the distance  $r$  from the crack tip for both the long and short crack cases under constant  $K_I$ . It should be noted here that the collocation solution and the Westergaard solution (Eq 9) are represented by the same curve for the long crack data. On the basis of the Westergaard analysis, however, under constant  $K_I$ , the short crack solution would coincide with that for the long crack, that is, the curves in Fig. 10 should fall upon one another. As can be observed in Fig. 10, an increasing deviation from the singular solution is detected for short cracks, indicating the increasing significance of the nonsingular terms in the series as the crack tip approaches the traction free boundary  $AB$ .

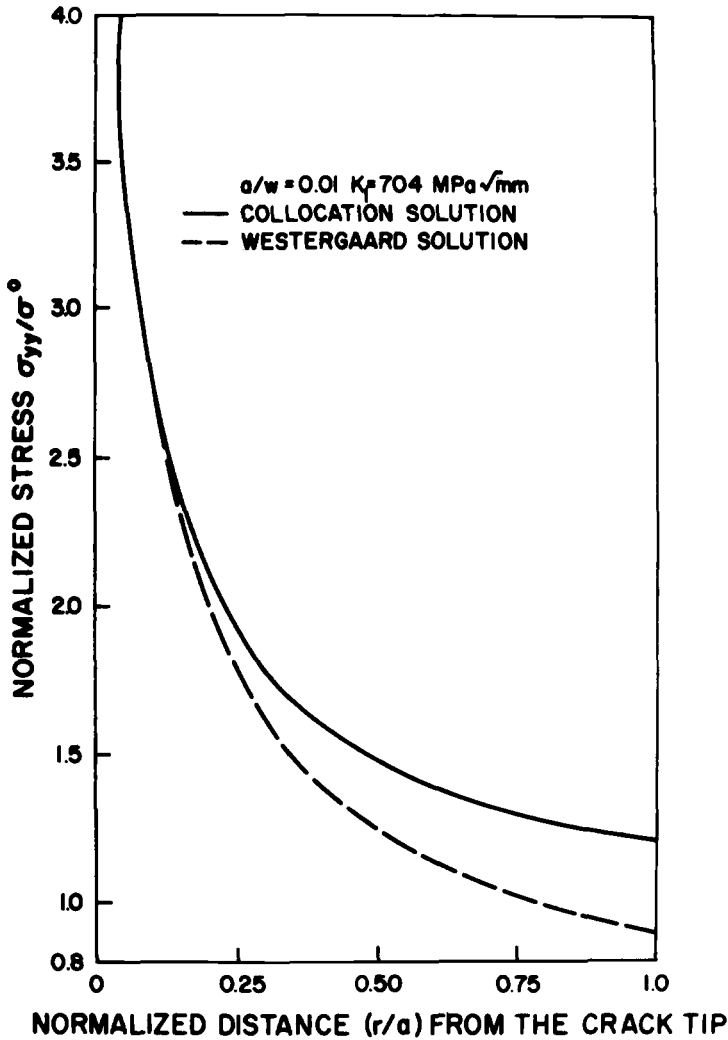


FIG. 9—Comparison between the Westergaard and full-field collocation solutions for a short crack.

### Conclusions

As the crack length  $a$  decreases, the distance from the crack tip to the traction-free specimen edge decreases, and the effect of this boundary on the distribution of stresses around the crack tip increases for smaller cracks.

The effect is to reduce the size of the singular region for smaller cracks in the normalized sense. To be more precise, if the extent of the singular region along the crack axis is denoted by  $r_s$ ,

$$(r_s/a)_{\text{short crack}} < (r_s/a)_{\text{long crack}}$$

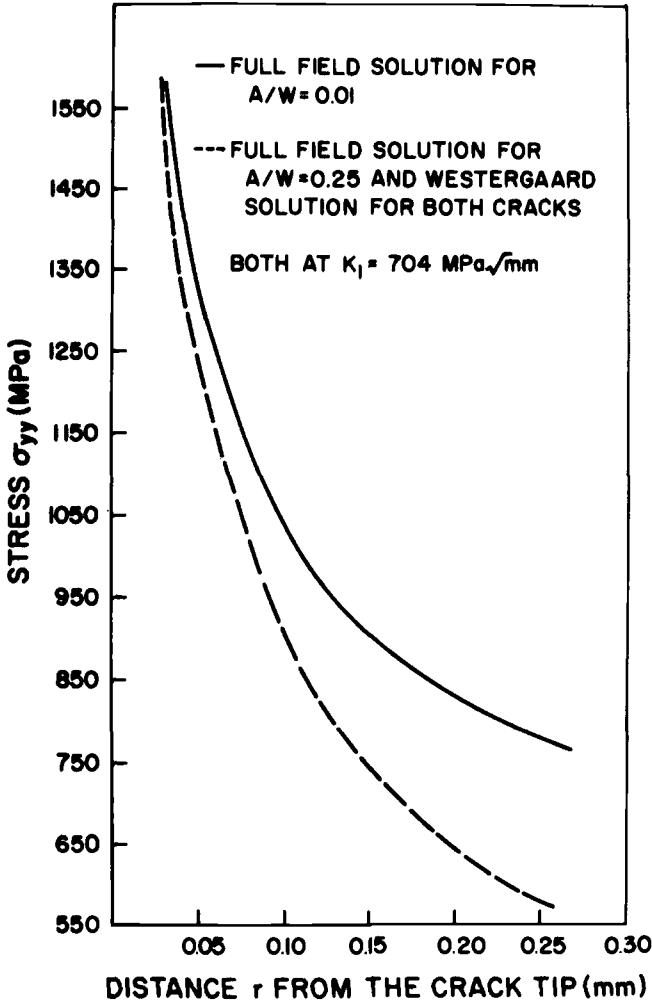


FIG. 10—Comparison of full-field and Westergaard solutions for long and short cracks at constant  $K_I$  as a function of absolute distance  $r$  from the crack tip.

Therefore the region over which the stresses can be determined on the basis of a single parameter  $K_I$  becomes small for small cracks, emphasizing the importance of a full-field solution for stress analysis in crack initiation problems. If a region of influence  $r_i$  is to be defined such that

$$\sigma(r, \theta) \leq \sigma_c \text{ for } r \leq r_i$$

where  $\sigma_c$  is a critical stress value, it is observed that, for the same material property  $\sigma_c$ , the region of influence would be larger for smaller cracks under

constant  $K_I$  in the sense that a larger volume of material is subjected to high stresses in the case of small cracks. This can be observed from Fig. 10. This is due to the fact that the nonsingular stress terms make a larger contribution to the region of significant influence in the case of a short crack.

It follows from this argument that the description of fatigue crack propagation rate by a Paris relationship

$$\frac{da}{dN} \propto (\Delta K_I)^n$$

which is based on the singular part ( $\Delta K_I$ ) of the stress field becomes questionable for extremely small cracks, unless an artifice such as an effective crack length (corrected for plastic zone size, for example) is introduced. Otherwise, a higher crack propagation rate would be expected for smaller cracks under constant  $K_I$  loading, providing at least a partial answer to one of the questions raised earlier. This type of behavior is demonstrated by Fig. 1 which presents one example of our experimental data for the variation of the crack propagation rate under constant  $K_I$  for a propagating crack in aluminum.

A second question raised earlier is the possible meaning of and relationship between the threshold for crack propagation  $\Delta K_{\min}$  (or  $K$  threshold, depending upon the nomenclature) and the endurance limit of a given material, below which fatigue crack propagation does not occur. For the purpose of argument, let us consider a high-strength steel having an ultimate strength of about 1379 MPa and a  $\Delta K_{\min}$  of about  $347 \text{ MPa}\sqrt{\text{mm}}$ . (See for example, D6ac steel, Ref 8.) Using the singular stress field only, and restricting our attention to the crack axis as in Fig. 10, we notice that if

$$\sigma_{yy} = \frac{\Delta K_{\min}}{\sqrt{2\pi r}} = \sigma_{\text{ultimate}} \quad (11)$$

then  $r \approx 0.0101 \text{ mm}$ , that is, if we neglect plasticity for the moment, the ultimate strength is reached at a distance of about  $10^{-2} \text{ mm}$  from the crack tip. Such a dimension compares to characteristic material dimensions on a microscale in many cases. The simplest such comparable dimension is the grain size which we will use for discussion here. If the region of significant influence defined by Eq 11 as the region of material in front of the crack tip wherein the fictitious stress  $\sigma_{yy}$  exceeds the ultimate strength for an applied  $\Delta K_{\min}$  is smaller than the grain size, there are several physical effects that would act to confuse or prevent crack propagation. The grains are anisotropic, for example, causing the local stress distribution to change abruptly across a grain boundary. The physics of crack propagation should also change to the extent that slip occurs on crystallographic planes in preferred directions across the grain in the manner most compatible with the neigh-

boring grains that are relatively unaffected by the singular field unlike larger  $\Delta K$  stress states. Finally, grain boundaries and the impurity and other crystallographic disturbances associated with them would be expected to be very effective crack stoppers (Ref 9). It would appear, then, that such an argument is consistent with the existence of a physical property  $\Delta K_{\min}$  below which cracks do not propagate.

Our earlier implication was that the concept of  $\Delta K_{\min}$  could be related to the endurance limit. That connection follows from the definition of the stress intensity factor. For general purposes let us consider the form

$$K = \sigma^0 \sqrt{2\pi a} \quad (12)$$

where  $\sigma^0$  = remote applied stress and  $a$  = crack length. If  $K$  is set equal to  $\Delta K_{\min}$  and  $\sigma^0$  is set equal to the ultimate strength,  $a$  should be the maximum dimension of a flaw which cannot be propagated by any application of stress which does not fail the material by gross fracture. For the material considered previously, that dimension is about  $10^{-2}$  mm as before. If we set  $\sigma^0$  equal to the endurance limit, we imply that flaws of length  $a$  preexist in the material. For our example material, that result is about  $4 \times 10^{-2}$  mm which compares well to a common grain size, for example. If the maximum dimension of the preexisting flaws and  $\Delta K_{\min}$  are known, a fatigue endurance limit can be predicted, and so on. The choice of grain size as a characteristic dimension is only a convenience. Characteristic impurity inclusion dimensions, machining scratches, etc., could have been used instead. However, for a fixed  $\Delta K_{\min}$ , Eq 12 implies that a smaller grain size (smaller  $a$ ) will allow a higher fatigue endurance limit, an effect which is observed in most metals, other things being relatively constant [10]. Inclusions, however, although more difficult to characterize, are more commonly associated with initiation of small flaw growth [11].

Finally, it should be noted that the method of solution employed here involves an established stress function that satisfies the governing equation and a part of the boundary conditions of the problem. The remaining boundary conditions are only satisfied at discrete points. It is, therefore, expected that the accuracy of the solution would improve as the number of boundary stations is increased. It should be noted that, if a direct elimination type of solution scheme is employed, a practical limit to the number of boundary stations exists. Possible alternatives for the solution method would be an iterative scheme for solving the linear system of equations or making use of a least squares approach in applying the boundary conditions rather than the point collocation method.

## References

- [1] Clark, W. G., Jr., *Metals Engineering Quarterly*, Aug. 1974, pp. 16-22.
- [2] Conle, A., Newack, H., and Hauschmann, D., "The Effect of Engineering Approx-

- imation on Fatigue Life Evaluation for Variable Amplitude Loading," presented at the International Committee of Aeronautical Fatigue Symposium, Lausanne, 2-4 June 1975.
- [3] Conle, A. and Newack, H., "Experimental Verification of a Computerized Neuber-Based Notch Analysis by Means of the Companion-Specimen Method," Society for Experimental Stress Analysis Spring Meeting, Paper No. 23891, 1975.
- [4] Brown, W. F. and Srawley, J. E., *Plane Strain Crack Toughness Testing of High-Strength Metallic Materials, ASTM STP 410*, American Society for Testing and Materials, 1967.
- [5] Pearson, S., *Engineering Fracture Mechanics*, Vol. 7, 1975, pp. 235-247.
- [6] Williams, M. L., *Journal of Applied Mechanics*, Vol. 24, No.1, March 1957.
- [7] Gross, B., Srawley, J. E., and Brown, W. F., "Stress Intensity Factors for a Single-Edge-Notch Tension Specimen by Boundary Collocation of a Stress Function," Lewis Research Center, National Aeronautics and Space Administration, Cleveland, Ohio, 1964.
- [8] Paris, P. C., Bucci, R. J., and Little, C. A., *Stress Analysis and Growth of Cracks, ASTM STP 513*, American Society for Testing and Materials, 1972, pp.196-217.
- [9] McClintock, F. A. and Argon, A. S., *Mechanical Behavior of Materials*, Addison-Wesley, 1966, pp. 556-557.
- [10] Forrest, P. G., *Fatigue of Metals*, Pergamon Press, New York, 1962.
- [11] Bowles, C. Q. and Schijve, J., *International Journal of Fracture*, Vol. 9, No. 2, June 1973.

N. E. Dowling<sup>1</sup>

# Crack Growth During Low-Cycle Fatigue of Smooth Axial Specimens

---

**REFERENCE:** Dowling, N. E., "Crack Growth During Low-Cycle Fatigue of Smooth Axial Specimens," *Cyclic Stress-Strain and Plastic Deformation Aspects of Fatigue Crack Growth*, ASTM STP 637, American Society for Testing and Materials, 1977, pp. 97-121.

**ABSTRACT:** Crack growth data are reported for small axially loaded smooth specimens of A533B steel subjected to strain cycling fatigue at large plastic strains. Surface crack lengths were monitored using cellulose acetate replicas, and occasional specimens were broken open to determine crack depth. Experimental crack growth rates for different strain levels are correlated in fracture mechanics fashion by the  $J$  integral concept, with  $J$  values being estimated from stress-strain hysteresis loops. The crack growth rate data of this investigation are compared with previous data for the same material obtained from linear elastic fracture mechanics tests. It is suggested that research on the behavior of small cracks is fundamental to a better understanding of the fatigue process.

**KEY WORDS:** stresses, strains, fatigue, cracks, deformation

Fatigue crack initiation has been studied in considerable detail from the viewpoint of dislocations and metallurgy to determine the mechanisms involved. In such studies, the size scale of interest is usually of the order of the crystallographic grain size or smaller. At a size scale on the order of 1 in., the growth of fatigue cracks has been studied intensely from the viewpoint of linear elastic fracture mechanics.

Less attention has been given to the specific nature of fatigue damage at intermediate size scales. In particular, relatively few studies have been made of the growth and behavior of small cracks, those of sizes on the order of  $10^{-3}$  to  $10^{-1}$  in. However, cracks in this size range are of major importance. Many components in service and many test specimens in fatigue studies probably spend the major portion of their lives with such cracks being present.

This paper reports an experimental study of crack growth in small axially loaded smooth specimens subjected to cyclic plastic deformation. Such tests are usually thought of as measuring the resistance of a material to macro-

<sup>1</sup>Senior engineer, Westinghouse Research, Pittsburgh, Pa. 15235.

cracking. The total number of cycles to failure and the stress-strain behavior are the principal information sought, and crack growth data generally are not obtained. In contrast to the tests normally employed in fatigue crack growth studies, those reported here involve specimen widths one order of magnitude smaller, crack sizes one to three orders of magnitude smaller, and plastic rather than elastic load versus deflection behavior. An attempt nevertheless will be made to make a fracture mechanics type of interpretation of the data obtained.

### Laboratory Investigation

In this section of the paper, the material and test specimens employed are described first. Test procedures are then discussed, followed by presentation of test results.

#### Material and Specimens

The material tested was A533B pressure vessel steel having the following mechanical properties: 70 ksi yield, 91 ksi ultimate, 187 ksi true fracture strength, 69 percent reduction in area, and 95° F Charpy fracture appearance transition temperature.

Cyclic stress-strain and low-cycle fatigue data for this material are shown in Figs. 1 and 2. An equation fitted to the cyclic stress-strain data is given in Fig. 1. In Fig. 2, intercepts at 1/2 cycle,  $\epsilon'_f$  and  $\sigma'_f$ , and also slopes, are given for lines fitted to both plastic strain versus life and elastic strain versus life. These may be used to obtain an equation relating total strain and life as described in Ref 1 and ASTM Recommended Practice for Constant-

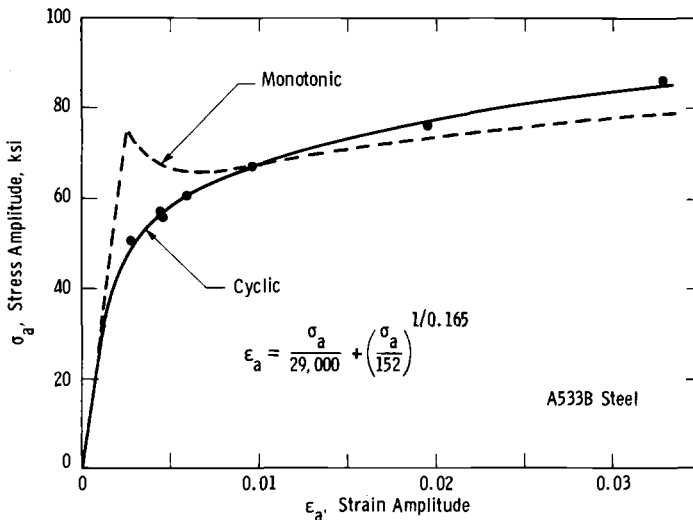


FIG. 1—Cyclic and monotonic stress-strain curves.

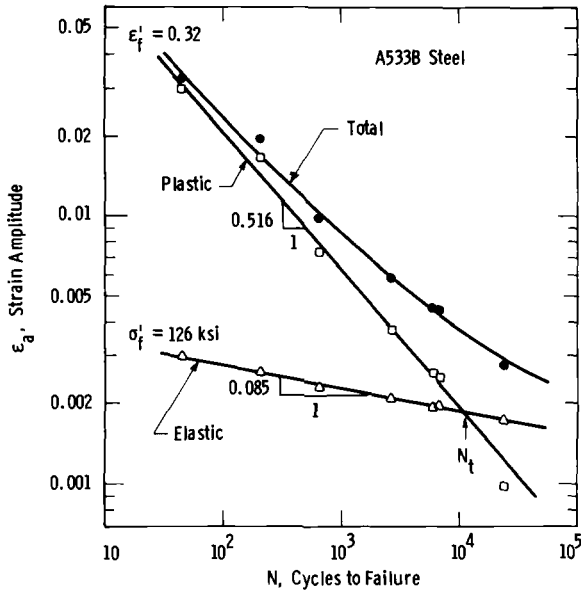


FIG. 2—Low-cycle fatigue properties—elastic, plastic, and total strain versus life.

Amplitude Low-Cycle Fatigue Testing (E 606-77T). The data in Figs. 1 and 2 were obtained during the course of this investigation, as described in detail in the following section.

Threaded-end specimens with reduced-diameter, cylindrical test sections were employed, the test sections being 0.55 in. long and 0.30 in. in diameter. This type and size of specimen is typical of those used in strain-controlled, axial low-cycle fatigue testing (ASTM Method E 606-77T and [2]).<sup>2</sup>

Material for these specimens was obtained from broken fracture specimens of large size, which had in turn been taken from a 12-in.-thick plate. Two inches of material on both surfaces of the original plate was avoided, as was any region of plastic deformation in the fracture specimens. The tension axis for the small axial specimens was perpendicular to both the rolling direction and thickness of the original plate.

### Test Procedures

All tests were conducted on a closed-loop electrohydraulic testing system. A Wood's metal grip similar to that described in Ref 2 or ASTM Method E 606-77T was employed. To prevent specimen buckling and to ensure that alignment was maintained, it was necessary to stiffen the hydraulic actuator against lateral motion.

It was desired to follow crack growth while measuring strain in the test

<sup>2</sup>The italic numbers in brackets refer to the list of references appended to this paper.

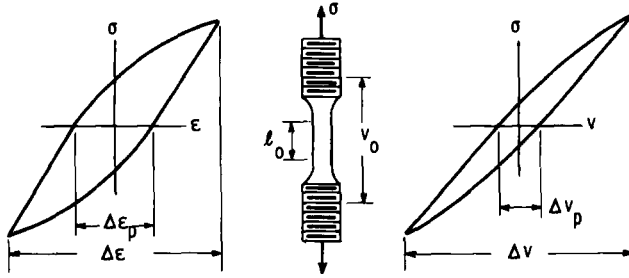


FIG. 3—Strain and deflection measurements.

section using a gage length such as  $l_0$  in Fig. 3. However, this was not done as the clip gage used for measuring strain hindered crack observations, and it was found to be impractical to repeatedly remove and reattach this clip gage. Deflections therefore were controlled across the threaded ends of the specimen, as suggested by gage length  $v_0$  in Fig. 3. Pairs of tests under identical control were conducted, with a 0.50-in. test section clip gage being employed in the first test so that strains could be measured, and crack growth being followed in the second test.

Constant-amplitude deflection control was employed with a completely reversed sinusoidal waveform. Six different values of deflection amplitude were used in the various tests conducted, with more than the nominal pair of tests being run in some cases.

Crack growth was monitored on the specimen surface by means of cellulose acetate replicas. The replicating tape thickness used was 0.005 in., and acetone was employed in softening it to obtain an impression of the specimen surface. Each crack growth test was interrupted approximately ten times for replicating, and each time it was necessary to take two replicas so as to cover the entire test section. No shading or special treatment of the replicas was needed.

Some of the crack length measurements from replicas were checked with a low-power ( $\times 20$ ) travelling microscope while the tests were in progress. All replicas were saved for more detailed examination later, and thus provided permanent records allowing a number of cracks to be traced back to lengths of a few thousandths of an inch. Several photographs of replicas showing the progress of a crack during one test are shown in Fig. 4. Crack length versus cycles data for this same test are shown in Fig. 5, and for another test in Fig. 6.

A limited number of extra tests were conducted which were interrupted, the specimen then being either sectioned or cooled in liquid nitrogen and fractured to reveal the crack shape. Such a broken-open crack is shown in Fig. 7.

### *Test Results*

Constant-amplitude deflection control across the specimen ends resulted, as expected, in the strain amplitude in the test section being approximately constant during most of the fatigue life. Pertinent data are plotted in Fig. 8. Also, the plastic strain and the plastic deflection,  $\Delta\epsilon_p$  and  $\Delta v_p$ , defined in Fig. 3, were found to be proportional over the entire range of measurement. This is illustrated by the data plotted in Fig. 9.

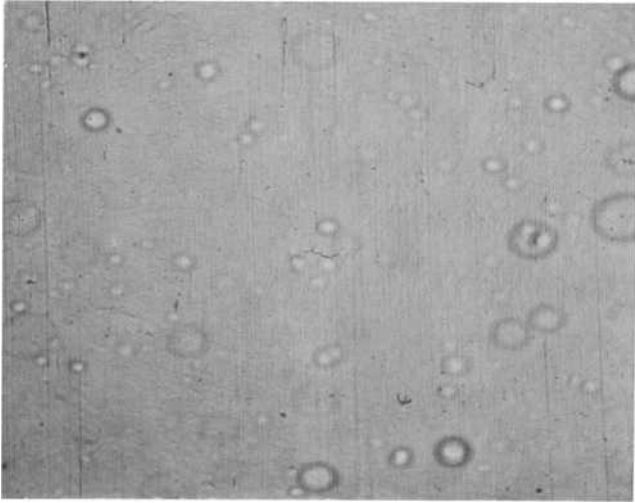
Stress-strain hysteresis loops at half the fatigue life were taken as representative of the approximately stable behavior observed during most of the fatigue life. Such loops for all but the highest strain level are plotted in Fig. 10, where the axes of each loop have been shifted so that all compressive tips coincide. The stress and strain parameters of such stable loops were used to obtain the cyclic stress-strain and strain-life properties of this material, which have already been presented in Figs. 1 and 2.

Crack length versus cycles data, as from Figs. 5 and 6, are shown in Fig. 11, with the lives being normalized to the number of cycles to failure. Data are plotted in Fig. 11 for only the longest surface crack present at any particular time. Often, as in Fig. 5, more than one crack was observed. However, a single dominant crack usually resulted in failure. In a small fraction of the specimens, two cracks joined to cause failure as in Fig. 6. These cases of crack joining account for the data points in Fig. 11 which are farthest from the central tendency. As crack joining was observed only near the end of the fatigue life, this process did not appear to have a major effect on fatigue life.

Strain versus cycles data for surface crack lengths of 0.003 and 0.01 in., and also for specimen failure, are plotted in Fig. 12. The former crack length was usually present at about one tenth of the total life, and the latter at about half the life. The strains plotted in Fig. 12 as open symbols were estimated from deflection measurements using Fig. 9, and also by noting that the elastic and plastic strains must sum to give the total strain. (Elastic strain is of course simply related to stress by the elastic modulus.) This allowed minor errors in programming the deflection and also minor differences in stress-strain behavior to be accounted for. Satisfactory crack growth data could not be obtained at the highest strain level due to extreme surface roughness and specimen necking.

Several cracks having surface lengths between 0.01 and 0.07 in. were broken open or sectioned. In all cases, the crack formed a thumbnail having an approximately half-circular shape. In other words, the maximum depth was approximately equal to half the surface length.

Growth rates for crack depth were determined by computing point-to-point slopes on surface crack length versus cycles plots such as Figs. 5 and 6, and by assuming the depth was always half the measured surface length. These data are plotted in Fig. 13 versus  $\Delta J$ . The parameter  $\Delta J$  was obtained

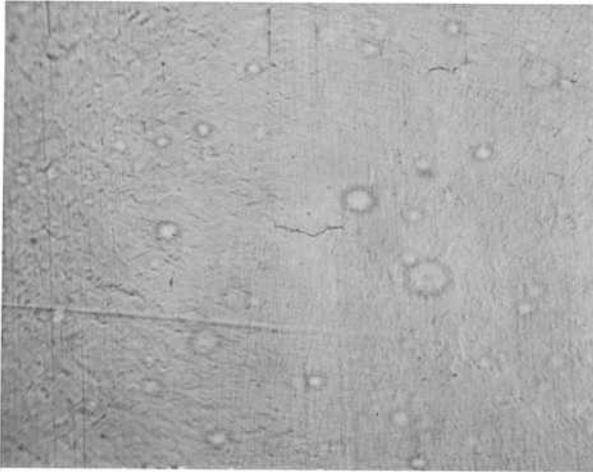


(a) 100 Cycles



(c) 500 Cycles

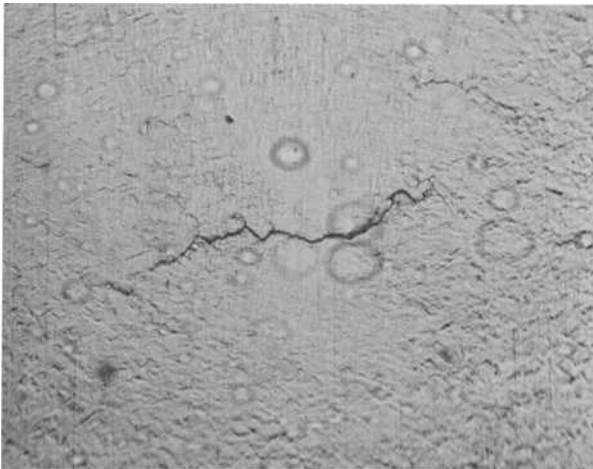
**FIG. 4—***Photographs of replicas showing the progress*



(b) 300 Cycles

0.01 inches

↑  
Loading Axis  
↓



(d) 739 Cycles

*of a fatigue crack (Spec. No. 1F7, Crack No. 1).*

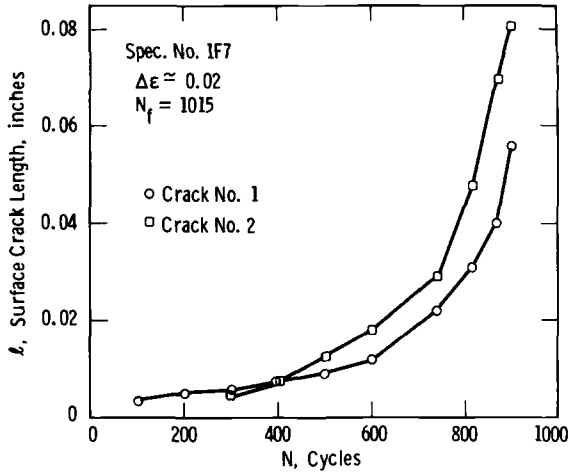


FIG. 5—Typical crack length versus cycles data obtained from surface replicas.

from the  $J$  integral of fracture mechanics and will be explained fully in the later discussion section of this paper. Data are plotted in Fig. 13 for all cracks which could be followed on the replicas. Thus, secondary cracks which did not cause failure are included, as are cracks in tests which were terminated, either accidentally or intentionally.

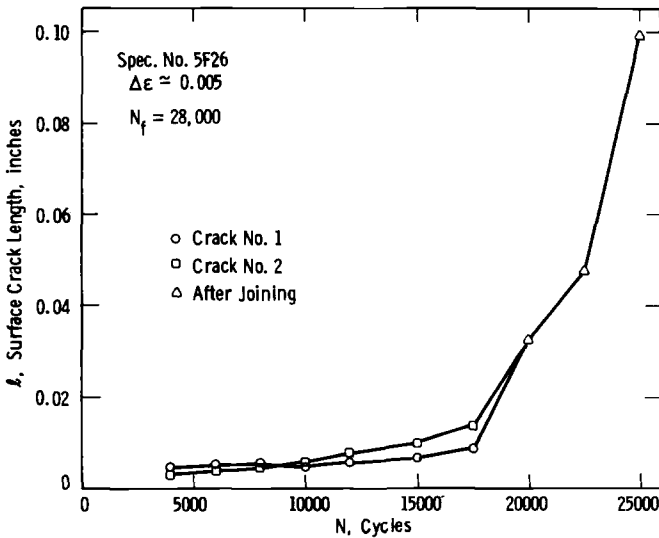


FIG. 6—Crack length versus cycles data for two cracks which joined.

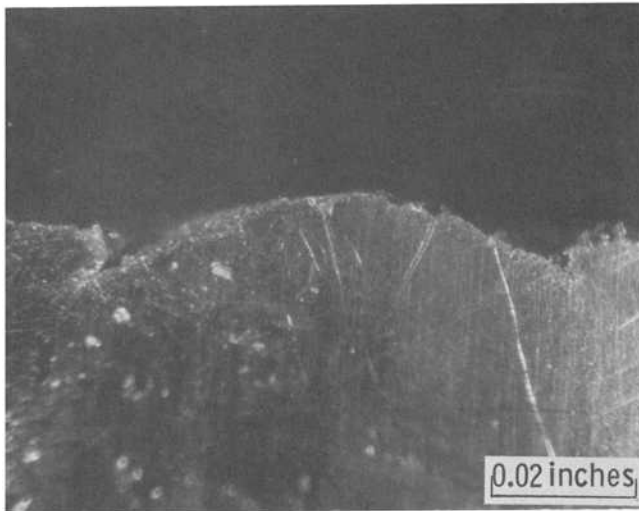
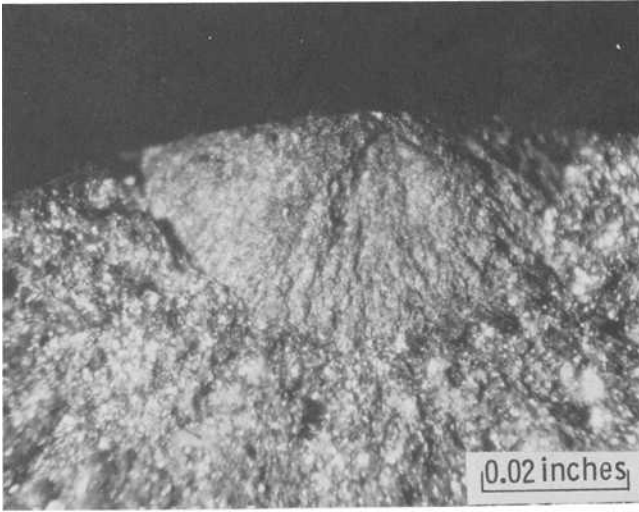


FIG. 7—Broken open fatigue crack (Spec. No. 5F31).

### Discussion

Three topics are considered in this discussion section. First, the fraction of the fatigue life required for initiation of various size cracks is discussed. Some possible applications of small crack initiation data are then noted.

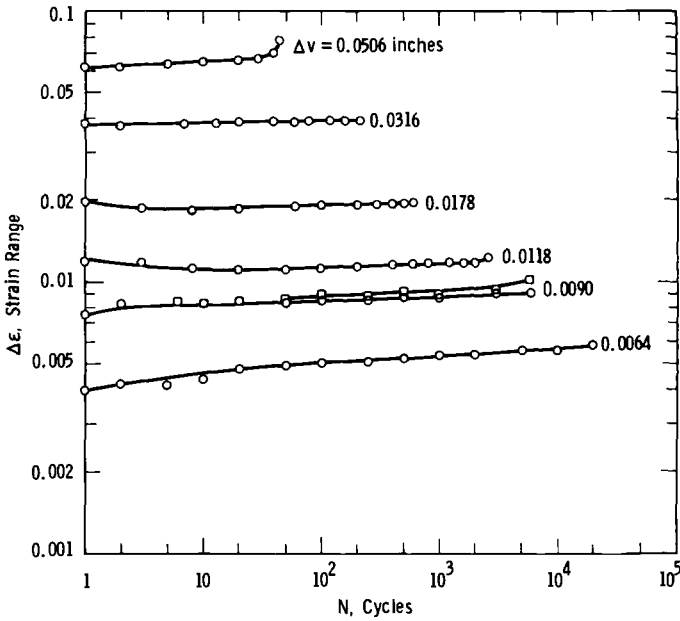


FIG. 8—Variation of strain with cycles under constant-amplitude deflection control.

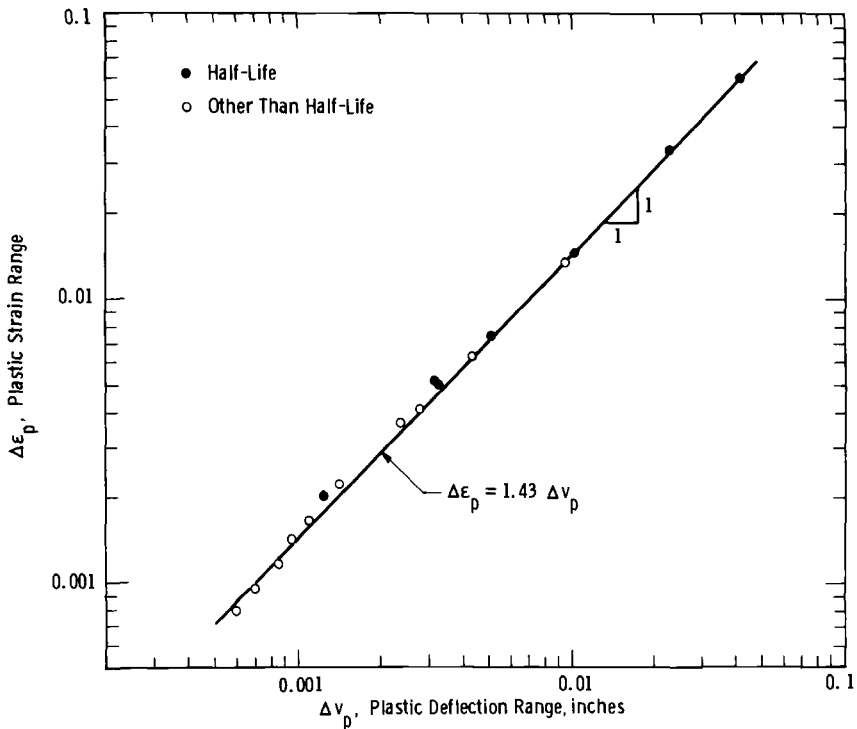


FIG. 9—Proportionality between plastic strain and plastic deflection.

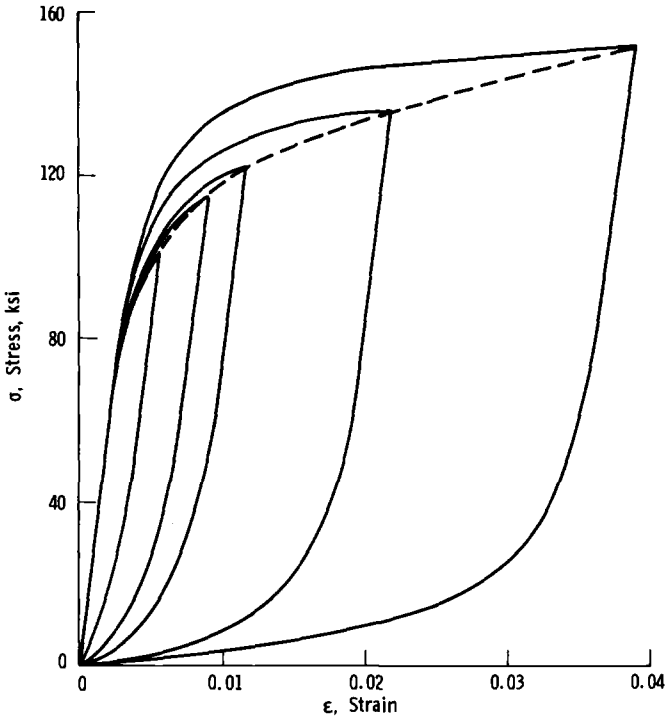


FIG. 10—Stress-strain hysteresis loops plotted on shifted axes.

And finally, the possibility is considered of applying a fracture mechanics type of approach to growth of small cracks under cyclic plastic deformation.

#### *Life Fraction Required for Initiation*

From Figs. 11 and 12, cracks a few thousandths of an inch long were present at one tenth of the fatigue life. Other combinations of crack length and life fraction may be obtained from Fig. 11. Note that there are no trends with strain level in Fig. 11, and in Fig. 12 the various lines are approximately parallel. In other words, the fraction of life corresponding to any given crack size was independent of life over the range investigated.

This appears to conflict with the data collected in Ref 3, where the life fraction for initiation increases with life. It is not clear whether these differences are due to the materials tested or to the experimental techniques employed. Additional experimental work is obviously needed in this area.

For long-life, low-stress fatigue, the available data [3-5] suggest that the initiation process becomes the dominant factor in the fatigue life as the "fatigue limit" is approached. If this is the case for A533B, the propagation-dominated nature of the strain-life curve (Fig. 12) must change rapidly to initiation-dominated behavior at strain levels just below those investigated.

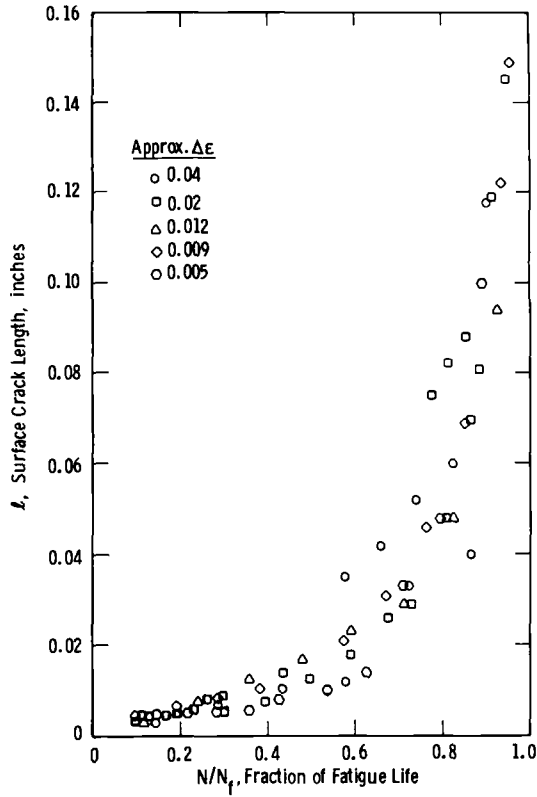


FIG. 11—Length of largest crack present versus fraction of fatigue life.

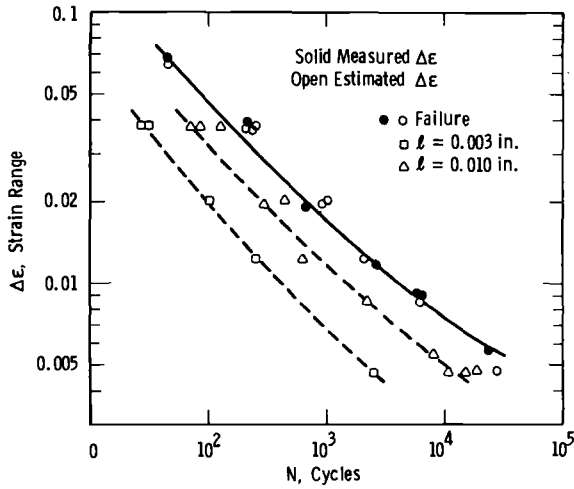


FIG. 12—Strain versus life data for initiation of small cracks and for failure.

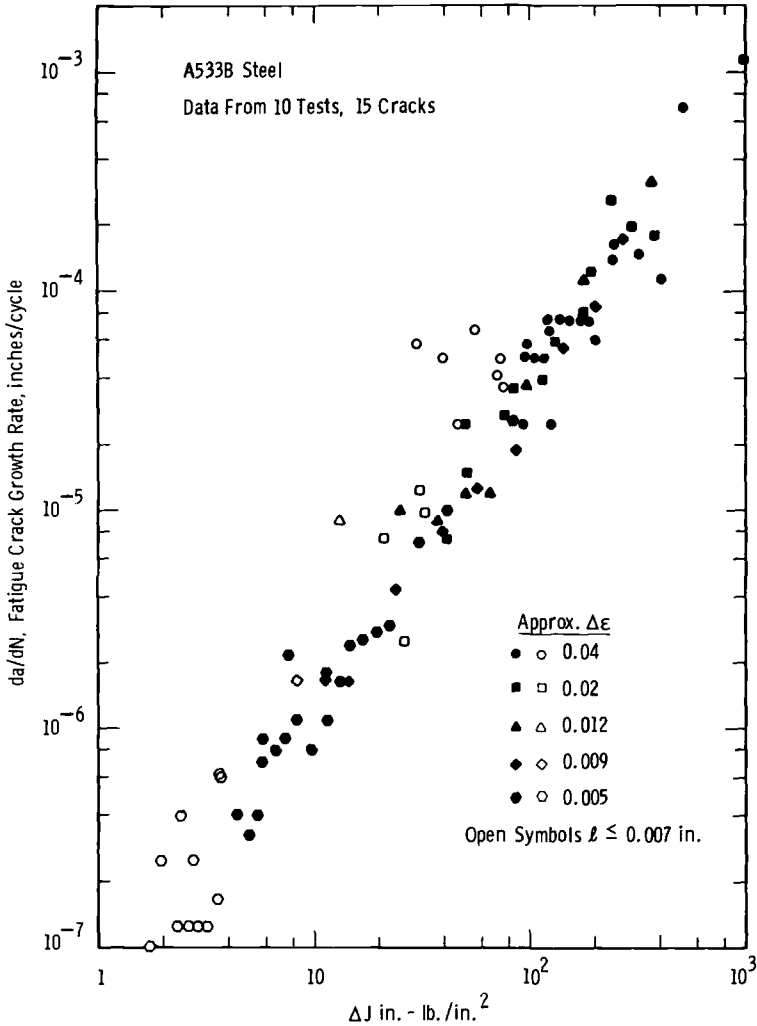


FIG. 13—Fatigue crack growth rate versus  $\Delta J$  for small cracks under plastic deformation.

Such a rapid transition has been observed [5] in aluminum alloys and is not inconsistent with the data reported here.

Note from Fig. 2 that the transition fatigue life,  $N$ , where the elastic and plastic strains are equal, occurs near the longest lives investigated. Thus, at lower strains and longer lives, the plastic strains will become small compared to the elastic strains. It is interesting to speculate that this transition in stress-strain behavior may be involved in the expected transition from propagation-dominated to initiation-dominated strain-life behavior. If this is indeed the case, the relative importance of initiation and propagation in determining the total fatigue life will be highly material dependent. This

is a result of the fact that the transition fatigue life,  $N_t$ , may be as low as ten cycles for high hardness materials, or as long as  $10^5$  cycles for very ductile materials [6].

#### *Applications of Crack Initiation Data*

It is pertinent to note some of the possible uses of strain-life curves corresponding to the initiation of specific size cracks. First, consider the Palmgren-Miner rule [7,8] for linear summation of cyclic ratios, which commonly is employed in estimating cumulative fatigue damage. The essence of this rule is that it assumes a state of physical damage which is independent of the loading level to exist at any given fraction of the fatigue life. This assumption is violated, and difficulty with the Palmgren-Miner rule is encountered, when the life fraction corresponding to a given crack size varies with the strain level. However, this problem may be overcome in some cases by summing cycle ratios separately for initiation and propagation [9,10]. Strain life curves corresponding to the initiation of a specific small crack size could be used as a basis for this approach.

Size effects may occur which are related to the behavior of small cracks. For example, if different size specimens of identical material are tested, the larger specimens should tend to have longer fatigue lives due to the increased number of cycles required to propagate a crack across the specimen. Note from Fig. 11 that a factor of 100 decrease in specimen diameter to 0.003 in. would reduce the fatigue life to roughly one tenth of that observed in the 0.3 in. specimens tested. This may explain why metal foil strain gages have much shorter fatigue lives [11,12] than expected based on the applied strain and the various rules of thumb and correlations [3,6] with tensile properties that have been developed. In particular, the expected life is unrealistic as it is based on experience with test specimens of much larger size than the foil elements.

However, the total problem of size effect is quite complicated. Weakest-link statistical-type size effects have long been recognized [13]. In this case, a larger size is expected to have an increased probability of a weak region or flaw of a given severity being present, and hence a lowered average fatigue strength. Note that, for increased size, this weakest link effect is detrimental, not beneficial as for the other type of size effect just mentioned. Also, note that the effect is in this case due to an altered initial condition for the fatigue process, rather to an altered final crack size. If it is desired to develop improved methods of predicting size effects, both of these effects, and in general the behavior of small cracks, should be considered.

Sharp notches reduce the fatigue strength less than is expected based on the locally elevated stresses and strains at the surface of the notch. A likely explanation for this is that, for most of the fatigue life, a crack is present which has grown out of the localized region of highest stress. Cracks are indeed observed during most of the life of sharply notched members [4], and

this explanation is consistent with the observation [4] that increases in notch sharpness beyond a certain point do not further reduce fatigue strength.

Assume that smooth specimen strain-life data as in Fig. 12 are available for the initiation of a crack size that is small compared to the notch radius of interest. Initiation at the notch could be predicted on this basis. And crack propagation beyond this point could be handled using a fracture mechanics type of approach, with proper consideration being given to the effect of the notch geometry.<sup>3</sup> This procedure would result in initiation dominating the life for blunt notches, in propagation dominating the life for sharp notches and in both initiation and propagation being important for intermediate cases.

#### *Fracture Mechanics Interpretation of the Growth of Small Cracks Under Plastic Deformation*

The stress intensity parameter,  $K$ , is used widely for correlating fatigue crack growth rates. However, being based on linear elastic analysis,  $K$  has no physical meaning for situations involving large-scale plasticity, which is the case for the test results of this investigation.

Thus, a more general parameter is needed which is capable of accounting for plasticity effects. The most likely candidate is the  $J$  integral. As originated by Rice [15],  $J$  is the two-dimensional path-independent line integral illustrated in Fig. 14a. Counterclockwise integration is performed around a path  $\Gamma$  connecting the crack faces, with  $x$  and  $y$  being the coordinates indicated,  $W$  the strain energy density,  $\vec{T}$  the traction vector on the boundary of a free body defined by  $\Gamma$ ,  $\vec{u}$  the displacement, and  $s$  the arc length along  $\Gamma$ .

Originally,  $J$  was developed for nonlinear elastic materials and, for such materials, can be expressed as illustrated in Fig. 14b in terms of the potential energy available for crack extension. For the special case of linear elastic materials,  $J$  reduces to the strain energy release rate,  $G$ . Assuming plane stress,  $J$  for the elastic case is simply related to  $K$  and the elastic modulus,  $E$ , as follows

$$J_{\text{elastic}} = G = \frac{K^2}{E} \quad (1)$$

For elastic-plastic materials,  $J$  loses its interpretation in terms of the potential energy available for crack extension, but retains physical significance as a measure of the characteristic crack-tip strain field. Note that this latter interpretation of  $J$  is similar in philosophy to the stress intensity concept,  $K$ , which, for linear elasticity, gives the intensity of the stress field surrounding the crack tip.

Based on this crack-tip strain field interpretation,  $J$  has been employed successfully as a criterion for static plastic fracture [16,17]. Preliminary study on ordinary-size fracture specimens of A533B steel also indicates that  $J$  is

<sup>3</sup>Note that linear elastic stress intensity analyses are at present available [14] for cracks near notches in certain geometric configurations.

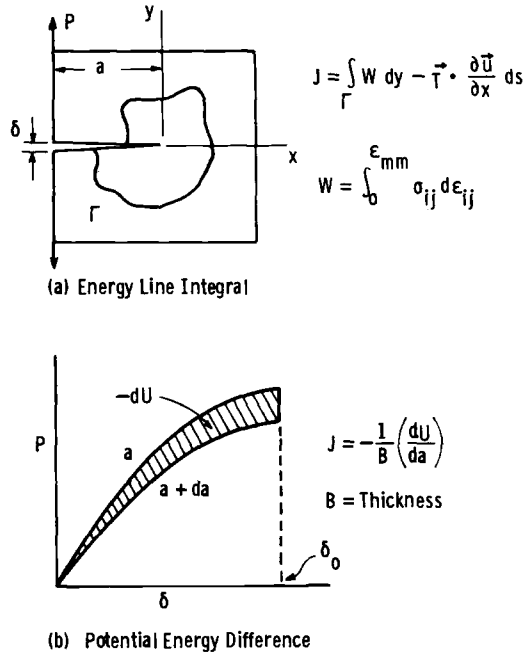


FIG. 14—The *J* integral of Rice.

promising as a correlation parameter for fatigue crack growth under plastic conditions.

Data pertinent to fatigue crack growth [18,19] are shown in Fig. 15, with the specimen geometries involved being shown in Fig. 16. Also shown in Fig. 16, for purposes of comparison, is the cylindrical specimen used in this investigation. In this previous work, large-size compact specimens were used to obtain high rates of crack growth under linear elastic conditions. And ordinary-size compact and center-cracked specimens were employed to obtain both low rate data under linear elastic conditions and high rate data under plastic loading. A portion of the linear elastic data of Fig. 15, in particular those at very low growth rates, were obtained from Ref 20. In Fig. 15, note that linear elastic data are plotted versus  $(\Delta K)^2/E$  as open symbols, and plastic data are plotted versus  $\Delta J$  as solid symbols. Different shape symbols are used in Fig. 15 to indicate different specimen sizes, the dimension  $W$  referring to half the width of the center-cracked specimens, and to the distance from pinhole to back edge for the compact specimens. For more detailed information concerning these data, the reader is referred to Refs 18–20.

To compare the growth rate data of this investigation with the data of Fig. 15, it is necessary to compute  $\Delta J$  values for the small surface cracks observed. Unfortunately, no rigorous solutions are available, and an estimate is necessary. The specific estimate employed is given in Fig. 17, with detailed

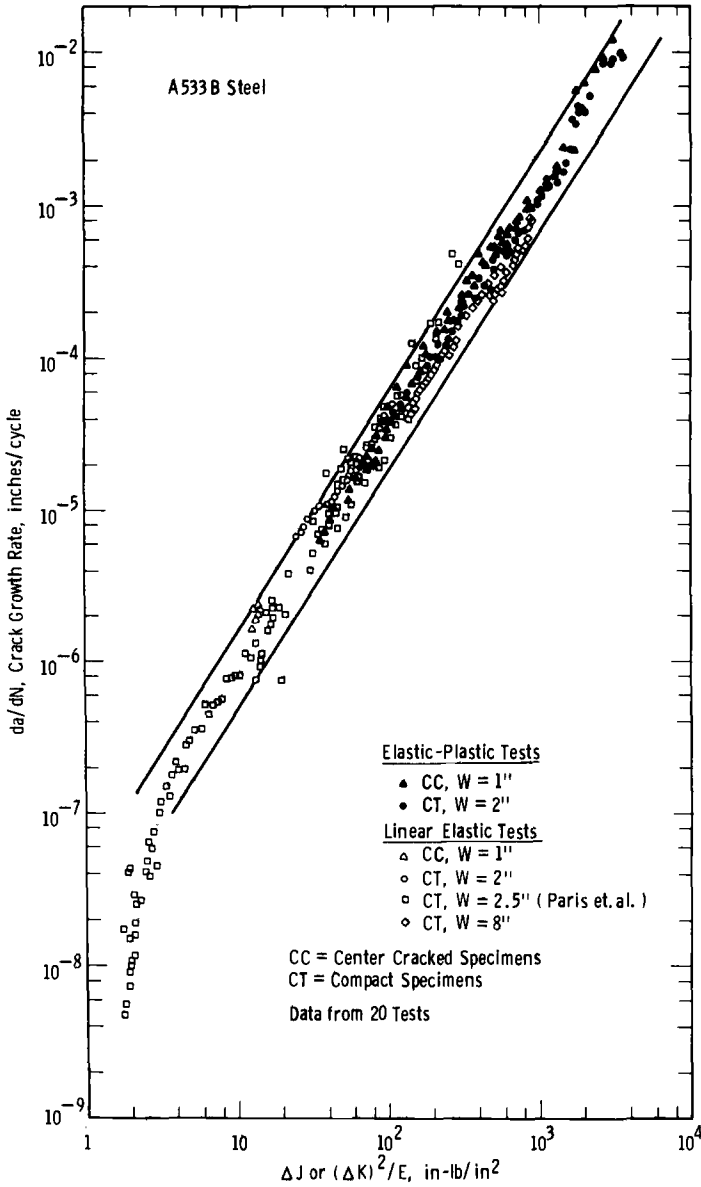


FIG. 15—Fatigue crack growth rate versus  $\Delta J$  for various geometries.

derivation and discussion being provided by the Appendix. The crack dimension  $a$  in the expression shown is the crack depth, estimated by taking half the measured surface length. Note that the stress and plastic strain ranges from a stress-strain hysteresis loop are needed. As the stress-strain behavior was approximately stable during most of the fatigue life, all  $J$  cal-

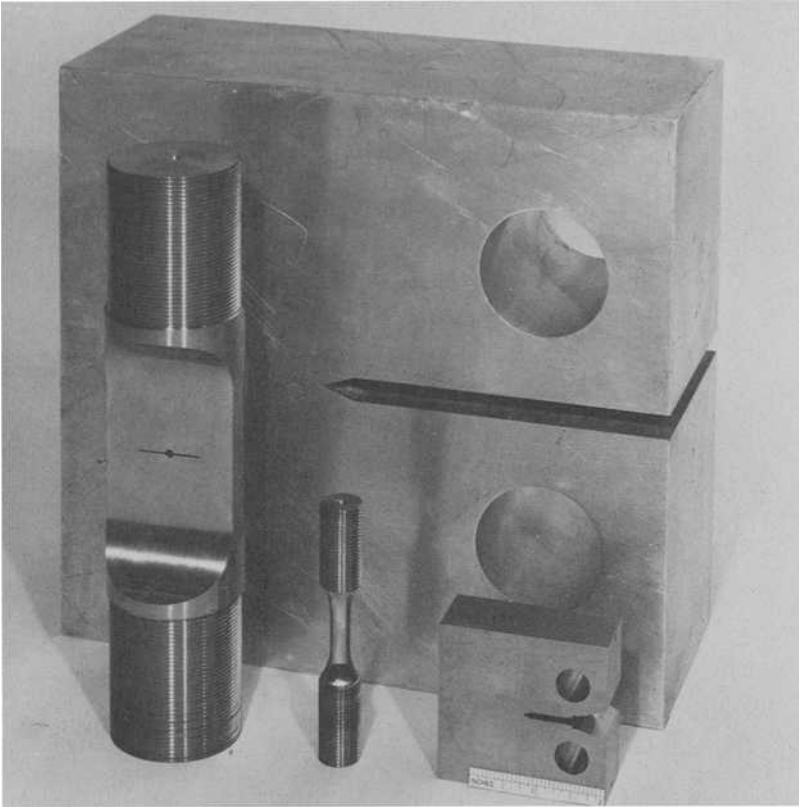


FIG. 16—Specimen geometries used to obtain fatigue crack growth rate data.

culations for each crack growth test were estimated based on the stable stress range and the stable plastic strain range, with the latter being estimated from the measured threaded end deflections by means of Fig. 9.

The crack growth rate versus  $\Delta J$  data from Fig. 13, for which  $\Delta J$  was computed as just described, are compared in Fig. 18 with the scatterband from Fig. 15. The boundaries of this scatterband are separated by a factor of three in growth rate, which is typical variability [21] for ordinary linear elastic fatigue crack growth rate testing. Excellent agreement is obtained except for cracks smaller than 0.007 in. There are two possible explanations for this. First, 0.007 in. is approximately ten times the average crystallographic grain diameter of this material, suggesting that the lack of correlation may be due to the continuum nature of fracture mechanics being violated. Or second, as cracks of such small size were not broken open or sectioned, the depth assumed based on a half-circular shape may have been in error. However, this assumed crack depth was used in computing

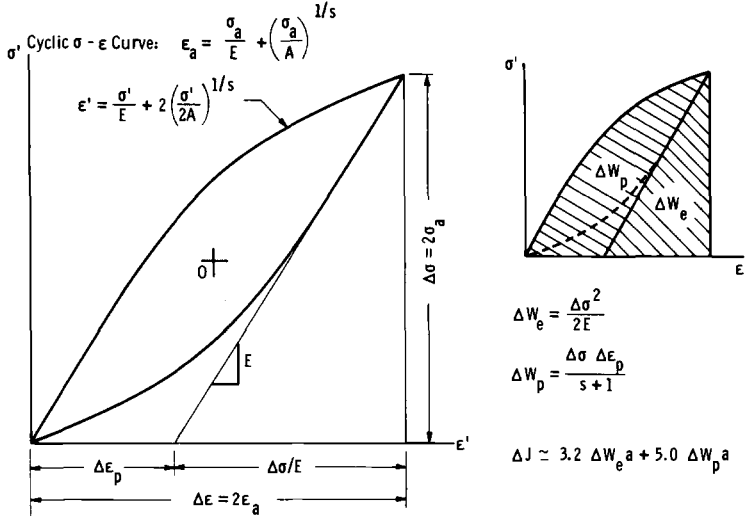


FIG. 17—Estimation of small crack  $\Delta J$  from stress-strain hysteresis loops.

both  $da/dN$  and  $\Delta J$ , and, when the combined effect of errors in both quantities is considered, it is difficult to explain the observed trends. The lack of correlation for very small cracks thus probably reflects a physical size effect.

Despite the difficulty with very small cracks, the correlation that does exist is quite impressive. Comparing the width,  $W$ , of the compact specimens with the diameter of the small cylindrical specimens, a factor of about 25 in specimen size is covered. And the solid data points and scatterband in Fig. 18 together represent a factor of about 1500 in crack size.

From comparison of Figs. 15 and 18, note that linear elastic data cover the entire four orders of magnitude for which small crack plastic data are available. If one attempts to correlate the small crack data with the larger specimen linear elastic data through the use of the linear elastic stress intensity calculated simply from stress and crack size, an extreme lack of correlation is encountered. Thus, although exploratory and tentative in nature at the present time, the use of  $J$  for fatigue has a major advantage in its ability to account for plasticity effects.

At rates just below the lowest rates measured in this investigation for small cracks, the ordinary-size specimen data in Fig. 15 exhibit the transition in behavior associated with the threshold for fatigue crack growth [20,22]. It is interesting to speculate as to whether or not small cracks obey a similar transition in behavior. If they do not, then the threshold concept is of much less practical value than is currently thought. Obviously, verifying the threshold concept for small cracks is an important area for further work.

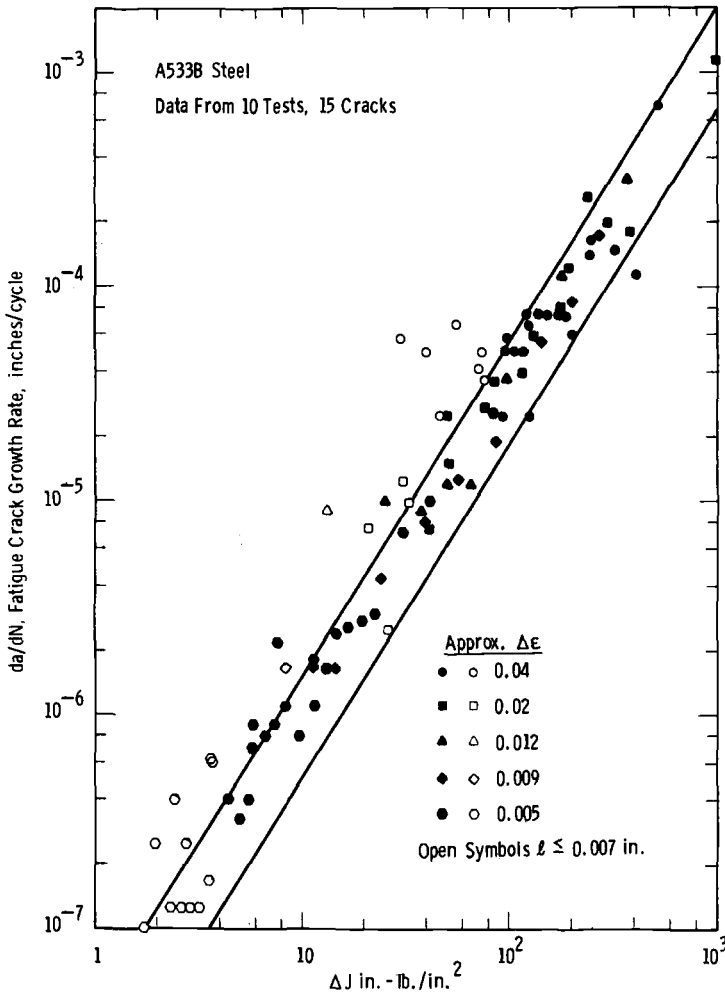


FIG. 18—Comparison of small crack data with scatterband from test results for ordinary and large-size specimens.

**Conclusions and Recommendations**

Study of the behavior of small cracks is promising as a means of better understanding, and hence of more effectively predicting, the process of metal fatigue. The following more specific conclusions and recommendations are drawn from the foregoing test results and discussion:

1. For failure lives between 200 and 25 000 cycles in A533B steel, the life fraction at which specific small crack sizes were present did not vary significantly. Surface cracks a few thousandths of an inch long were observed at 10 percent of the fatigue life.

2. Additional work in a variety of materials is needed where the life to various specific small crack sizes is determined. It is particularly important that the effect of different transition fatigue lives, that is, of different relative amounts of ductility, be investigated.

3. Small crack initiation data have several potentially important applications. Among these are cumulative fatigue damage, size effects, and notch effects.

4. The  $J$  integral shows considerable promise as a parameter for correlating fatigue crack growth rates under elastic-plastic conditions. Although the correlation failed for surface crack lengths less than ten crystallographic grain diameters, it was successful over a factor of 1500 in crack size, a factor of 25 in specimen size, and four orders of magnitude in growth rate. In obtaining  $J$  values, it was necessary to employ an estimate, and an uncertainty exists concerning the possibility that cracks are closed during a portion of the strain cycle.

5. The concept of a threshold for fatigue crack growth should be verified for small cracks.

### *Acknowledgments*

Gratitude is expressed to laboratory technicians F. X. Gradich and L. W. Burtner for their care and expertise in performing the replication and photography work. D. R. Young, Jr., supervisor of the Mechanics of Materials Laboratory, aided in planning laboratory tests and in detailed design of experimental apparatus. This work was made possible by the sponsorship of Westinghouse Electric Corporation, the atmosphere and facilities which resulted in this paper existing largely due to the efforts of E. T. Wessel, Manager of Mechanics of Materials, Westinghouse Research Laboratories.

## APPENDIX

### **Estimation of $\Delta J$ for Small Half-Circular Surface Cracks**

In making this estimate, the linear elastic and exponential hardening plastic cases will be considered separately, and then combined for the more general elastic-plastic Ramberg-Osgood type of stress-strain behavior. These three idealized stress-strain relationships are illustrated in Fig. 19.

Consider the classical case of a crack in a wide plate remotely loaded in tension, Fig. 20a. The stress intensity is obtained [23] from the familiar expression

$$K = \sigma\sqrt{\pi a} \quad (2)$$

where  $\sigma$  = remote tension stress. Noting that the remote strain energy density,  $W$ , is given by the expression in Fig. 19a, Eqs 1 and 2 combine to give

$$J_{\text{elastic}} = 2\pi W a \quad (3)$$

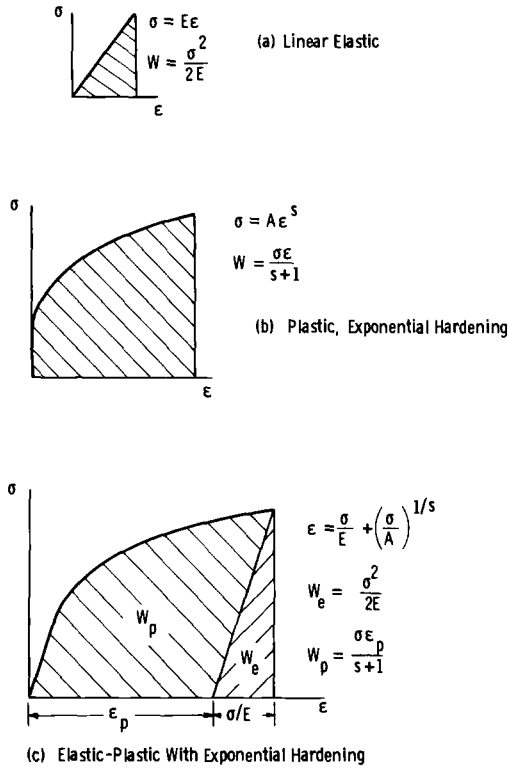


FIG. 19—Three types of idealized stress-strain behavior.

If the geometry of Fig. 20a is bisected to obtain a surface crack as in Fig. 20b, the stress intensity is elevated slightly [23]

$$K = 1.12\sigma\sqrt{\pi a} \tag{4}$$

Now consider the expression for an embedded circular crack [23]

$$K = \frac{2}{\pi} \sigma\sqrt{\pi a} \tag{5}$$

Again bisect to obtain a surface crack, in this case a half-circular surface crack, Fig. 20c. Note that this geometry approximates the geometry encountered in the laboratory tests, as long as the crack size is small compared to the specimen diameter. It is reasonable to assume that the surface correction factor of 1.12 implied by Eq 4 is at least approximately applicable here also, resulting in

$$K = 0.714\sigma\sqrt{\pi a} \tag{6}$$

The combined surface and flaw shape correction factor of 0.714 in Eq 6 must be squared to obtain the corresponding correction factor for  $J$  of 0.51. Applying this factor to Eq 3 gives

$$J_{\text{elastic}} = 3.2Wa \tag{7}$$

Rigorous  $J$  solutions for the exponential-hardening plastic case are not available for tension-loaded cracked members of infinite dimension. However, an estimate has

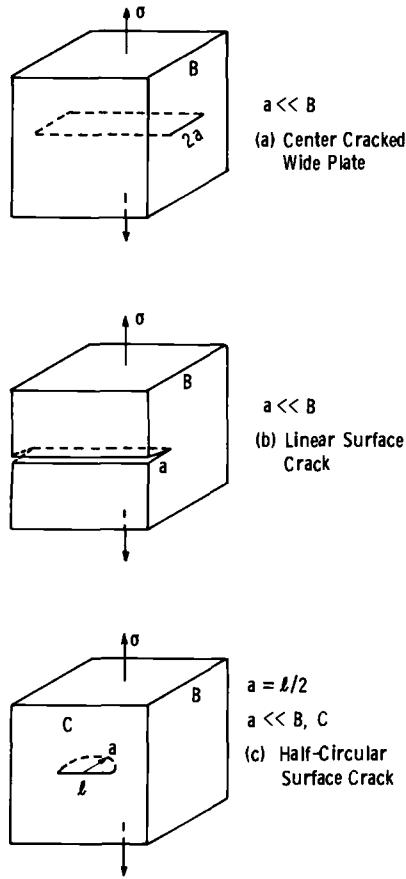


FIG. 20—Various idealized crack geometries.

been made by Shih and Hutchinson [24] for the geometry of Fig. 20a under plane stress

$$J_{\text{plastic}} = 2\pi f(s) Wa \tag{8}$$

where  $f(s)$  is a function of the strain-hardening exponent. For  $s = 0.165$  from Fig. 1, the analysis of Ref 24 implies a value  $f(s) = 1.56$ . Note that  $J$  is still proportional to both the strain energy density and the crack size. To obtain an expression for the half-circular surface crack geometry of Fig. 20c, assume that the combined surface and flaw shape correction factor of 0.51 used for the linear elastic case is applicable here also. Equation 8 is thus modified to give

$$J_{\text{plastic}} = 5.0 Wa \tag{9}$$

An estimate qualitatively similar to Eq 9 was applied previously by Mowbray [25].

Consider the Ramberg-Osgood type elastic-plastic, stress-strain relationship, Fig. 19c. The work of Shih [26] and also that of Shih and Hutchinson [24] suggests that  $J$  solutions for this case may be approximated by simply adding the separately computed elastic and plastic solutions. Equations 7 and 9 thus result in the following estimate of  $J$  for the half-circular surface crack geometry

$$J = 3.2W_e a + 5.0W_p a \tag{10}$$

where  $W_e$  and  $W_p$  = elastic and plastic components of the remote strain energy density, as illustrated in Fig. 19c.

For application to cyclic loading, it will be assumed valid to compute  $J$  for the loading portion of a cycle. The procedure used is illustrated in Fig. 17. Note that ranges of stress and plastic strain obtained from hysteresis loops such as those in Fig. 10 are used to compute the quantity here called  $\Delta J$ . The particular expression for  $\Delta W_p$  which is shown depends on the assumption that hysteresis loop curves may be obtained by expanding the cyclic stress-strain curve with a scale factor of two, as indicated in Fig. 17 by the stress-strain equation involving primed quantities. If this assumption were valid for A533B, the dashed locus of loop tips line in Fig. 10 and all of the upper loop curves would fall together along a single line. However, this difficulty never affects the value of  $J$  by more than about 10 percent, and, in view of the fact that the  $J$  expression used is only an estimate, refinements in this area are inappropriate.

Note that the analysis [24] used as a basis for this estimate is for plane stress. A degree of approximation is thus involved in this regard also. The specimens tested were free to contract transversely so that the nominal plastic strain in any transverse direction was approximately half that in the axial direction. But a degree of constraint violating the plane stress assumption exists near the crack due to the strain being locally elevated there.

Ideally,  $\Delta J$  should be computed only for that portion of the cycle during which the crack is open. An attempt was made to observe crack opening with a low-power microscope, but no well-defined opening event could be resolved. The only evidence available was the effect on the load versus deflection behavior of cracks that had grown relatively large near the end of the fatigue life. In such cases, stiffness changes indicating the closing and opening of the crack were observed only at high compressive loads. Thus, it was decided, as illustrated in Fig. 17, to use the entire compressive loading portion of the hysteresis loop in estimating  $\Delta J$ . Until additional experimental or analytical work clarifies the details of the crack closure effect, this uncertainty will exist in all fracture mechanics type approaches to the fatigue problem, including the familiar linear elastic approach.

Thus, the method used in obtaining cyclic  $J$  involves approximations in several areas and can be regarded as a rough estimate only.

## References

- [1] Raske, D. T. and Morrow, J. in *Manual on Low Cycle Fatigue Testing, ASTM STP 465*, American Society for Testing and Materials, 1969, pp. 1-26.
- [2] Feltner, C. E. and Mitchell, M. R. in *Manual on Low Cycle Fatigue Testing, ASTM STP 465*, American Society for Testing and Materials, 1969, pp. 27-66.
- [3] Manson, S. S., *Experimental Mechanics*, Society for Experimental Stress Analysis, Vol. 5, No. 7, July 1965, pp. 193-226.
- [4] Hunter, M. S. and Fricke, W. G., Jr., *Proceedings*, American Society for Testing and Materials, Vol. 57, 1957, pp. 643-654.
- [5] Schijve, J. in *Fatigue Crack Propagation, ASTM STP 415*, American Society for Testing and Materials, 1967, pp. 415-459. (See also Report No. NLR-TR M. 2128, National Aerospace Laboratory, Amsterdam, May 1964.)
- [6] Landgraf, R. W. in *Achievement of High Fatigue Resistance in Metals and Alloys, ASTM STP 467*, American Society for Testing and Materials, 1970, pp. 3-36.
- [7] Palmgren, A., *Ball and Roller Bearing Engineering*, translated by G. Palmgren and B. Rulley, SKF Industries, Inc., Philadelphia, 1945, pp. 82-83.
- [8] Miner, M. A., *Journal of Applied Mechanics, Transactions of the American Society of Mechanical Engineers*, Vol. 12, Sept. 1965, pp. A-159-164.
- [9] Grover, H. J. in *Symposium on Fatigue of Aircraft Structures, ASTM STP 274*, American Society for Testing and Materials, 1959, pp. 120-124.

- [10] Manson, S. S., Freche, J. C., and Ensign, C. R. in *Fatigue Crack Propagation*, ASTM STP 415, American Society for Testing and Materials, 1966, pp. 384-412.
- [11] Gowda, C. V. B. and Topper, T. H., *Experimental Mechanics*, Society for Experimental Stress Analysis, Jan. 1970, pp. 27N-38N.
- [12] Dowling, N. E., *Experimental Mechanics*, Society for Experimental Stress Analysis, Vol. 17, No. 5, May 1977, pp. 193-197.
- [13] Weibull, A., "A Statistical Theory of the Strength of Materials," *Proceedings*, The Royal Swedish Institute for Engineering Research, Stockholm, No. 151, 1939.
- [14] Newman, J. C., Jr., "An Improved Method of Collocation for the Stress Analysis of Cracked Plates with Various Shaped Boundaries," NASA TN D-6376, National Aeronautics and Space Administration, Washington, D. C., Aug. 1971.
- [15] Rice, J. R., *Journal of Applied Mechanics*, *Transactions of the American Society of Mechanical Engineers*, Vol. 35, June 1968, pp. 379-386.
- [16] Landes, J. D. and Begley, J. A. in *Fracture Toughness*, *Proceedings of the 1971 National Symposium on Fracture Mechanics, Part II*, ASTM STP 514, American Society for Testing and Materials, 1972, pp. 24-39.
- [17] Logsdon, W. A. in *Mechanics of Crack Growth*, ASTM STP 590, American Society for Testing and Materials, 1976, pp. 43-60.
- [18] Dowling, N. E. and Begley, J. A. in *Mechanics of Crack Growth*, ASTM STP 590, American Society for Testing and Materials, 1976, pp. 82-103.
- [19] Dowling, N. E. in *Cracks and Fracture*, ASTM STP 601, American Society for Testing and Materials, 1976, pp. 19-32.
- [20] Paris, P. C., Bucci, R. J., Wessel, E. T., Clark, W. G., Jr., and Mager, T. R. in *Stress Analysis and Growth of Cracks*, *Proceedings of the 1971 National Symposium on Fracture Mechanics, Part I*, ASTM STP 513, American Society for Testing and Materials, 1972, pp. 141-176.
- [21] Clark, W. G., Jr. and Hudak, S. J., Jr., *Journal of Testing and Evaluation*, American Society for Testing and Materials, Vol. 3, No. 6, Nov. 1975, pp. 454-476.
- [22] Bucci, R. J., Paris, P. C., Hertzberg, R. W., Schmidt, R. A., and Anderson, A. F. in *Stress Analysis and Growth of Cracks*, *Proceedings of the 1971 National Symposium on Fracture Mechanics, Part I*, ASTM STP 513, American Society for Testing and Materials, 1972, pp. 125-140.
- [23] Paris, P. C. and Sih, G. C. in *Symposium on Fracture Toughness Testing and its Applications*, ASTM STP 381, American Society for Testing and Materials, 1965, pp. 30-83.
- [24] Shih, C. F. and Hutchinson, J. W., "Fully Plastic Solutions and Large Scale Yielding Estimates for Plane Stress Crack Problems," Report No. DEAP-S-14, Division of Engineering and Applied Physics, Harvard University, Cambridge, Mass., July 1975.
- [25] Mowbray, D. F. in *Cracks and Fracture*, ASTM STP 601, American Society for Testing and Materials, 1976, pp. 33-46.
- [26] Shih, C. F. in *Mechanics of Crack Growth*, ASTM STP 590, American Society for Testing and Materials, 1976, pp. 3-26.

M. F. Kanninen,<sup>1</sup> C. Atkinson,<sup>2</sup> and C. E. Feddersen<sup>1</sup>

# A Fatigue Crack Growth Analysis Method Based on a Simple Representation of Crack-Tip Plasticity

---

**REFERENCE:** Kanninen, M. F., Atkinson, C., and Feddersen, C. E., "A Fatigue Crack Growth Analysis Method Based on a Simple Representation of Crack-Tip Plasticity," *Cyclic Stress-Strain and Plastic Deformation Aspects of Fatigue Crack Growth, ASTM STP 637*, American Society for Testing and Materials, 1977, pp. 122-140.

**ABSTRACT:** A new approach to fatigue crack propagation is described. The key element in the analysis is the inclined strip-yield superdislocation representation of crack-tip plasticity. The basis of the model is given and its potential application in a cycle-by-cycle analysis of fatigue crack growth under arbitrary cycle-by-cycle loads indicated. It is shown that, to perform a fatigue crack growth computation for a given load sequence, only the material's shear modulus, tensile yield strength, and Poisson's ratio need to be specified. In the process, some account is taken of crack closure during the load cycle. Illustrative calculations for uniform cyclic loading are described and comparisons with experimental results made.

**KEY WORDS:** stress, strains, fatigue, crack propagation, loads (forces), fracture properties, displacement, plastic properties, dislocations

Fatigue crack propagation rates can be predicted using empirical relations when simple constant-amplitude cyclic loading is applied. However, the load interaction phenomenon occurring in variable-amplitude loading has not yet been satisfactorily introduced into an empirical crack growth relation. This currently precludes the accurate prediction of fatigue crack growth rates under the spectrum (service) loadings that act on aircraft and other engineering structures. To provide a quantitative formulation for fatigue crack growth under arbitrary load sequences, an analysis technique that is sound from a mechanics standpoint must be developed.

There is no complete agreement on the exact mechanisms that control fatigue crack propagation. Nevertheless, there are several features of the

<sup>1</sup>Senior researcher and principal researcher, respectively, Battelle, Columbus, Ohio 43201.

<sup>2</sup>Reader, Department of Mathematics, Imperial College of Science and Technology, London, England.

problem that are generally accepted as playing an essential role in the process:

1. The interaction between the plastic deformation produced by the current load and the residual plasticity created in previous load cycles.
2. The connection that exists between the local deformation at the crack tip—as characterized by the crack-tip crack-opening displacement—and the crack growth increment.
3. The impingement (closure) of the crack faces during the unloading portion of the load cycle.

While fatigue models have been developed from one or another of these basic effects, no currently known attempt rigorously incorporates them all.

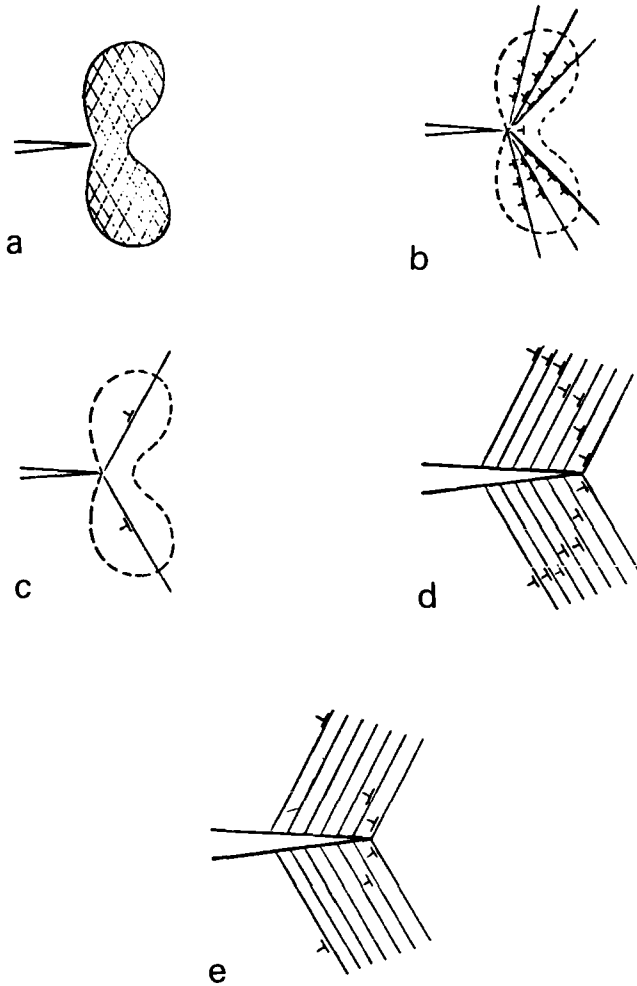
The goal of the research described here is to develop an accurate computational model for the prediction of fatigue crack propagation that can be used in actual engineering applications. To achieve this goal, three conditions must be met. First, the model must be capable of handling load cycles that vary arbitrarily from cycle to cycle while taking the load interaction effects properly into account. Second, the material properties required by the model must be based upon well-established material properties that are independent of the particular load spectrum under consideration. Third, the computational procedure evolved must be efficient enough to enable calculations to be carried out over load histories comparable to actual service conditions.

To meet these criteria, a new approach leading to a mathematical predictive model for fatigue crack propagation has been initiated. The approach is based on the inclined strip-yield superdislocation representation of crack-tip plasticity [*I*].<sup>3</sup> This approach is expected to give an effective compromise between approaches that sacrifice some basic aspects in the interest of simplicity and a completely rigorous but exceedingly cumbersome approach. The preliminary stages of the development of this model, together with some computational results for uniformly applied cyclic loading, are described in this paper.

### **Conceptual Basis of the Model**

The key element in the fatigue crack propagation model described in this paper is the inclined strip-yield superdislocation representation of the plastic zones surrounding a crack tip [*I*]. This model, in turn, stems from the well-established fact that macroscopic plasticity can be considered in terms of dislocation arrays. Figure 1 illustrates how this basic concept has evolved into the fatigue model being developed here. The following discussion elaborates on the conceptual picture given by Fig. 1 and, in addition, delineates the individual roles played in this work by the various

<sup>3</sup>The italic numbers in brackets refer to the list of references appended to this paper.



- (a) Plane strain plastic deformation at the tip of a crack under fixed load.
- (b) Representation of crack-tip plasticity by dislocation arrays.
- (c) Representation of crack-tip plasticity by a superdislocation pair confined to slip planes emanating from the crack tip.
- (d) Representation of crack-tip plasticity during fatigue by superdislocations.
- (e) Representation of crack-tip plasticity during fatigue by combination of superdislocations and super-superdislocations.

FIG. 1—Evolution of a fatigue crack growth model using the inclined strip-yield superdislocation representation of crack-tip plasticity.

components (for example, the super-superdislocation concept) of the complete cycle-by cycle fatigue crack propagation model.

Figure 1a shows a typical plastic enclave surrounding a crack tip under plane-strain conditions. Figure 1b shows an equivalent way of characterizing

crack-tip plasticity through the use of dislocation arrays. While there is no significant advantage, in general, of the dislocation point of view over the conventional continuum approach, the dislocation concept can be reduced to a simpler way of looking at the problem. This can offer significant computational advantages in applications to fracture and fatigue. In particular, by representing crack-tip plasticity by planar (one-dimensional) dislocation arrays in a strip-yield zone model, considerable mathematical simplification can be obtained without sacrificing too much accuracy. This fact is the prime motivation for adopting a dislocation-based approach here.

Strip-yield zone characterizations of crack-tip plasticity are most easily made if the dislocation array is confined to the plane of the crack. While reasonably accurate for the plane-stress conditions existing in a thin section, this is a poor representation for plane-strain conditions where, as indicated in Fig. 1a, plasticity tends to spread out in the direction normal to the crack plane. To characterize the latter case, Bilby and Swinden [2] took the dislocation slip plane to be inclined to the crack plane. But they were then able to obtain only an approximate numerical solution.

Atkinson and Kay [3] circumvented the mathematical difficulties in the Bilby-Swinden model by introducing the idea of a superdislocation. As shown in Fig. 1c, the superdislocation is considered to be a dislocation of arbitrary strength on a given slip plane that represents the net effect of the entire plastic zone. By the superdislocation approach, the problem is reduced to two algebraic equations in two unknowns. It is important to recognize that, although this simple representation has its limitations (for example, in predicting the plastic zone size), it offers a very accurate prediction of the crack-tip crack-opening displacement. This has been shown by Atkinson and Kanninen [1] by comparison with fully elastic-plastic finite-element computations made for small-scale yielding conditions.

The ultimate goal of the work described in this paper is to develop a computational model that can be applied to predict fatigue crack growth rates in actual service conditions. This calls for a mathematical model that is versatile enough to accept essentially random changes in the cycle-to-cycle applied loadings. At the same time, it must be simple enough to be applied to lengthy load histories. The work reported here has progressed far enough to make it clear that a model in which one superdislocation pair is generated and retained in the computation for each and every load cycle considered, as shown in Fig. 1d, can satisfy only the first of these requirements. However, a modification to represent the residual plasticity in the wake of the crack by lumping several superdislocations into one or more single degree of freedom super-superdislocations will reduce the computational effort required. This can allow the model to achieve the second criterion. Figure 1e shows the modified cycle-by-cycle computational model.

### Analysis Procedure

#### Basic Equations for the Model

The derivation of the basic equations for the inclined strip yield superdislocation model and its use in a predictive model for fatigue crack growth under arbitrary spectrum loading has been given by Atkinson and Kanninen [1]. For this reason, it need be outlined only briefly here.

The approach followed in developing the basic equations for the model is completely within the linear theory of elasticity. The reason is that crack-tip plasticity is represented by discrete singularities (dislocations). The most convenient representation is the complex variable method of Muskhelishvili in which the stress and displacement fields are given by

$$\sigma_{xx} + \sigma_{yy} = 4 \operatorname{Re} \{ \phi'(z) \} \quad (1)$$

$$\frac{1}{2}(\sigma_{yy} - \sigma_{xx}) + i\tau_{xy} = \bar{z} \phi''(z) + \psi'(z) \quad (2)$$

$$\frac{E}{1+\nu} (u_1 + iu_2) = \kappa\phi(z) - \overline{z\phi'(z)} - \overline{\psi(z)} \quad (3)$$

where

- $\sigma_{xx}, \sigma_{yy}, \sigma_{xy}$  = stress components,
- $u_1, u_2$  = displacement components,
- Re = real part of a complex function,
- $\phi, \psi$  = functions of the complex variable  $z = x + iy$  that depends on the boundary conditions, and
- $E$  = elastic modulus.

$$\kappa = \begin{cases} 3 - 4\nu, & \text{plane strain} \\ \frac{3 - \nu}{1 + \nu}, & \text{plane stress} \end{cases} \quad (4)$$

where  $\nu$  is Poisson's ratio.

The technique used for determining the solution to the problem employs linear superposition of potential functions valid for an infinite domain that satisfy the boundary conditions for four subproblems. These four subproblems are

1. Remotely applied uniform stress (for example, uniaxial tension, biaxial tension, shear) for an infinite domain without cracks.
2. A crack with surface tractions equal and opposite to the remotely applied stresses.

3. Isolated dislocation pairs in an infinite medium.

4. A crack with surface tractions equal and opposite to the stresses arising from the dislocation pairs.

Note that, in both crack solutions, there is a singularity at the crack tip. Because the form of the singularity is the same in each case (that is,  $r^{-1/2}$  where  $r$  is the radial distance from the crack tip), these can be made to cancel, if desired.

The key element in the approach is the use of a single superdislocation pair (in the case where the deformation is symmetric with respect to the crack plane) to present the plastic zone in each load cycle. This requires only two new unknowns to be determined in each load cycle: the strength and the position of one of the superdislocations in the pair. The unknowns are partly determined by imposing a force equilibrium condition for shear along the superdislocation's slip plane. Consider the simple situation where a uniform tensile stress  $\sigma$  acts in the direction normal to a crack of length  $2a$ . Then, for plane-strain conditions, the equilibrium equation for each of the  $M$  superdislocation pairs which might exist at some point in the computation (for example, after  $M$  load cycles with no super-superdislocations) are expressed as

$$\tau_i = \sigma h_n + \frac{E}{8\pi(1 - \nu^2)} \sum_{j=1}^M b_j (g_{jn} + k_{jn}) \quad n = 1, 2, \dots, M \quad (5)$$

where the  $b_j$ s are the strengths of the  $M$  superdislocations and  $\tau_i$  is an internal friction stress that opposes dislocation motion. ( $\tau_i$  will be related to the tensile yield stress later.) The undefined quantities in Eq 5 are complex functions of the dislocation positions indicated in Fig. 2. Because these expressions are rather lengthy, they have been relegated to the appendix. Their complete derivation is given in Ref 1.

*Relation Between the Singularity Canceling Equation and Crack Closure*

The role of the singularity canceling equation is an important one in this work. To show this, an expression can be derived for the combined strength of the singular term. Because of the general relation that exists between the strain energy release rate  $\mathcal{G}$  and the stress intensity factor  $K$ , that is, for plane strain  $K^2 = E\mathcal{G}/(1 - \nu^2)$ , it is found that

$$\mathcal{G} = \frac{1 - \nu^2}{E} \pi a \left[ \sigma - \frac{E}{8\pi(1 - \nu^2)} \frac{1}{a} \sum_{j=1}^M b_j f_j \right]^2 \quad (6)$$

where, as shown in the Appendix,  $f_j$  is also a complex function of the dislocation positions. Thus, to cancel the singularity, the bracketed term is set equal to zero. This gives

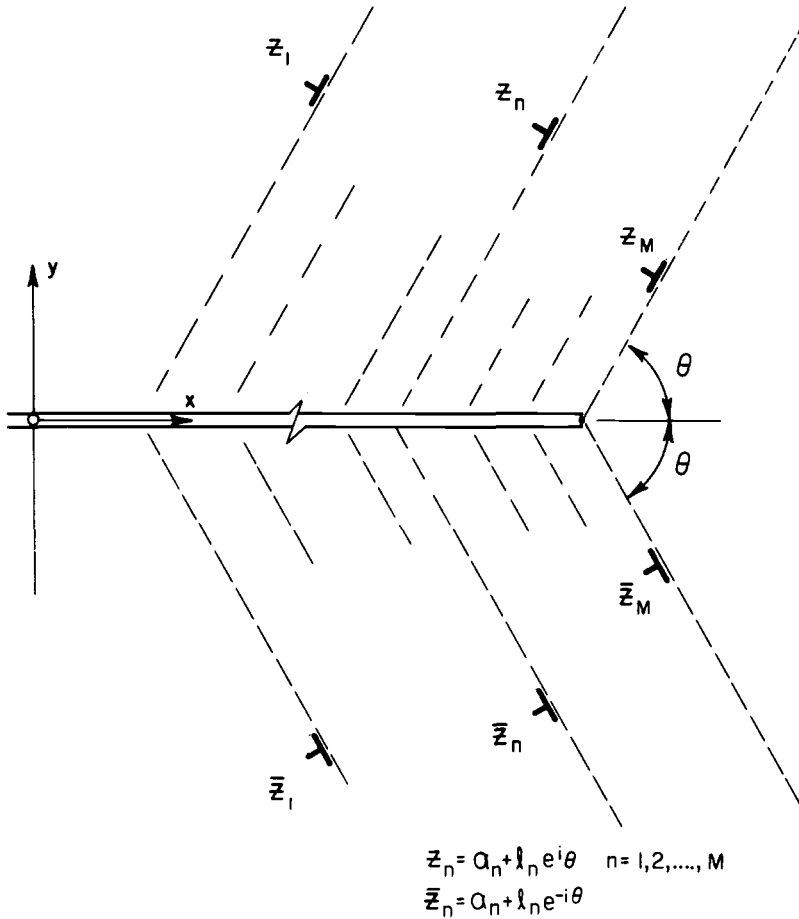


FIG. 2—Dislocation positions for multicycle loading.

$$\sigma a = \frac{E}{8\pi(1 - \nu^2)} \sum_{j=1}^M b_j f_j \tag{7}$$

Note that, as a direct consequence of Eq 7,  $\mathcal{G}$  becomes zero when the crack-tip singularity is abolished.

In fracture mechanics,  $\mathcal{G}$  has the physical interpretation of being the driving force for crack advance. Consequently, allowing crack growth to occur with  $\mathcal{G}$  equal to zero—as is the case when Eq 7 is imposed during the maximum load in a fatigue cycle—is inconsistent with the basic notions of fracture mechanics. This inconsistency is not resolved completely in the present model as it has been necessary to enforce this condition. The singularity canceling equation

is also enforced at the minimum load. However, this is quite appropriate because the singularity canceling equation can be identified readily with crack closure under a nonzero load in the decreasing load portion of a cyclic loading sequence. This can be seen in connection with the crack-face displacements as follows.

An expression for the crack-face displacements is derived in Ref 7 and given in the Appendix as Eq 18. Now, let the distance from the crack tip be given by  $r = a - x$  and consider that  $r \ll a$ . Equation 18 can then be written

$$u_2(r) = r^{1/2} \left\{ 8\sigma \frac{(1 - \nu^2)}{E} \left(\frac{a}{2}\right)^{1/2} - \frac{2}{\pi} \sin \theta \cos \frac{\theta}{2} \sum_{j=1}^M b_j D_j \right\} \quad (8)$$

where the  $D_j$ s are related to the quantity given in Eq 19 in the Appendix. If the distances of the superdislocations from the crack plane along their slip planes are denoted as  $l_j$ , then small-scale yielding can be approximated by taking  $l_j \ll a$ . The right-hand side of the Eq 8 can then be expanded in powers of  $r$  and found to be

$$u_2(r) = r^{1/2} \left\{ 8\sigma \frac{(1 - \nu^2)}{E} \left(\frac{a}{2}\right)^{1/2} - \frac{6}{\pi} \sin \theta \cos \frac{\theta}{2} \sum_{j=1}^M \frac{b_j}{l_j^{1/2}} \right\} + O(r^{3/2}) \quad (9)$$

It can be readily shown that, for small-scale yielding conditions, the coefficient of the  $r^{1/2}$  term in Eq 9 is just the singularity canceling equation. Consequently, satisfying the singularity canceling equation removes the  $r^{-1/2}$  dependence from the slope of the displacements and forces the crack faces to close smoothly at the crack tip with no interpenetration. Because this is a necessary condition for crack closure, imposing Eq 7 in a cyclic loading sequence will take the crack-closure condition into account.

#### *The Crack Growth Criterion*

As already demonstrated, the displacement field associated with the superdislocation-crack interaction distorts the crack-opening displacement in the proximity of the crack tip. This allows the possibility of crack closure under positive load. At the same time, an intrusion into the unbroken material at the crack tip is predicted. This can be taken as a measure of the crack advance increment in the load cycle. The latter effect arises from the displacement discontinuity associated with the dislocation intersecting the crack at its tip giving a "sliding-off" region there.

Because the magnitude of the displacement discontinuity is just equal to the superdislocation strength, the crack growth rate can be simply related to the strength of the most recently emitted superdislocation. Hence, the crack growth at the  $N$ th cycle of loading is given by

$$(\Delta a)_N \equiv \left( \frac{da}{dn} \right)_N = b_N \cos \theta \quad (10)$$

where, as shown in Fig. 2,  $\theta$  is the angle between the superdislocation slip plane and the crack plane. As described in Ref 1, by taking the slip plane to be the plane of maximum shear, it is found that  $\theta = \cos^{-1}(1/3) = 70.3$  deg. This is the value used in the present work.

### The Solution Procedure

The solution procedure involves an iterative technique to determine the superdislocation strengths and positions in each load cycle. This is done currently by solving the system of nonlinear algebraic equations given by Eqs 5 and 7. A Runge-Kutta method is used. Having the solution, the crack growth increment is obtained from Eq 10. Therefore, it can be recognized that no arbitrary disposable parameters are introduced in order to determine the crack growth rates. The only parameters that enter the computation are the ordinary mechanical properties of the material being considered in addition, of course, to the cyclic load history.

The iterative procedure used to determine the equilibrium dislocation positions considers that an internal friction stress  $\tau_i$  acts along the slip plane so as to always oppose dislocation motion. The net stress  $\tau_n$ , given by the right-hand side of Eq 5, can be considered to push the  $n$ th dislocation along the slip plane. If a positive force is one that acts away from the crack plane and a negative force one that acts toward the crack plane,  $F_n$ , the driving force for dislocation motion, can be expressed as

$$F_n = \begin{cases} 0, & |\tau_n| \leq \tau_i \\ \tau_n - \text{sgn}(\tau_n)\tau_i, & |\tau_n| \geq \tau_i \end{cases} \quad (11)$$

where  $\tau_i$  is taken to be a material constant related to the yield stress,  $Y$  (that is,  $\tau_i = Y/\sqrt{3}$ ) and  $\text{sgn}(x) = x/|x|$ . Note that the friction force resisting movement back towards the crack tip need not (and probably is not) equal to that resisting motion outwards. But, this does not come into play under ordinary load histories.

Consider that  $M - 1$  superdislocation pairs have been generated in  $M - 1$  load cycles where  $M > 1$ . The computation for the  $M^{\text{th}}$  load cycle then starts by setting the applied load to  $\sigma = (K_{\text{max}})_M / (\pi a)^{1/2}$  and considering that a nascent dislocation exists at the crack tip. An equilibrium solution is determined that all dislocations move along the slip plane at a speed that is proportional to the net force acting on them; that is,

$$\frac{dl_n}{dt} = F_n \quad n = 1, 2, \dots, M$$

where  $F_n$  is given by Eq 11, the  $l_n$ s denote distance along the slip plane and  $t$

is time. Then, the Runge-Kutta method is used to allow the  $M$  superdislocations to move towards their new equilibrium positions. The strength of the nascent superdislocation,  $b_M$ , will be determined in this procedure by satisfying the singularity canceling equation. The strengths of the previously generated superdislocations remain fixed.

The iterative solution procedure will be continued until an equilibrium solution has been achieved. Next, the crack growth increment

$$(\Delta a)_M = b_M \cos \theta$$

will be calculated and the crack length increased to

$$a = a_0 + \sum_{j=1}^M (\Delta a)_j$$

The applied load will then be reduced to  $\sigma = (K_{\min})_M / (\pi a)^{1/2}$ , the secondary superdislocation will appear, an equilibrium solution that satisfies the crack-closure condition determined, and  $b_M$  replaced by  $b_M + b'_M$  at  $l_M$ . This completes the load cycle.

These steps are repeated for each cycle after the first until the specified load history is exhausted. Note that this procedure is exactly the same whether  $K_{\max}$  (and  $K_{\min}$ ) is unchanged from cycle to cycle or whether completely different values are specified in each cycle.

### Computational Results for Constant $\Delta K$ Load Cycles

To test the applicability of the model by comparison with measured crack growth rates, the computational procedure for multicycle loading just described has been used to obtain numerical results for constant  $\Delta K$ . Computations have been performed for both an aluminum and a titanium alloy using the property values given in Table 1. It is believed that the differences between these two sets of values are large enough to test the ability of the model to distinguish between different materials.

Example calculated crack growth rates for the titanium alloy are shown in Fig. 3. These are for three different values of  $\Delta K = K_{\max} - K_{\min}$  with  $R = K_{\min} / K_{\max} = 0.5$ . The most important feature of the results shown in Fig. 3 is that, while an accelerated growth is evident in the first few cycles, the growth rate quickly levels off to a constant rate characteristic of the  $\Delta K$  value applied. This feature is in good qualitative agreement with observations of fatigue crack growth. Quantitative comparisons based on the steady-state growth rates for both the titanium alloy and the aluminum

TABLE 1—Material properties used in computation of fatigue crack propagation.

Material Simulated	$E$ , ksi	$\nu$	$Y$ , ksi
2024-T3 Aluminum	10 000	0.34	52.5
Ti-6Al-4V	16 000	0.33	120

alloy are shown in Figs. 4 and 5, respectively. Comparison is made with the experimental data of Feddersen et al [4,5] on titanium and of Hudson [6] on aluminum. On the basis of the agreement evident in these two figures, it is believed that the model has proven to be more than adequate, particularly in view of the fact that no arbitrary factors have been introduced to adjust these results.

It is also of interest to determine the relative importance of each of the material property parameters that enter into the crack growth rate cal-

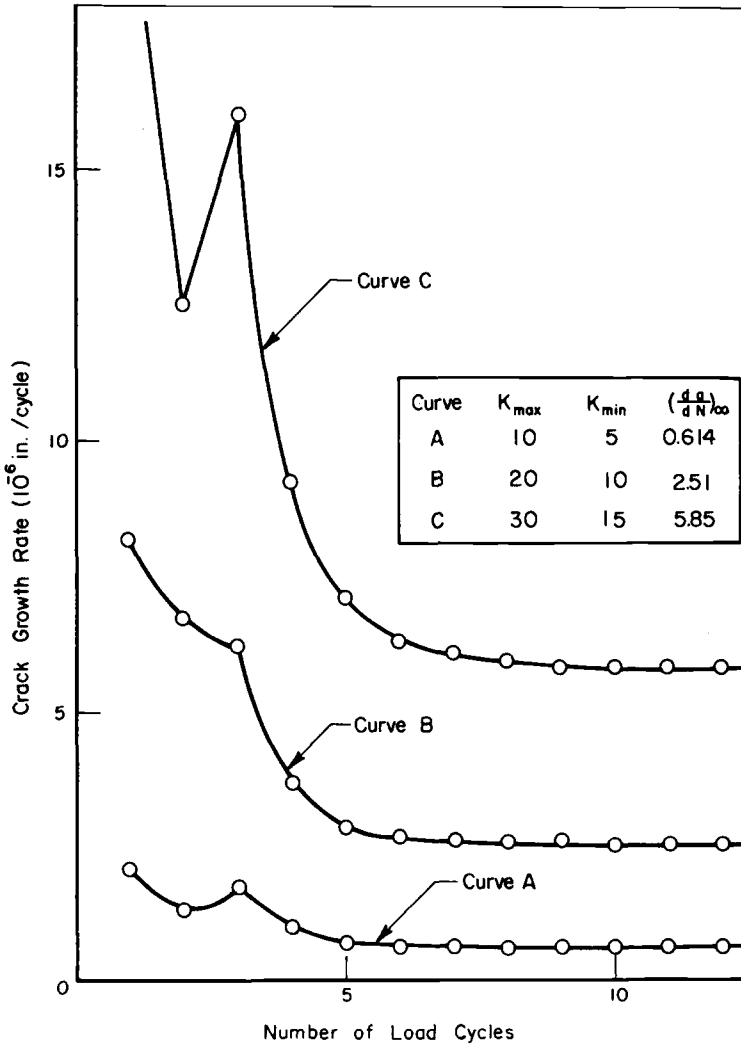


FIG. 3—Computational results for fatigue crack growth in titanium using inclined strip yield super dislocation model for  $R = 0.5$ .

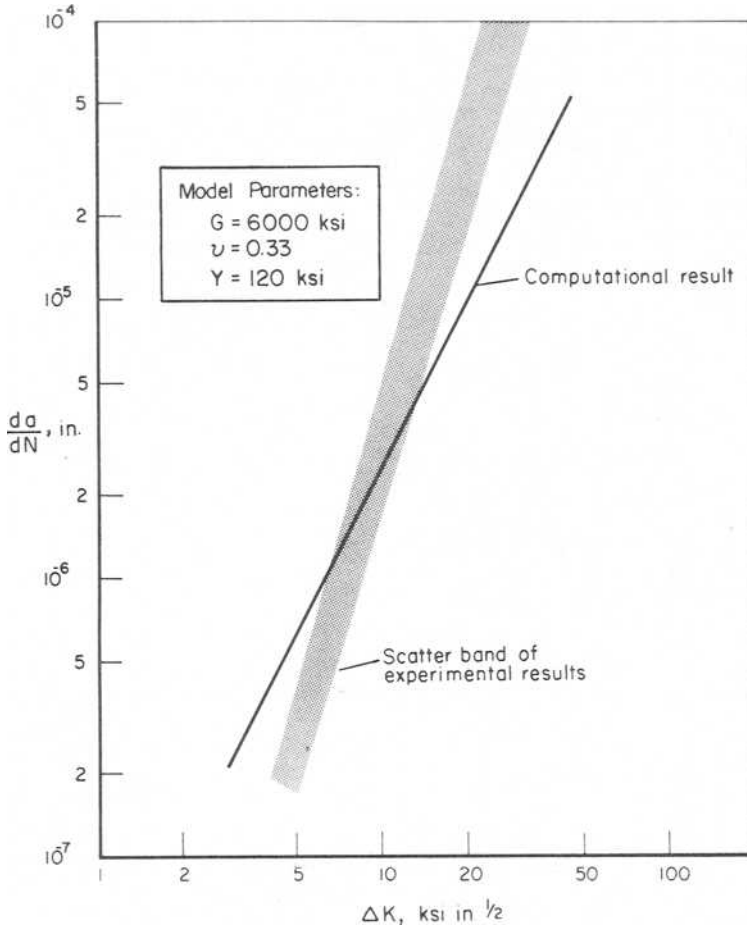


FIG. 4—Computational results for fatigue crack propagation in titanium for steady-state conditions with  $R = 0.5$  and comparison of experimental results of Feddersen et al [4,5].

culations. From consideration of the basic equations of the model, Poisson's ratio can be seen to have little effect. So, only  $E$  and  $Y$  need to be varied. This has been done by taking the particular values used for the aluminum and titanium simulations and interchanging them. The results demonstrate a  $(EY)^{-1}$  dependence of the fatigue crack growth rates in the cycle-by-cycle computations.

For reasons that are not entirely clear at this point, computations made for the special case where  $R = K_{\min}/K_{\max} = 0.5$  are in better agreement with the experimental data than are the computations made for other  $R$  values. This is true for both the aluminum and the titanium calculations for a range of  $\Delta K$  values. Thus, while the calculations do show both an

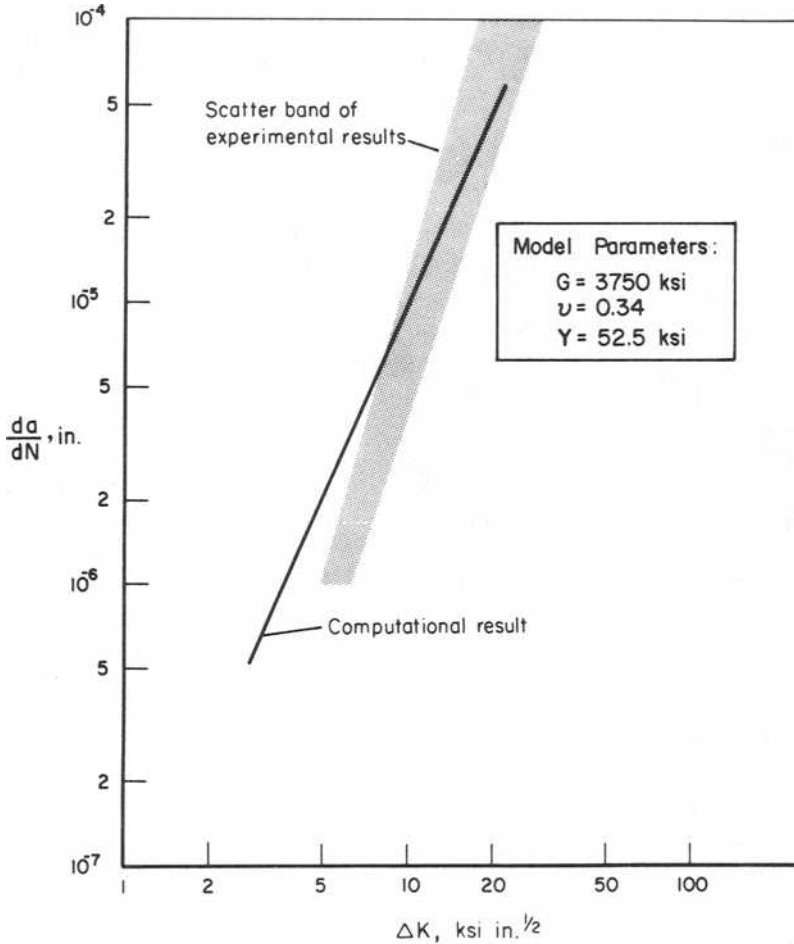


FIG. 5—Computational results for fatigue crack propagation in 2024-T3 aluminum for steady-state conditions with  $R = 0.5$ .

$R$  effect and a load interaction effect in nonconstant-amplitude cycling, in neither case are the results satisfactory as yet. These are probably connected so that the remedy for one will likely make a substantial improvement in the other. A number of options are open to which improvement of the model can be made, and subsequent work is planned to achieve these improvements.

#### Discussion and Comparison with Alternative Approaches

Conceptually, the analytical approach developed in this paper stands somewhere between the approximate semiempirical treatments of Wheeler

[7] and of Willenborg et al [8], on the one hand, and the more precise, but cumbersome, finite-element elastic-plastic computation of Newman and Armen [9] on the other. To put the present model into somewhat better perspective, the four classes of techniques for fatigue crack growth prediction that can be identified on the basis of their treatment of crack-tip plasticity are given in Table 2. In addition to Refs 7-9, the work of Elber [10], Rice [11], Weertman [12], and Bilby and Heald [13] are included in this categorization. Other models which might be mentioned are those of Yokobori and Yoshida [14] and Neumann [15]. While these have some resemblance to the present work, they have not exploited the potential of this approach to the extent given in this paper.

The model described in this paper allows an estimate of the plastic flow at each stage in a reasonably simple way using the superdislocation idea. This allows a look at cycle-by-cycle growth with residual plasticity left behind from previous cycles still playing a role. Thus, a sequential calculation can be made in a logically self-consistent manner. The main general criticism that can be leveled at this approach is that the superdislocation is an oversimplification of the plastic field which may limit the chances of the present model exhibiting the trends usually observed in experiments on fatigue. In fact, the present results do not agree entirely with the experiments. However, this is believed to be due to the details contained in the present model rather than to the overall philosophy.

With the complete model, a strictly logical game is played, with the results being a direct consequence of the growth criterion and the variety of stress interactions occurring between the dislocations and the crack. As one highly significant result, the cycle-by-cycle calculations do predict a steady-state crack growth rate with  $\Delta K$  constant. Without discussing possible changes that could be made in the model, consider the computational results in terms of a simple-minded view of the steady-state situation as applied to the current model. At the  $\sigma_{\min}$  load, the crack closes at the crack tip after advance. The superdislocation on the crack-tip slip band changes its strength or position or both to accommodate this condition as well as being in equilibrium. Thus, when  $\sigma_{\max}$  is applied, it is acting on a residual stress that just balanced  $\sigma_{\min}$ . Hence, an effective stress of  $(\sigma_{\max} - \sigma_{\min})$  can be considered to be acting. This is proportional to  $\Delta K = K_{\max} - K_{\min} = \sqrt{\pi a} (\sigma_{\max} - \sigma_{\min})$ . It is then expected from the linearized results, where the crack-tip crack-opening displacement is proportional to  $K^2$ , that the steady-state crack growth rate will be proportional to  $(\Delta K)^2$ .

This argument, of course, neglects any effect that neighboring dislocations have on the current one being emitted from the crack tip so that this result is only approximate. But the current computational results are quite close to the results suggested by this simple argument. Hence, the numerical results for the model demonstrate that retaining dislocations in the wake of a crack will in fact lead to a steady-state growth rate which is approxi-

TABLE 2—Analytical procedures for the predictions of fatigue crack growth under spectrum loading.

Technique	Investigators	Strong Points	Weak Points
Semiempirical extensions of linear elastic fracture mechanics	Wheeler [7], Willenborg, Engle and Wood [8], Elber [10]	Gives simple relations that are easy to apply; offers insight into controlling mechanisms	Lack of firm fundamental basis; difficulty in treating complicated histories; cannot easily be generalized
Dugdale strip yield model with cumulative crack-opening displacement criterion	Rice [11], Weertman [12], Bilby and Heald [13]	Gives closed-form result for steady-state growth rate	Cannot distinguish load history effects; crack closure does not occur
Inclined strip-yield superdislocation model with critical crack-opening displacement criterion	this paper	Plastic deformation in different load cycles is distinguishable; closure effects handled directly; can be generalized to treat wide range of situations	Computations for complicated load histories may require lengthy computation
Elastic-plastic finite-element analysis	Newman and Armen [9]	Highly accurate; can be used to treat wide variety of situations; useful for examining details of crack growth process	Very time-consuming computations so only a few load cycles can be treated; crack extension criterion must be arbitrary

← Accuracy / Convenience →

mately proportional to  $(\Delta K)^2$  even when all the dislocation stress fields are currently taken into account.

No previous models have shown this type of growth rate law with a self-consistent logical scheme in which the process of producing plastic deformation is followed through in a sequential way. It might be emphasized that the model demonstrates a deviation from the  $(\Delta K)^2$  law which depends precisely on the dislocation interactions (the model of the plastic field). Thus, even though the precise form of the complete numerical results do not always show the desired experimental trend, modifications can clearly be made in order to bring the model into better correspondence with experimental results.

### Conclusions

The analytical approach taken in this work rests on two fundamental assumptions. The first is that the crack-tip crack-opening displacement arising from the intense plastic deformation attending the crack tip is the parameter that governs crack growth. The second is that the interaction between the plastic deformation created in different load cycles can be represented by an inclined strip-yield superdislocation model. The approach taken here therefore uses what is perhaps the simplest mathematical model in which these considerations (that is, crack-tip crack-opening displacement and distinguishable plastic zones in each load cycle) can be taken into account in a rigorous fashion. There are two additional features on the model that make its use attractive. First, the sliding off at the crack tip gives rise to a crack-tip crack-opening displacement which suggests a value for the increment of crack advance per load cycle. Second, crack closure, if it is to occur, will occur naturally in this model and need not be imposed arbitrarily. The results obtained for two different materials indicate that the approach is quite reasonable.

### Acknowledgments

This work was supported by the Structures Research Branch of the Naval Air Development Center through Contract Number N62269-73-C-0664 and N62269-74-C-0618. The authors would like to thank Dr. E. McQuillen, Dr. S. Huang, and P. Kozel of that agency for their support of this work. Thanks are also due to Dr. G. T. Hahn of Battelle's Columbus Laboratories for his helpful comments and advice and to Dr. Carl Popelar of The Ohio State University for his assistance with the analysis.

## APPENDIX

### Basic Relations Used in the Inclined Strip-Yield Zone Superdislocation Model

#### Singularity Canceling Equation

$$\sigma a = \frac{E}{8\pi(1-\nu^2)} \sum_{n=1}^M b_n f_n \quad (12)$$

where

$$f_n = 4 \sin \theta \left[ \operatorname{Re} \left\{ \frac{(Z_n^2 - a^2)^{1/2}}{Z_n - a} \right\} + a \ln \operatorname{Re} \left\{ \frac{e^{i\theta}}{(Z_n - a)(Z_n^2 - a^2)^{1/2}} \right\} \right] \quad (13)$$

#### Force Equilibrium Equation

$$\tau_i = \sigma h_n + \frac{E}{8\pi(1-\nu^2)} \sum_{j=1}^M b_j (g_{jn} + k_{jn}) \quad (14)$$

$n = 1, 2, \dots, M$

$$h_n = \sin \theta \left[ \cos \theta + a^2 \ln \operatorname{Re} \left\{ \frac{e^{2i\theta}}{(Z_n^2 - a^2)^{3/2}} \right\} \right] \quad (15)$$

$$k_{jn} = \begin{cases} -\frac{1}{l_n} \cos 2\theta, & j = n \\ -\operatorname{Re} \left\{ e^{2i\theta} \left[ \frac{e^{i\theta}(Z_j - \bar{Z}_n) + e^{-i\theta}(Z_j - Z_n)}{(Z_j - Z_n)^2} \right. \right. \\ \left. \left. - \frac{e^{i\theta}(Z_j - Z_n) + e^{-i\theta}(Z_j - \bar{Z}_n)}{(Z_j - \bar{Z}_n)^2} \right] \right\} & j \neq n \end{cases} \quad (16a)$$

$$g_{jn} = 2l_j \sin^2 \theta \operatorname{Re} \left[ \frac{e^{2i\theta}}{((Z_j^2 - a^2)^{1/2})} \left\{ -\frac{2Z_j^2 + a^2}{2(Z_j^2 - a^2)^{3/2}} + \frac{Z_j(\bar{Z}_j - a^2)^{1/2}}{(Z_j^2 - a^2)(Z_j - Z_j)} \right. \right.$$

$$\left. \left. + \frac{(\bar{Z}_j - a^2)^{1/2} - (Z_j^2 - a^2)^{1/2}}{(Z_j - \bar{Z}_j)^2} \right\} + \frac{l_j e^{2i\theta}}{(Z_j^2 - a^2)^{1/2}} \left\{ -\frac{a^2 Z_j e^{i\theta}}{(Z_j^2 - a^2)^{5/2}} \right. \right.$$

$$\begin{aligned}
 & + \frac{e^{-i\theta}}{(Z_j - \bar{Z}_j)^2 (\bar{Z}_j^2 - a^2)^{1/2}} \left\{ \frac{a^2(Z_j - \bar{Z}_j)}{Z_j^2 - a^2} + 2 \right. \\
 & \left. \frac{(Z_j^2 - a^2)^{1/2} (Z_j^2 - a^2)^{1/2} + a^2 - Z_j \bar{Z}_j}{Z_j - \bar{Z}_j} \right\} \Bigg\} j = n \tag{16b} \\
 g_{jn} = & 2l_n \sin^2 \theta \operatorname{Re} \left\{ \frac{e^{2i\theta}}{(Z_n^2 - a^2)^{1/2}} \left\{ \frac{(Z_j^2 - a^2)^{1/2} - (Z_n^2 - a^2)^{1/2}}{(Z_n - Z_j)^2} \right. \right. \\
 & + \frac{(Z_j^2 - a^2)^{1/2} - (Z_n^2 - a^2)^{1/2}}{(Z_n - \bar{Z}_j)^2} + \frac{Z_n}{Z_n^2 - a^2} \left[ \frac{(Z_j^2 - a^2)^{1/2}}{Z_n - Z_j} + \frac{(Z_j^2 - a^2)^{1/2}}{Z_n - \bar{Z}_j} \right] \Bigg\} \\
 & + \frac{l_j e^{2i\theta}}{(Z_n^2 - a^2)^{1/2}} \left\{ \frac{e^{i\theta}}{(Z_n - Z_j)^2 (Z_j - a^2)^{1/2}} \left[ \frac{a^2(Z_n - Z_j)}{Z_n^2 - a^2} \right. \right. \\
 & + 2 \frac{(Z_n^2 - a^2)^{1/2} (Z_j^2 - a^2)^{1/2} + a^2 - Z_j Z_n}{Z_n - Z_j} \\
 & + \frac{e^{-i\theta}}{(Z_n - \bar{Z}_j)^2 (\bar{Z}_j^2 - a^2)^{1/2}} \left[ \frac{a^2(Z_n - \bar{Z}_j)}{Z_n^2 - a^2} \right. \\
 & \left. \left. + 2 \frac{(Z_n^2 - a^2)^{1/2} (Z_j^2 - a^2)^{1/2} + a^2 - \bar{Z}_j Z_n}{Z_n - \bar{Z}_j} \right] \right\} \Bigg\} j \neq n \tag{17}
 \end{aligned}$$

*Crack-Opening Displacements*

$$u_1 = 4\sigma \frac{(1 - \nu^2)}{E} (a^2 - x^2)^{1/2} + \sin \theta \sum_{j=1}^M b_j d_j \tag{18}$$

in which  $x$  is measured from the center of the crack and

$$\begin{aligned}
 d_j = & 2\delta(a_j - |x|) - \frac{4}{\pi} l_j (a^2 - x^2)^{1/2} \operatorname{Re} \left\{ \frac{Z_j e^{i\theta}}{(Z_j^2 - a^2)^{1/2} (Z_j^2 - x^2)} \right\} \\
 & + \frac{1}{\pi} \operatorname{Im} \left\{ \log \left[ \frac{a^2 - xZ_j + i(Z_j^2 - a^2)^{1/2} (a^2 - x^2)^{1/2}}{a^2 - xZ_j - i(Z_j^2 - a^2)^{1/2} (a^2 - x^2)^{1/2}} \right] \right\} \\
 & + \log \left[ \frac{a^2 + xZ_j + i(Z_j^2 - a^2)^{1/2} (a^2 - x^2)^{1/2}}{a^2 + xZ_j - i(Z_j^2 - a^2)^{1/2} (a^2 - x^2)^{1/2}} \right] \Bigg\} \tag{19}
 \end{aligned}$$

where  $\delta =$  Dirac delta function defined as

$$\delta(x) = \begin{cases} 0, & x \neq 0 \\ 1, & x = 0 \end{cases}$$

In these relations,  $Z_j = a_j + l_j e^{i\theta}$  denotes the position of the  $j^{\text{th}}$  superdislocation. Hence,  $a_j$  is the distance from the center of the crack to the intersection of the  $j^{\text{th}}$  slip plane and the crack plane,  $l_j$  is the distance from the crack plane to the superdislocation position measured along the slip plane, and  $\theta$  is the angle between the crack plane and the slip plane. The parameter  $a$  (without subscript) denotes the distance from the center of the crack to the actual crack tip.

## References

- [1] Atkinson, C. and Kanninen, M. F., "A Simple Representation of Crack-Tip Plasticity: The Inclined-Strip-Yield-Superdislocation Model," *International Journal of Fracture Mechanics*, Vol. 13, 1977, p. 151.
- [2] Bilby, B. A. and Swinden, K. H., *Proceedings*, Royal Society, Vol. 22, 1965, p. A285.
- [3] Atkinson, C. and Kay, T. R., *Acta Metallurgica*, Vol. 19, 1971, p. 679.
- [4] Feddersen, C. E. and Hyler, W. S., "Fracture and Fatigue Crack-Propagation Characteristics of 1/4-Inch Mill-Annealed Ti-6Al-4V Titanium Alloy Plate," Final Report to Naval Air Development Center from Battelle's Columbus Laboratories, Contract No. N00156-C-1336, 1 Nov. 1976.
- [5] Feddersen, C. E., Porfilio, T. L., Rice, R. C., and Hyler, W. S., "Part-Through Crack Behavior in Three Thicknesses of Mill-Annealed Ti-6Al-4V Plate," Final Report to Naval Air Development Center from Battelle's Columbus Laboratories, Contract No. N62269-73-C-0036, 31 Dec., 1972.
- [6] Hudson, C. M., "Effect of Stress Ratios on Fatigue-Crack Growth in 7075-T6 and 2024-T3 Aluminum-Alloy Specimens," NASA TN D-5390, Langley Research Center, Aug. 1969.
- [7] Wheeler, D. E., *Journal of Basic Engineering*, Vol. 94 1972, p.181.
- [8] Willenborg, J., Engle, R. M., Jr., and Wood, H. A., "A Crack-Growth-Retardation Model Using an Effective Stress Concept," AFFDL-TM-71-1-FBR, Air Force Flight Dynamics Laboratory, 1971.
- [9] Newman, J. C., Jr., and Armen, H., Jr., "Elastic-Plastic Analysis of a Propagating Crack Under Cyclic Loading," *AIAA Journal*, American Institute of Aeronautics and Astronautics, 1976.
- [10] Elber, W., *Engineering Fracture Mechanics*, Vol. 2, 1970, p. 37.
- [11] Rice, J. R. in *Fatigue Crack Propagation*, ASTM STP 515, American Society for Testing and Materials, 1967, p. 247.
- [12] Weertman, H., *International Journal of Fracture Mechanics*, Vol. 5, 1969, p. 13.
- [13] Bilby, B. A. and Heald, P. T., *Proceedings*, Royal Society, A305, 1968, p. 429.
- [14] Yokobori, T. and Yoshida, M., *International Journal of Fracture Mechanics*, Vol. 10, 1974, p. 467.
- [15] Neuman, P., *Acta Metallurgica*, Vol. 22, 1974, p. 1167.

# Analysis of Crack Growth Following Compressive High Loads Based on Crack Surface Displacements and Contact Analysis

---

**REFERENCE:** Dill, H. D. and Saff, C. R., "Analysis of Crack Growth Following Compressive High Loads Based on Crack Surface Displacements and Contact Analysis," *Cyclic Stress-Strain and Plastic Deformation Aspects of Fatigue Crack Growth*, ASTM STP 637, American Society for Testing and Materials, 1977, pp. 141-152.

**ABSTRACT:** A method for prediction of crack growth behavior based on analysis of crack surface contact stresses has been extended to include compressive effects. The method is based on evaluations of the effective minimum stress intensity occurring during a load cycle. An analysis of crack surface displacements during loading and unloading is used to determine the permanent plastic deformation left in the wake of the growing crack. Contact stresses are determined by treating the interference as a wedge between the crack surfaces and performing an elastic-plastic analysis of stresses caused by the wedge. Comparisons of predictions with test data show the method can accurately account for the effects of compression loads.

**KEY WORDS:** stresses, strains, crack propagation

A method for prediction of crack growth behavior based on analysis of crack surface contact stresses has been extended to include compressive load effects. The initial development of the method, called the contact stress model, is reported in the reference cited in Footnote 2. The contact stress model is based on evaluations of the effective minimum stress intensity factor occurring during a load cycle. An analysis of crack surface displacements during loading and unloading is used to determine the permanent plastic deformation left in the wake of a growing crack. Contact stresses caused by interference of these permanent deformations at minimum load are determined by treating the interference as a wedge between the crack surfaces and performing an elastic-plastic analysis of stresses caused by

<sup>1</sup>Section chief and senior engineer, respectively, Technology, McDonnell Aircraft Company, St. Louis, Mo. 63166.

<sup>2</sup>Dill, H. D. and Saff, C. R. in *Fatigue Crack Growth Under Spectrum Loads*, ASTM STP 595, American Society for Testing and Materials, 1976, pp. 306-319.

the wedge. The effective minimum stress intensity factor is the sum of the minimum applied stress intensity factor and the stress intensity factor due to these contact stresses. Because the permanent deformations left in the wake of the growing crack preserve a memory of all previous load cycles, the interference, and consequently the effective minimum stress intensity factor, contain the effects of the total load history. Thus, analysis of crack surface contact can account for many of the observed details of crack growth behavior.

Comparison with test and a more detailed description of the model are included in the reference cited in Footnote 2. The comparisons therein show that the contact stress model can accurately account for effects of stress ratio, delayed retardation, increased retardation following multiple high loads, and acceleration during high loads.

Because test results have indicated that compressive loads have significant influence on crack growth interactions, we have initiated a study on the effects of compressive loads on crack growth behavior both with and without high loads. As an initial step in this study, comparisons of contact stress analyses have been made with the compression test data of Hsu and Lassiter.<sup>3</sup> These comparisons indicate the model can accurately account for the effects of compression loads.

### Crack Surface Displacement Analysis

An analysis method has been developed to determine displacements along the crack surfaces caused by loading and unloading during a single load cycle. The displacement analysis is based upon the Dugdale model of the plastic zone, treating the plastic zones as an extension of the elastic crack surface over which a constant yield stress acts. The plastic zone size is determined to be that length of constant yield stress required to produce zero stress intensity for the extended crack. The crack surface displacement at  $K_{max}$  is found from the superposition of the Westergaard solution for elastic displacement near the crack tip, and the displacement due to the constant yield stress of the plastic zone. The Westergaard solution for displacements under remote loading is shown in the upper portion of Fig. 1. The displacements due to the plastic zone stress are presented schematically in the middle portion of Fig. 1, and the sum is shown in the lower portion.

The displacements during unloading are shown in Fig. 2. During unloading, the reversed plastic zone stress is increased to twice the yield stress used during loading, accounting for an elastic stress range equal to the difference of tensile and compressive yield stresses.

The crack surface displacements at the minimum applied load, shown

<sup>3</sup>Hsu, T. M. and Lassiter, L. W., "Effects of Compressive Overloads on Fatigue Crack Growth," AIAA Paper No. 74-365, AIAA/ASME/SAE Structures, Structural Dynamics and Materials Conference, Las Vegas, Nev., 17-19 April 1974.

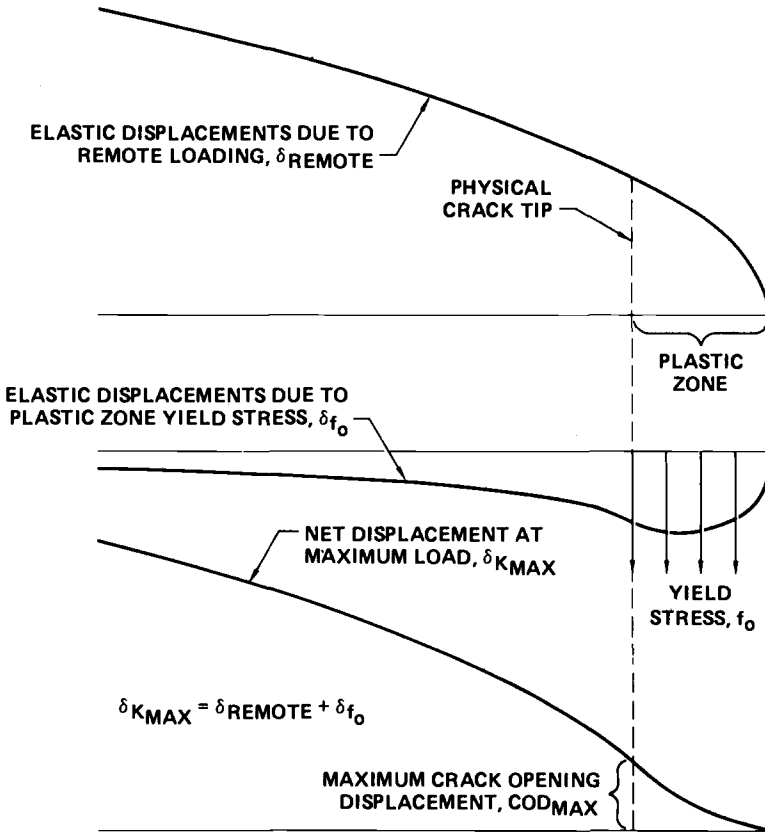


FIG. 1—Elastic crack surface displacement at maximum load.

in Fig. 3, are found by subtracting the displacements occurring during unloading from those at maximum load. The crack surface remains wedged open by the stress distributions within the plastic zone even when the minimum load is zero, if permanent plastic deformations caused by prior crack growth are not considered. The center portion of Fig. 3 shows results of this wedging effect. However, when the permanent plastic deformations are considered, the crack surfaces will interfere upon unloading. The interference is visualized as though the surfaces were allowed to pass through each other. The potential interference of either surface is the displacement of that surface past the centerline of the crack.

In modeling the residual deformation and surface interference, the plastic deformation at the crack tip at minimum load is considered to be equal to the crack opening displacement (COD) at that load. This crack opening displacement for tensile minimum loads is approximated as

$$\text{COD}_{K_{\text{min}}} = \alpha (K_{\text{max}}^2 - 1/2 \Delta K^2) / 2E f_0 \quad (1)$$

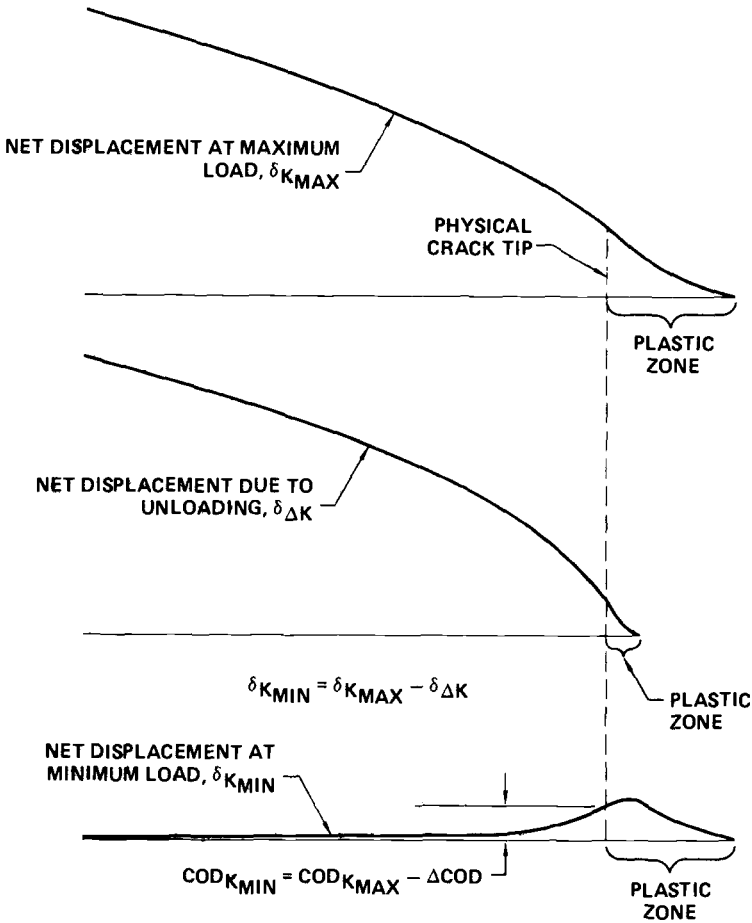


FIG. 2—Elastic crack surface displacement at minimum load.

where

- $\alpha = 1$  for plane stress,
- $\alpha = (1 - \nu^2)/2$  for plane strain,
- $K$  = stress intensity,
- $\Delta K$  = stress intensity range,
- $E$  = Young's modulus, and
- $f_0$  = yield stress.

This deformation exists just behind the crack tip as well since material adjacent to the crack tip, both ahead and behind, is compressed to this value on unloading. Correlation with constant-amplitude closure stress intensity

data from Elber<sup>4</sup> shows that a closer approximation to the permanent plastic deformation is

$$\delta_{\text{residual}} = \alpha (K_{\text{max}}^2 - 0.4 \Delta K^2) / 2E\epsilon_0 \quad (2)$$

where  $\delta$  = crack surface displacement.

The potential interference is the difference between the permanent plastic deformation and the minimum displacement of the elastic surface as shown in Fig. 3.

The potential interference acts as a wedge behind the crack tip, creating a stress intensity at the crack tip. To determine the stresses behind the tip caused by this wedge, a simple contact stress model of closure was developed. This model, symbolized in Fig. 4, uses twenty-five constant stress elements to idealize the wedge. Bueckner's weight function approach<sup>5</sup> was used to develop an influence coefficient matrix for the displacement-stress relationship between elements. The analysis is iterative so that a solution is determined wherein the maximum contact stress is limited to the yield stress and there is no tensile contact stress.

The stresses determined from interference are used to compute the contact stress intensity occurring at zero load, the effective minimum stress intensity, and the effective stress intensity range.

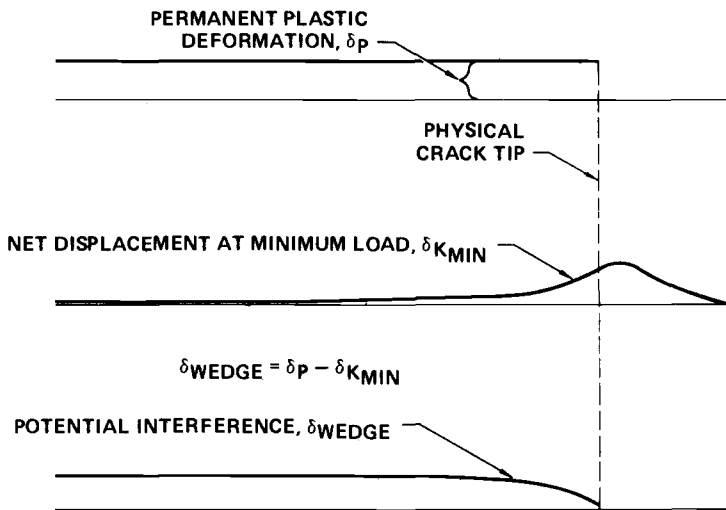
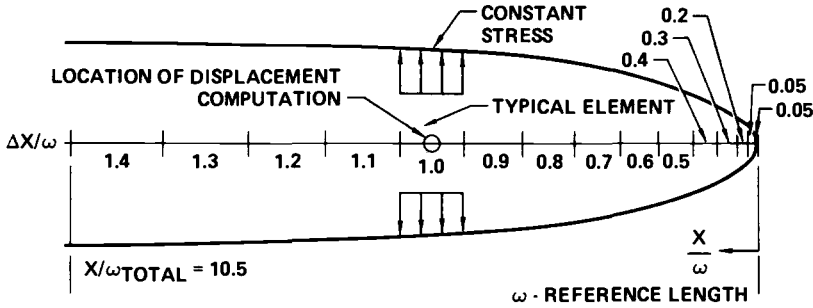


FIG. 3—Potential interference at minimum load under constant-amplitude cycling.

<sup>4</sup>Elber, W. in *Damage Tolerance in Aircraft Structures*, ASTM STP 486, American Society for Testing and Materials, 1971, pp. 230–242.

<sup>5</sup>Bueckner, H. F., *Zeitschrift Fuer Angewandte Mathematik und Mechanik*, Vol. 50, 1970, pp. 529–546.



- 25 x 25 INFLUENCE COEFFICIENT MATRIX DERIVED THROUGH BUECKNER'S WEIGHT FUNCTION APPROACH
- MAXIMUM STRESS LIMITED TO YIELD
- NO TENSILE STRESSES
- DISPLACEMENTS AND STRESS INTENSITY COMPUTED FOR INPUT VALUES OF  $K_{MAX}$ ,  $K_{APP}$ ,  $E$ , AND  $f_0$

FIG. 4—Contact stress model of closure.

### Analysis of COD With Compressive Loads

The Westergaard-Dugdale analysis, including the computation of  $COD_{K_{min}}$  through use of Eq 2, is applicable for minimum loads equal to or greater than zero. However, when the minimum load is less than zero, a portion of the crack surface is in contact, even when permanent plastic deformations caused by crack growth are not considered. In order to compute  $COD_{K_{min}}$  for compression loads, a necessary step in determining the permanent plastic deformation left in the wake of the growing crack, a separate analysis was performed. Ordinarily, the computation of displacements and contact stresses is made with the origin of reference for the contact stress model placed at the physical tip. However, for the analysis of  $COD_{K_{min}}$  for compression loads, the reference origin of the model was placed at the end of the forward plastic zone. Figure 5 depicts the displacements input to the computation. The wedge is composed of the sum of the residual displacements in the forward plastic zone caused by loading and the elastic displacements due to applying the compressive load. This wedge is depicted in the lower portion of Fig. 5, and the resulting displacement and stress distribution is depicted in the bottom of Fig. 5.

The results of this analysis procedure are summarized in Fig. 6. Normalized crack surface displacements are shown for both positive and negative loads. The analyses of positive minimum loads were performed to verify the analysis procedure by comparison to previous Dugdale-Westergaard analysis results. Figure 7 summarizes the COD at minimum load, for various  $R$  ratios. ( $R$  = ratio of minimum to maximum applied load.) It can be seen that there is a rapid decrease in COD for positive  $R$  ratios, as the minimum load is reduced. However, for negative  $R$  ratios, the crack surface contact

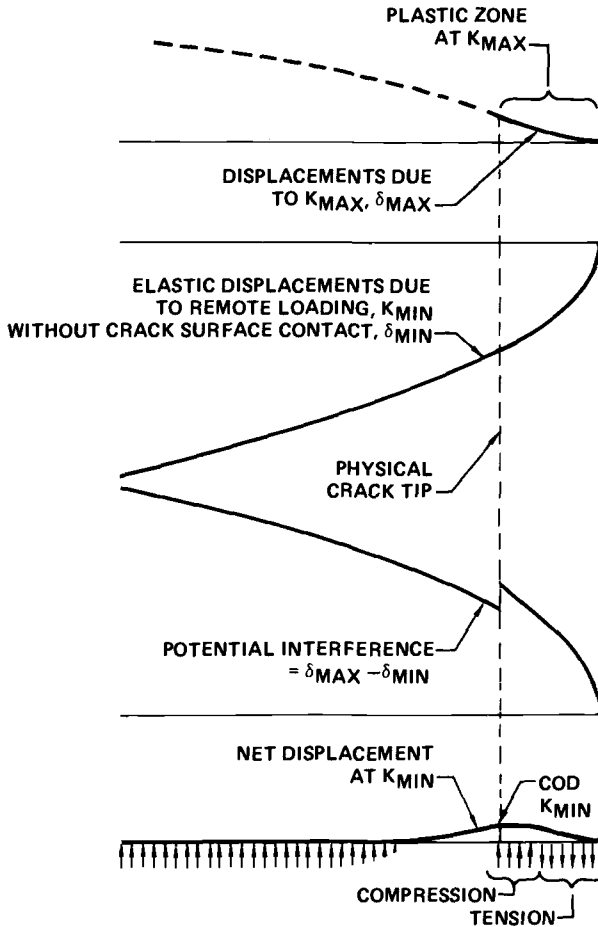


FIG. 5—Computation of crack surface displacements under compression loading.

prevents this decrease in COD from continuing, and, even at  $R = -3.0$ , the COD is greater than half the COD at  $R = 0$ .

With the effects of compression loads upon residual plastic deformation accounted for, analysis of contact stress intensity, including the effects of compression, could be performed in the same manner as under tensile loading.

### Crack Growth Following Compressive High Loads

An excellent test program was conducted by Hsu and Lassiter on Ti-6Al-4V beta annealed titanium and 7050-T73 aluminum plate materials and was reported in the source cited in Footnote 3. Two types of crack geometries shown in Fig. 8 were utilized: center-through-the-thickness crack, and

through-the-thickness crack emanating from one side of a 0.636-cm hole.

An electrodischarge machine was used to introduce the initial notch. The specimens were then precracked with constant-amplitude fatigue cycling until the initial crack lengths were 1.12 cm for the center-crack panels and 0.17 cm for the open-hole panels. The four basic constant-amplitude load spectra are shown in Fig. 9. Each block of loading consisted of 1 overload cycle and 49 cycles of constant-amplitude stress at  $137 \text{ MN/m}^2$  for Ti-6Al-4V specimens and  $68.95 \text{ MN/m}^2$  for 7050-T73 specimens.

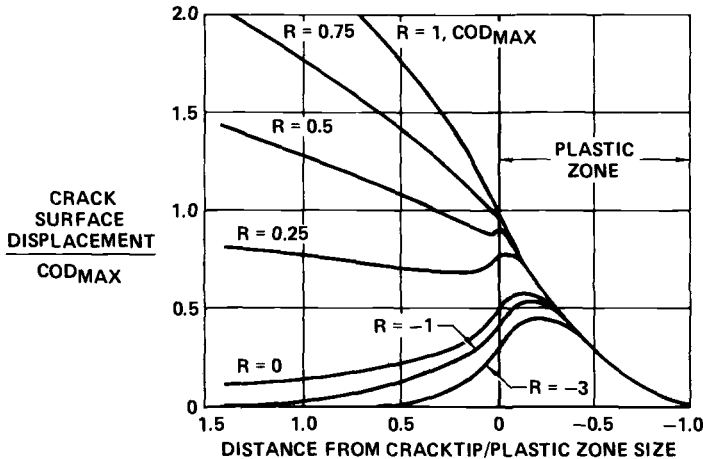


FIG. 6—Crack surface displacements at minimum load.

The high load ratios, defined as the ratio of the tensile stress high load and the constant-amplitude stress load in the Type A spectrum were 1.0, 1.2, 1.5, and 2.0. The high load ratios in the Type B spectrum were 1.2 and 1.5 with  $R = -1.0$  for the tension-compression high load cycle, where  $R$  is the applied stress ratio defined as  $\sigma_{\min}/\sigma_{\max}$ . The sequence of tension-compression cycles used in Type C loading was fully reversed from Type B. The compressive high load ratios applied in the Type D spectrum were  $-1.2$  and  $-1.5$ .

An example of the correlation of contact stress model analysis with experimental results is shown in Fig. 9. Test results shown are typical of results obtained from each test series: Type A spectra having longest lives, Types B and C spectra showing very similar retardation, and Type D having lives slightly shorter than that in constant amplitude. The predictions of the effects of overloads using the contact stress model are dependent upon the plastic zone size assumption. The Type A, 1.5 high load ratio, test data for center-crack panels were used to select zone size assumptions for the aluminum and titanium materials. For the spectra involving tensile overloads, Types A, B, and C, the predicted crack growth in aluminum is slower than that

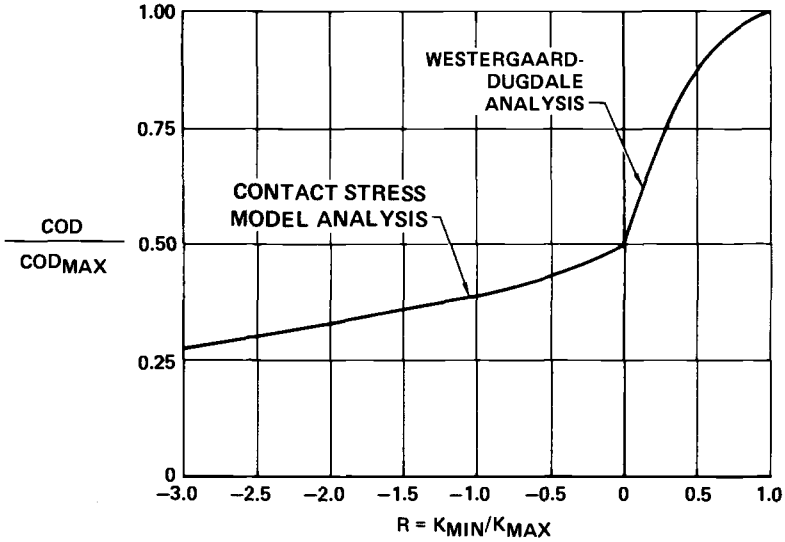


FIG. 7—COD at minimum load.

measured at short crack lengths, and increasing to beyond that measured as crack length increases. The curve shape error is not great, and several possible explanations for this phenomenon exist, including stress level or finite width effects on plastic zone displacements and size.

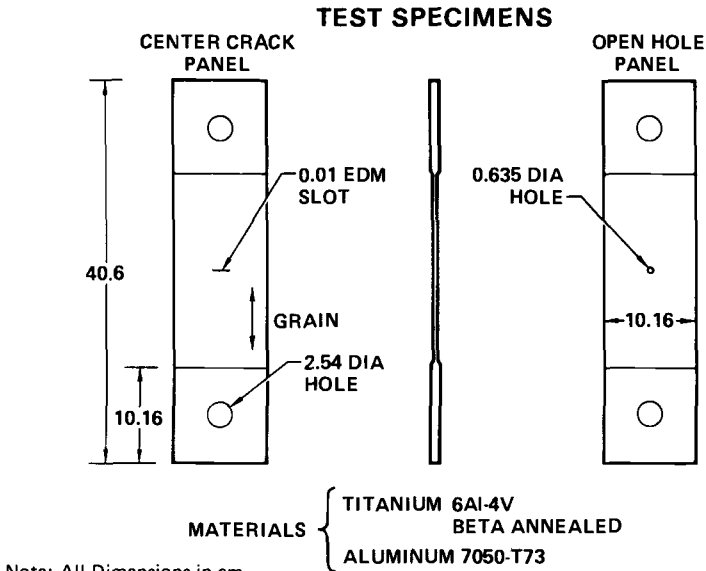


FIG. 8—Specimens and materials.

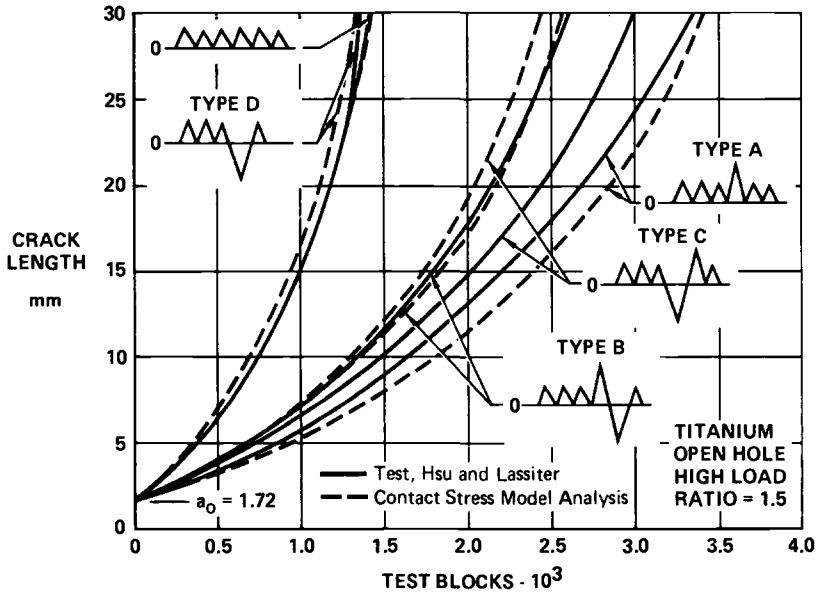
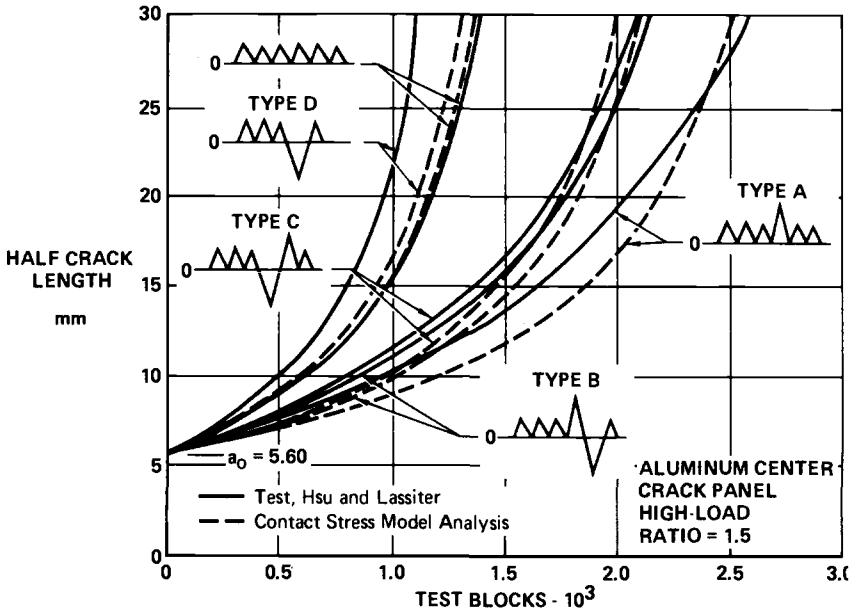


FIG. 9—Comparison of analysis with constant amplitude and compression with high loads tests.

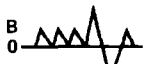
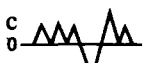
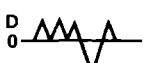
Table 1 summarizes comparisons of test and analysis for all of the test types. The retardation ratio, used to summarize concisely the results, is defined as the number of blocks required to grow to 2.5 cm with high loads, divided by the number of constant-amplitude blocks required to grow to 2.5 cm. In all cases, the Type A spectra resulted in the slowest crack growth rate. Test results for Type B and C spectra indicate no clear trend; in about half the tests, Type B spectra resulted in faster growth, and vice versa. The contact stress model predicts a slightly faster growth rate for the Type C spectra than for Type B. As expected, the Type D spectra generally resulted in the fastest growth rate. The correlation of contact stress model analysis and test results is consistently good.

**Effect of Cyclic Strain Hardening/Softening**

The effects of cyclic hardening and softening are incorporated into the contact stress model by considering that plastic deformation accrues at loading according to monotonic properties, but that deformation recovery on unloading occurs according to cyclic properties. Since most deformation under spectrum loadings occurs as a result of a few overloads, the use of monotonic properties to compute the deformation seems justified. Deformation recovery occurs as a result of repeated loading; this recovery is dependent on cyclic properties. The model predicts less deformation recovery for a cyclically hardening material than for a stable or softening

TABLE 1—Effects of compressive high loads.

$$RR = \text{RETARDATION RATIO} = \frac{\text{BLOCKS TO GROW TO 2.5 CM WITH HIGH LOADS}}{\text{BLOCKS TO GROW TO 2.5 CM WITHOUT HIGH LOADS}}$$

TEST TYPE	HIGH LOAD RATIO	CENTER CRACK PANELS				OPEN HOLE PANELS			
		ALUMINUM		TITANIUM		ALUMINUM		TITANIUM	
		TEST RR	THEORY RR	TEST RR	THEORY RR	TEST RR	THEORY RR	TEST RR	THEORY RR
 A 0	1.2	1.30	1.29	1.12	1.39	1.15	1.30	1.37	1.42
	1.5	1.83	1.85	2.37	2.31	1.83	1.94	2.30	2.44
 B 0	1.2	1.22	1.15	1.03	1.16	1.06	1.16	1.22	1.20
	1.5	1.57	1.55	1.57	1.71	1.30	1.62	1.80	1.81
 C 0	1.2	1.04	1.12	1.06	1.10	1.06	1.12	1.25	1.13
	1.5	1.50	1.48	1.47	1.63	1.37	1.55	2.07	1.71
 D 0	1.2	0.83	0.97	0.99	0.94	0.80	0.97	1.04	0.95
	1.5	0.83	0.96	1.06	0.94	0.91	0.96	0.99	0.94

material; hence more permanent deformation is left in the wake of the crack, and the effective stress intensity range is reduced, slowing the crack growth rate. The contact stress model predicts a slower crack growth rate under spectrum loadings for a cyclically hardening material than for an equivalent stable material, and a faster growth rate will be predicted for a softening material.

The plastic zone size assumed was smaller for the cyclic-stable 7075-T73 aluminum than for the cyclic-softening 6Al-4V titanium. This reduces the predicted retardation in aluminum and enhances correlation with the test data summarized in Table 1. The data in Table 1 show little difference between the materials except at the 1.5 high load ratio of Type A and the Type D results, wherein the titanium results show greater retardation than those for aluminum. These results are contrary to the general trend of available data such as that in the reference cited in Footnote 6. It appears from these data that materials which cyclically strain soften should show less retardation than those which cyclically strain harden. The data presented in Table 1 indicate the increase in growth rate beyond constant amplitude for the Type D spectra is greater in aluminum than in titanium. This result is consistent with the expected differences in behavior of stable and softening materials. Whether the test results are due to differences in cyclic strain behavior, or merely to test scatter, requires further evaluation.

### **Summary**

In conclusion, this series of analyses indicates that contact stress model analysis can predict accurately the effects of both tensile and compressive high loads on crack growth. In addition, the contact stress model predicts that cyclic hardening/softening to have an effect on crack growth retardation. However, further analysis and testing are required to allow accurate prediction of the effects of cyclic properties on crack growth.

## Fatigue Analysis of Cold-Worked and Interference Fit Fastener Holes

---

**REFERENCE:** Rich, D. L. and Impellizzeri, L. F., "Fatigue Analysis of Cold-Worked and Interference Fit Fastener Holes," *Cyclic Stress-Strain and Plastic Deformation Aspects of Fatigue Crack Growth, ASTM STP 637*, American Society for Testing and Materials, 1977, pp. 153-175.

**ABSTRACT:** Crack initiation and crack growth behavior were determined experimentally for aluminum and titanium specimens with fastener holes that were either cold worked or were propped by interference fit fasteners. The specimens were subjected to a randomized flight-by-flight spectrum. Analytical procedures were evaluated, based on correlation with the test data. These procedures included elastic-plastic analysis which was utilized to determine the stress-strain distributions surrounding the fastener holes. Estimates of elastic proportional limits in tension and compression were based on material cyclic stress-strain characteristics. Purely elastic analysis was used to determine the  $K_T$  and stress gradient for the propped fastener holes with various ratios of plate-to-fastener modulus of elasticity. Finite-element model elastic-plastic computer results provided the stress-strain distributions for the cases of superimposed cold working and external loading, and superimposed interference fit fasteners and external loading. Approximate analytic equations were developed to fit the finite-element model computations. These equations were used to calculate the stress-strain excursions that would occur during flight-by-flight spectrum fatigue loading. The stress-strain excursions were then used to enter strain-life curves to compute crack initiation. They were also used to determine stress intensities to enter  $da/dn$  versus  $\Delta K$  curves to compute crack growth. The delay in crack initiation due to beneficial compressive residual stresses that would be induced during spectrum loading was accounted for by using a stress ratio correction factor based on strain-life data generated at different stress ratios. Crack growth retardation due to periodically applied high loads was accounted for, using the Wheeler plastic zone model. The comparison of the crack initiation life calculations to the test data was favorable if initiation was defined as the development of a 0.25-mm crack. Good agreement between the crack growth calculations and the test data was also obtained for growth from a 0.25-mm crack.

**KEY WORDS:** stresses, strains, aluminum alloys, crack propagation, fatigue (materials), cyclic loads, aircraft, tensile properties, mathematical prediction, stress analysis, residual stress, plastic deformation, titanium alloys

Fatigue failures invariably begin at stress concentrations caused by local changes in the load path. Fastener holes are by far the most common stress concentrations existing in aircraft structure. They have elastic geometric

<sup>1</sup>Lead engineer and branch chief, Technology, respectively, McDonnell Aircraft Company, McDonnell Douglas Corporation, St. Louis, Mo. 63166.

stress concentration factors ( $K_T$ ) of 2.5 to 7.0, depending on the specimen geometric configuration and load transfer. Such  $K_T$  levels significantly affect fatigue lives and are usually the controlling factor in fatigue life of structural components.

Fastener hole cold working and interference fit fasteners are two processes being used in design and construction of high-performance fighter aircraft to improve structural efficiency. These processes produce favorable residual stresses that significantly reduce the effect of the stress concentration. Numerous element and full-scale test programs have been conducted, showing large improvements gained through utilization of these fastener systems. Due to the high cost of testing, however, it is virtually impossible to provide 100 percent test coverage of the multitude of stress levels, design details, spectrum variations, materials, etc., that are necessary to provide all essential design information. Analytical techniques are also required to calculate the fatigue life of structural components containing cold-worked and interference fit fastener holes. It is the purpose of this paper to present the techniques being used by the authors in the design of advanced fighter aircraft and to correlate the analysis with specific element test results.

#### Fatigue Life: Crack Initiation Plus Crack Growth

Since the advent of the electron microscope's use in fatigue fracture surface examination, it has become increasingly apparent that the crack growth period represents a significant percentage of the total life for spectrum fatigue. Figures 1 and 2 show average crack growth trends for

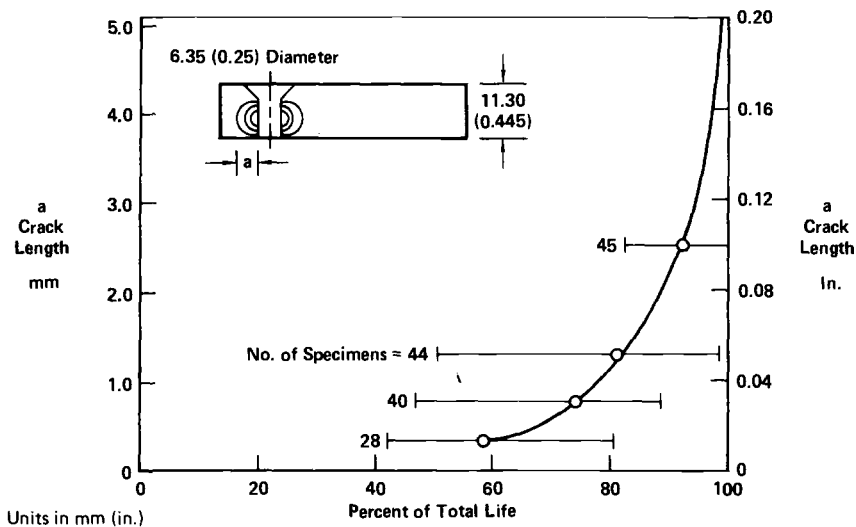


FIG. 1—Crack growth: average trends for 7075T-T651 aluminum specimens.

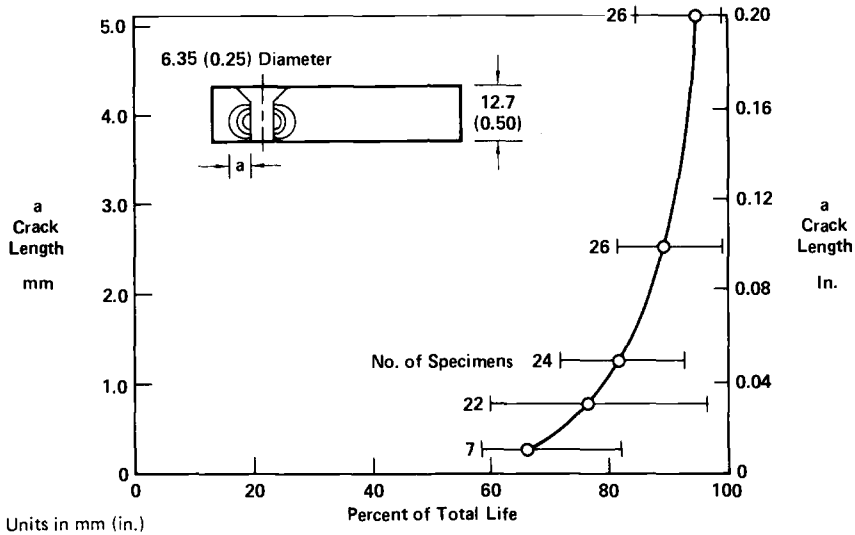


FIG. 2—Crack growth: average trends for Ti-6Al-4V titanium specimens.

7075-T651 aluminum and 6Al-4V titanium, respectively, tested to various fighter aircraft stress spectra. All of the spectra were of the flight-by-flight variety, with ground loads included between each flight. The data, in terms of percentage of total life spent in crack growth from a fastener hole, can be summarized as follows:

7075-T651 Aluminum (45 Specimens), %		
From 0.25-mm Crack	From 0.76-mm Crack	From 1.27-mm Crack
43	26	19
6Al-4V Mill-Annealed Titanium (26 Specimens), %		
From 0.25-mm Crack	From 0.76-mm Crack	From 1.27-mm Crack
33	24	18

The aluminum and titanium test specimens, all of which had fastener holes, represent typical aircraft quality.

The preceding data indicate that a significant percentage of the total fatigue life is spent in both crack initiation and crack growth; neither stage can be neglected. Residual stress cumulative fatigue damage analysis could not accurately predict variations in fatigue life associated primarily with crack growth. Residual stress cumulative damage techniques account for only the plasticity effects at the edge of the fastener hole, and therefore could not account for crack growth as the crack propagates away from the hole. Similarly, crack growth analysis techniques based on continuum

mechanics would not seem applicable for the crack initiation stage. For example, the crack initiation life can be affected significantly by variations in stress concentration factor ( $K_T$ ) while the crack growth would be affected much less. Crack growth analysis would, therefore, be relatively insensitive to small variations in  $K_T$  and would underestimate the effect of  $K_T$ . Fatigue life predictions given in subsequent portions of this paper are thus made by computing both a crack initiation life and a crack growth life. Since crack initiation is somewhat of a subjective term, it is defined for the purposes of this paper as the development of a 0.25-mm crack.

**Test Program**

The objective of the test program was to determine the improvement in fatigue life of structural components through utilization of fastener hole cold working and interference fit fasteners. Test variables included two material types, aluminum and titanium, and three fastener hole configurations: (a) open hole, (b) cold-worked holes with clearance fit fasteners, and (c) interference fit fasteners. Specimens, design fatigue spectrum, and test results are given in the following paragraphs.

*Specimen Design*

The test specimen shown in Fig. 3 is representative of a fighter aircraft wing skin where it would be attached to a spar cap. In these types of structures, the load transfer is a relatively small percentage of the total load and a single piece or monobloc specimen is considered adequate for evaluating

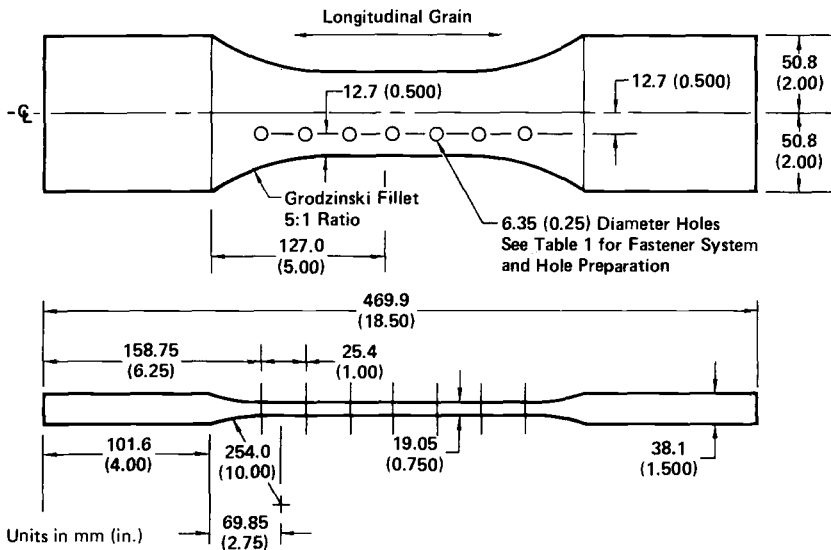


FIG. 3—Test specimen.

fatigue life. Six of the specimens were fabricated from 7075-T7351 aluminum plate and three from 6Al-4V mill-annealed titanium plate. A single row of seven fastener holes were located with a standard  $2D$  (two times the fastener diameter) edge distance and  $4D$  fastener spacing. The specimens were fabricated with the test section parallel to the longitudinal grain direction and with a 19.05-mm thickness. Two specimens each of the aluminum alloy and titanium were fabricated with 6.35-mm-diameter open holes. Two specimens of the aluminum and one of the titanium alloy were fabricated with cold-worked 6.35-mm-diameter holes using a split sleeve process wherein a steel mandrel is pulled through a 0.152-mm-thick split stainless steel sleeve. A diametral interference of 0.28 mm was achieved between the mandrel/sleeve combination and the fastener hole. The holes were reamed to final hole size of 6.35 mm after cold working, and then clearance fit fasteners were installed. The remaining two aluminum specimens were fabricated with 6.35-mm titanium fasteners installed with a 0.06-mm-diametral interference.

All of the specimens were tested to a typical fighter aircraft flight-by-flight spectrum. The positive and negative cumulative peak exceedances for this spectrum are shown in Fig. 4. A ground load was applied between each flight to simulate takeoff and landing loads. The highest load in the spectrum was 126.7 percent design limit stress (DLS) and the lowest was -30 percent DLS. The spectrum was repeated every 120 h. The gross section DLS was 207 MN/m<sup>2</sup> for the aluminum specimens and 462 MN/m<sup>2</sup> for the titanium specimens.

The fracture surfaces of each specimen were viewed with optical and scanning electron microscope after specimen failure to define individual striation patterns and to define a chronological map of the crack location

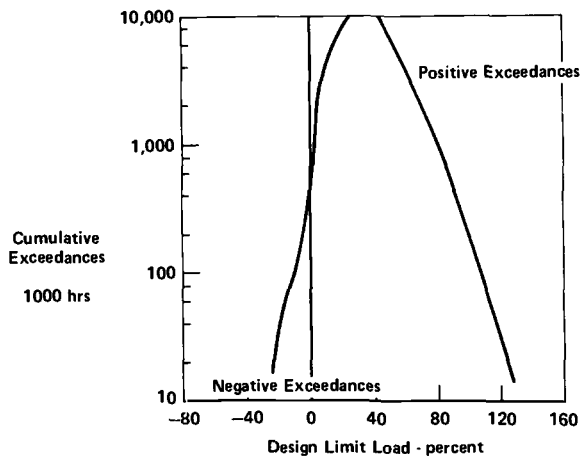


FIG. 4—Fatigue spectrum positive and negative cumulative peak exceedances.

and shape. The time to a 0.25-mm crack was determined from the chronological map.

### *Spectrum Test Results*

The complete summary of tests and results is given in Table 1. The data are divided into two stages: crack initiation and crack growth. As stated previously, crack initiation was defined to occur when a 0.25-mm crack had developed. The division of the life data into these two stages was made using the crack growth measurements following specimen failure. The percentage of total fatigue life spent in crack initiation varied among the groups of specimens. The average percentage of crack initiation life for the open-hole specimens was 48 percent and 64 percent for the aluminum and titanium specimens, respectively, which is within the range shown in Figs. 1 and 2. Crack initiation from cold-worked holes in aluminum represented 35 percent of the total life, whereas, for titanium, it was 77 percent. For the interference fit fastener specimens in aluminum, crack initiation was 46 percent of the total life. These varying percentages between different fastener hole conditions and material types indicate that, for accurate life predictions, one must consider both crack initiation and crack growth. An important reason for the differences in percentages of life spent in crack initiation and crack growth is the location of the crack initiation site. All of the fatigue origins were at the hole wall with the exception of the interference fit fastener specimens, for which the origins were on the surface. The reason for the crack origin on the surface for these specimens will be discussed in subsequent sections.

### **Analytical Techniques**

The following discussion describes methods being used by the authors to predict fatigue crack initiation and crack growth. The following sections define how the stress distributions surrounding fastener holes are determined and how these distributions are used in crack initiation and in crack growth analysis.

TABLE 1—*Spectrum test results.*

Material	Fastener System	Specimen Number	Crack Initiation, h <sup>a</sup>	Crack Growth, h	Total Life, h
7075-T7351	open holes	1	6 500 <i>H</i>	6 412	12 912
		2	7 300 <i>H</i>	8 904	16 212
	cold-worked holes with clearance fasteners	3	16 000 <i>H</i>	40 152	56 152
		4	26 000 <i>H</i>	34 852	60 852
	titanium interference fit fasteners	5	25 000 <i>S</i>	33 814	58 814
		6	26 000 <i>S</i>	27 411	53 411
Ti-6Al-4V	open holes	7	6 100 <i>H</i>	4 834	10 934
		8	10 300 <i>H</i>	4 082	14 382
	cold-worked holes with clearance fasteners	9	40 000 <i>H</i>	12 090	52 090

<sup>a</sup>*H* and *S* indicate fatigue origins at hole wall and on surface, respectively.

### Stress Distributions at Fastener Holes

The stress concentration is very high at a fastener hole. Figure 5 shows the elastic stress distribution on one side of an open fastener hole in an infinite plate loaded with a uniform stress at infinity [1].<sup>2</sup> The stress is three times the gross section stress at the hole wall and decreases rapidly away from the hole. At a distance of one half the radius, the stress has decreased to 1.44 times the gross stress, and, at two radii away from the hole, it is less than 1.10 times the gross stress. For loaded holes, the stress concentration and stress gradient are even greater. Cold working the hole surfaces and using interference fit fasteners reduces the fastener hole stress concentration effect by creating beneficial residual stresses at the hole wall. These residual stresses are created by plastic deformation of the material surrounding the hole resulting from expansion of the hole with an interference fit mandrel or fastener. Equations defining these stress distributions and demonstrating the fatigue strength optimizing features of these fastening systems are given in the following paragraphs.

*Cold-Worked Fastener Holes*—Approximate closed-form solutions are developed, defining residual stresses surrounding cold-worked holes and interference fit fasteners. These solutions are developed from elastic-perfectly plastic analysis of thick-walled tubes with internal pressure [2]. Assumptions include plane strain, Von Mises-Hencky yield conditions, and incompressibility of plastic flow wherein  $\sigma_z = (\sigma_r + \sigma_\theta)/2$  and  $\mu_p = 0.5$ , where  $\sigma_z$  = through-the-thickness stress,  $\sigma_\theta$  = circumferential stress,  $\sigma_r$  =

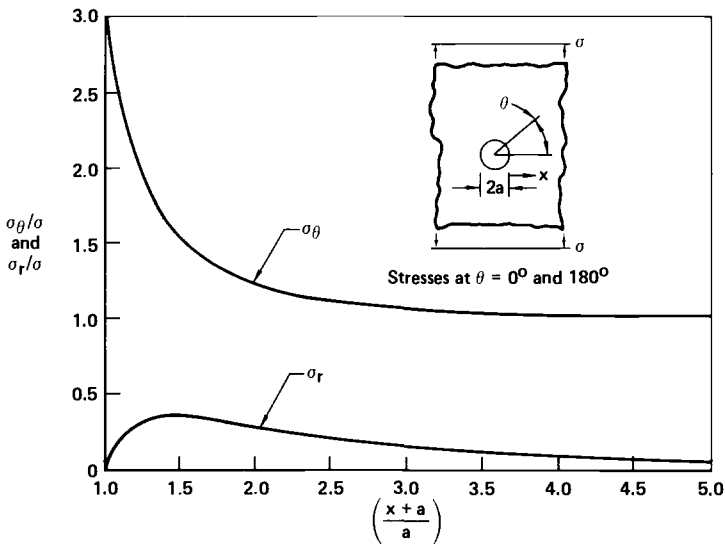


FIG. 5—Stresses at open hole: infinite plate.

<sup>2</sup>The italic numbers in brackets refer to the list of references appended to this paper.

radial stress, and  $\mu_p$  = Poisson's ratio of plate. The material yield stress is obtained from an elastic/plastic representation of the monotonic stress strain curve for the material. A fastener hole located near a plate edge is idealized, as shown in Fig. 6, as a tube having an inner radius  $a$  equal to the fastener hole radius and an outer radius  $b$  equal to the fastener hole edge distance. An internal pressure  $p$  is applied, simulating the forces created by insertion of either an oversize mandrel or an oversize fastener into the hole, thus creating an interference and hole expansion. The following analysis defines the plastic zone created around the hole. The radial interference is set equal to the sum of the radial displacements of the bolt [3],  $\delta_B$ , and the plate [2],  $\delta_p$ .

$$I = \delta_B + \delta_p$$

$$\delta_B = p \frac{a}{E_B} [1 - \mu_B - 2\mu_B^2]$$

$$\delta_p = \frac{\sigma_{ys} \rho^2 (1 + \mu_p)}{\sqrt{3} E_p a}$$

$$p = \frac{\sigma_{ys}}{\sqrt{3}} \left( 2 \ln \frac{\rho}{a} + 1 - \left( \frac{\rho}{b} \right)^2 \right)$$

where

- $I$  = radial interference,
- $E_B$  = modulus of insert material,
- $E_p$  = modulus of plate material,
- $\sigma_{ys}$  = yield stress of plate material,
- $\rho$  = radius of plastic zone,
- $\mu_B$  = Poisson's ratio of bolt, and
- $\mu_p$  = Poisson's ratio of plate.

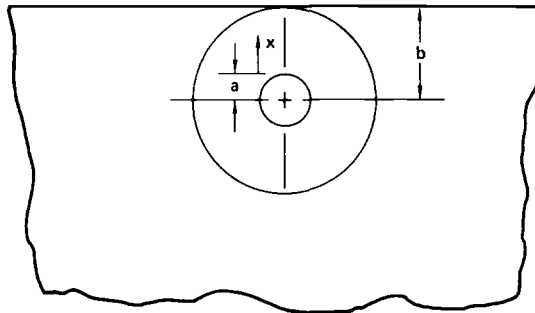


FIG. 6—Idealization of fastener hole near plate edge.

Setting  $\mu_B = 0.3$  and  $\mu_p = 0.5$ , the following equation results

$$\frac{I}{a} = \frac{\sigma_{ys}}{\sqrt{3} E_B} \left[ 0.52 \left( 2 \ln \frac{\rho}{a} + 1 - \left( \frac{\rho}{b} \right)^2 \right) + 1.5 \left( \frac{\rho}{a} \right)^2 \frac{E_B}{E_p} \right] \quad (1)$$

Equation 1 can be solved for values of  $\rho/a \geq 1$ , knowing the material properties and geometric configuration. Figure 7 shows Eq 1 solved for aluminum and titanium with yield stresses of 483 MN/m<sup>2</sup> and 896 MN/m<sup>2</sup>, respectively and  $a/b = 0.25$ .

The circumferential stresses surrounding the hole are taken from the tube analysis [2] and shown schematically in Fig. 8.

For  $a \leq x + a \leq \rho$  ( $x$  is defined in Fig. 6)

$$\sigma_\theta = \frac{\sigma_{ys}}{\sqrt{3}} \left[ 2 \ln \left( \frac{x+a}{\rho} \right) + 1 + \left( \frac{\rho}{b} \right)^2 \right] \quad (2)$$

For  $\rho \leq x + a \leq b$

$$\sigma_\theta = \frac{\sigma_{ys}}{\sqrt{3}} \left[ \left( \frac{\rho}{b} \right)^2 + \left( \frac{\rho}{x+a} \right)^2 \right] \quad (3)$$

Up to this point, the analyses for a cold-worked hole and an interference fit fastener are the same. The next step for the cold-worked hole is to remove the mandrel and thus the internal pressure, creating an elastic unloading defined by

$$(\Delta\sigma_\theta)_{\text{unloading}} = \frac{\sigma_{ys}}{\sqrt{3}} \left[ 2 \ln \frac{\rho}{a} + 1 - \left( \frac{\rho}{b} \right)^2 \right] \left\{ \frac{\left( \frac{a}{b} \right)^2 + \left( \frac{a}{x+a} \right)^2}{1 - \left( \frac{a}{b} \right)^2} \right\} \quad (4)$$

The residual stresses are derived by subtracting Eq 4 from Eqs 2 and 3. The resulting residual stress distributions, shown in Fig. 8, are valid as long as compressive yield is not exceeded at the hole wall on elastic unloading. Substituting these equations for circumferential stress as well as similar equations for the radial and through-the-thickness stress into the Von Mises yield criteria, it can be shown that compressive yielding will occur if the plastic zone  $\rho \geq ae^\gamma$ , where  $e$  = natural logarithm base and  $\gamma = (1/2 - (a/b)^2 + 1/2 (\rho/b)^2)$ . Also, it can be shown that, if compressive yielding occurs, the approximate compressive yield zone size,  $\rho_c$ , is given by

$$\rho_c = \sqrt{\frac{a^2}{2 \left( 1 - \left( \frac{a}{b} \right)^2 \right)} \left( 2 \ln \frac{\rho}{a} + 1 - \left( \frac{\rho}{b} \right)^2 \right)} \quad (5)$$

and the circumferential residual stress at the hole wall is,  $(\sigma_\theta)_{\text{RES}}$ ,

$$(\sigma_\theta)_{\text{RES}} = \frac{4\sigma_{ys}}{\sqrt{3}} \left[ -\gamma + \left( \frac{a}{b} \right)^2 e^\gamma \right] \quad (6)$$

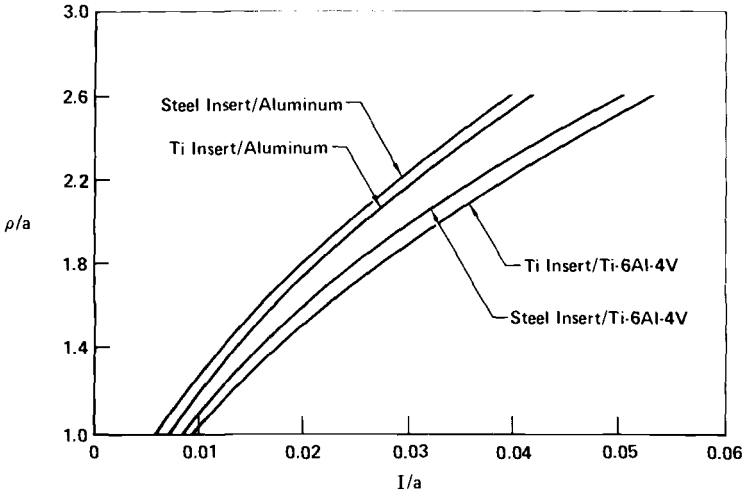


FIG. 7—Plastic zones surrounding interference fit inserts.

The circumferential stresses near a cold-worked hole were determined for a 6.35-mm-diameter hole in a 127-mm-wide aluminum panel having a yield stress of 483 MN/m<sup>2</sup> and cold worked with a steel mandrel with a diametral interference of 0.22 mm. The approximate closed form solutions shown in Fig. 9 are in fair agreement with elastic-perfectly plastic finite-element solu-

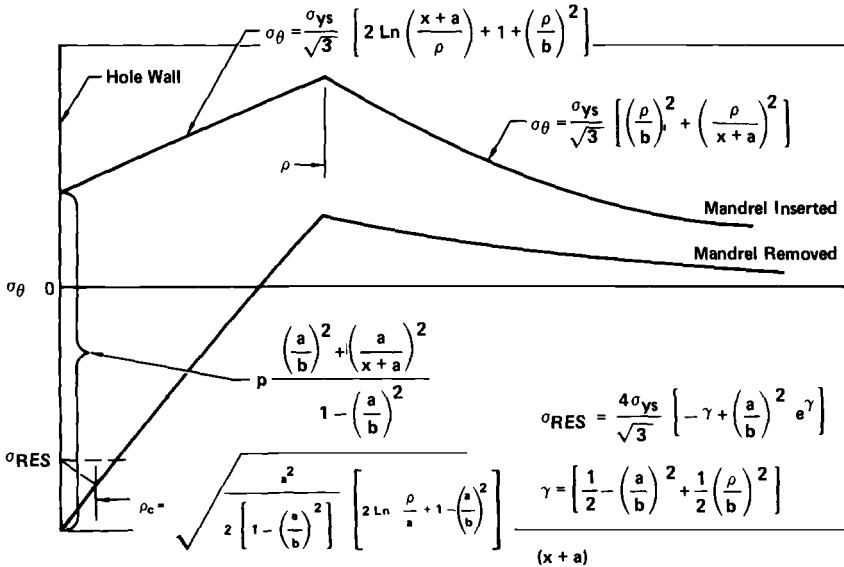


FIG. 8—Stresses surrounding a cold-worked hole.

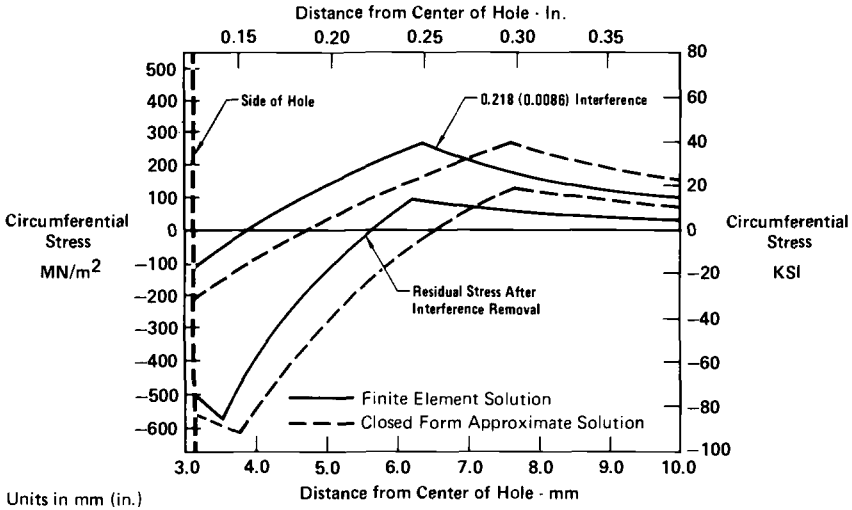


FIG. 9—Stresses surrounding a cold-worked hole: comparison to finite-element solution.

tions by Brombolich [4]. At the hole wall, the cold working produces a significant residual compressive stress of  $-558 \text{ MN/m}^2$  and at the elastic-plastic interface, a residual positive stress of  $131 \text{ MN/m}^2$ . The residual stress at the hole wall is greater in magnitude than the material yield stress due to a built-in compressive through-the-thickness stress created when the mandrel was inserted. The combined stress distribution caused by externally applied remote load after cold working is determined by adding the elastic stress distribution given by Fig. 5 to the residual stresses given by Fig. 9. Reyielding both in tension or compression is possible, depending on the magnitude of the applied load, and has a significant effect on the stress at the hole wall, but a minimal effect on the stresses away from the hole wall. The changes to the residual stresses at the hole wall are accounted for in subsequent crack initiation analyses.

For an applied gross section stress of  $207 \text{ MN/m}^2$ , the distribution remains elastic and the stress at the hole wall is  $63 \text{ MN/m}^2$ . A cyclic gross stress of 0 to  $207 \text{ MN/m}^2$  to 0 produces a cyclic notch stress of  $-558 \text{ MN/m}^2$  to  $63 \text{ MN/m}^2$  to  $-558 \text{ MN/m}^2$  for a cold-worked hole. The authors have determined in a separate analysis that the cyclic notch stress would be  $-78 \text{ MN/m}^2$  to  $543 \text{ MN/m}^2$  for an open non-cold-worked hole. Although the cyclic stress ranges are the same,  $621 \text{ MN/m}^2$ , the cold-worked hole will have a lower mean stress and therefore will be subjected to less fatigue damage. At the elastic-plastic interface, the cold-worked hole will be subjected to more damage because of the positive residual stress and thus higher mean stress. Cold working the hole decreases the rate of damage accumulation at the hole wall but increases the rate of damage accumulation away from the hole. The overall net effect is a large gain in fatigue life.

For small applied stress cycles, fatigue cracks in a cold-worked hole specimen will initiate away from the hole wall on the surface of the plate. High cyclic stress levels, such as in the tests reported herein, can be of sufficient magnitude to initiate cracks at the hole wall, but at a much longer life than for the non-cold-worked hole.

*Interference Fit Fasteners*—Interference fit fasteners, similar to cold-worked holes, increase fatigue life by reducing the rate of damage accumulation at the hole wall. The interference fit fastener in combination with high applied tensile stresses produces significant residual compressive stresses adjacent to the hole wall. The theoretical analysis of the stress behavior around an interference fit fastener hole is based on the analysis for pressure loading in thick wall tubes, described previously, and Goodier's work on stress concentration effects around cylindrical inclusions [5]. Zero shear continuity is assumed at the fastener-plate interface. The resulting equations give stresses in agreement with elastic-plastic finite-element solutions [6].

The circumferential and radial stresses surrounding a cylindrical inclusion are

$$\begin{aligned}
 (\sigma_{\theta})_E &= \frac{\sigma}{2} \left[ 2 + \left( \frac{a}{x+a} \right)^2 \left( \frac{1-E_R}{1+2.5E_R} \right) + \left( \frac{a}{x+a} \right)^2 \left( \frac{3+0.5E_R}{1+1.33E_R} \right) \right] \\
 (\sigma_r)_E &= \frac{\sigma}{2} \left\{ \left( \frac{a}{x+a} \right)^2 \left[ \left( \frac{6+E_R}{1.33E_R+1} \right) - \left( \frac{1-E_R}{1+2.5E_R} \right) - 2 \right] \right. \\
 &\quad \left. - \left( \frac{a}{x+a} \right)^4 \left[ \frac{E_R+6}{2.66E_R+2} \right] \right\} \quad (7)
 \end{aligned}$$

where  $E_R$  = ratio of modulus of fastener to modulus of plate. Equation 7 is shown in Fig. 10 for typical cases of titanium interference fit fasteners installed in aluminum and in titanium. This equation is applicable as long as gapping does not occur between the fastener and plate, which is the case for the problems solved herein. The stress concentration is 1.75 for titanium in titanium and 1.55 for titanium in aluminum. The interference fastener allows some of the load to pass from one side of the hole through the fastener to the other side rather than being diverted to each side of the hole. The reduction in  $K_T$  alone will produce significant increases in fatigue life. In addition, the material adjacent to the hole is yielded when the interference fit fastener is installed. Subsequent remote tensile loading produces more tensile yielding, and, upon unloading, beneficial compressive residual stresses are introduced.

Calculation of the circumferential stresses for the interference fit fastener includes three basic calculations: (a) stress distribution for an unloaded plate with just the interference fit fastener installed, (b) changes to the stress

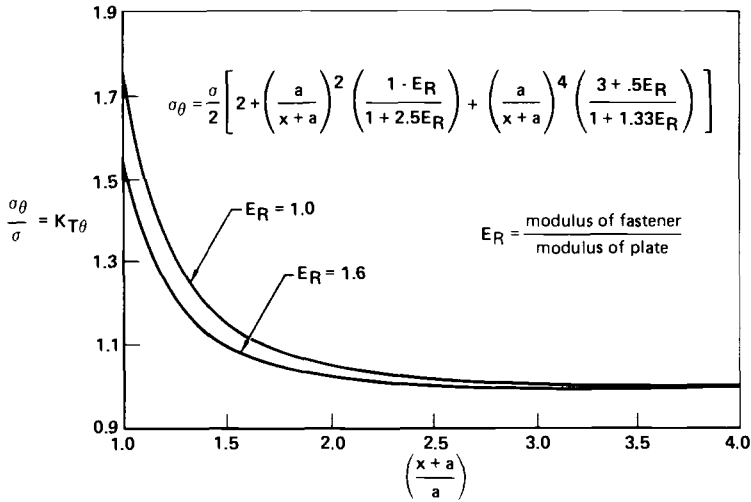


FIG. 10—Circumferential stress concentration factors for interference fit fasteners.

distribution as affected by an applied loading, and (c) residual stress distributions following removal of the applied load. These stress distributions are shown schematically in Fig. 11.

The first calculation is the same as for cold-worked holes, that is, an insert expanding the hole. Equations 1 through 3 define the initial state of stress surrounding the hole. On subsequent applications of an external load, the material adjacent to the hole already being at yield is unable to

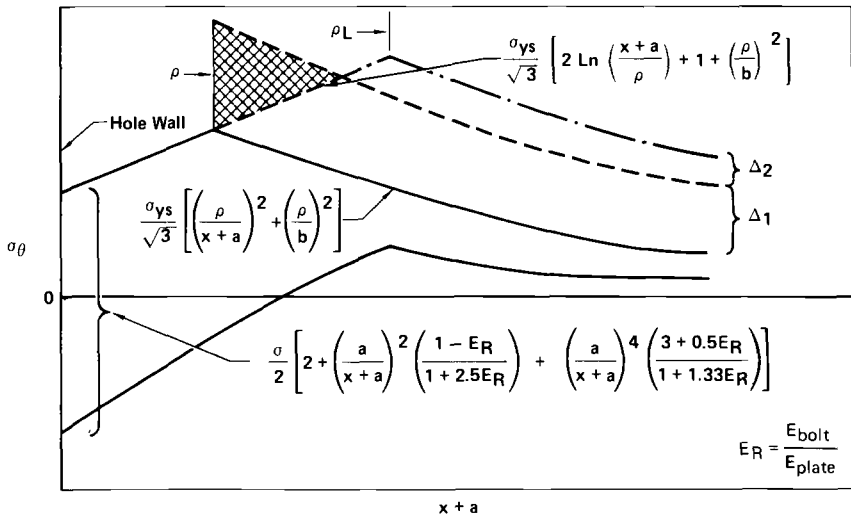


FIG. 11—Stresses surrounding an interference fit fastener hole.

carry additional stress. Material adjacent to the plastic zone quickly yields, extending the plastic zone further from the hole wall. The extension of the plastic zone to a value  $\rho_L$  is approximated by Eq 2.

For  $a \leq x + a \leq \rho_L$

$$(\sigma_\theta)_L = \frac{\sigma_{ys}}{\sqrt{3}} \left[ 2 \ln \frac{(x+a)}{\rho} + 1 + \left( \frac{\rho}{b} \right)^2 \right] \quad (8)$$

The stresses outboard of the new plastic zone  $\rho_L$  are approximated by the following equation.

For  $\rho_L \leq x + a \leq b$

$$\begin{aligned} (\sigma_\theta)_L = & \frac{\sigma_{ys}}{\sqrt{3}} \left[ \left( \frac{\rho}{x+a} \right)^2 + \left( \frac{\rho}{b} \right)^2 \right] \\ & + \frac{\sigma}{2} \left[ 2 + \left( \frac{\rho}{x+a} \right)^2 \left( \frac{1-E_F}{1+2.5E_F} \right) + \left( \frac{\rho}{x+a} \right)^4 \left( \frac{3+0.5E_F}{1+1.33E_F} \right) \right] \quad (9) \\ & + \frac{\sigma_A}{2} \left[ \left( \frac{\rho}{x+a} \right)^2 \left( \frac{1-E_F}{1+2.5E_F} \right) + \left( \frac{\rho}{x+a} \right)^4 \left( \frac{3+0.5E_F}{1+1.33E_F} \right) \right] \end{aligned}$$

where

$E_F$  = effective modulus ratio as determined in the following paragraph,  
and

$A$  = average stress as determined in the following paragraphs.

The value of  $\rho_L$  can be determined numerically for the intersection of curves given by Eqs 8 and 9.

The first term of Eq 9 is due to the fastener interference and is given by Eq 3. The second term is an approximation representing the increase in stress,  $\Delta_1$  shown in Fig. 11. It was derived by considering the plastic zone  $\rho$  as an inclusion having a modulus ratio  $E_F$  given by

$$E_F = \frac{1}{1.43 \left( \frac{\rho^2 + a^2}{\rho^2 - a^2} \right) - 0.43}$$

$E_F$  is used to account for the combination of bolt stiffness and plastic zone stiffness.

A wedge of stresses exists, represented by the cross-hatched area of Fig. 11, which must be redistributed outboard of the new plastic zone front. This redistribution defined by  $\Delta_2$  in Fig. 11 is given by the third term of Eq 9. The wedge was considered to be triangular with a height of

$$\frac{\sigma}{2} \left[ 2 + \left( \frac{1 - E_F}{1 + 2.5E_F} \right) + \left( \frac{3 + 0.5E_F}{1 + 1.33E_F} \right) \right]$$

and a base of  $(\rho_L - \rho)$ . The stresses were then averaged over the entire radius  $\rho_L$  and then distributed outboard. The average stress is given by

$$\sigma_A = \frac{1\sigma(\rho_L - \rho)}{4\rho_L} \left[ 2 + \left( \frac{1 - E_F}{1 + 2.5E_F} \right) + \left( \frac{3 + 0.5E_F}{1 + 1.33E_F} \right) \right]$$

Upon removal of the external load, the stresses undergo an elastic unloading defined by Eq 7, starting at the hole wall and extending outboard to the edge of the plate. The complete set of equations for stresses surrounding an interference fit fastener are illustrated in Fig. 11.

The stresses have been computed for a 6.35-mm hole in a 127-mm-wide plate of aluminum including the effects of an applied 345 MN/m<sup>2</sup> edge loading and shown in Fig. 12 in comparison with finite-element results. A diametral interference of 0.10-mm is produced by a steel fastener in a plate having a yield strength of 483 MN/m<sup>2</sup>. On application of the interference, the region surrounding the hole yields to the point 5.2 mm from the hole center. The circumferential stress at the hole wall is 20 MN/m<sup>2</sup> and increases for distances to the elastic-plastic interface and then decreases. On application of the 345 MN/m<sup>2</sup> edge loading, the plastic zone extends

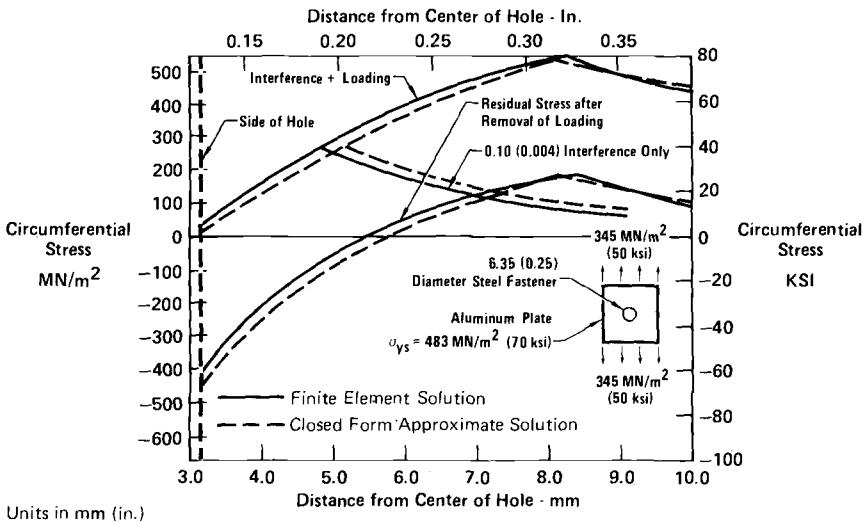


FIG. 12—Stresses surrounding an interference fit fastener hole: comparison to finite-element solution.

further into the plate. The stresses within the original yield zone do not change since they are already at yield. On removal of the 345 MN/m<sup>2</sup> edge loading, the residual stresses within the plate are changed significantly. At the hole wall, the residual stress is 450 MN/m<sup>2</sup> compression, and the peak residual stress is 185 MN/m<sup>2</sup> tension. As shown in Fig. 12, the stresses calculated using the closed-form approximate equations agree well with the finite-element solutions.

As with cold-worked holes, cyclic stresses applied to an interference fit fastener hole produce less damage at the hole wall and greater damage at the elastic-plastic interface in comparison with an open non-cold-worked hole. Contrary to that for the cold-worked holes, crack initiation sites with interference fit fasteners will nearly always be on the surface of the plate away from the hole even for high cyclic stresses. This is due to the stress concentration at the hole wall being much less for a specimen with an interference fit fastener than one with either a cold-worked hole or an open hole.

*Crack Initiation Model*

The model used to determine crack initiation is based on cumulative damage analysis accounting for prior load history as shown in Fig. 13. Such models have been described by various investigators [7-13]; therefore only a brief mention of the highlights of the technique used herein will be given. The stresses and strains at the root of a notch are tracked using rules defined by Jhansale and Topper [13]. Cyclic and hysteresis stress strain curves are used in conjunction with Impellizzeri's procedures for Neuber notch

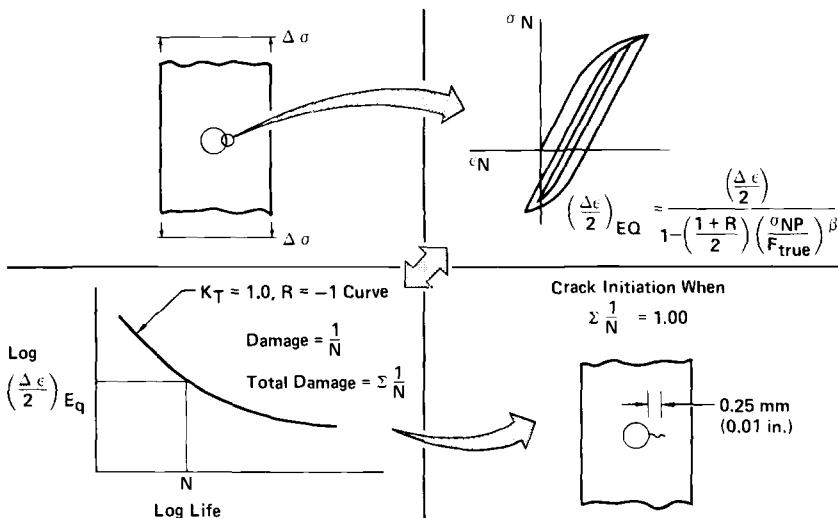


FIG. 13—Crack initiation analysis.

analysis [7]. The stresses and strains are computed for each point of load reversal and are retained for use in performing damage computations. The strain amplitude and notch stress ratio are used for each load cycle in the following equation developed by the authors to calculate an equivalent strain amplitude  $(\Delta\epsilon/2)_{EQ}$

$$\left(\frac{\Delta\epsilon}{2}\right)_{EQ} = \frac{\left(\frac{\Delta\epsilon}{2}\right)}{1 - \frac{(1 + R)}{2} \left(\frac{\sigma_{NP}}{F_{true}}\right)^\beta} \tag{11}$$

where

- $\Delta\epsilon/2$  = strain amplitude for particular load cycle,
- $\sigma_{NP}$  = maximum notch stress for particular load cycle in MN/m<sup>2</sup>,
- $R$  = notch stress ratio for particular load cycle, and
- $F_{true}, \beta$  = material constants.

The equivalent strain amplitude  $\Delta\epsilon/2$  will produce the same cycles to failure at  $R = -1$  as the strain amplitude  $\Delta\epsilon/2$  for the particular notch stress ratio. Equation 11 is applicable for all values of  $R$  including  $R < -1$ . The material constants  $\beta$  and  $F_{true}$  can be evaluated to best fit strain life data obtained from constant-amplitude tests at various stress ratios. Values of  $\beta$  and  $F_{true}$  determined for the alloys used in the element test program are:

Material	$\beta$	$F_{true}$
Ti-6Al-4V	0.85	1655.0
7075-T73	0.80	621.0

Figure 14 shows the correlation provided by Eq 11 for unnotched 7075-T73 data.

The equivalent strain amplitude is entered on a strain amplitude-life plot of constant-amplitude data from smooth specimens tested at stress ratios of  $-1$  and a life determined. The inverse of the life so obtained, that is,  $1/N$ , is the damage produced by that particular load cycle. These steps are continued for each load cycle applied for the complete spectrum of loads to obtain the usual  $\Sigma 1/N$  value. Crack initiation is predicted when  $\Sigma 1/N = 1.00$ .

Strain life data taken from constant-amplitude tests are assumed to represent the cycles to crack initiation to a 0.25-mm crack. Figure 15 shows that, for 2024-T851, it was 93 percent of the total life. The percentage of total life spent in crack growth is considerably different for constant amplitude testing than for spectrum testing. In general, crack growth represents a larger percentage of spectrum test life because of the crack growth retardation effects of intermittently applied high load cycles.

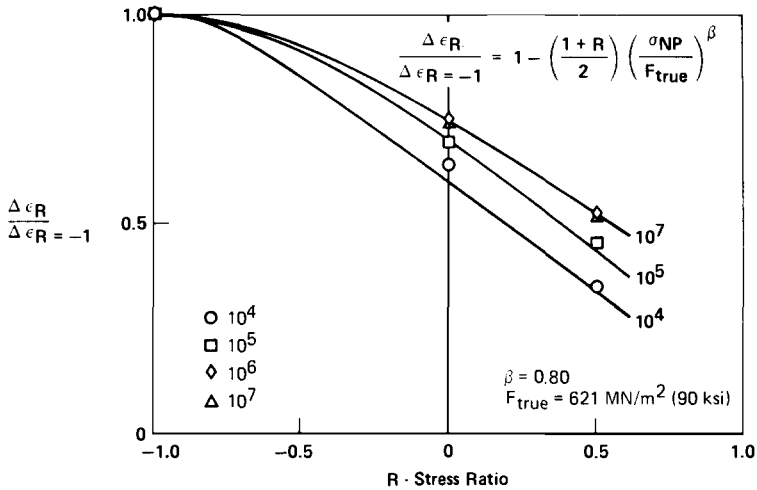


FIG. 14—Range over range versus R: effect of stress ratio on fatigue life for 7075-T73 aluminum.

The percentage of total life spent in crack growth is also dependent on a variety of other parameters such as material type, fracture toughness, stress level, stress concentration, and stress gradient, etc. For example, if a particular material has a low fracture toughness with a resulting small critical crack size, failure will occur relatively soon after crack initiation. For higher toughness materials, crack growth can be considerably longer. These variations in relative amounts of total life for crack growth can only be taken into account by accurate analytical techniques predicting both crack initiation and crack growth.

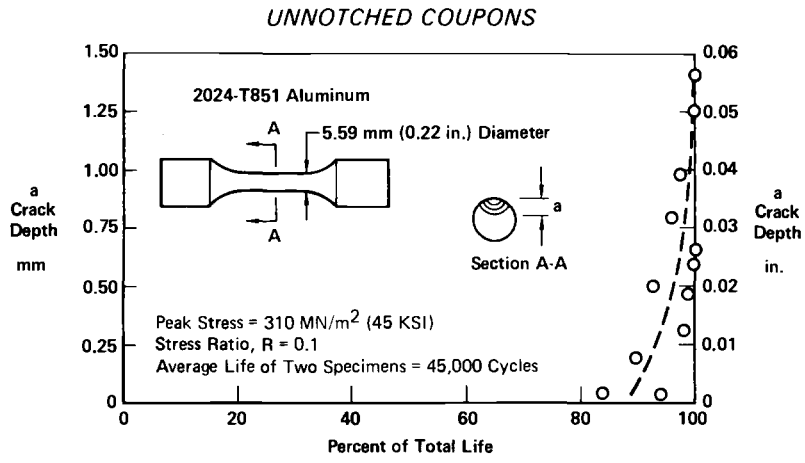


FIG. 15—Crack growth trends: constant-amplitude fatigue.

Crack initiation estimates for a structure with cold-worked holes and interference fit fasteners are calculated at both the hole wall and the elastic-plastic interfaces by using these procedures to account for the residual stresses surrounding the hole. Figure 16 shows how the stresses are initialized for the crack initiation analysis. For crack initiation prediction at the hole wall, an initial dummy load cycle is applied to produce the residual stress calculated using the elastic-perfectly plastic analysis described previously. This procedure sets the stresses and strains within the tracking routine so that subsequent cyclic stresses will have the proper value. This is particularly important for the cold-worked hole where the residual circumferential stress is near or at compressive yield and the application and removal of subsequent compressive applied stresses will reduce the magnitude of the residual compressive stresses.

At the elastic-plastic interface, the residual stress is an input parameter, and subsequent cycling is entirely elastic. This is the case for both the cold-worked hole and interference fit fastener since the stress concentration at the elastic-plastic interface is close to one. In addition, the residual stress at the elastic-plastic interface for the interference fit fastener analysis is determined by an elastic unloading from the highest applied stress in the spectrum. Any subsequent loading cycles will be of a lower magnitude and thus will be elastic.

Predictions of life to crack initiation were made using the preceding analysis to correlate with the test results given previously. These predictions, shown in Figs. 17, 18, and 19, agreed well with the test data. The titanium and aluminum interference fit predictions were conservative, whereas the other aluminum predictions were slightly conservative. The agreement

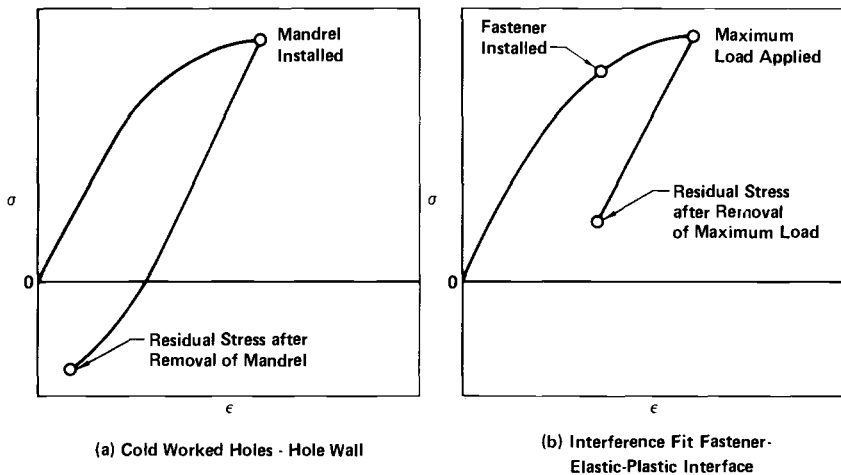


FIG. 16—Initialization of stresses for crack initiation analysis.

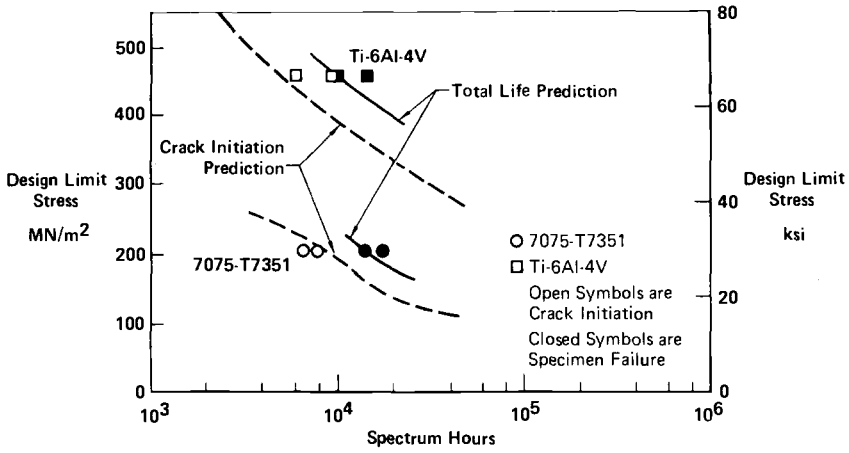


FIG. 17—Spectrum fatigue life correlation: open holes.

was slightly better for the 7075-T7351 aluminum specimens than for the titanium specimens.

*Spectrum Crack Growth*

The spectrum crack growth predictions were made using the applied intensity range,  $\Delta K$ , for each cycle in the flight-by-flight spectrum. The stress intensities were calculated using superposition of a residual stress intensity and the stress intensity resulting from the applied load. The residual stress intensities were determined as defined by Impellizzeri and Rich [14] in their analysis of cold-worked lugs using Bueckner's weight function

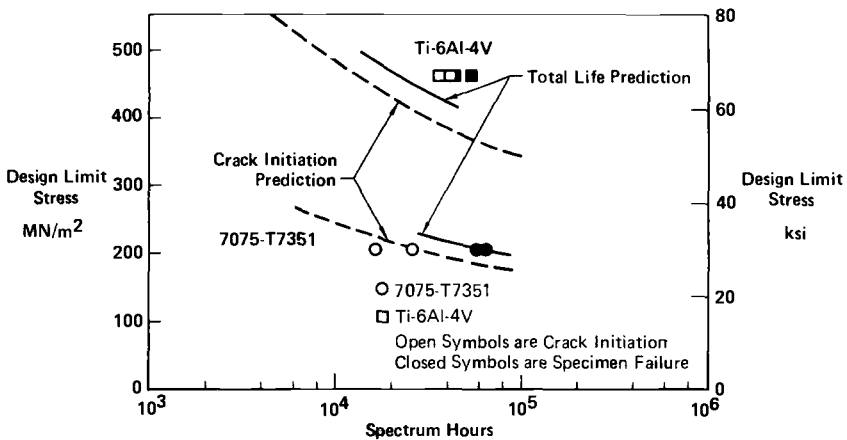


FIG. 18—Spectrum fatigue life correlation: cold-worked holes.

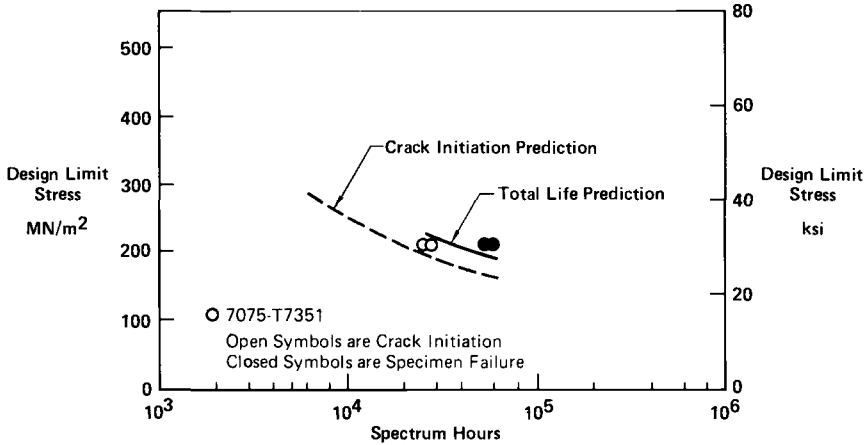


FIG. 19—Spectrum fatigue life correlation: Interference fit fasteners.

approach and the residual stress distributions as determined from Figs. 8 and 11. The flaw shape parameter  $Q$  [15] was utilized to account for the flaws being surface cracks rather than through-the-thickness cracks. It was assumed that the stress intensity was  $1/Q$  multiplied times the through-the-thickness stress intensity. The calculated values of  $\Delta K$  were used to enter a curve of  $da/dn$  versus  $\Delta K$  for the applicable material to obtain the crack extension for each cycle. The crack growth was linearly summed on a cycle-by-cycle basis.

Stress ratio adjustments in crack growth rates were made using Forman's equation [16]. The residual stress intensity plays an important role here in that most of the cycles have large negative stress ratios and thus the crack growth rates are decreased significantly.

Crack growth retardation due to intermittently applied higher load cycles was predicted using the Wheeler plastic zone model [17]. The magnitude of the retardation parameter  $M$  used in the spectrum crack growth analysis was taken as the average value from work by Pinckert [18] for the applicable material and stress levels.

The values of  $M$  used for the aluminum predictions were 1.38 for the open and cold-worked hole specimens and 1.85 for the interference fit fastener specimens. The titanium predictions were made with an  $M$  of 2.02.

Correlation of the crack growth predictions with the test data are shown in Figs. 20 and 21 starting with 0.25-mm crack. In general, the crack growth rate predictions were faster than the data, giving a slightly conservative prediction except for the titanium cold-worked specimen in Fig. 21. The crack growth lives were added to the predicted crack initiation lives, as shown in Figs. 17, 18, and 19, to give the total life predicted. The total life predictions were all in reasonable agreement with the test data.

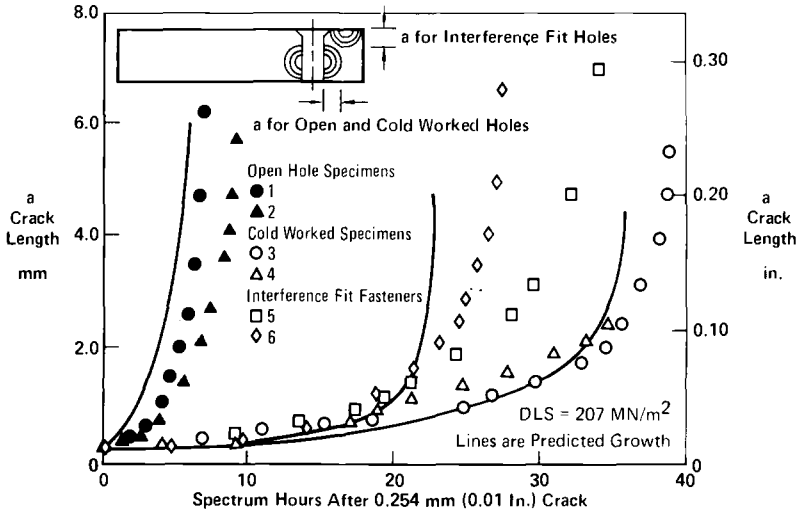


FIG. 20—Spectrum crack growth correlation: open, cold-worked, and interference fit holes in 7075-T7351 aluminum.

**Conclusions**

Fatigue life is composed of two important stages: crack initiation and crack growth. Neither stage can be neglected, and each must be calculated using different analysis procedures. Spectrum fatigue tests of element specimens demonstrate the potent benefit of cold working and interference fit

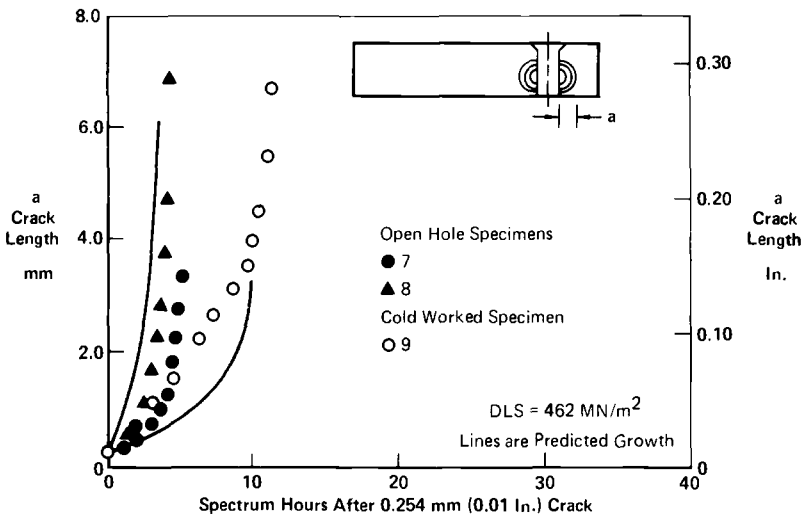


FIG. 21—Spectrum crack growth correlation: open and cold-worked holes in Ti-6Al-4V titanium.

fasteners in comparison with open non-cold-worked holes. Approximate analytical procedures were given to define stress distributions surrounding cold-worked and interference fit fastener holes. Stress distributions determined for particular combinations of insert material, plate material, and interference agreed well with finite-element solutions. These stress distributions can be used to predict crack initiation and crack growth. The total fatigue life made up of crack initiation and crack growth is then the sum of the individual lives predicted and agreed favorably with test data.

## References

- [1] Timoshenko, S. and Goodier, J. N., *Theory of Elasticity*, McGraw-Hill, New York, 1951, pp. 80-81.
- [2] Hoffman, O., *Introduction to the Theory of Plasticity for Engineers*, McGraw-Hill, New York, 1953, pp. 80-94.
- [3] Brombolich, L. J., "Elastic-Plastic Analysis of Stresses near Fastener Holes," McDonnell Aircraft Company Report MDC A1769, 14 June 1972.
- [4] Brombolich, L. J., unpublished information. McDonnell Aircraft Company, St. Louis, Mo., July 1973.
- [5] Goodier, J. N., *Transactions of the ASME*, Vol. 55, 1933, American Society of Mechanical Engineers, p. 39.
- [6] Brombolich, L. J., "Elastic-Plastic Analysis of Stresses Near Fastener Holes," AIAA Paper No. 73-252, American Institute of Aeronautics and Astronautics, 1973.
- [7] Impellizzeri, L. F. in *Effects of Environment and Complex Load History on Fatigue Life*, ASTM STP 462, American Society for Testing and Materials, 1970, pp. 40-68.
- [8] Dowling, N. E., *Journal of Materials*, American Society for Testing and Materials, Vol. 7, No. 1, March 1972, pp. 71-87.
- [9] Koibuchi, K. and Kotani, S. in *Cyclic Stress-Strain Behavior—Analysis, Experimentation, and Failure Prediction*, ASTM STP 519, American Society for Testing and Materials, 1973, pp. 229-245.
- [10] Crews, J. H., Jr. in *Achievement of High Fatigue Resistance in Metals and Alloys*, ASTM STP 467, American Society for Testing and Materials, 1969, pp. 37-52.
- [11] Endo, T. and Morrow, J. D., *Journal of Materials*, American Society for Testing and Materials, Vol. 4, No. 1, March 1969, pp. 159-175.
- [12] Tucker, L. E., "A Procedure for Designing Against Fatigue Failure of Notched Parts," Society of Automotive Engineering Paper No. 720265, 1972.
- [13] Jhansale, H. R. and Topper, T. H. in *Cyclic Stress-Strain Behavior—Analysis, Experimentation and Failure Prediction*, ASTM STP 519, American Society for Testing and Materials, 1973, pp. 246-270.
- [14] Impellizzeri, L. F. and Rich, D. L. in *Fatigue Crack Growth Under Spectrum Loads*, ASTM STP 595, American Society for Testing and Materials, 1976, pp. 320-336.
- [15] Brown, W. F., Jr., and Srawley, J. E. in *Plane Strain Crack Toughness Testing of High-Strength Metallic Materials*, ASTM STP 410, American Society for Testing and Materials, Dec. 1967, p. 102.
- [16] Forman, R. G., Kearney, V. E., and Engle, R. M., "Numerical Analysis of Crack Propagation in Cycle-Loaded Structures," ASME Paper No. 66-WA-MWT-4, American Society of Mechanical Engineers, 1966.
- [17] Wheeler, V. E., *Transactions*, American Society of Mechanical Engineers, *Journal of Basic Engineering*, Vol. 94, March 1972, pp. 181-186.
- [18] Pinckert, R. E., "Damage Tolerance Assessment of F-4 Aircraft," AIAA paper 76-904, American Institute of Aeronautics and Astronautics, Sept. 1976.

# Fatigue Crack Growth and Life Predictions in Man-Ten Steel Subjected to Single and Intermittent Tensile Overloads

---

**REFERENCE:** Stephens, R. I., Sheets, E. C., and Njus, G. O., "Fatigue Crack Growth and Life Predictions in Man-Ten Steel Subjected to Single and Intermittent Tensile Overloads," *Cyclic Stress-Strain and Plastic Deformation Aspects of Fatigue Crack Growth*, ASTM STP 637, American Society for Testing and Materials, 1977, pp. 176-191.

**ABSTRACT:** Fatigue crack growth behavior was investigated in Man-Ten steel under conditions of constant load amplitude, single tensile overloads followed by constant load amplitude and intermittent single tensile overloads. Constant-amplitude ratios,  $R_l = P_{lmin}/P_{lmax}$ , were +1/2, 0, -1/2, -1 and -2. The single overload test program excluded  $R_l = +1/2$ , and the intermittent overload program was for  $R_l = 0$  only. A new simplified mathematical model was introduced which assumes that fatigue crack growth retardation is primarily a function of the overload ratio and the load ratio. The model predicted intermittent tensile overload life within 57 to 112 percent of the experimental life. The average prediction was 77 percent of experimental life. For Man-Ten steel, constant-amplitude crack growth rate versus positive  $\Delta K$  fell within a reasonable scatter band for  $R_l = 1/2$  to -1. However, substantial decrease in life occurred with  $R_l = -2$ . Negative values of  $R_l$  following a single tensile overload substantially reduced retardation life. Thus compressive stress, either large or small, cannot be neglected in spectrum loading fatigue crack growth life predictions.

**KEY WORDS:** stresses, strains, fatigue (materials), fracture, crack growth, retardation, residual stress, mathematical models, overloads, spectrum analysis, steels

## Nomenclature

- $a$  Crack length, in. (mm)
- $a_i$  Initial crack length at 1.0 in. (25.4 mm)
- $a_{dr}$  Delayed retardation crack extension, in. (mm)
- $a_{ag}$  Retardation crack extension, in. (mm)
- $A$  Crack growth rate coefficient
- $da/dN$  Crack growth rate, in./cycle (mm/cycle)

<sup>1</sup>Professor, Materials Engineering Division; formerly research assistant, Mechanical Engineering Department; and research assistant, Materials Engineering Division, The University of Iowa, Iowa City, Iowa 52242.

- B* Plate thickness, in. (mm)  
*b* Net plate thickness, in. (mm)  
*K* Stress intensity,  $\text{ksi}\sqrt{\text{in.}}$  ( $\text{MN}\cdot\text{m}^{-3/2}$ )  
*K<sub>e</sub>* "Elastic" fracture toughness,  $\text{ksi}\sqrt{\text{in.}}$  ( $\text{MN}\cdot\text{m}^{-3/2}$ )  
*K<sub>o</sub>* Maximum tensile overload stress intensity,  $\text{ksi}\sqrt{\text{in.}}$  ( $\text{MN}\cdot\text{m}^{-3/2}$ )  
*K<sub>I,max</sub>* Maximum constant-amplitude stress intensity,  $\text{ksi}\sqrt{\text{in.}}$  ( $\text{MN}\cdot\text{m}^{-3/2}$ )  
*K<sub>I,min</sub>* Minimum constant-amplitude stress intensity,  $\text{ksi}\sqrt{\text{in.}}$  ( $\text{MN}\cdot\text{m}^{-3/2}$ )  
 $\Delta K_I$  Positive constant-amplitude stress intensity range,  $\text{ksi}\sqrt{\text{in.}}$  ( $\text{MN}\cdot\text{m}^{-3/2}$ )  
 $\Delta K_{II}$  Positive initial constant-amplitude stress intensity range,  $\text{ksi}\sqrt{\text{in.}}$  ( $\text{MN}\cdot\text{m}^{-3/2}$ )  
*N* Applied cycles  
*n* Crack growth rate exponent  
 OLR Overload ratio =  $P_o/P_{I,max} = K_o/K_{I,max}$   
*P<sub>o</sub>* Tensile overload force, kips (kN)  
*P<sub>I,max</sub>* Maximum constant-amplitude force, kips (kN)  
*P<sub>I,min</sub>* Minimum constant-amplitude force, kips (kN)  
 $\Delta P_I$  Positive constant-amplitude load range, kips (kN)  
*R<sub>I</sub>* Load ratio =  $P_{I,min}/P_{I,max}$   
 RPZ Reversed plastic zone size =  $1/4 (2r_y)$ , in. (mm)  
 RF Retardation factor  
*2r<sub>y</sub>* Monotonic plastic zone size, in. (mm)  
*S<sub>y</sub>* Tensile yield strength, ksi ( $\text{MN}/\text{m}^2$ )  
*W* Specimen width, in. (mm)  
 $\Delta\sigma_I$  Positive constant-amplitude stress range, ksi ( $\text{MN}/\text{m}^2$ )

Fatigue crack growth life predictions under spectrum loading are extremely complex. Appreciable efforts to advance the understanding of fatigue crack growth interaction under various loading spectra along with mathematical models to predict known behavior have only recently been expanded [1-10].<sup>2</sup> This research provides additional phenomenological crack growth behavior of a low-strength steel, Man-Ten,<sup>3</sup> subjected to single and intermittent tensile overloads along with a simplified predictive mathematical retardation model. The research includes the effects of positive and negative load ratio under constant amplitude, and following single tensile overloads. Intermittent single tensile overload effects were also studied with a load ratio, *R<sub>I</sub>*, of zero. The retardation model is based upon an assumed linear retardation while the crack progresses completely through the tensile overload reversed plastic zone and that retardation is dependent upon the overload ratio and *R<sub>I</sub>*.

<sup>2</sup>The italic numbers in brackets refer to the list of references appended to this paper.

<sup>3</sup>Man-Ten is a U.S. Steel Corporation trade name for a steel which meets ASTM Specification for High-Strength Structural Steel (A 440-75).

### Material and Test Procedures

Man-Ten steel was chosen for this research because of its common usage in the ground vehicle industry and because of its extensive use in the Society of Automotive Engineers (SAE) Fatigue Design and Evaluation Committee round-robin test program [11]. Representative chemical composition [11] and average monotonic tensile and fracture toughness properties for this material are given in Table 1. Man-Ten steel cyclically softens at small strain amplitudes and cyclically hardens at larger strain amplitudes [11]. The cyclic yield strength, 0.2 percent offset, for Man-Ten is about 49.5 ksi which is within 8 percent of the monotonic yield strength.

All fatigue crack growth studies were performed using compact or modified compact specimens as shown in Fig. 1a. Overall dimensions satisfy ASTM Test for Plane-Strain Fracture Toughness of Metallic Materials (E 399-74.) Most tests with load ratio  $R_i$  equal to zero were conducted using the single pinhole shown dotted in Fig. 1a. Tests with negative  $R_i$  were run with the three-hole configuration connected to a spherical bearing gripping system. The spherical bearings allowed for both compressive and tensile loads while ensuring axial ram loading.

Specimens were machined from hot-rolled 1/4-in. (6.3-mm) plate. Side grooves were machined on both sides to control the crack growth plane which resulted in net specimen thickness of 0.225 in. (5.7 mm). The side grooves were polished with progressively finer emery paper for better crack front observation. Precracks were induced from chevron starter notches with the same maximum load,  $P_{i\max}$ , as used in subsequent testing. All tests were begun at a crack length of 1.0 in. (25.4 mm) and were monitored with a  $\times 36$  traveling microscope using stroboscopic illumination. A scale with a least reading of 0.01 in. (0.25 mm) was attached to the specimen above the side groove. All tests were performed at room temperature in a closed-loop electrohydraulic test system using load control conditions. Fracture toughness,  $K_{Ic}$ , was obtained at crack lengths of 1.0 in. (25.4 mm) and 1.25 in. (31.7 mm). Crack length effects were negligible, and an average value of  $150 \text{ ksi}\sqrt{\text{in.}}$  ( $164 \text{ MN}\cdot\text{m}^{-3/2}$ ) was used in all calculations.  $K_{Ic}$  is an assumed elastic fracture toughness which neglects crack extension during loading and is calculated using the maximum load and the initial crack length.

TABLE 1—Representative chemical composition by weight and average monotonic tensile properties.

C	Mn	Si	Cr	Mo
0.16	0.96	0.07	0.08	0.05
Yield strength, $S_y$				
Ultimate strength				
reduction in area, %				
elongation, %				
Rockwell B hardness				
Fracture toughness, $K_{Ic}$				

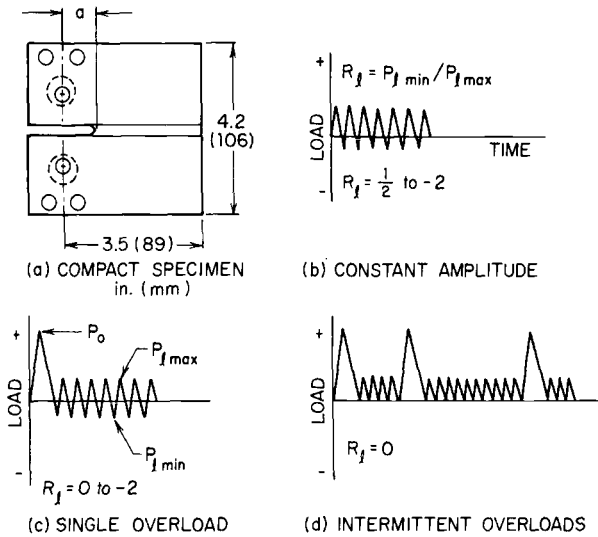


FIG. 1—Compact specimen and load histories.

The fatigue crack growth test program is depicted schematically in Fig. 1*b* to 1*d*. Fourteen reference constant-amplitude tests, Fig. 1*b*, were conducted with  $R_I$  equal to  $+1/2$ ,  $0$ ,  $-1/2$ ,  $-1$ , and  $-2$ . For  $R_I \approx 0$ , individual tests were run with the initial positive stress intensity range,  $\Delta K_{II}$ , equal to 26.8, 40.2, 53.6, and 67  $\text{ksi}\sqrt{\text{in.}}$  (29.4, 44.2, 58.8, and 73.6  $\text{MN}\cdot\text{m}^{-3/2}$ ), while, for other  $R_I$  ratios, only  $\Delta K_{II}$  equal to 26.8 and 40.2  $\text{ksi}\sqrt{\text{in.}}$  (29.4 and 44.2  $\text{MN}\cdot\text{m}^{-3/2}$ ) were used. Fifteen single tensile overload tests were run, as shown in Fig. 1*c*, with  $R_I = 0$ ,  $-1/2$ ,  $-1$ , or  $-2$ . Values for  $\Delta K_{II}$  were 40.2, 53.6, and 67  $\text{ksi}\sqrt{\text{in.}}$  (44.2, 58.8, and 73.6  $\text{MN}\cdot\text{m}^{-3/2}$ ), and overload ratios (OLR) ranged from 1.4 to 2.75. For negative  $R_I$  tests, only  $\Delta K_{II} = 40.2$   $\text{ksi}\sqrt{\text{in.}}$  (44.2  $\text{MN}\cdot\text{m}^{-3/2}$ ) and OLR = 1.67 were run. Twenty-six intermittent single tensile overload tests, Fig. 1*d*, were obtained with  $R_I$  equal to zero. The number of single intermittent tensile overloads per test specimen ranged from two to eight. All constant-amplitude cycling was conducted using a positive haversine at 5 or 15 Hz. The lower frequency was needed for the higher values of  $\Delta K_{II}$ . Overloads were applied at 0.5 Hz.

## Test Results

### Constant Amplitude

The constant-amplitude fatigue crack growth results were correlated using  $\log (da/dN)$  versus  $\log (\Delta K_I)$  where  $\Delta K_I$  refers only to the positive applied stress intensity range. Representative results are shown in Fig. 2 for  $R_I$  equal to  $+1/2$ ,  $0$ ,  $-1/2$ ,  $-1$ , and  $-2$ . For values of  $R_I$  between  $+1/2$ , and  $-1$ , the fatigue crack growth rate behavior is quite similar when correlated with the positive stress intensity range and falls in a narrow scatter band. The actual life of each specimen, however, dropped up to 25 percent as  $R_I$  de-

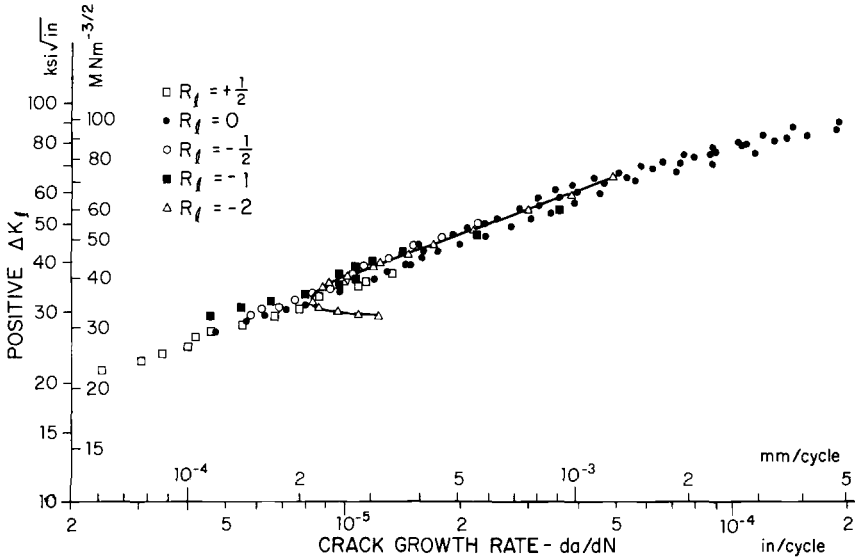


FIG. 2—Positive stress intensity range versus crack growth rate, constant-amplitude loading.

creased from 0 to  $-1$ . A straight line relationship for Fig. 2 can be depicted as

$$da/dN = A(\Delta K_I)^n \tag{1}$$

Values of  $A$  and  $n$  were obtained by a least-square regression analysis using a computer (IBM 360). For  $R_I = 0$ , the value of  $A$  was  $2.73 \times 10^{-10}$  in./cycle when using  $\text{ksi}\sqrt{\text{in.}}$  for  $\Delta K_I$  and  $9.16 \times 10^{-9}$  mm/cycle when using  $\text{MN}\cdot\text{m}^{-3/2}$  for  $\Delta K_I$ ;  $n$  was equal to 2.96. At higher values of  $\Delta K_I$ , piecewise straight lines can be obtained. For negative values of  $R_I$ , the coefficient  $A$  generally increased while the exponent  $n$  decreased.

The crack growth behavior with  $R_I = -2$  was quite different from the other load ratios. As shown in Fig. 2 for  $R_I = -2$ , the crack growth rate decreased and then increased. This initially high crack growth rate at the beginning of the test was responsible for the large decrease in life which was from 40 to 80 percent compared with  $R_I = 0$ . The high initial crack growth rate can be attributed somewhat to precracking with  $R_I = 0$  which provides for a sharp crack and low residual stress field at the crack tip.

### Single Tensile Overloads

Representative crack growth results for single tensile overloads with  $R_I = 0$  are shown in Fig. 3. The effect of overload ratio, OLR, for  $R_I = 0$  is shown for  $\Delta K_{II} = 67$  ksi/in. ( $73.6 \text{ MN}\cdot\text{m}^{-3/2}$ ) and OLR ranging from 1.6 to 2.2. All overloads were applied at crack length,  $a$ , equal to 1.0 in. (25.4

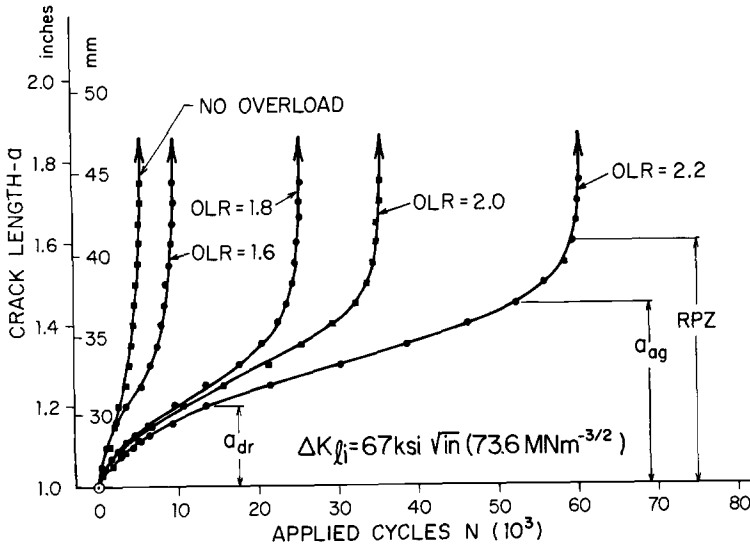


FIG. 3—Crack growth following single tensile overloads.  $R = 0$ .

mm). The overload position is represented by an open circle. It is quite evident that, the higher the OLR, the greater the life. In each case, following the overload, a region of delayed retardation designated by  $a_{dr}$  existed, followed by a region having essentially constant crack growth rate. The termination of the constant crack growth region is labeled  $a_{ag}$ , and, at this point, the specimen experienced accelerated crack growth. The influence of the overload essentially is completed at crack extension  $a_{ag}$ . The plane stress overload reversed plastic zone boundary RPZ, calculated from Ref 12

$$RPZ = \frac{1}{4} (2r_p) = \frac{1}{4} \left[ \left( \frac{2}{2\pi} \right) \left( \frac{K_o}{S_y} \right)^2 \right] \quad (2)$$

is also labeled for  $OLR = 2.2$ . Values of  $a_{dr}$ ,  $a_{ag}$ , and RPZ are given in Table 2 for each single overload test with  $R_I = 0$ .  $a_{dr}$  ranged from about 25 to 50 percent of the RPZ, while  $a_{ag}$  ranged from 55 to 108 percent of the RPZ value. Table 2 implies that, for Man-Ten steel and smaller overloads, the influence of the overload with  $R_I = 0$  persists until the crack front essentially reaches the overload RPZ. For higher overloads, the influence terminates before the overload RPZ is reached.

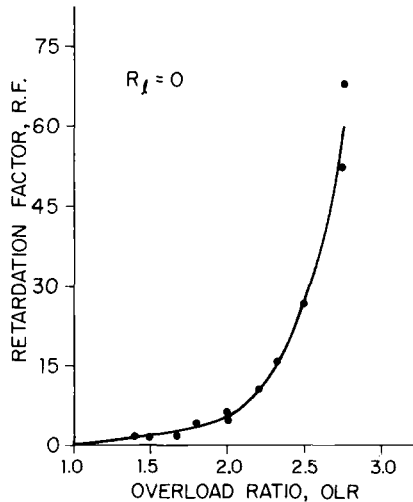
Retardation factors, RF, for single tensile overloads with  $R_I = 0$  are given in Fig. 4. The retardation factor is defined as the number of applied cycles for the crack to reach the RPZ, following a single tensile overload divided by the number of cycles to reach this same crack length with no

TABLE 2—Single tensile overload delayed retardation and retardation crack lengths,  $R_l = 0$ .

$\Delta K_{li}$ , ksi $\sqrt{\text{in.}}$ (MN $\cdot\text{m}^{-3/2}$ )	OLR	$a_{dr}$ , in. (mm)	$a_{ag}$ , in. (mm)	RPZ, in. (mm)	$a_{ag}/\text{RPZ}$
67(73.6)	2.2	0.20(5.0)	0.42(10.6)	0.60(15.2)	0.70
	2.0	0.18(4.6)	0.39( 9.9)	0.45(11.4)	0.87
	1.8	0.13(3.3)	0.35( 8.9)	0.40(10.1)	0.88
	1.4	0.13(3.3)	0.25( 6.3)	0.24( 6.1)	1.0
53.6(58.8)	2.75	0.20(5.0)	0.33( 8.4)	0.60(15.2)	0.55
	2.5	0.25(6.3)	0.40(10.1)	0.45(11.4)	0.89
	2.0	0.10(2.5)	0.34( 8.6)	0.32( 8.1)	1.06
	1.5	0.05(1.3)	0.18( 4.6)	0.18( 4.6)	1.0
40.2(44.2)	2.33	0.07(1.8)	0.20( 5.0)	0.24( 6.1)	0.83
	1.67	0.06(1.5)	0.13( 3.3)	0.12( 3.0)	1.08

overload applied. The retardation factor for this material and specimen, however, is essentially the same as the ratio of the number of cycles to failure with and without the overload. It is evident in Fig. 4 with  $R_l = 0$  that the retardation factor is influenced primarily by the OLR ratio and not the value of  $\Delta K_{li}$ . Retardation factors with  $R_l = 0$  ranged from 1.5 to 68.

The effect of  $R_l < 0$  on fatigue crack growth following single tensile overloads was investigated for  $R_l = 0, -1/2, -1,$  and  $-2$  with  $\Delta K_{li} = 40.2$  ksi/in. (44.2 MN $\cdot\text{m}^{-3/2}$ ) and OLR = 1.67. Retardation factors are shown in Fig. 5 where RF dropped almost 50 percent as  $R_l$  went from zero to  $-1$ . Comparative  $a$  versus  $N$  curves for no overload and single tensile overloads with  $R_l = 0$  and  $-1$  are shown in Fig. 6. With  $R_l = -1$ , the no overload curve and single overload curves are quite similar, that is, the retardation region essentially has been eliminated with  $R_l = -1$ . Thus, low-amplitude cyclic

FIG. 4—Single tensile overload retardation factor,  $R_l = 0$ .

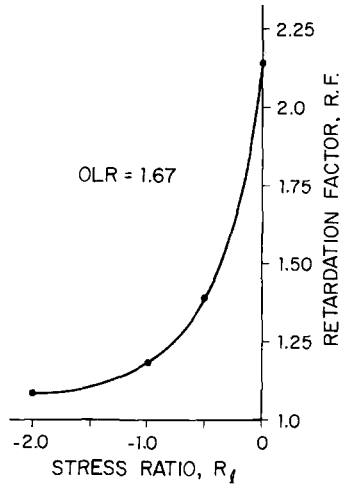


FIG. 5—Single tensile overload retardation factor,  $R_f \leq 0$ .

stressing with  $R_f < 0$  following a single tensile overload can reduce life drastically compared to  $R = 0$  life. This behavior also has been observed in 2024-T3 and 7075-T6 aluminum [13-15] and 4140 steel with three different yield strength levels [16].

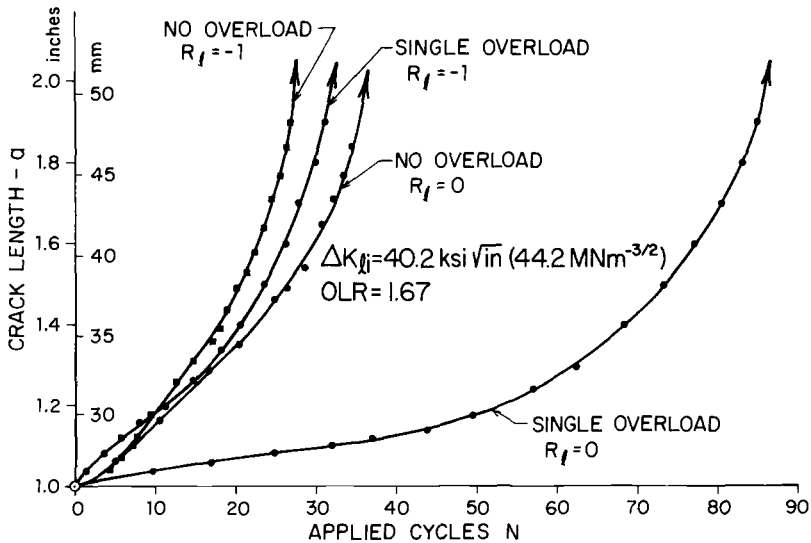


FIG. 6—Effect of  $R_f$  on crack growth following single tensile overloads.

*Intermittent Tensile Overloads,*

The program consisting of 26 specimens subjected to intermittent tensile overloads with  $R_l = 0$  included  $\Delta K_{fi}$  equal to 40.2, 53.6, and 67  $\text{ksi}\sqrt{\text{in}}$ . (44.2, 58.8, and 73.6  $\text{MN}\cdot\text{m}^{-3/2}$ ), OLR = 1.5 to 2.75, and number of single overloads from two to eight per specimen. Overloads were applied at crack lengths equal to, less than, or greater than a previous overload RPZ boundary. The overload stress intensity,  $K_o$ , varied from 67  $\text{ksi}\sqrt{\text{in}}$ . (73.6  $\text{MN}\cdot\text{m}^{-3/2}$ ) to 148  $\text{ksi}\sqrt{\text{in}}$ . (162.6  $\text{MN}\cdot\text{m}^{-3/2}$ ) which was from 45 to 98 percent of the fracture toughness,  $K_c$ . Macroscopic crack extension from overloads ranged from essentially zero to 0.10 in. (2.5 mm). In all cases, the intermittent overload fatigue crack growth life was greater than the constant-amplitude reference life. Increases in life ranged from factors of 2.24 to 52, depending upon  $\Delta K_{fi}$ , OLR,  $K_o$ , and the relationship between a previous overload RPZ. Total life to fracture ranged from 12 200 to 871 000 cycles. Two separate duplicate tests were performed which involved widely different spectra. The fatigue crack growth life difference for both duplicate tests was 19 percent. The goal of the intermittent overload tests was to attempt to determine criteria for maximizing life and to compare experimental results with a new simplified mathematical model.

Figure 7 shows the results of a series of tests where tensile overloads were applied precisely when the crack length reached a previous calculated overload RPZ. The open circles again represent crack length and cycles when an overload was applied. It is quite evident that, with  $P_{l\text{max}}$  and OLR constant, successive overloads at the previous RPZ provided additional life.

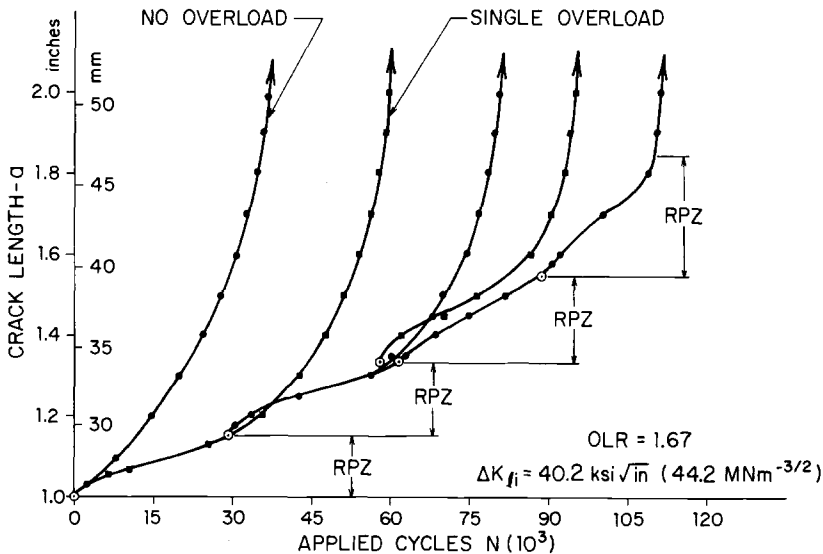


FIG. 7—Crack growth with intermittent overloads applied at RPZ.

This behavior did not occur at the larger values of  $P_{I \max}$  and OLR because of the large delayed retardation that occurs in Man-Ten steel following a single tensile overload.

Figure 8 shows the effect of overloads applied at various percentages of a previous calculated RPZ. Five specimens were tested with overload applied at 0.5, 0.75, 1.0, 1.25, and 1.50 times the previous RPZ. Only three of the results are plotted in Fig. 8 because of the overlap of data. The total life to failure for these five tests ranged from 93 690 to 113 000 cycles or a maximum difference of just 21 percent. This result indicates the exact relationship between an overload and the overload RPZ is not that critical.

**Mathematical Model**

The mathematical model for spectrum fatigue crack growth life predictions involves results from constant-amplitude and single tensile overload tests, along with fracture toughness  $K_c$ . There are just four major assumptions as follows:

1. A crack is delayed linearly as it grows through an overload RPZ.
2. The delay is a function of OLR and  $R_I$  for a given environment.
3. If the crack is outside an overload RPZ region, then crack growth is governed by  $da/dN = A(\Delta K_I)^n$ .
4. Each overload stress intensity can be a controlling condition, depending on its RPZ.

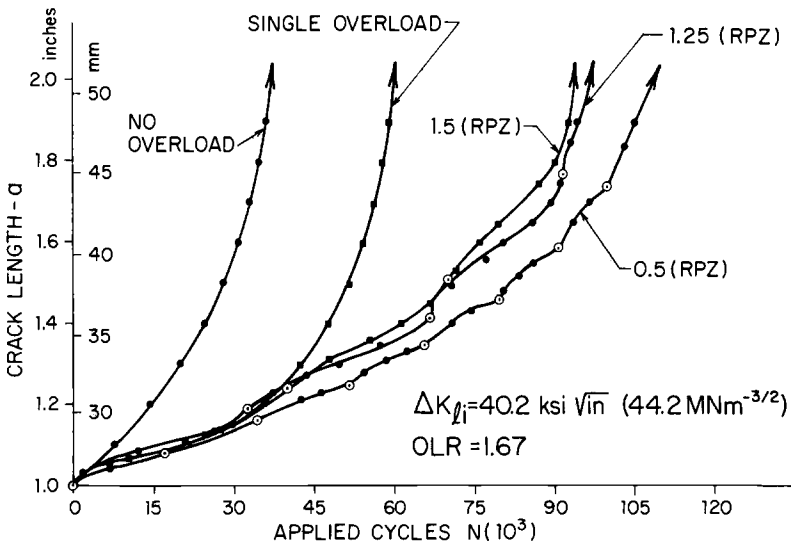


FIG. 8—Effect of intermittent overloads applied between 0.5 and 1.5 times RPZ.

When the crack is outside a controlling RPZ, life increments can be found by integrating

$$da/dN = A(\Delta K_i)^n \quad (1)$$

where  $\Delta K_i = \Delta\sigma_i f(a)$ , which yields

$$\Delta N_i = \frac{1}{A(\Delta\sigma_i)^n} \int_{a_i}^{a_{i+1}} \frac{da}{[f(a)]^n} \quad (3)$$

The integral expression is usually such that numerical integration with a computer is needed. If the crack is within a controlling RPZ, then the life increment is found by multiplying Eq 3 by the proper retardation factor such as in Figs. 4 and 5 and replacing  $a_{i+1}$  with  $a_i + \text{RPZ}_i$  which yields

$$\Delta N_i = (\text{RF}) \frac{1}{A(\Delta\sigma)^n} \int_{a_i}^{a_i + \text{RPZ}_i} \frac{da}{[f(a)]^n} \quad (4)$$

This expression yields the life increment to grow completely across the  $\text{RPZ}_i$ . If a change in load amplitude occurs before the crack grows completely across the  $\text{RPZ}_i$ , then the linear assumption must be used by multiplying Eq 4 by  $\Delta a_i / \text{RPZ}_i$  where  $\Delta a_i$  is the crack extension during this calculation interval, thus

$$\Delta N_i = \frac{\Delta a_i}{\text{RPZ}_i} (\text{RF}) \frac{1}{A(\Delta\sigma)^n} \int_{a_i}^{a_i + \text{RPZ}_i} \frac{da}{[f(a)]^n} \quad (5)$$

Final fracture occurs when  $K_{lmax}$  or  $K_o$  equals the governing fracture toughness. Multiple step tests can be handled by the model, assuming multiple overloads and single overloads yield similar retardation factors. In order to use the model, the load spectrum must be followed step by step from beginning to end. It can be used to find the number of cycles within a given crack extension or the amount of crack extension within a given cycle history. Its best usage occurs when complex spectra can be reduced to a more simplified series of block loadings and intermittent peak loads. Thus the total fatigue crack growth life can be found by sequentially using either Eqs 3, 4, or 5. The choice is made by comparing RPZ values. The largest RPZ is the controlling one.

The model was used to predict all the lives of the intermittent tensile overloads described previously. The predictions varied from 57 to 112

percent of experimental life, with an average of 77 percent. This means an average difference of 23 percent in predicted and experimental life, which is quite good considering that two separate duplicated tests varied by 19 percent in life. Only three predictions were unconservative, and these were within 12 percent. The model predicted the trends in Figs. 7 and 8. The cyclic yield strength was also used in six predictions in place of the monotonic yield strength, and only small decreases existed. This small change is due to the small differences in the two yield strengths.

## Discussion

The compression portion of a cyclic load has been considered to have secondary influence on fatigue crack growth. This idea has come largely from constant-amplitude loading and the idea that a crack will not grow appreciably while it is closed. The constant-amplitude results for Man-Ten steel agree fairly well with this idea except for larger negative load ratios. However, as  $R_l$  varied from 0 to  $-1$ , life decreases of up to 25 percent did occur. This small deviation is not readily seen on the usual log-log scatter band of  $da/dN$  versus  $\Delta K_I$ . With  $R_l = -2$ , appreciable decrease in life was evident. Thus, even under constant-amplitude loading, compressive loads can be detrimental; the larger the compressive load, the shorter the life.

Compressive loads have a very large detrimental effect in a variable-amplitude loading spectrum. It has been well established that a single compressive overload immediately following a high tensile overload can eliminate the beneficial effects of the tensile overload [3,13,14]. However, research [13-16] has shown that small compressive loads following a single overload can also decrease or eliminate the beneficial tensile overload effects. This is a very important point and must be considered in all retardation models.

The simplified mathematical model developed in this research provides a very realistic approach to the complex phenomena of fatigue crack growth under spectrum loads. It predicted conservative life in most cases of this research and within a normal expected scatter band when unconservative. Perhaps a large disadvantage of this simplified model is that delayed retardation is neglected, in that crack growth within an overload RPZ is assumed linear. However, the predicted and experimental results of this research are quite realistic despite the appreciable amount of delayed retardation found in Man-Ten steel. Much of this delayed retardation may be just surface effects because appreciable tunneling did occur with the higher overload ratios.

The primary information needed to use the model is the retardation factor, RF, and the distance of crack extension where it is applicable. This type of information has become quite plentiful in the past five years for  $R_l \geq 0$  due to the broad interest in retardation. However, retardation in-

formation with  $R_l \geq 0$  cannot be extrapolated to spectrum with  $R_l < 0$ . For  $R_l \geq 0$ , the retardation factor can be considered to operate across the RPZ. This is not true with  $R_l < 0$  since compressive cycling following tensile overloads alters both crack closure [17] and controlling plastic zone sizes. Thus the model currently is rather restricted to  $R_l \geq 0$  spectra. In concept, however, it includes all values of  $R_l$ . The experimental data are just not yet available.

### Summary and Conclusions

1. Constant-amplitude  $da/dN$  versus positive  $\Delta K$  fell within a reasonable log-log scatter band for Man-Ten steel with load ratios of  $+1/2$  to  $-1$ . Decreases in life up to 25 percent, however, occurred as the load ratio varied from 0 to  $-1$ . The insensitivity of a log-log scale does not readily pick up this difference.

2. With the load ratio equal to  $-2$ , the constant-amplitude life of Man-Ten steel was substantially less than the  $+1/2$  to  $-1$  data. This was due primarily to high crack growth rates following tensile precracking.

3. Retardation of crack growth following single tensile overloads depended on the magnitude of the overload ratio and the load ratio. Negative constant-amplitude load ratios following single tensile overloads reduced or eliminated retardation.

4. With a constant-amplitude load ratio of zero following a single tensile overload, the crack growth retardation occurred over 55 to 108 percent of the reversed plane stress plastic zone. The smaller the overload ratio, the greater the percentage.

5. Retardation with negative constant-amplitude load ratios following single tensile overloads could not be correlated with overload plastic zones.

6. Intermittent single tensile overloads applied at each successive reversed plastic zone continued to increase life except at high overload ratios where delayed retardation was substantial.

7. A new simplified mathematical model predicted intermittent tensile overload life within 57 to 112 percent of experimental life. The average prediction was 77 percent of experimental life. Most predictions were conservative, and unconservative values were within the experimental scatter of duplicate tests.

8. Compressive stresses (both small and large) can be extremely detrimental and should not be excluded in fatigue crack growth life predictions.

### References

- [1] *Fatigue Crack Propagation*, ASTM STP 415, American Society for Testing and Materials, 1967.
- [2] *Fatigue Crack Growth Under Spectrum Loads*, ASTM STP 595, American Society for Testing and Materials, 1976.
- [3] Schijve, J., "Fatigue Crack Growth Under Variable-Amplitude Loading," Conference on the Prospects of Advanced Fracture Mechanics, Delft, Netherlands, June 1974.

- [4] Corbly, D. M. and Packman, P. F., *Engineering Fracture Mechanics*, Vol. 5, 1973, pp. 479-497.
- [5] Barsom, J. M. in *Progress in Flaw Growth and Fracture Toughness Testing*, ASTM STP 536, American Society for Testing and Materials, 1973, pp. 147-167.
- [6] Elber, W. in *Damage Tolerance in Aircraft Structures*, ASTM STP 486, American Society for Testing and Materials, 1971, pp. 230-251.
- [7] Wheeler, O. E., "Spectrum Loading and Crack Growth," Paper No. 71-Met-X, American Society of Mechanical Engineering, 1971.
- [8] Willenborg, J., Engle, R. M., and Wood, H. A., "A Crack Growth Retardation Model Using an Effective Stress Concept," Technical Memorandum 71-1-FBR, Air Force Flight Dynamics Laboratory, Jan. 1971.
- [9] Gallagher, J. P. and Stalnaker, H. D., "Methods for Analyzing Fatigue Crack Growth Rate Behavior Associated with Flight-By-Flight Loading," AIAA/SAE 15th Structures, American Institute of Aeronautics and Astronautics, Society of Automotive Engineers, Structural Mechanics and Materials Conference, Las Vegas, Nevada, April 1974.
- [10] Probst, E. P. and Hillberry, B. M., *AIAA Journal*, American Institute of Aeronautics and Astronautics, Vol. 12, No. 3, 1974, pp. 330-335.
- [11] Tucker, L. and Bussa, S., "The SAE Cumulative Fatigue Damage Test Program," Paper 750038, The Society of Automotive Engineers, 1975.
- [12] Rice, J. R. in *Fatigue Crack Propagation*, ASTM STP 415, American Society for Testing and Materials, 1967, pp. 247-309.
- [13] Stephens, R. I., McBurney, G. W., and Oliphant, L. J., *International Journal of Fracture*, Vol. 10, No. 4, 1974, pp. 587-589.
- [14] Stephens, R. I., Chen, D. K., and Hom, B. W. in *Fatigue Crack Growth Under Spectrum Loads*, ASTM STP 595, American Society for Testing and Materials, 1976, pp. 27-40.
- [15] Stephens, R. I., *International Journal of Fracture*, Vol. 12, No. 2, 1976, pp. 323-326.
- [16] Njus, G. O., "Fatigue Crack Growth in 4140 Steel as a Function of Yield Strength, Tensile Overload and Mean Stress," Master of Science Thesis, The University of Iowa, July 1976.
- [17] Musil, D. P. and Stephens, R. I., *Proceedings Fourth International Conference on Fracture*, Vol. 2, Waterloo, Canada, June 1977, pp. 1017-1024.

## DISCUSSION

---

*L. F. Impellizzeri*<sup>1</sup> (written discussion)—The use of compact tension specimens for evaluation of compression load effects causes uncertainties in data interpretation. There are two concerns. During the unloading portion of a cycle for any type of specimen, crack closure occurs at a positive load value. As the applied load is reduced below the closure value, crack surface contact stresses increase, and compression yielding occurs at the tip. This compressive yielding reduces the residual tensile deformation at the crack tip. Compression overloads, therefore, accelerate growth by reducing the beneficial tensile residual deformation. This effect is described in detail in the paper by Dill and Saff in this publication. Because of the limited crack surface length available for reacting compression loads in a compact tension specimen, the resulting contact stresses will be greater, causing more compressive yielding, and the residual tensile deformation

<sup>1</sup>Branch chief, Technology—Strength, McDonnell Aircraft Company, Saint Louis, Mo. 63166.

will be less than in a center-crack panel. Therefore, it is expected that the detrimental effects of compression loads will be exaggerated in a compact tension specimen as compared to a center-crack panel. The second concern is the potential for creating an unusual stress state at the crack tip due to what might be called pivoting about the back edge of the crack during compression loading. Whether or not pivoting occurred in this test program depends on load magnitudes and crack lengths, but it should be evaluated whenever compact tension specimens are loaded in compression.

*R. I. Stephens, E. C. Sheets, and G. O. Njus (authors' closure)*—The authors wish to thank Mr. Impellizzeri for raising a very important question concerning the application of compression loads to the compact tension (CT) specimen. Others have also questioned the use of the CT specimen using compression loadings [15]. The current proposed ASTM method of test for constant-amplitude crack growth rates below  $10^{-8}$  m/cycle restricts the CT specimen to only tensile loadings. However, the importance of compression in variable-amplitude load spectra cannot be neglected, particularly if retardation models are being used. Thus the choice of a proper test specimen with variable-amplitude load spectra involving compression is a very important problem.

Mr. Impellizzeri has raised two possible concerns with using the CT specimen in compression. His first concern indicates that the CT specimen may exaggerate the detrimental effects of compression loading, while his second concern deals with "pivoting" at the machined notch which will tend to reduce the detrimental effects. This latter concern, we feel, is by far the major and more realistic concern. That is, the CT specimen may give less damaging results from compression than other specimens.

Reference 15 provides limited comparative experimental data using compression loads in both single edge notch (SEN) and CT specimens of 2024-T3 and 7075-T6 aluminum. Tests involved both constant load amplitude crack growth tests and single tensile overloads with overload ratios, OLR, ranging from 2.0 to 2.3. Stress ratios  $R_l$  were 0,  $-1/2$ ,  $-1$ , and  $-2$ . Essentially, no differences existed in the results for both SEN and CT specimens. That is, under constant load amplitude conditions, crack growth rates were slightly increased by going from  $R_l = 0$  to  $R_l = -2$ , while retardation following single tensile overloads was substantially reduced as  $R_l$  varied from zero to  $-2$  for both CT and SEN specimens.

In addition, 4140 steel CT specimens with three different yield strengths of  $757 \text{ MN/m}^2$  (110 ksi),  $1136 \text{ MN/m}^2$  (165 ksi), and  $1412 \text{ MN/m}^2$  (205 ksi) have been tested subjected to constant stress intensity amplitude testing and  $a/w$  ranging from 0.34 to 0.7 [16]. Crack growth behavior was obtained optically at 0.25 mm (0.01 in.) increments.  $da/dN$  was essentially independent of crack length for all three yield strength levels for a given  $R_l$  ratio.  $R_l$  values tested were 0,  $-1/2$ , and  $-1$ . Crack growth rates increased as  $R_l$  varied from 0 to  $-1$ ; however,  $da/dN$  was more sensitive to yield

strength than to  $R_I$  for these constant stress intensity tests. This tends to partially negate concerns over using the CT specimen in compression when constant-amplitude testing is used. However, appreciable pivoting at the machined notch occurred in the  $757 \text{ MN/m}^2$  (110 ksi) steel following single tensile overloads applied at large crack lengths of  $a/w \geq 0.52$ . Here, retardation incorrectly was unaffected by the addition of compression loadings with  $R_I = 0, -1/2,$  and  $-1$  following single tensile overloads. Fractographic observations indicated appreciable pivoting existed at the machined notch region which decreased crack tip stressing.

In conclusion, concerning the CT specimens, we have found no experimental data at this time to invalidate negative stress ratio (Fig. 1*b, 1c*), constant-amplitude behavior, and single tensile overload behavior for overloads applied at small  $a/w$  values. The major error found in using the CT specimen in compression is with high tensile overloads applied at long crack lengths. Thus, we believe all the results of this paper are material characteristics and not just configuration characteristics.

W. J. Mills,<sup>1</sup> R. W. Hertzberg,<sup>2</sup> and R. Roberts<sup>2</sup>

# Load Interaction Effects on Fatigue Crack Growth in A514F Steel Alloy

---

**REFERENCE:** Mills, W. J., Hertzberg, R. W., and Roberts, R., "Load Interaction Effects on Fatigue Crack Growth in A514F Steel Alloy," *Cyclic Stress-Strain and Plastic Deformation Aspects of Fatigue Crack Growth*, ASTM STP 637, American Society for Testing and Materials, 1977, pp. 192-208.

**ABSTRACT:** Variable-amplitude fatigue tests of A514F steel alloy were performed within a linear-elastic fracture mechanics framework in order to characterize the retardation response of a cyclic strain softening material. Results of single and multiple overload tests on A514F steel alloy suggested that a material's cyclic properties have little effect on the phenomenology of retardation behavior. For instance, single high load excursions (of different magnitudes and at different baseline  $\Delta K$  levels) in this cyclic strain softening alloy caused fatigue crack growth rate retardation trends comparable to those exhibited by 2024-T3 aluminum, a cyclic strain hardening alloy. In addition, under complex loading conditions, the A514F steel alloy, like the 2024-T3 aluminum alloy, exhibited maximum interaction between single peak load excursions when two peak cycles were separated by a small distance.

Additional retardation caused by a greater number of overload cycles more than compensated for increased crack extension during the high load excursions. Electron fractographic results are presented and discussed in terms of the macroscopic crack growth rate findings.

**KEY WORDS:** stresses, strains, fatigue (materials), crack propagation, loads, retarding, striations, closures, fractography, steel alloys

## Nomenclature

- $a$  Crack length
- $a'$  Increment of crack extension separating peak loads
- $a^*$  Size of region affected by a single peak overload
- $a_1^*$  Size of region affected by the first overload

<sup>1</sup>Research engineer, Hanford Engineering Development Laboratory, Westinghouse Hanford Company, Richland, Wash. 99352.

<sup>2</sup>Professor, Department of Metallurgy and Materials Science, and professor, Department of Mechanical Engineering and Mechanics, respectively, Lehigh University, Bethlehem, Pa. 18015.

- $a_2^*$  Size of region affected by the second overload  
 $a_{OL1}$  Crack extension during application of first overload  
 $a_{OL2}$  Crack extension during application of second overload  
 $\Delta ar = a_{OL1} + a' + a_{OL2} + a_2^*$  when  $a' < a_1^*$   
 $= a_{OL1} + a_1^* + a_{OL2} + a_2^*$  when  $a' > a_1^*$   
 $a'_{min}$  Distance from an overload where fatigue crack propagation rates reached a minimum  
 $b_1$  Fatigue crack growth rate prior to overload  
 $b_2$  Steady-state fatigue crack growth rate following overload  
 $da/dN$  Fatigue crack propagation rate  
 $K$  Stress intensity factor  
 $\Delta K_b$  Baseline stress intensity range  
 $K_{max_{OL}}$  Maximum stress intensity factor associated with an overload  
 $\Delta K_{max}$  Maximum stress intensity range associated with an overload  
 $\Delta K_{PL} = \Delta K_{max} - \Delta K_b$   
 $N$  Number of applied cycles  
 $N^*$  Number of cycles required to propagate a crack through the overload-affected region,  $a^*$   
 $N_d^*$  Number of delay cycles over which there was effectively no fatigue crack propagation  
 $N_{d2}^*$  Number of delay cycles following a second overload over which there was effectively no fatigue crack propagation  
 $\%_{PL}$  Percent peak load ( $= (\Delta K_{PL} / \Delta K_b) \times 100$ )  
 $2r_y$  Overload plastic zone size  
 $\sigma_{ys}$  Yield strength

Overload interaction effects on fatigue crack propagation (FCP) retardation have been observed in numerous investigations [1-31].<sup>3</sup> Three of these studies [22,27,29] have reported that the monotonic yield strength strongly influences FCP retardation. In light of this finding, it seems reasonable to expect that cyclic properties would influence delay also, especially since constant-amplitude fatigue behavior has been related to a material's cyclically stabilized mechanical response [32-34]. To date, the effect of cyclic properties on fatigue crack retardation has not been characterized.

Since crack closure and compressive residual stress concepts are related to material behavior in the vicinity of the crack tip, cyclically stabilized mechanical properties within the plastic zone could possibly affect retardation phenomena. For instance, the tensile displacements formed during an overload may "smash down" more quickly in a cyclic strain softening material, thereby resulting in less crack closure and delay. Furthermore, since material directly ahead of a crack front cyclically softens or hardens, depending on a material's cyclic response, it would be of interest to examine the effect of multiple overloads and complex combinations of peak excursions on delay as a function of cyclic properties.

<sup>3</sup>The italic numbers in brackets refer to the list of references appended to this paper.

Consequently, the objective of this investigation is to characterize single peak overload retardation behavior of A514F steel, a cyclic strain softening alloy [32,35], and compare this response with that reported elsewhere [7,30,31] for 2024-T3 aluminum, a cyclic strain hardening alloy [35,36]. In addition, delay behavior resulting from block loading and complex loading conditions in A514F steel will be investigated; here again, potential differences in the retardation phenomenology exhibited by the steel and aluminum alloys will be examined [31].

### Experimental Procedure

Compact tension specimens (3.2 by 76.2 by 76.2 mm) of ASTM A514F steel alloy, oriented in a longitudinal (LT) direction were fatigue tested in a 20-kip electrohydraulic closed-loop testing machine at a cyclic frequency of 10 Hz. Throughout each test, cycling was interrupted periodically to measure the increment of crack extension (with a Gaertner traveling microscope) and the associated number of cycles. All testing was performed under constant  $\Delta K_b$  conditions similar to the procedure outlined by Von Euw et al [7], Trebules et al [8], and Mills et al [30,31].

Delay behavior in A514F steel was determined by introducing single 50, 75, and 100 percent peak overloads (frequency  $\approx 0.2$  Hz) at various  $\Delta K_b$  conditions ranging from 33 to 65.9  $\text{MPa}\sqrt{\text{m}}$  (Fig. 1a). Fracture surface

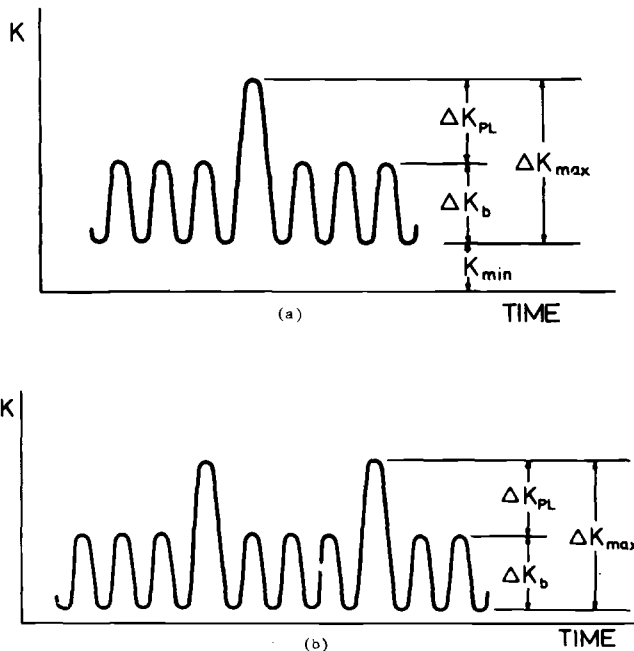


FIG. 1—Schematic representation of tests performed during the current investigation.

micromorphology was characterized by fractographic examination of standard two-stage platinum-carbon replicas on an electron microscope (Philips EM300) at an acceleration potential of 80 kV.

Multiple overload effects were studied by applying block overloads ( $\Delta K_b = 44 \text{ MPa}\sqrt{\text{m}}$ , %PL = 75 percent) ranging from 1 to 1000 peak load cycles. When the number of high load excursions was ten or less, they were introduced manually at a frequency of 0.2 Hz. 100 and 1000-cycle block overloads were applied at a frequency of 1.0 Hz, with loads being shed every 0.2 mm of crack extension to maintain constant  $\Delta K$  conditions.

Complex loading conditions were simulated by introducing a second overload ( $\Delta K_b = 44 \text{ MPa}\sqrt{\text{m}}$ , %PL = 75 percent, frequency  $\approx 0.2$  Hz) after the fatigue crack had extended various distances,  $a'$ , into the region affected by a previously applied high load excursion of equal magnitude (Fig. 1b).

## Presentation and Discussion of Results

### *Effect of Single Peak Overloads on FCP Rates*

Results from single peak overload tests conducted on A514F steel with  $\Delta K_b$  ranging from 33 to 65.9  $\text{MPa}\sqrt{\text{m}}$  (%PL = 50, 75, 100 percent) are reported in Table 1 and Fig. 2. The overall retardation behavior exhibited by this cyclic strain softening alloy (Fig. 2) is similar to that reported in 2024-T3 aluminum alloy (Ref 7: Fig. 11). Note that the steel, like the aluminum alloy, exhibited a rapid increase in  $N_d^*$  at higher  $\Delta K_b$  levels (100 percent PL) which is believed to be associated with a change in stress state from plane strain to plane stress [30]. In addition, the A514F steel alloy exhibited an excellent correlation (Fig. 3) between the experimentally determined affected zone size,  $a^*$ , and the calculated plastic zone size,  $2r_p$ , comparable to that observed in 2024-T3 aluminum alloy [7,30]. (The Dugdale model [37] was used to calculate the size of the overload plastic zone

TABLE 1—Summary of delay behavior resulting from multiple overloads in A514F steel ( $\Delta K_b = 44 \text{ MPa}\sqrt{\text{m}}$ , %PL = 75 percent).

Specimen	Number Overload Cycles	$a^*$ , mm	$\Delta a_T / N_d$ , ( $10^{-4}$ mm/cycle)	$N_d^*$ , $10^3$ cycle
Single Peak Overload				
7A	1	4.8	3.84	12.5
1-12A	1	4.5	3.75	12
1-14A	1	4.2	3.36	12.5
Multiple Overloads				
4A	2	4.3	3.07	14
7	10	4.3	2.15	20.5
5A	100	4.5	1.33	37
6	1000	5.5	0.54	165

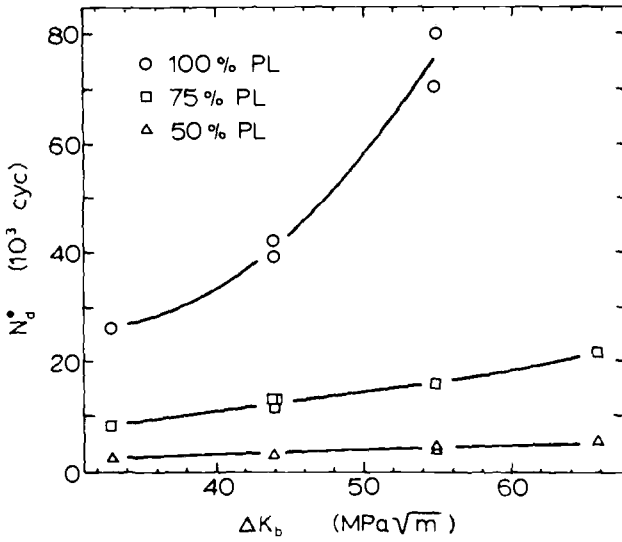


FIG. 2—Number of delay cycles as a function of the baseline stress intensity range.

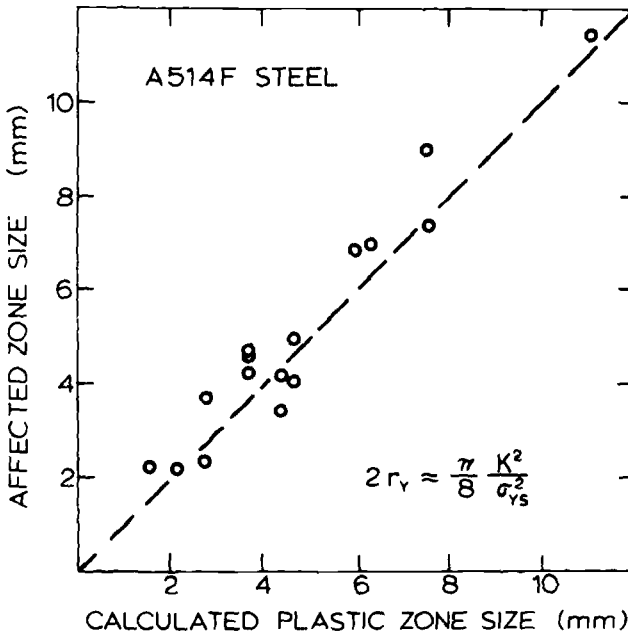


FIG. 3—Plot illustrating correlation between the experimentally determined affected zone size,  $a^*$ , and the calculated plastic zone size,  $2r_y$ , as computed with the Dugdale model. ( $\sigma_{ys} = 814$  MPa).

in the A514F steel alloy since experimentally determined plastic zone sizes in steel alloys are in good agreement with this model [37,38].)

Based on these observations, it is concluded that A514F steel, a cyclic strain softening material, exhibited comparable delay phenomenology to that observed in 2024-T3 aluminum, a cyclic strain hardening alloy, for conditions involving single peak overloads. Furthermore, the extent of the delay region in both materials is related to the overload plastic zone dimension.

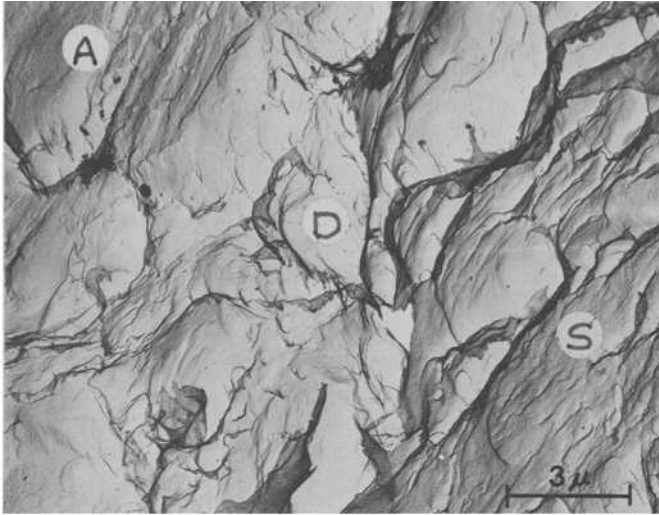
Examination of steel fracture surfaces revealed that the overload region (Fig. 4) was characterized by a duplex dimple structure [39-41], followed by limited evidence of abrasion. A well-defined stretch zone does not appear in this region, thereby making it difficult to identify the area where the peak load was introduced. This phenomenon is believed to be related to the fact that striations in steel alloys are generally poorly defined (note the ill-defined fatigue striations (Fig. 4a) formed under constant  $\Delta K_b$  loading prior to the high load excursion).

In the region affected by a single peak load,  $a^*$ , the fracture surface exhibited considerable evidence of abrasion and fatigue fissures; only a limited amount of faceted appearance was observed in contrast to that found in the 2024-T3 aluminum alloy [30,31,42]. Under low  $\Delta K_b$  conditions, the amount of abrasion was relatively slight (Fig. 5a), whereas, under high  $\Delta K_b$  conditions, increased evidence of heavy abrasion (Fig. 5b) was observed, indicative of enhanced crack closure and compressive residual stresses. This behavior is in agreement with the macroscopic FCP response where maximum retardation resulted at higher  $\Delta K_b$  levels. Near the end of the affected region, only a limited amount of abrasion was noted, here again consistent with crack closure concepts and the results for the 2024-T3 aluminum alloy [7,30].

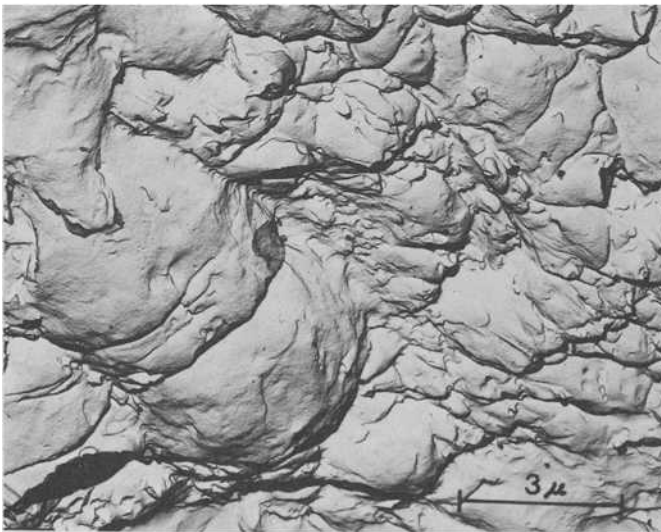
Fatigue fissures and striations were also found in the overload-affected region. Immediately following a peak load cycle (up to  $\approx a^*/4$ ), ill-defined fatigue fissures (Fig. 6a), the deepest feature associated with fatigue striations [43,44], were all that remained after interference of tensile displacements which formed during the high load excursion. However, near the end of the affected region, striations were better defined (Fig. 6b). Recall that a limited amount of abrasion was observed in this area; hence, striations were not obliterated since the amount of rubbing of the fracture surfaces in this region was less extensive.

#### *Effect of Multiple Overloads on FCP Rates*

Results of multiple overload tests on A514F steel ( $\Delta K_b = 44 \text{ MPa}\sqrt{\text{m}}$ , %PL = 75 percent), reported in Table 1, indicate that the number of delay cycles significantly increased as the number of high load excursions increased (a single peak overload caused a 12 000-cycle delay, while a 1000-cycle block overload resulted in 165 000 cycles of delay). This observation is



(a)

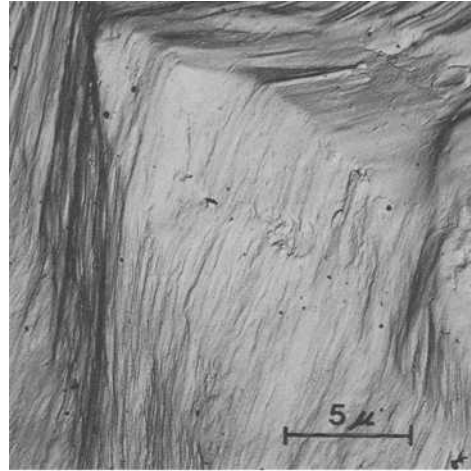


(b)

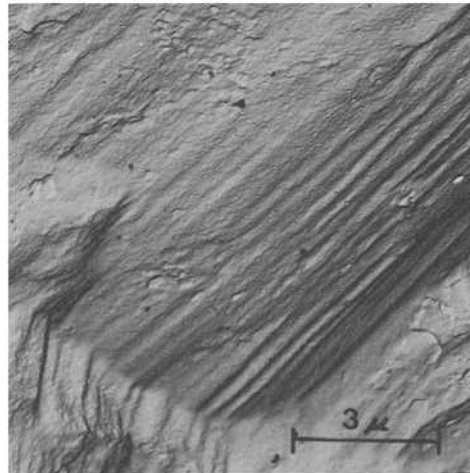
- (a) Poorly defined fatigue striations (*S*), followed by dimples (*D*), followed by light abrasion (*A*) ( $\Delta K_b = 44 \text{ MPa}\sqrt{\text{m}}$ , %PL = 75 percent).
- (b) Duplex dimple structure ( $\Delta K_b = 54.9 \text{ MPa}\sqrt{\text{m}}$ , %PL = 100 percent).

FIG. 4—Electron fractographs revealing the overload region.

consistent with the multiple overload response observed by Trebules et al [8] in 2024-T3 aluminum.



(a)

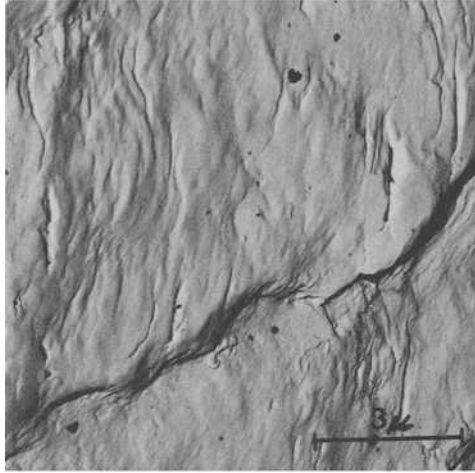


(b)

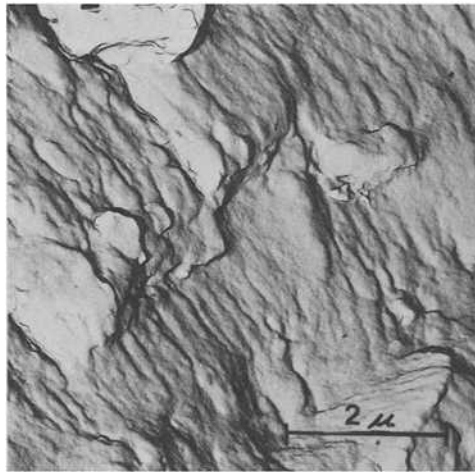
- (a) Low  $\Delta K_b$  conditions ( $\Delta K_b = 44 \text{ MPa}\sqrt{\text{m}}$ , %PL = 75 percent).  
 (b) High  $\Delta K_b$  conditions ( $\Delta K_b = 65.9 \text{ MPa}\sqrt{\text{m}}$ , %PL = 75 percent).

FIG. 5—Electron fractographs illustrating evidence of abrasion in the overload-affected region.

To better understand the total effect of multiple overloads, retardation data were normalized by a parameter introduced in Ref 31,  $\Delta a_T / N_d^*$ —the total crack length affected by the overload (including crack extension during the application of the high load excursions) divided by the number of delay cycles. As pointed up in Ref 31, this ratio represents the total crack extension required to produce a given  $N_d^*$ . Hence, any loading conditions



(a)



(b)

- (a) Ill-defined fatigue fissures observed in the region immediately following the peak load excursion.
- (b) Fatigue striations observed near the end of the affected zone,  $a^*$ .

FIG. 6—Electron fractographs revealing cyclic markings in the overload-affected zone ( $\Delta K_b = 54.9 \text{ MPa}\sqrt{m}$ , %PL = 100 percent).

that would minimize  $\Delta a_T / N_d^*$  would enhance the overall fatigue performance of a structure. Table I reveals that this ratio decreases as the number of high load excursions in the block overload increases, thereby suggesting that the beneficial effects resulting from the increased number of over-

loads more than compensate for the additional crack extension associated with peak load excursions.

Fatigue crack propagation behavior through the region affected by multiple overloads (Fig. 7) in A514F steel was consistent with that observed in 2024-T3 aluminum (Ref 8: Fig. 13). As expected, a greater number of over-

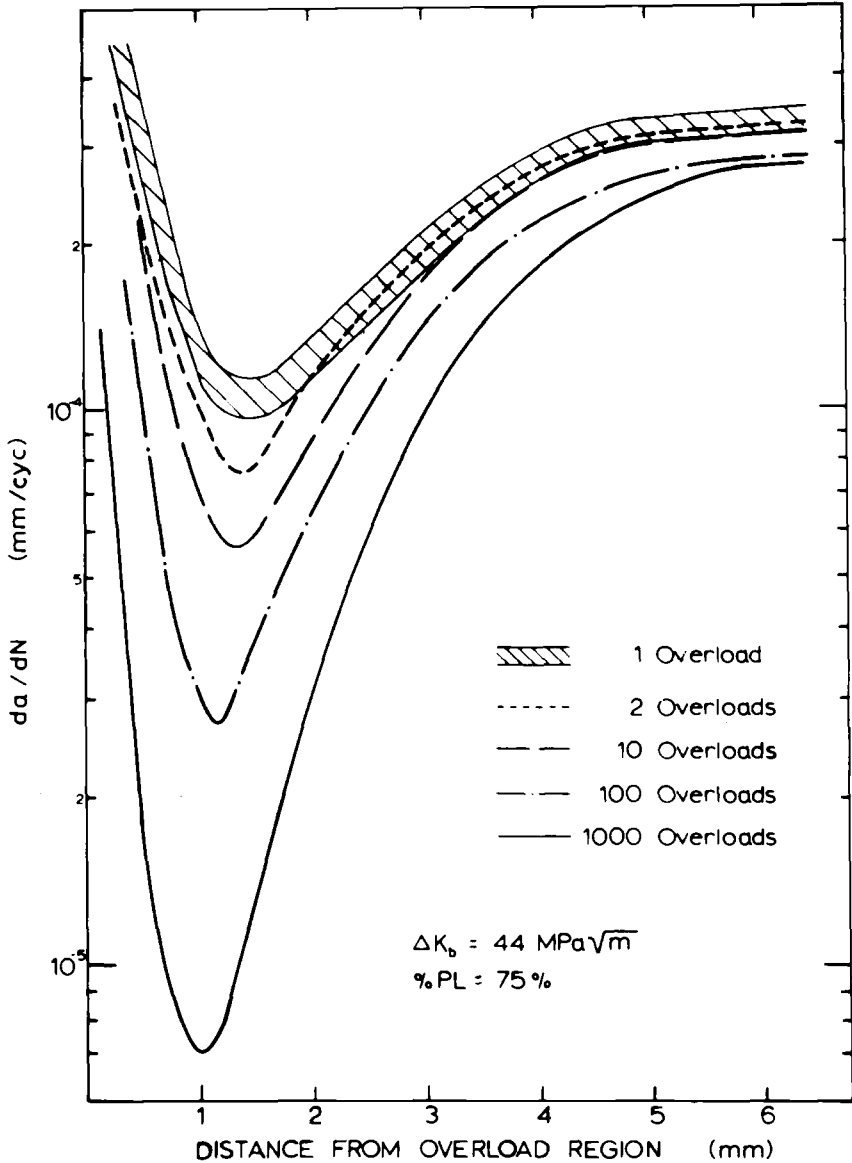


FIG. 7—FCP response through the region affected by multiple overloads in A514F steel alloy.

loads resulted in a considerably deeper growth rate "trough" which was responsible for enhanced delay. In addition, it should be noted that the growth rate trough was found to shift slightly toward the origin (the location of the high load excursions) as the number of overload cycles increased.

### Complex Peak Load Interaction Effects

Retardation behavior of A514F steel resulting from two single 75 percent peak overloads separated by a distance  $a'$  (Table 2; all complex overload terminology is defined in Fig. 8) is comparable to that exhibited by 2024-T3 aluminum alloy [31]. For instance, when a second high load excursion immediately followed the first, delay (14 000 cycles) was slightly greater than that associated with a single peak load (12 000 to 12 500 cycles). Retardation after the second overload (Fig. 9),  $N_{d_2}^*$ , increased with increasing  $a'$ , reaching a maximum value when  $a' = a'_{\min}$  ( $a'_{\min}$  represents the distance from the location of a single peak overload where FCP rates reach a minimum value; see scatter band in Fig. 10,  $a'_{\min} = 1.36$  mm). As  $a'$  was increased beyond 1.36 mm,  $N_{d_2}^*$  decreased until the two overloads acted independently.

The amount of crack extension required to eliminate interaction between overloads was two to three times  $a^*$ . This phenomenon was more fully characterized by introducing a second overload at  $a' = 5.02$  mm after the tensile displacements resulting from the first peak excursion were removed by a jeweler's saw cut (Specimen 12).  $N_{d_2}^*$  (Fig. 9) returned from 16 000 cycles, normally associated with this loading condition (Specimen 4), to 11 500 cycles, consistent with isolated single peak load results, thereby indicating that interaction of two overloads results from interference of tensile dis-

TABLE 2—Summary of delay behavior resulting from complex overloads in A514F steel ( $\Delta K_b = 44 \text{ MPa}\sqrt{\text{m}}$ , %PL = 75 percent).

Specimen	$a'$ , mm	$a_1^*$ , mm	$a_2^*$ , mm	$\Delta a_T / N a^*$ , $10^{-4}$ mm/cycle	$N_{d_2}^*$ , $10^3$ cycle	$N_{d_1}^*$ , $10^3$ cycle
Single Peak Overloads						
7A	...	4.8	...	3.84	...	12.5
1-12A	...	4.5	...	3.75	...	12
1-14A	...	4.2	...	3.36	...	12.5
Complex Overload Interactions (Interaction Between Single Peak Overloads)						
4A	0.00	...	4.3	3.07	14	14
17A	0.73	...	4.4	2.77	18	18.5
10	1.36	...	4.3	2.51	19.5	22.5
5	2.46	...	4.8	2.85	17	25.5
4	4.30	...	4.6	3.29	16	27
12A	7.53	4.5	4.2	3.28	14.5	26.5
14A	9.88	4.2	4.3	3.47	12	24.5
12 $\Delta a$	5.02	4.3	4.3	3.74	11.5	23

$a_{12\Delta}$  = Tensile displacements resulting from first overload were removed by a saw cut prior to the application of the second overload.

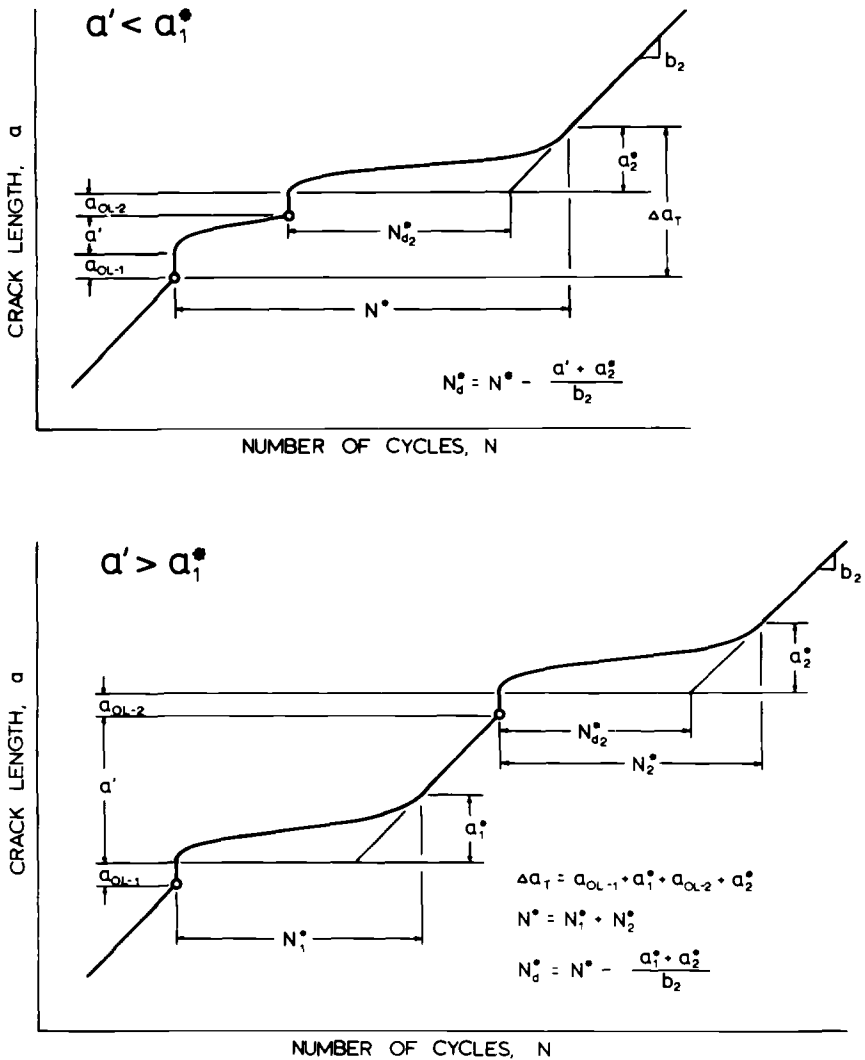


FIG. 8—Definition of overload terminology.

placements produced during the first high load excursion. This finding is similar to that reported previously for the 2024-T3 aluminum alloy [31].

Figure 10, which illustrates fatigue crack growth behavior following the second overload, reveals that the lowest FCP rates resulted when the distance between overloads was  $a_{min}^1$ . This behavior is consistent with finding maximum retardation when  $a^1 \approx a_{min}^1$ . In addition, note that the growth rate trough was shifted toward the origin as the distance separating the high load excursions was increased, here again in agreement with previous findings

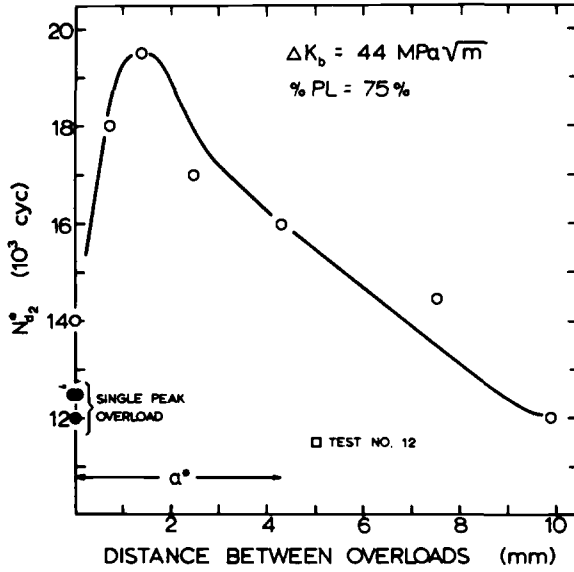


FIG. 9—Number of delay cycles following the second overload,  $N_{a_2}^*$ , as a function of distance between overloads,  $a'$ .

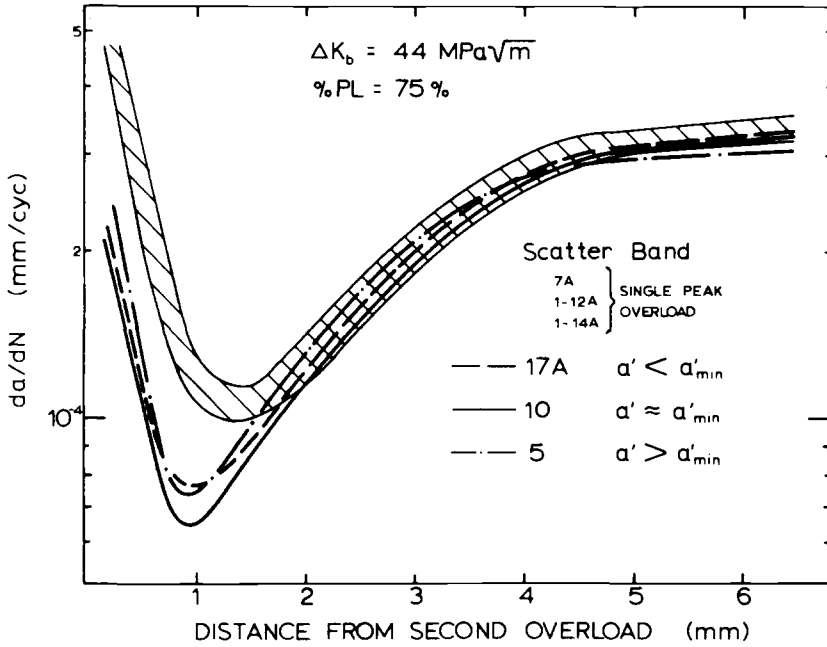


FIG. 10—FCP behavior following the second overload for various values of  $a'$ .

[31]. (Recall that this same behavior was observed following multiple overloads—see Fig. 7.)

The total amount of delay,  $N_d^*$  (Fig. 11), increases very rapidly as  $a'$  increases, reaching a maximum value at  $a' \approx a^*$  (4.3 mm). By further increasing  $a'$  beyond  $a^*$ ,  $N_d^*$  decreases to 24 500 cycles (at  $a' = 9.88$  mm) where the two overloads acted as isolated events. To better understand the overall interaction phenomena, retardation data were normalized by the delay parameter  $\Delta a_T / N_d^*$  (Fig. 12). A minimum  $\Delta a_T / N_d^*$  ratio resulted when the two overloads were separated by a distance  $a'_{\min}$ , here again consistent with the behavior observed in 2024-T3 aluminum [31].

It is tempting at this point to speculate as to what causes the maximum overall interaction to occur when the second overload is placed a distance from the first overload equal to the location of the trough shown in Fig. 10. Since the fatigue crack growth rate varies with the prevailing  $\Delta K$  level at the crack tip, a plot of  $\Delta K$  versus distance from the first overload should possess the same form as shown in Fig. 10. Consequently,  $\Delta K$  (considered in this context to be an effective value and less than  $\Delta K_{\text{applied}}$ ) is seen to be a minimum at the point of minimum crack growth rate. Combining this with the fact that fatigue delay increases with the percent overload (Fig. 2) where

$$\%PL = \Delta K_{PL} / \Delta K_b \times 100$$

the maximum effective  $\%PL$  occurs at the growth rate trough. Thus maximum delay due to the second overload should occur at this point.

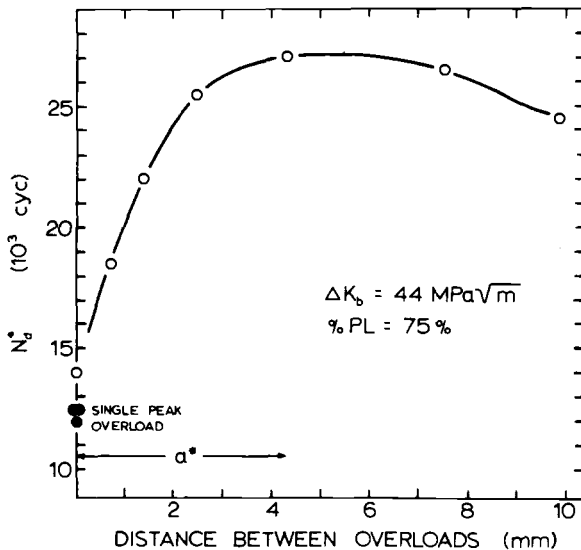


FIG. 11—Total delay,  $N_d^*$ , associated with two peak overloads separated by a distance  $a'$ .

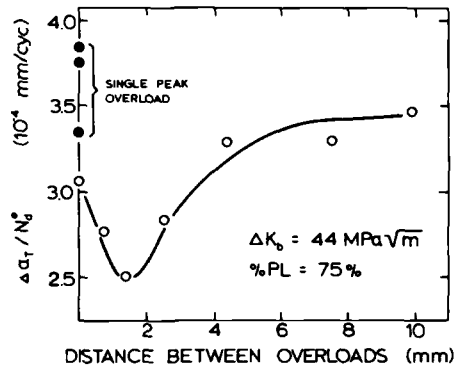


FIG. 12—Retardation parameter  $\Delta a_T / N_d^*$  as a function of distance between single peak overloads,  $a'$ .

### Conclusions

Based on the experimental results and subsequent discussion, the following conclusions have been drawn:

1. The overall FCP retardation trends resulting from single and multiple overloads in A514F steel were similar to those exhibited by 2024-T3 aluminum alloy, thereby suggesting that the phenomenology of FCP delay response is independent of a material's cyclic properties.
2. Additional retardation caused by a greater number of overload cycles more than compensated for increased crack extension during the high load excursions.
3. Maximum interaction between two isolated overloads occurred when the peak excursions were separated by a distance  $a'_{min}$ , here again consistent with the behavior observed in 2024-T3 aluminum alloy.

### References

- [1] Hardrath, H. F. and McEvily, A. T., *Proceedings of the Crack Propagation Symposium*, Vol. 1, Canfield, England, Oct. 1961.
- [2] Hudson, C. M. and Hardrath, H. F., "Effects of Changing Stress Amplitude on the Rate of Fatigue Crack Propagation of Two Aluminum Alloys," NASA Technical Note D-960, National Aeronautics and Space Administration, Sept. 1961.
- [3] Schijve, J. and Broek, D., *Aircraft Engineering*, Vol. 34, 1962, p. 314.
- [4] Schijve, J., Broek, D., and de Rijk, P., "Crack Propagation under Variable Amplitude Loading," NLR Report M 2094, Nationaal Lucht-En Ruimtevaartlaboratorium, Jan. 1962.
- [5] Christensen, R. H., *Metal Fatigue*, McGraw Hill, New York, 1959.
- [6] Elber, W., *Damage Tolerance in Aircraft Structures*, ASTM STP 486, American Society for Testing and Materials, 1971, p. 230.
- [7] Von Euw, E. F. J., Hertzberg, R. W., and Roberts, R., *Stress Analysis and Growth of Cracks*, ASTM STP 513, American Society for Testing and Materials, 1972, p. 230.

- [8] Trebules, V. W., Jr., Roberts, R., and Hertzberg, R. W., *Progress in Flow Growth and Fracture Toughness Testing, ASTM STP 536*, American Society for Testing and Materials, 1973, p. 115.
- [9] Schijve, J., *Engineering Fracture Mechanics*, Vol. 5, 1973, p. 269.
- [10] Wei, R. P., Shih, T. T., and Fitzgerald, J. H., "Load Interaction Effects on Fatigue Crack Growth in Ti-6 Al-4 V Alloy," NASA CR-2239, National Aeronautics and Space Administration, 1973.
- [11] Jonas, O. and Wei, R. P., *International Journal of Fracture Mechanics*, Vol. 7, 1971, p. 116..
- [12] Schijve, J., *Advances in Aeronautical Science*, Vol. 3, 1961, p. 387.
- [13] Porter, T. R., *Engineering Fracture Mechanics*, Vol. 4, 1972, p. 717.
- [14] Katcher M., *Engineering Fracture Mechanics*, Vol. 5, 1973, p. 793.
- [15] Rice, R. C. and Stephens, R. I., *Progress in Flaw Growth and Fracture Toughness Testing, ASTM STP 536*, American Society for Testing and Materials, 1973, p. 95.
- [16] Vargas, L. G. and Stephens, R. I., *Third International Conference on Fracture*, Munich, Germany, 1973.
- [17] Stephens, R. I., McBurney, G. W., and Oliphant, L. J., *International Journal of Fracture Mechanics*, Vol. 10, 1974, p. 587.
- [18] Mathews, W. T., Baratta, F. I., and Driscoll, G. W., *International Journal of Fracture Mechanics*, Vol. 7, 1971, p. 224.
- [19] Jones, R. E., *Engineering Fracture Mechanics*, Vol. 5, 1973, p. 585.
- [20] Corby, D. M. and Packman, P. F., *Engineering Fracture Mechanics*, Vol. 5, 1973, p. 479.
- [21] Smith, S. H., *Structural Fatigue in Aircraft, ASTM STP 404*, American Society for Testing and Materials, 1966, p. 74.
- [22] Gallagher, J. P. and Hughes, T. F., "Influence of Yield Strength on Overload Affected Fatigue Crack Growth Behavior in 4340 Steel," AFFDL-TR-74-27, Air Force Flight Dynamics Laboratory, 1974.
- [23] Shih, T. T. and Wei, R. P., "Load and Environment Interactions in Fatigue Crack Growth," Contract Nonr N00014-67-A-0370-0008, NR036-097, Lehigh University, 1974.
- [24] Schijve, J., *Engineering Fracture Mechanics*, Vol. 6, 1974, p. 245.
- [25] Lankford, J. and Davidson, D. L., *Journal of Engineering Materials and Technology, Transactions*, American Society of Mechanical Engineers, 1976, p. 17.
- [26] Pitoniak, F. J., Grandt, A. F., Montulli, L. T., and Packman, P. F., *Engineering Fracture Mechanics*, Vol. 6, 1974, p. 663.
- [27] Petrak, G. J., *Engineering Fracture Mechanics*, Vol. 6, 1974, p. 725.
- [28] Shih, T. T. and Wei, R. P., *Journal of Testing and Evaluation*, American Society for Testing and Materials, 1975, p. 46.
- [29] Nisitani, H. and Takao, K., *Proceedings of the Kyoto 1973 Symposium on Mechanical Behavior of Materials*, 1973, p. 119.
- [30] Mills, W. J. and Hertzberg, R. W., *Engineering Fracture Mechanics*, Vol. 7, 1975, p. 705.
- [31] Mills, W. J. and Hertzberg, R. W., *Engineering Fracture Mechanics*, Vol. 8, 1976, p. 657.
- [32] Hickerson, J. P. and Hertzberg, R. W., *Metallurgical Transactions*, Vol. 3, 1972, p. 179.
- [33] Majumdar, S. and Morrow, J. D., *Fracture Toughness and Slow-Stable Cracking, ASTM STP 559*, American Society for Testing and Materials, 1974, p. 159.
- [34] Tomkins, B., *Philosophical Magazine*, Vol. 18, 1968, p. 1041.
- [35] Tucker, L. E., Landgraf, R. W., and Brose, W. R., "Proposed Technical Report on Fatigue Properties for the SAE Handbook," Automotive Engineering Congress, Detroit, Mich., 1974.
- [36] Endo, T. and Murrow, JoDean, *Journal of Materials*, Vol. 4, 1969, p. 159.
- [37] Dugdale, D. S., *Journal of the Mechanics and Physics of Solids*, Vol. 8, 1960, p. 100.
- [38] Hahn, G. T. and Rosenfield, A. R., *Acta Metallurgica*, Vol. 13, 1965, p. 293.
- [39] Rogers, H. C., *Ductility*, American Society for Metals, Cleveland, 1968, p. 31.
- [40] Tanaka, J. P., Pampillo, C. A., and Low, J. R., Jr., *Review of Developments in Plane Strain Fracture Toughness Testing, ASTM STP 463*, American Society for Testing and Materials, 1970, p. 191.
- [41] Cox, T. B. and Low, J. R., Jr., *Metallurgical Transactions*, Vol. 5, 1974, p. 1457.

- [42] Hertzberg, R. W. and Mills, W. J., *Fractography—Microscopic Cracking Processes*, ASTM STP 600, American Society for Testing and Materials, 1976, p. 220.
- [43] Beachem, C. D., *Transactions of the American Society for Metals*, Vol. 60, p. 324.
- [44] Broek, D., *Engineering Fracture Mechanics*, Vol. 1, 1970, p. 691.

# Critical Remarks on the Validity of Fatigue Life Evaluation Methods Based on Local Stress-Strain Behavior

---

**REFERENCE:** Schutz, D. and Gerharz, J. J., "Critical Remarks on the Validity of Fatigue Life Evaluation Methods Based on Local Stress-Strain Behavior." *Cyclic Stress-Strain and Plastic Deformation Aspects of Fatigue Crack Growth, ASTM STP 637*, American Society for Testing and Materials, 1977, pp. 209–223.

**ABSTRACT:** The conventional fatigue analysis using nominal stresses and Miner's rule is known to give inaccurate life predictions. It has been speculated that the major deficiencies can be overcome if local stresses and strains in the immediate vicinity of a stress raiser, instead of nominal stresses, are considered in the estimation of fatigue life. At present, there are a number of proposals which consider local stress-strain concepts, some of which are already developed to a state of practical applicability. In this paper, the best-known concepts are reviewed. It was found that all methods involving the determination of the stress-strain behavior at the notch root retained the conventional methods for computing damage accumulation. The question which arises is: What improvement in life prediction can be expected eventually when the correct local stress-strain history is known, but the damage due to local stress-strain cycles is linearly accumulated?

Open-hole specimens of the aluminum alloys 2024-T3 and 7075-T6 were subjected to a flight-by-flight load program. The corresponding local strain and stress histories were determined by local strain measurements and the companion specimen method, respectively. Fatigue life was estimated by three different methods using: (a) the local stress cycles and unnotched specimen applied stress-cycles to failure (*S-N*) data, (b) the nominal stress cycles and *S-N* data from prestressed open-hole specimens, and (c) for comparison, the nominal stress cycles and *S-N* data from the open-hole specimen. In each case the damage was linearly accumulated.

For the flight-by-flight testing sequences, the companion specimen method indicated that the residual stresses at the notch root stabilized asymptotically to a limiting value at between 5 and 20 percent of the life-to-crack initiation. Virgin open-hole specimens were also prestressed to develop, at the hole, the stress-strain status of the stabilized residual stresses determined previously during flight-by-flight loading. The prestressed specimens were subjected to constant amplitude loading and the resulting lives used for the damage calculation in Method B.

The ratios of test life to estimated life obtained using the three methods were compared and the following conclusions drawn: with increasing accuracy of the incorporation of local stress-strain behavior in future analysis methods (and using linear damage accumulation), the predicted life may still differ from the actual life. The estimated lives may be both conservative and unconservative, so that a scatter of life estimates of 1:3.0 is possible. This is, however, smaller than that of the life estimates using the conventional nominal stress concept which was found to be 1:6.0.

<sup>1</sup>Chief, Research Group for Structural Concepts and Methods of Life Estimation, and fatigue research engineer, Laboratorium für Betriebsfestigkeit, Darmstadt, Germany.

**KEY WORDS:** stresses, strains, fatigue life, stress concentration, cyclic loads

Life prediction is a task which requires, at least, the specification of local stress-strain behavior and of a method of fatigue damage accumulation. The concepts on which these requirements are based should be verified by appropriate testing procedures. Whereas in the last decade, fatigue research workers have advanced in the determination of local stress-strain histories [1-5]<sup>2</sup> a method of damage accumulation which is consistently better than the Palmgren-Miner linear hypothesis [6] has not yet been found.

For the crack propagation stage of the fatigue process, an encouraging approach has been developed recently in the United States (see Ref 7, for example) in which load sequence effects are allowed for by considering deformation processes in the crack tip plastic zone. Further advances in assessing the general applicability of this method will be possible with continued systematic observations of crack propagation rates under complex loading sequences. However, during crack initiation, the physical phenomena of damage accumulation during cyclic fatigue loading cannot be observed and impede the development of a more reliable damage accumulation rule than that of Palmgren-Miner. Therefore, in the near future, the fatigue analyst will have no choice but to accept the deficiencies and limitations of this rule.

This paper deals with the fatigue lives predicted using different methods for defining local stress histories, yet retaining the linear method of cumulative damage assessment. It compares the results with those of fatigue tests under flight-by-flight loading typical of that experienced by the wing lower surface of transport airplanes.

## **Life Prediction**

### *Nominal Stress Fatigue Analysis*

Most of the common methods of fatigue life evaluation are based on the use of nominal stresses. These methods frequently have resulted in inaccurate life prediction. For structural parts subjected to constant-amplitude loading, the major reason is the lack of real equivalence of fatigue behavior between large structures and small specimens, that is, there is no constancy of the ratio  $K_t/K_f$  (where  $K_t$  = stress concentration factor and  $K_f$  = fatigue notch factor) between structure and specimens either at different lives or different mean stresses. Under variable-amplitude loading, the basic problem is associated with the residual stresses developed at stress concentrators. Peak loads cause local plastic deformation at notch roots, and the surrounding elastic material tries to force the strain remaining in the plastically deformed regions to return to zero during the reversed loading part of the

<sup>2</sup>The italic numbers in brackets refer to the list of references appended to this paper.

cycle. During subsequent loading at a lower level, these residual stresses will then shift the corresponding notch root stress. The development and behavior of these induced residual stresses are not considered in the nominal stress fatigue analysis.

### *Local Stress Fatigue Analysis*

These shortcomings of the nominal stress analysis methods can be overcome if the fatigue life estimation is based on the actual notch root stresses and strains instead of nominal stresses ( $S = F/A$ ;  $S$  = nominal stress,  $F$  = load, and  $A$  = area of net section). Several life estimation procedures have been developed that include local cyclic stress-strain behavior. Although these procedures are relatively new and more experience regarding their applicability must be gathered, it can now be predicted that the more recent local stress procedures will replace nominal stress procedures.

Fatigue life estimation using local stress fatigue analysis procedures can be subdivided into two parts:

1. The notch root stresses and strains under service loading are determined. The result is a presentation of local stress-strain sequence or a continuous illustration of notch root stress-strain hysteresis loops.

2. The stress-strain sequence is split up into individual load cycles, that is, ranges of stress or strain with corresponding mean values. The damage contributed by each cycle is determined and accumulated to give the total damage. Some of the local stress analysis methods known from the literature [1-5] will now be reviewed briefly, but we will restrict ourselves to analysis programs already available.

The characteristics of the various local stress analysis methods are summarized in Figs. 1 and 2 for the first and second parts just mentioned, respectively. Although there are apparent differences in both the various parameters and their treatment, the authors of the different proposals do agree on the application of Neuber's rule in the first part and of Miner's rule in the second part. Thus the values of partial damage are derived differently but in every case summed linearly to obtain total damage. One exception is made by the authors of Ref 1 who decompose total life into two parts and use different applied stress-cycles to failure ( $S-N$ ) curves for damage accumulation within the resulting life spans.

However, there is no simple correlation between the various sections of the individual local stress-life estimation proposals, and it is difficult to check and compare the correctness of the individual assumptions made in each instance. Usually, each of these procedures has been assessed by comparing the final results of the complete calculation with test results under the particular loading histories adopted.

The question which arises is: what differences in life prediction can be expected from the various proposals, knowing local stress-strain history, but assuming that the damage due to local stress-strain cycles is linearly

Ref.	Simulation of Metal - Deformation	Material Behavior Strain Hardening Strain Softening	Cycle Dependent Stress Relaxation	Local Stress and Strain at Stress Concentration
1	Rheological Model: Hysteresis Loops	$n^* = \text{konst.}$ $K^* = f(N, \epsilon_{pa})^*$	Reduction of Model Element Stiffness	Modified Neuber Rule $\sigma \cdot \epsilon = \frac{K_t \cdot \Delta S^2}{E}$
2	Memory Rules: Hysteresis Loops	Modification of Ramberg - Osgood Type Equation	Reduction of Local Mean Stress	
3	Memory Rules: Hysteresis Loops	$n^* = \text{konst.}$ $K^* = f(N/N_f)^*$	Reduction of Polygon Stress Component	
4	Peaks of Hysteresis Loops (Residual Stress)	...	Reduction of Residual Stress	Neuber Rule $\sigma \cdot \epsilon = \frac{K_t \cdot \Delta S^2}{E}$
5	Ideal Elastic - Plastic Stress - Strain - Curve	...	...	$K_t \cdot S_{\max} \geq F_{ty}, \sigma_{\max} = F_{ty}$ $[\sigma_{\max} - K_t \cdot \Delta S] \geq F_{cy}, \sigma_{\min} = F_{cy}$
$* \epsilon_{p,a} = \left( \frac{\sigma}{K^*} \right)^{\frac{1}{n^*}}$				

FIG. 1—Simulation of local stress-strain behavior.

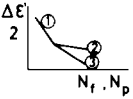
Ref.	Unit of Damage	S-N Data Required		Consideration of Mean Stress	Accu- mulation
		Const. Amplitude Test	Representation		
1	Hysteresis Loop: $\epsilon_a, \sigma_m$	Strain Control $R_\xi = -1.0$ (Unnotched)	Three Line- S-N-Curve 	$\frac{\Delta \epsilon'}{2} = \frac{\Delta \epsilon}{2} \cdot \frac{\sigma_m^{0.73}}{E}$	Linear, Initiation ② + ③ Propagation ① + ③
2					
3	Damage per Polygon Element	Strain Control $R_\xi = -1.0$ (Unnotched)	S-N-Curve $2 \sigma_{\max}, 2 \epsilon_a = f(N_f)$	Determination of $2 \sigma_{\max} \cdot 2 \epsilon_a$	Linear
4	Stress Cycle $S_r, \Delta \sigma_m$	Stress Control (Notched or Unnotched)	Constant Life Diagram	Change of S-N Curve Slope with Change of Residual Stress	Linear
5	Stress Cycle $S_a, S_m$	Stress Control $S_m = 0$ (Notched)	S-N-Curve $(K_t \cdot S_a)_{S_m} = f(N)$	RAE-Method $S_a = f(S_m)$	Linear

FIG. 2—Damage calculation in local stress fatigue analysis methods.

accumulated? Some research work has been undertaken to answer this particular question, but it was not intended to develop a procedure of general applicability or to compete with the available local stress fatigue analysis methods. To achieve this goal, the stress-strain history at a notch root was determined experimentally, thus avoiding the uncertainties inherent in the theoretical simulation of the elastoplastic stress-strain behavior at the notch root.

## Procedure

### *Specimen Load Program*

Notched and unnotched specimens shown in Fig. 3 were manufactured from both the aluminium alloys Al-Cu-2Mg (sheet) and AZ 74/72 (extrusion) equivalent to 2024-T 3 and 7075-T 6, respectively. The center notched specimens had an 8-mm-diameter hole which, for the geometry adopted, corresponded to a stress concentration factor of  $K_t = 2.5$ .

Two program load sequences (Fig. 4) were chosen to represent the load history at the wing lower surface of a transport airplane. The first stress sequence (Fig. 4 *a*) contained a ground-air-ground (GAG) cycle and was called the standard program. This standard program was modified by omitting the ground load, and was then called program without GAG cycle (Fig. 4 *b*). Both programs included one large air-load cycle occurring once

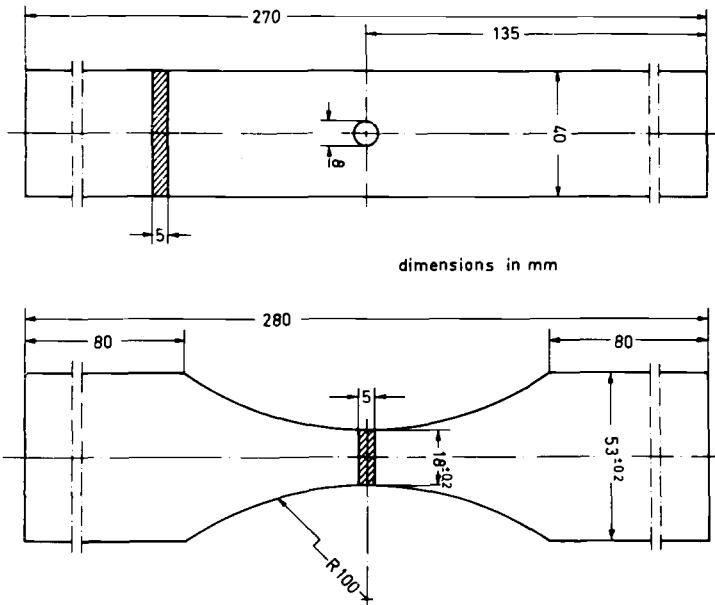


FIG. 3—Specimens, notched and unnotched.

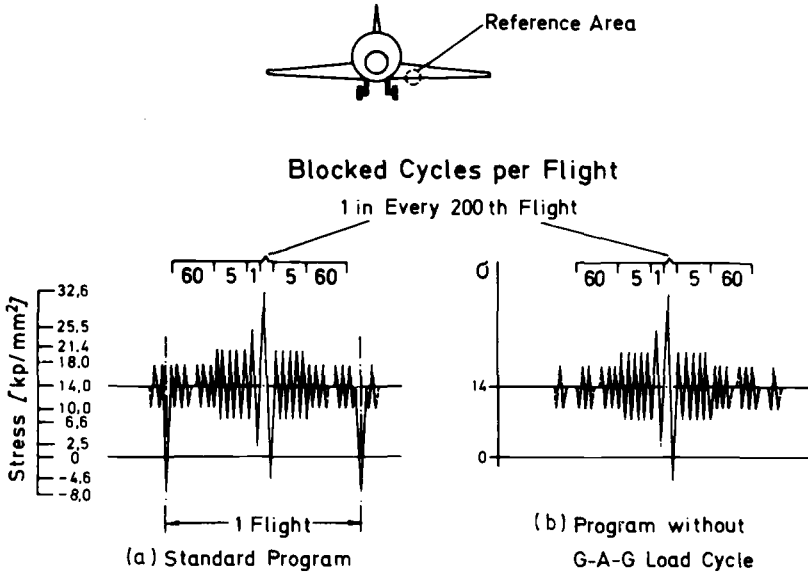


FIG. 4—Loading programs.

in every 200 flights which was first applied in the 100th flight. Excluding the GAG cycles and the large air-load which occurred every 200 flights, each flight contained 131 load cycles. More detailed information on the load program is given in Ref 8.

### *Experimental Procedures*

Notched and unnotched specimens were loaded with the flight-by-flight nominal stress sequences and also under constant-amplitude loading conditions in a tape-controlled servohydraulic testing machine (Schenck-Hydropuls) by a 60-kN cylinder. The deformation of the hole was recorded continuously during fatigue testing as described in Ref 8 to determine the life-to-crack initiation. At that stage, the crack was still very small with a projected surface of 0.3 mm<sup>2</sup>. It is the authors' opinion that, for this size of crack and severity of stress concentration, the crack development is still governed by the stress concentration. Local strain at the hole was measured continuously and recorded by strain gages installed in the hole [8]. Because of both poor fatigue strength of the strain gages and the zero-point drift, the measured values can be relied on only over a relatively short portion of the lifetime. Accordingly, a measuring procedure was developed which was able to distinguish between the zero-point drifts of the strain gages arising in the course of long recording times and the actual strain redistributions that occurred at the notch root.

The loads needed to force an unnotched specimen to follow the recorded strain sequence were also measured and recorded continuously. This method, called the companion specimen method, generally is applied [9-11] for determining the stress behavior at the notch root.

*Life Predictions*

From the continuous records of the local stress and strain sequences, the mean strains and mean stresses were determined and plotted over the elapsed lifetime (number of flights). Figure 5 shows (for the Al-Cu-2 Mg material) the mean strain and mean stress sequences for the air loads between the large air load occurring in every 200th flight. It was found that the mean strains and stresses tended to stabilize within 5 to 20 percent of the life-to-crack initiation. The average mean stress approached by the stabilization process may be designated the "effective mean stress." After stabilization, the residual stresses ( $\sigma_R$ ) can be defined by  $\sigma_R = \bar{\sigma} - K_t S_m$ , where  $\bar{\sigma}$  = effective

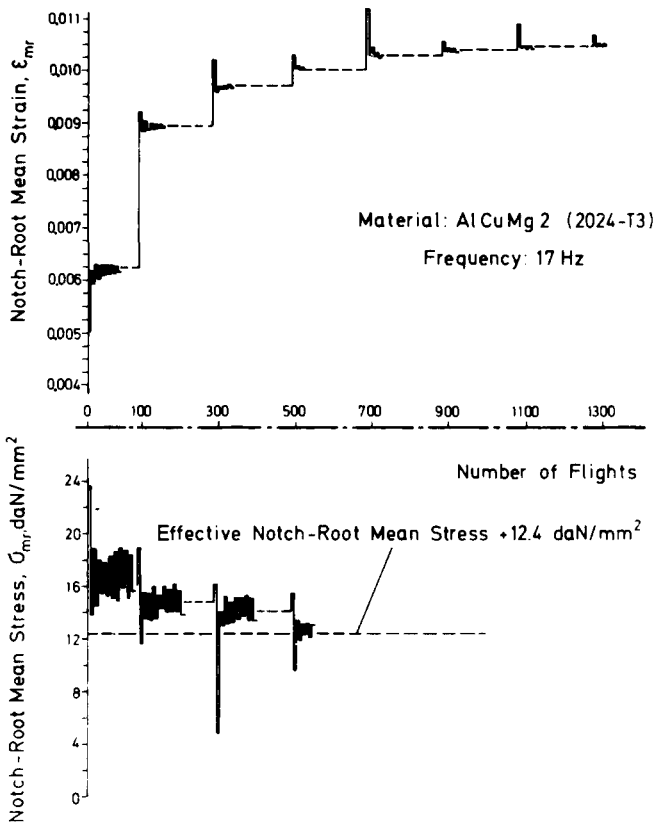


FIG. 5a—Measured notch root mean stress and mean strain sequence: standard load program.

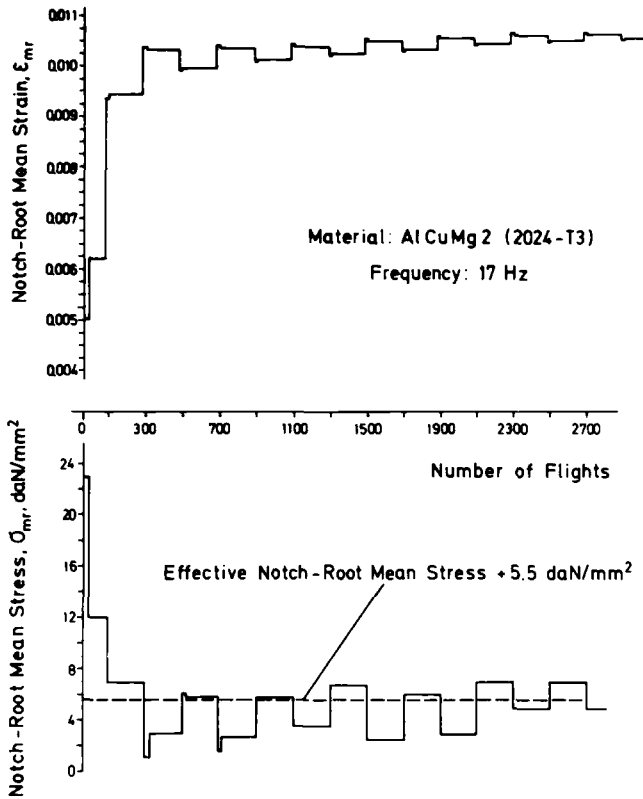


FIG. 5b—Measured notch root mean stress and mean strain sequence: load program without GAG cycle.

mean stress, and  $S_m$  = nominal mean stress. The effective mean stresses derived from flight-by-flight and constant-amplitude loading are summarized in Table 1.

Fatigue life-to-crack initiation was predicted using three methods for defining the stresses to be used in the damage calculations. Within each method, the partial damage was linearly accumulated, and the phenomenon of rapid local mean stress stabilization was utilized by Methods A and B. Method A employed the local mean stresses (Table 1) and the cyclic stress-strain curves together with plots of “quasi-elastic” notch root stress versus measured notch root strain as shown in Fig. 6 to determine the local alternating stresses. Unnotched specimen  $S-N$  data reported in Ref 12 for Al-Cu-2 Mg (2024-T 3) and in Ref 13 for AZ 74/72 (7075-T6) were used as a basis for these damage calculations.

For Method B, the virgin open-hole specimens were preloaded by one load cycle (Ref 8) to induce stresses and strains of the same magnitude as those of the effective mean stresses (Table 1) and mean strains measured

TABLE 1—Measured effective mean stresses.

Aluminum Alloy	Load Program	Nominal Stress Cycle		Flight-by-Flight Loading,		Constant-Amplitude Loading,	
		$S_m$ , daN/mm <sup>2</sup>	$S_a$ , daN/mm <sup>2</sup>	Effective Mean Stress, $\bar{\sigma}_m$ , daN/mm <sup>2</sup>			
Al-Cu-2Mg (2024-T3)	standard	14.0	18.6	1.5	1.0	1.0	1.0
		14.0	11.5	12.5	11.5	11.5	11.5
		14.0	7.4	12.5	21.0	21.0	21.0
		14.0	4.0	12.5	27.5	27.5	27.5
		12.3	20.3	0	0	0	0
	without GAG cycle	8.7	16.8	4.0	2.5	2.5	2.5
		14.0	18.6	1.5	1.0	1.0	1.0
		14.0	11.5	5.5	11.5	11.5	11.5
		14.0	7.4	5.5	21.0	21.0	21.0
		14.0	4.0	5.5	27.5	27.5	27.5
AZ 74/72 (7075-T6)	standard	14.0	18.6	5.0	7.5	7.5	7.5
		14.0	11.5	16.0	21.5	21.5	21.5
		14.0	7.4	16.0	29.0	29.0	29.0
		14.0	4.0	16.0	33.5	33.5	33.5
		12.3	20.3	3.5	7.0	7.0	7.0
	without GAG cycle	8.7	16.8	4.0	8.0	8.0	8.0
		14.0	18.6	5.0	7.5	7.5	7.5
		14.0	11.5	11.0	21.5	21.5	21.5
		14.0	7.4	11.0	29.0	29.0	29.0
		14.0	4.0	11.0	33.5	33.5	33.5

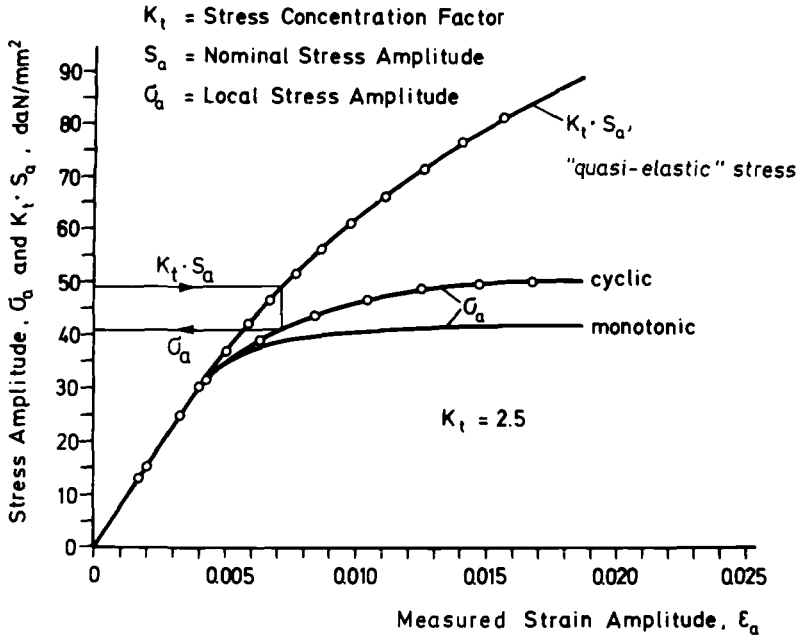


FIG. 6—Stress-strain behavior of Al-Cu-2Mg (2024-T3).

during flight-by-flight loading. The preloaded specimens were then subjected to constant-amplitude loading using the nominal stress cycles of the flight-by-flight load programs, including the peak-to-peak GAG cycles. The local stresses and strains induced at the hole by preloading did not change during the constant-amplitude loading. Life was estimated using nominal stresses and the results of the constant-amplitude tests.

Method C is the conventional method employing nominal stresses ( $S = F/A$ ) and notched specimen  $S-N$  data and is included for comparison. The cycles of nominal stress of the flight-by-flight load programs and constant-amplitude fatigue test results of the open-hole specimen were used to calculate damage. The damage calculations for a single load cycle are shown as examples in Table 2.

In both the flight-by-flight and the constant-amplitude experiments with open-hole specimens, crack initiation had occurred between 60 and 70 percent of the life to fracture.

## Results and Discussion

The results of the life predictions and the flight-by-flight tests are summarized in Table 3. The conventional nominal stress analysis (Method C) gives conservative life estimates for the load program without GAG cycle and unconservative life estimates for the standard program. This has been

TABLE 2—Example of damage calculation for an open-hole specimen,  $K_t = 2.5$ .

Load cycle: $S_m = 14 \text{ daN/mm}^2$ ; $S_a = \pm 7.4 \text{ daN/mm}^2$ (standard program). Number of occurrences: $n = 4.0 \times 10^5$ (within 40 000 flights). Material: 2024-T3.					
Method A					
(local stress cycle, $S$ - $N$ data from unnotched specimens)					
Local Mean Stress, $\sigma_m$ , da N/mm <sup>2</sup>	Quasi-elastic Stress Amplitude, $K_t \cdot S_a$ , da N/mm <sup>2</sup>	Local Stress Amplitude, $\sigma_a$ , da N/mm <sup>2</sup>	Life to Failure of Unnotched Specimen, $N_f$	Damage, $n/N_f$	
12.5 (Table 1)	18.5	18.5 <sup>a</sup>	$1.0 \times 10^7$ (Ref 12)	4.0	
Method B					
(nominal stress cycle, $S$ - $N$ data from prestressed open-hole specimens)					
Nominal Mean Stress, $S_m$ , da N/mm <sup>2</sup>	Nominal Stress Amplitude, $S_a$ , da N/mm <sup>2</sup>		Life-to-Crack Initiation of Pre- stressed Open-Hole Specimen, $N_p$	Damage, $n/N_p$	
14	7.4		$1.3 \times 10^5$	3.08	
Method C					
(nominal stress cycle, $S$ - $N$ data from open-hole specimens)					
Nominal Mean Stress, $S_m$ , da N/mm <sup>2</sup>	Nominal Stress Amplitude, $S_a$ , da N/mm <sup>2</sup>		Life-to-Crack Initiation of Open-Hole Specimen, $N$	Damage, $n/N$	
14	7.4		$8.6 \times 10^4$	4.65	

<sup>a</sup>  $\sigma_a$  is equal to  $K_t \cdot S_a$  because this load cycle does not create plastic deformation in the stabilized stage; for the determination of  $\sigma_a$ , see Fig. 6.

TABLE 3—Results of life predictions and tests.

Aluminum Alloy	Load Program	Predicted Life for Crack Initiation, No. of Flights <sup>a</sup>			Test Life, No. of Flights <sup>a</sup>	
		Method A	Method B	Method C	Crack Initiation	Final Failure
Al-Cu-2Mg (2024-T3)	standard	2840	5510	4540	1600	2600
	without GAG cycle	10 350	11 900	6540	7800	12 200
AZ 74/72 (7075-T6)	standard	1620	4450 <sup>b</sup>	2490 <sup>b</sup>	1390 <sup>b</sup>	2250
	without GAG cycle	5400	38 500 <sup>b</sup>	4210 <sup>b</sup>	9270 <sup>b</sup>	14 500

<sup>a</sup>Log average.<sup>b</sup>Estimated from 2024-T3 test results.

found previously and was therefore not unexpected. For this method of defining stress, the load programs used were considered as extremes, and any improvements in life prediction methods should thus have opposite tendencies when applied to each of the two programs. To illustrate this, the ratios, test life to estimated life, are plotted in Fig. 7 where ratios above 1.0 indicate conservative estimations and ratios below 1.0, unconservative estimations. In case of the program without GAG cycle, the expected tendencies occurred for Methods A and B and also for the standard program using Method A. However, the lives predicted by Method A still varied from the test lives by factors of up to 1.8.

Another important feature of the quality of life prediction is the consistency of their results. The predictions of the nominal stress fatigue analysis (Method C) vary between a minimum value of 0.35 and a maximum value of 2.2 which corresponds to a factor of 6.2. The predictions of Method A are spread between 0.56 and 1.72 corresponding to a factor of 3.1, and the predictions of Method B are scattered between 0.24 and 0.65 corresponding to a factor of 2.7. These are also indicated in Fig. 7. All life estimates of Method B were on the unconservative side, but they had the greatest consistency.

After the rapid stabilization of the local mean strains and stresses (see Figs. 5 a, b) the local stress-strain cycles would be described sufficiently by the effective mean stress (Table 1) and the alternating local stresses corresponding to the alternating nominal stress. In this stabilized stage, the sequence of

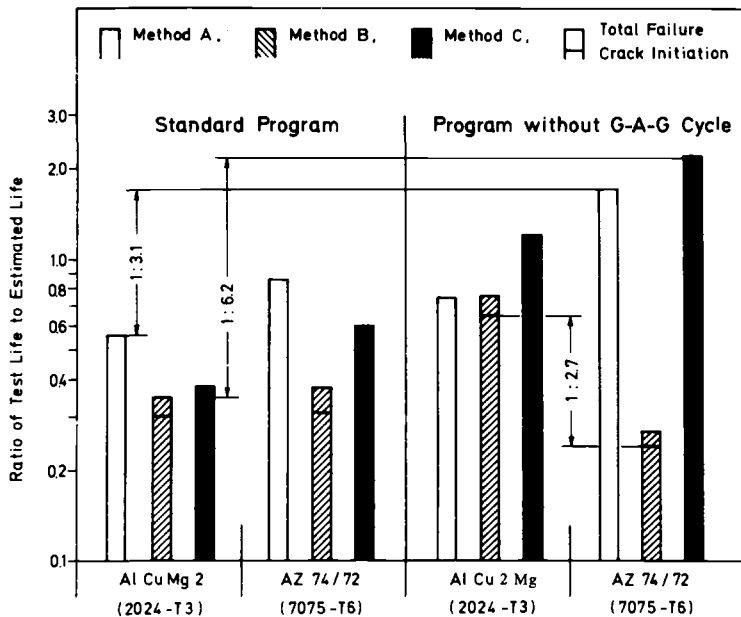


FIG. 7—Comparison of estimated life with test life.

nominal stresses resulted in only minor variations of the local mean stress and strain. These variations (and those which had occurred before the mean stress and strain stabilized) were not included in the determination of the local stress and strain cycles in Methods A and B.

The differences between flight-by-flight and constant-amplitude effective mean stresses (see Table 1) were reflected by the differences between the results using Methods B and C (Table 3). The differences between the results from Methods A and B can be related to the  $S-N$  data used which, for Method A, were derived from load-controlled testing to fracture of the unnotched specimens (Fig. 3) having a larger volume subjected to the local stress-strain cycles than the open-hole specimens used for Method B. In addition, as Method B incorporates experimentally most of the relevant parameters described in Figs. 1 and 2, the results contain less uncertainties than those involved in using the other methods. Method B is therefore regarded as the most accurate.

### Conclusion

Finally the aim of this research work is stated again: to establish what differences in life prediction would occur by using three different methods of specifying notch root stress-strain history, but using a linear cumulative damage rule in each case. Again it is emphasized that it was not intended to compete with the readily applicable procedures mentioned in the paper; in particular, the local stress fatigue analysis Method B used here requires extensive measurements at the structural element.

With respect to the load histories adopted for this paper, that is, transport aircraft wing spectrum with and without GAG cycles, the following conclusions and recommendations can be stated:

1. Using an analysis based on nominal stresses, the predicted lives varied by a factor of 6.
2. Although increasing accuracy of the incorporation of local stress-strain behavior in future fatigue life analyses methods will reduce this factor, it may not become less than 3.
3. The consistency of the ratio, test to predicted lives, should be a criterion for evaluating local stress or strain fatigue analysis methods.
4. For further improvements in life prediction, research effort should again be directed to the mechanism of damage accumulation.

### References

- [1] Martin, J. F., Topper, T. H., and Sinclair, G. M., *Materials Research and Standards*, Vol. II, No. 2, Feb. 1971, pp. 23-28, 50.
- [2] Jhansale, H. R. and Topper, T. H. in *Cyclic Stress-Strain Behavior-Analysis, Experimentation, and Failure Prediction*, ASTM STP 519, American Society for Testing and Materials, May 1973, pp. 246-270.
- [3] Wetzel, R. M., "A Method of Fatigue Damage Analysis," Department of Civil Engineering, University of Waterloo, Sept. 1971.

- [4] Impellizeri, L. F. in *Effects of Environment and Complex Load History on Fatigue Life*, ASTM STP 462, American Society for Testing and Materials, Jan. 1970, pp. 40-73.
- [5] "Cumulative Fatigue Damage Calculations (Effect of Correcting Mean Stress at Stress Concentrations)," Engineering Sciences Data Item Number 71028, Engineering Sciences Data Unit, London, Oct. 1971.
- [6] O'Neill, M. J., "A Review of Some Cumulative Damage Theories," Aeronautical Research Laboratories, Melbourne, Report SM 326, June 1970.
- [7] Wheeler, O. E., *Transactions of the ASME, Journal of Basic Engineering*, Vol. 94, No. 1, American Society of Mechanical Engineers, March 1972, pp. 181-186.
- [8] Schütz, D., "Residual Stresses in Notches Produced by Variable Operational Loads and their Importance for the Application of the Linear Cumulative Damage Hypothesis," Translation from LBF-Report FB-100, (1972), RAE Library Translation No. 1800, Royal Aircraft Establishment, Farnborough, March 1975.
- [9] Wetzell, R. M., *Journal of Materials*, Vol. 3, No. 3, Sept. 1968, pp. 646-657.
- [10] Crews, J. H., Jr., and Hardrath, H. F., *Proceedings*, Society for Experimental Stress Analysis, Vol. 23, No. 1, 1966, pp. 313-320.
- [11] Edwards, P. R., "An Experimental Study of the Stress Histories at Stress Concentrations in Aluminium Alloy Specimens under Variable Amplitude Loading Sequences," RAE Technical Report No. 70004, Royal Aircraft Establishment, Farnborough, Jan. 1970.
- [12] Schütz, W., "Zeit- und Betriebsfestigkeit gekerbter und ungekerbter Flachstäbe aus 3.1354.5," LBF TM No. 42/68, Laboratorium für Betriebsfestigkeit, Darmstadt, Germany, Dec. 1968.
- [13] Schütz, W., "Zeitfestigkeit gekerbter und ungekerbter Flachstäbe aus 3.4354.7 (Fuchs AZ 74/72, stranggepreßt)," LBF TM No. 24/67, Laboratorium für Betriebsfestigkeit, Darmstadt, Germany, May 1967.

